Local Helioseismology of Magnetic Activity

A thesis submitted for the degree of:
Doctor of Philosophy

by

Hamed Moradi
B. Sc. (Hons), B. Com

Centre for Stellar and Planetary Astrophysics
School of Mathematical Sciences
Monash University
Australia

February 12, 2009

Contents

Abstract

Over the years, local helioseismology has provided us with unprecedented insights into the structure and dynamics of solar active regions, in particular sunspots, which for a long time have been known to be dominated by strong magnetic activity. However, even though significant inroads have been made over the last two decades since the inception of the field, there are still a number of unanswered questions regarding physical conditions in the solar interior that need to be addressed. In this thesis, we aim to shed light on two of these open questions: i) what is the true nature and extent of the sub-surface structure of active regions and sunspots? ii) how do we effectively diagnose the seismic response of the solar interior to flare-induced energetic transients, and what is their underlying cause?

Addressing the first question requires the development of MHD simulations to test observational inferences made in regions of strong surface magnetic fields. We devise and apply a numerical forward model based on MHD ray theory to address some of the ambiguous and inconsistent interpretations of helioseismic travel times that have resulted from tomographic observations in the vicinity of sunspots. The resulting simulations have shown that it is feasible to use ray theory in model sunspots to produce travel-time shifts than can meaningfully be compared with observations. In order to validate the results from ray theory, we also conduct detailed comparative studies with an existing simulation code developed for analysing the interaction of linear waves with magnetic structures in nonuniform atmospheres. Together, these numerical forward models provide compelling evidence which indicates that the effect of the magnetic field on helioseismic waves can not be considered to be small near the surface, with travel time inhomogeneities observed through sunspots appearing to be dominated by MHD physics. These results are the strongest indication yet that surface magnetic fields are directly and significantly altering the magnitude and lateral extent of linear inversions of sunspot structure (i.e., sub-surface wave and sound speed perturbations) made by time-distance helioseismology.

On addressing the second question, we employ various local helioseismic methods to distinguish and analyse the multi-wavelength observational signatures of seismic emissions from three solar flares – X1.2-class flare of 15 January 2005, M7.4-class flare of 14 August 2004 and M6.7-class flare of 10 March 2001. In-depth correlative studies were conducted, with the resulting analysis showing that all three flares exhibited the same close spatial alignment between the sources of the seismic emission and impulsive visible continuum emission as previous flares, reinforcing the hypothesis that the acoustic emission may be driven by radiative "back-warming" – heating of the low photosphere by intense Balmer and Paschen continuum-edge recombination radiation from the overlying ionized chromospheric medium. Detailed analysis of the magnetic field topology of the host active regions also reveal the existence of a close relationship between the heights of the coronal magnetic loops that conduct high-energy particles from the flare and the seismicity of the energetic transients.

General Declaration

In accordance with Monash University Doctorate Regulation 17/Doctor of Philosophy and Master of Philosophy regulations the following declarations are made:

I hereby declare that this thesis contains no material which has been accepted for the award of any other degree or diploma at any university or equivalent institution and that, to the best of my knowledge and belief, this thesis contains no material previously published or written by another person, except where due reference is made in the text of the thesis.

This thesis includes five (5) original papers published in peer reviewed journals and one (1) unpublished paper. The core theme of the thesis is the local helioseismology of magnetic activity. The ideas, development and writing up of all the papers in the thesis were the principal responsibility of myself, the candidate, working within the Centre for Stellar and Planetary Astrophysics, School of Mathematical Sciences, under the supervision of Prof. Paul Cally and Dr. Alina Donea.

The inclusion of co-authors reflects the fact that the work came from active collaboration between researchers and acknowledges input into team-based research.

In the case of thesis chapters 2 - 4, my contribution to the work involved the following:

Thesis chapter	Publication title	Publication status	Nature and extent of candidate's contribution
2	Time-distance modelling in a simulated sunspot atmosphere.	Published, 2008 (Solar Phys., 251, 309-327)	Key ideas and initiation, development of the code, numerical modelling, produced all figures, wrote the paper.
3	Numerical models of travel-time inhomogeneities In sunspots.	Published, 2009 (ApJ, 690, L72-L75).	Key ideas and initiation, significant parts of the numerical modelling and analysis, produced all figures, significant contribution to discussion and analyses of results, wrote much of the text.
3	Deep-focus diagnostics of sunspot structure.	Submitted for review, February 2009 (ASSP).	Key ideas and initiation, numerical modelling and analysis, produced all figures, wrote the paper.
4	Helioseismic analysis of the solar flare-induced sunquake of 2005 January 15.	Published, 2007 (MNRAS, 374, 1155-1163).	Key ideas and initiation, data reduction and observational analysis, produced Figures 1-4 and 7, significant contribution to discussion and analyses of results, wrote much of the text.
4	From Gigahertz to millihertz: a multiwavelength study of the acoustically active 14 August 2004 M7.4 solar flare.	Published, 2007 (Solar Phys., 245, 121-139).	Key ideas and initiation, significant parts of data reduction and observational analysis, prepared Figures 1-4, significant contribution to discussion and analyses of results, wrote parts of the text.
4	Seismic emissions from a highly impulsive M6.7 solar flare.	Published, 2008 (Solar Phys., 251, 613-626).	Key ideas and initiation, significant parts of data reduction and observational analysis, prepared Figures 1-3, significant contribution to discussion and analyses of results, wrote parts of the text.

I have renumbered sections of submitted or published papers in order to generate a consistent presentation within the thesis.

Signed: ………………………………………………………………………

Date: ………………………………

Acknowledgements

First and foremost, I extend my deepest thanks to my supervisor, Paul Cally, who has not only provided me with continued support and guidance from day one, but has also taught me much of what I know about helioseismology today. It has been an absolute privilege to work with someone with such an astute knowledge of solar physics. Alina Donea, my co-supervisor, has also been an inspiring figure for me throughout my studies. I thank her for opening my eyes to the world of solar physics that fateful day in Honours, and for the amazing way she always has time for her students.

My extended gratitude also to a number of people outside of Monash who I've had the pleasure of meeting and working with over the years: Shravan Hanasoge, for teaching me a great deal about numerical modelling; Charlie Lindsey, for his great insights into flare seismology and helioseismic holography; and Aaron Birch, Paul Rajaguru and Sebastièn Couvidat, for their advice and patience in teaching me the many intricate aspects of time-distance helioseismology.

A belated thanks also to the student members of the Clique: Juan, Diana and John. It has been a pleasure to share an office and work with Juan over the years. I appreciated his insights into solar physics and also his great sense of humour and endless patience with my (unsuccessful) attempts at learning Spanish. Many thanks also to Diana and John for being such great friends and for our many entertaining discussions, and also to the rest of the astro/maths crew (past and present) for providing me with endless hours of entertainment over the years.

Finally, I would like to dedicate this work to my family, in particular my mum and dad, who have always provided me with unconditional love, support and encouragement in all my endeavours.

Chapter 1

Introduction

This chapter introduces the reader to the key issues and concepts required to appreciate the motivation for this research. A brief review of helioseismology is presented with a focus on the local helioseismology diagnostic techniques used extensively in this thesis. This is followed by a general overview of sunspots and sunspot seismology, familiarizing the reader with some of the pertinent issues faced by both observers and theoreticians. We then delve into the details of the different forward modelling tools at our disposal today, followed by a brief review of the observational aspects of solar flares and the detection of helioseismic responses to flare-driven seismic transients. We conclude by summarizing the key research aims and work contained in this thesis.

1.1 Helioseismology

Helioseismology is a diagnostic tool that allows one to probe the solar parameters to compare with theory and observation. Methods of helioseismology can be divided into two classes: global and local. The first tools to be generally employed in analysing the wave-field of the Sun were the techniques of global helioseismology. In this approach, the normal modes of the Sun are used to infer properties via calculation of the mode eigenfunctions given the changes brought about by perturbations to the background state[1]. With a sufficiently good theoretical forward model, it becomes possible to attempt to compute how changes in the observed modes of the Sun are related to changes throughout the entire sphere. Local helioseismology is a relatively young field of study that has transformed our view of the Sun through sub-surface imaging of active region dynamics. We shall discuss this particular field in greater detail a little later on.

The first observations of the oscillations of the solar surface were made by Leighton et al. (1962) and Evans and Michard (1962). Leighton et al. (1962) reported surface Doppler velocity observations with a combined amplitude of 500 ms^{-1}. They also noted that the observed surface velocities appeared to have a strong oscillatory behaviour with a period close to five minutes. Ulrich (1970) later described these as standing acoustic waves trapped in the solar interior by the photosphere. Deubner (1975) confirmed the predicted modal structure from definite ridges in the wavenumber-frequency, (k, ν), diagram. Figure 1.1 depicts the ridges of power associated with k and ν. A few years later, Claverie et al. (1979) identified lower wavenumber oscillations with the same period providing conclusive evidence of global modes of oscillation within the Sun. With a full range of modes, properties of the solar interior can be inferred by comparing theoretically calculated solar oscillation spectra, observationally obtained power spectra and diagnostic diagrams of pressure modes.

Today the signals from these oscillations can be detected using space-borne instruments such as the Michelson Doppler Imager (MDI) (Scherrer et al., 1995) aboard the Solar and Helioseismic Observatory (SoHO) satellite. Launched in 1995, SoHO overcomes the problems suffered by terrestrial observations (e.g., atmospheric turbulence and day-night cycle data gaps) to produce high-quality helioseismic data. The MDI instrument computes the vibration velocity by processing dark absorption line

[1]It should be noted that not all global methods use linearization about a background state. Some invert directly (see e.g., Gough, 1984).

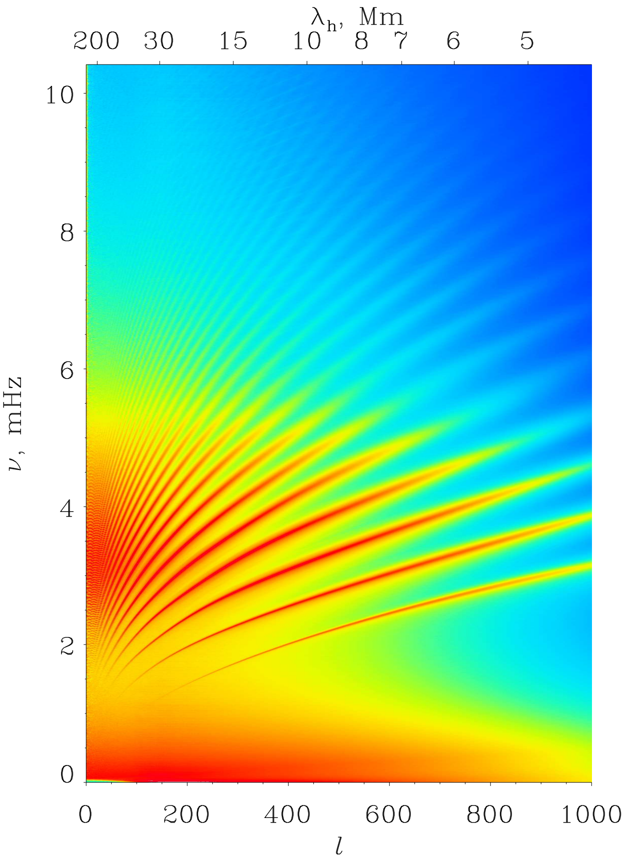

Figure 1.1: The Doppler velocity power spectrum of the Sun as observed by the MDI instrument. The lower horizontal axis is the spherical harmonic degree, ℓ, an alternate measure of the wave-length of the wave, shown on the upper part of the graph as λ_h. Image obtained from the soi.stanford.edu website

shifts in the Ca+ K-line spectrum. The dark absorption lines are formed by Ni atoms oscillating in the solar photosphere. The shifts can be used to infer the changes in the wavelength of light emitted from the photosphere and produce a map of velocities of the localized vibrations on the solar surface, also known as a Dopplergram. Continuous coverage is also provided by the Global Oscillations Network Group (GONG) array of ground-based instruments, which has achieved spatial resolutions similar in quality to that of MDI.

The normal modes of oscillation of the Sun can be categorized as either p-modes, f-modes, or g-modes. Each mode is characterized by its spherical harmonic degree, ℓ (which is approximately the number of wavelengths around the solar circumference), and the radial order, n (the number of nodes in the radial direction). The g- (or "gravity") modes are internal gravity waves for which the primary restoring force is buoyancy, and are almost totally confined to the deep solar interior. The f- (or "fundamental") mode ($n = 0$) is an incompressive, surface gravity wave with amplitude that decays roughly exponentially with depth away from the solar surface. The dispersion relation is similar to that for deep water waves, $\omega^2 = gk_h$, where ω is the angular temporal frequency of the wave, $g = 274$ ms^{-2} is the gravitational acceleration at the Sun's surface, $k_h = \sqrt{\ell(\ell+1)}/R_\odot$ is the horizontal wave-number and $R_\odot = 696$ Mm is the solar radius. The p- (or "pressure") modes are gravity-modified acoustic waves, with pressure the primary restoring force. The discrete mode pattern is a consequence of the existence of a resonant cavity with reflecting boundaries. As illustrated in Figure 1.2, the photosphere essentially acts like a mirror, with the change in physical parameters providing such an abrupt change in conditions that it represents a fixed node for oscillations.

In the absence of magnetic fields, most of the modes can be approximated by plane waves satisfying the dispersion relation,

$$\omega^2 = c^2k^2 + \omega_c^2, \tag{1.1}$$

where c is the sound speed, $k = |\mathrm{k}|$, and the wave-vector $\mathbf{k} = k_r\mathbf{e}_r + k_h\mathbf{e}_h$. The final term, ω_c^2, represents the square of the acoustic cut-off frequency, the uppermost limit below which radial acoustic waves will be reflected from the surface (this is at approximately 5.3 MHz in the quiet Sun). Above this frequency rays will propagate freely into the upper atmosphere where they are normally subject to non-linear and non-adiabatic effects. The lower turning point of the ray path (i.e. where a pure acoustic wave propagates horizontally) is determined by the Lamb frequency, $\omega_L^2 = \ell(\ell+1)c^2/r_t^2$ and r_t is the turning depth at $k_r = 0$. The horizontal surface wavelength of the mode is given by $\lambda_h = 2\pi/k_h = 2\pi R_\odot/\sqrt{\ell(\ell+1)}$. Rays with higher ℓ are shallow and have a smaller horizontal wavelength, whereas those with lower ℓ penetrate deeper and have a larger horizontal wavelength. Helioseismology exploits this property to infer structural details of the solar interior. For all helioseismic methods any deviations from the path are seen as acoustic anomalies along the ray path in the solar interior.

Global helioseismology has had much success in determining such features as the sound speed profile (e.g., Christensen-Dalsgaard et al., 1985), the depth of the convection zone (e.g.,Christensen-Dalsgaard et al., 1991; Basu and Antia, 1997), the solar differential rotation (e.g., Gough, 1984; Brown et al., 1989; Charbonneau et al.,

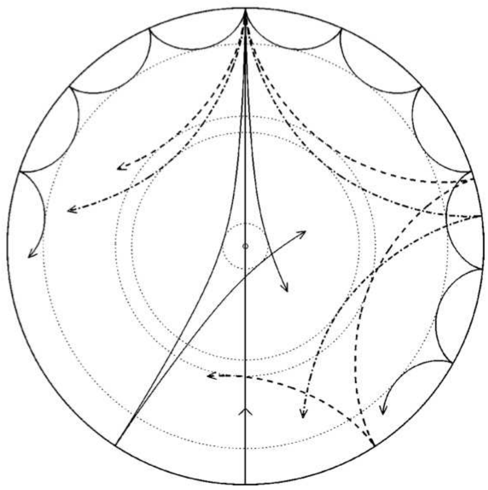

Figure 1.2: Propagation of rays of sound in a cross section of the solar interior, adopted from Christensen-Dalsgaard (2002). The ray paths are bent by the increase in sound speed with depth until they reach the inner turning point (indicated by the dotted circles), where they undergo total internal refraction. At the surface the waves are reflected by the rapid decrease in density.

1999), and the neutrino flux (e.g., Turck-Chièze et al., 2001) to name a few. Whilst the global approach is a method that has proved extremely successful, it is an approach that is spatially limited. The global modes also do not distinguish between the Northern and Southern hemispheres. Unless one considers the perturbations to the eigenfunctions themselves, the detailed spatial distribution of a parameter cannot be better determined. As a result, it is not possible to detect longitudinal variations or flows in meridional planes and other fine structures using global-mode helioseismology (Gizon and Birch, 2005).

In order to examine structure on local scales and those whose asymmetric properties are not visible with global methods, one must use modes that are more finely resolved in space, and can therefore sample local structure. Local helioseismology was developed to complement global helioseismology with the goal to interpret the full wave field observed at the surface, not just the eigenmode frequencies. Local helioseismology has provided promising results on the structure of localized features such as large-scale flows, sub-surface flows, emerging active regions, sunspots and magnetic structures in general, and their interactions in the solar interior. As the subject is reviewed comprehensively by Gizon and Birch (2005), in the proceeding section we shall provide only a brief overview of some of the diagnostic tools employed in local helioseismology.

1.2 Local Helioseismology Diagnostic Tools

There are several distinct but complementary methods for pursuing local helioseismology. In this section we describe the two complementing techniques that are most commonly used to conduct sunspot seismology, time-distance helioseismology and helioseismic holography (both referred to and used extensively in this thesis), and the subsequent observational results that have been gained. In passing only we briefly mention the methods of Fourier-Hankel spectral decomposition and ring-diagram analysis.

The Fourier-Hankel analysis procedure has been used successfully in the past for studying the interaction of p-modes with sunspots. This process essentially decomposes the solar oscillation signal, observed in an annulus around a sunspot, into inward and outward propagating wave modes. The annulus is usually chosen to be small so that the radial form of the wave is described approximately with Hankel functions. Braun et al. (1988), Bogdan et al. (1993) and Braun (1995) investigated p-mode absorption in sunspots and active regions using this method and observed that the amplitudes of the outward moving wave modes were significantly smaller than the inward moving wave components, and their phases were advanced.

The ring-diagram method was introduced by Hill (1988). Ring-diagrams are local power spectra of the wave-field. Cuts at constant frequency through the three-dimensional power-spectrum reveal nested ellipses or rings that change shape and shift centre under the influence of alterations to the solar medium. By fitting the position and shape of the ring (various methods can be used, e.g., Schou and Bogart, 1998; Basu et al., 1999), inversion methods can be used to recover the perturbation to the background model (e.g., flows or sound-speed) from power spectra obtained locally on the Sun. Ring-diagram analysis is ideally suited to large scale surveys of sub-surface conditions, such as large and global scale flow fields (e.g., Haber et al., 2002; Komm et al., 2004).

1.2.1 Time-distance Helioseismology

First introduced by Duvall et al. (1993) and later formalized by, e.g., D'Silva (1996); D'Silva et al. (1996) and Duvall et al. (1997), time-distance helioseismology represents a reworking of methods long used in terrestrial seismology. The method is based on the cross-covariances $C(\mathbf{r_1}, \mathbf{r_2}, t)$ between the solar oscillation signals at two locations in the photosphere. At the heart of time-distance analysis is the use of cross-correlation calculations to compare oscillation signals $\phi(\mathbf{r}, t)$, usually line-of-sight velocity or intensity, and pick out wave-packets that are travelling between points on the surface, producing data similar to the seismograms recovered on the Earth. Wave-packets can then be tracked from one location to another in the photosphere and changes to the propagation of the wave packet inside the Sun can be determined, traditionally by fitting an analytical model of the packets.

The point-to-point cross-covariance can be defined as (Gizon and Birch, 2005):

$$C(\mathbf{r_1}, \mathbf{r_2}, t) = \frac{dt}{T-t} \sum_{\tau} \phi(\mathbf{r_1}, \tau)\phi(\mathbf{r_2}, t+\tau) \tag{1.2}$$

where dt is the sampling rate, and T is the observation time. Figure 1.3 shows an example of a time-distance diagram obtained with MDI data: the x-axis shows the distance Δ between source and receiver, measured in angular separation at the solar surface, while the y-axis shows the time in minutes. The shape of the cross-covariances is clearly visible, as are the different ridges corresponding to the waves bouncing back at the solar surface in between the source and receiver.

Due to the stochastic excitation of acoustic waves by the solar convection zone and also due to the oscillation signal at any location being a superposition of a large number of waves of different travel distances (i.e., of different horizontal phase velocities $v = \omega/k$ for p-modes in the ray approximation, where k is the horizontal wave number and ω is the temporal frequency), these point-to-point cross-covariances are very noisy. As a result, the data cubes first require filtering and the cross-covariances need to be averaged (Duvall et al., 1996). A number of different filters are usually applied to the data. Initially, it is important to remove unwanted signal contributions from solar features like granulation and supergranulation, which are regular over certain scales and hence produce a strongly correlated measurement in a cross-correlation. Removing these features is done via knowledge of their spectral properties e.g. supergranulation has a period of greater than 10 minutes whilst we know that oscillations occur around a central period of 5 minutes and so can be removed with a high-pass filter with a Gaussian roll-off at about 1.7 mHz. Hence a temporal frequency filter is used to remove the unwanted signals due to such convective flows. The surface gravity modes may also be removed by multiplying the power-spectrum of the input

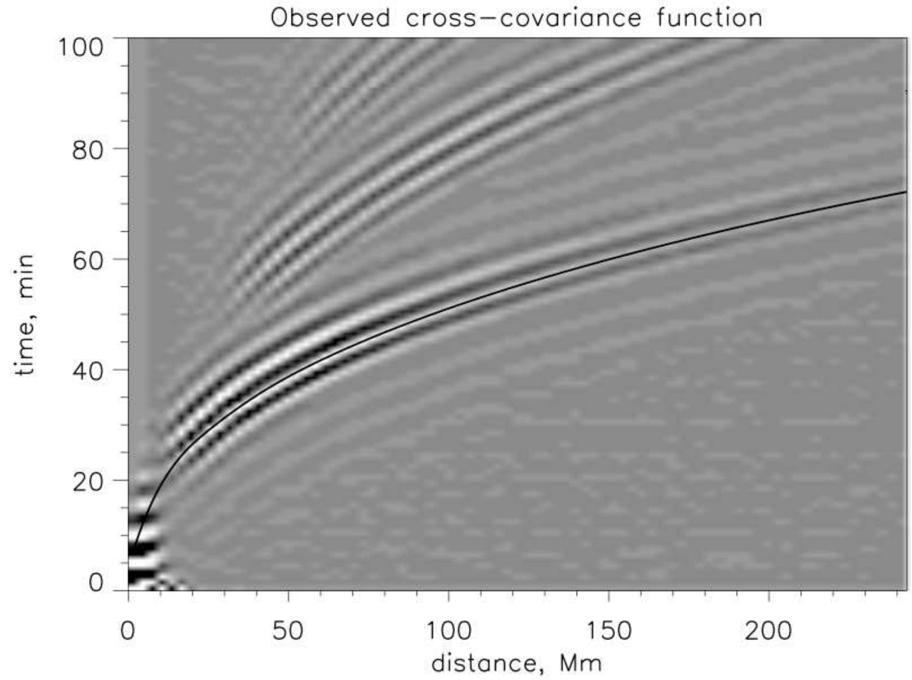

Figure 1.3: An example of a mean cross covariance function obtained from SOHO-MDI data, adopted from Duvall et al. (1997). The solid line is a theoretical plot representing the ray approximation. The greyscale picture is the cross covariance function. At the distance of around 50 Mm, the first, second and third bounces are visible near 30 minutes, 60 minutes and 90 minutes respectively. The fine structure in each of the ridges is caused by the finite band pass of the oscillations.

data with a three-dimensional filter constructed by approximating the locations of the f- and p_1-modes in $k-\omega$ space as polynomials in frequency (unless working with f-modes exclusively). Finally, phase-speed filters $F(k,\omega;\Delta)$ for each travel distance $\Delta = |\mathbf{r_2} - \mathbf{r_1}|$ are also applied to the data.

The rationale behind using a phase-speed filter (instead of only a frequency filter) is that for a particular separation of points that are being cross-correlated, one can calculate the phase-speed (equivalent to determining the lower turning point) associated with waves travelling along the appropriate ray path. In this way one weights against modes that are not of interest. Such filters can also help select waves travelling in specific directions. These filters are given by a simple multiplication in the

Fourier domain,

$$\phi_{\text{filt}} = (\mathbf{k}, \omega) = F(k, \omega)\phi(\mathbf{k}, \omega) \tag{1.3}$$

where ϕ_{filt} is the filtered data, and F is the filter function. Typically, the phase-speed filters are Gaussian,

$$F(k, \omega; \Delta) = \exp\left[-\frac{(\omega/k - v)^2}{2\delta v^2}\right], \tag{1.4}$$

where v is the central phase speed and δv is the width in phase speed. The central phase speeds of the Gaussian filters are derived from a solar model, usually using a ray tracer, but their widths are usually chosen empirically. For instance, if we use ray theory, δv can be related to the difference in horizontal phase speed between that of the shortest and longest rays used with a particular annulus geometry (Couvidat and Birch, 2006).

The averaging scheme depends on the information we wish to extract from the data. For example, in order to study sound-speed or flow perturbations, the point-to-point cross-covariances are averaged over annuli of radius Δ (see Figure 1.4). Then, to further increase the signal-to-noise ratio, such cross-covariances are computed for several distances respectively slightly smaller than, and slightly larger than, Δ (Couvidat et al., 2006). They are averaged to produce a point-to-annulus cross-covariance. A detailed explanation of all these steps in the analysis process can be found in Gizon and Birch (2005), along with a table of distances Δ and commonly used phase-speed filter characteristics.

The most widely used technique to obtain the travel times of the wave packets from the point-to-annulus or point-to-quadrant cross-covariances stems from Kosovichev and Duvall (1997), who modelled the measured cross-correlation function as a Gabor wavelet by expressing the wave-field as a superposition of global normal-mode solutions for standing waves of a spherically symmetric Sun. The cross-covariances are traditionally fitted with two Gabor wavelets, $G(A, \omega_0, \delta\omega, \Delta, \tau_p, \tau_g; t)$, one for the positive times (outgoing waves), and one for the negative times (ingoing waves):

$$G(A, \omega_0, \delta\omega, \Delta, \tau_p, \tau_g; t) = A\cos(\omega_0(t - \tau_p))\exp\left(-\frac{\delta\omega^2}{4}(t - \tau_g)\right) \tag{1.5}$$

where A is the amplitude of the wavelet, ω_0 is the wavepacket central angular frequency, $\delta\omega$ is the wave packet frequency width, t_p is the phase travel time, and t_g is the group travel time. It is most practical to attempt measurements of t_p, in effect to fix the location of a peak of the sinusoid. This is because t_g represents a calculation

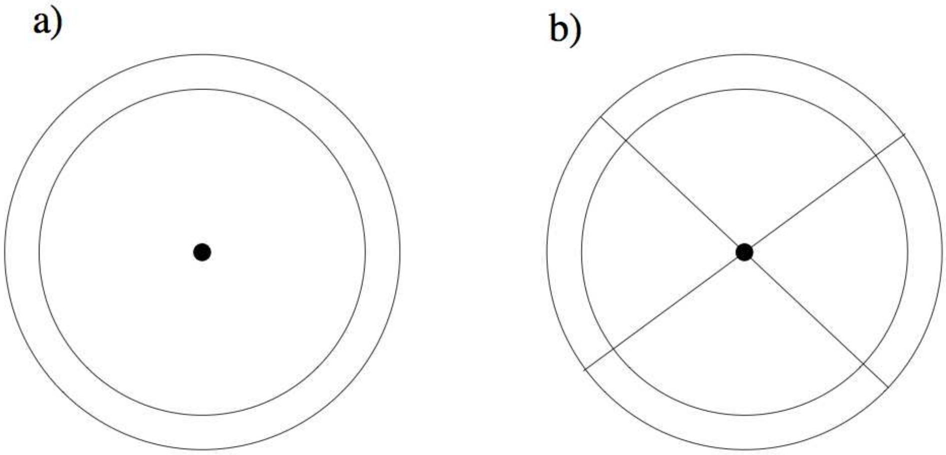

Figure 1.4: A sketch of the different averaging schemes commonly used in time-distance helioseismology: a) centre-to-annulus averaging; b) east-west and north-south quadrant averaging. The central black dots are the source $\mathbf{r_1}$.

of the centre of the wave-packet, i.e. the peak of the Gaussian, which is much harder to accurately determine, particularly at small distances (Δ).

The average of the ingoing and outgoing wave travel times, $\tau_{mean}(\mathbf{r}, \Delta)$, is, in first approximation (see §1.3.2 for a more detailed explanation), sensitive only to the sound-speed $c(r, z)$ in the region of the Sun traversed by the wave packet, while the difference $\tau_{diff}(\mathbf{r}, \Delta)$ in the travel times will be sensitive to flows. When travel times deviate in a consistent manner from the reference travel times (usually calculated in the quiet Sun), there is most likely a local disturbance or inhomogeneity that is source of these anomalies. Inverse theory/modelling then attempts to recover these perturbations from the observed travel-time shifts through the use of sensitivity kernels. This process is referred to as the *linear forward problem* and will be discussed in greater detail later on.

Using a solar model as a reference we can relate the mean travel-time perturbations $\delta\tau_{mean}(\mathbf{r}, \Delta)$ to the sound-speed perturbations $\delta c(\mathbf{r}, z)$ through an integral relation (e.g., Kosovichev and Duvall, 1997),

$$\delta\tau_{mean}(\mathbf{r}, \Delta) = \int\int_S d\mathbf{r}' \int_{-d}^{0} K_c(\mathbf{r}, \mathbf{r}', z; \Delta)\frac{\delta c^2}{c^2}(\mathbf{r}', z)dz, \tag{1.6}$$

where S is the area of the region, and d is its depth. The sensitivity kernel for the relative squared sound-speed perturbations is given by K_c. It is worth mentioning that Equation (1.6) is only approximate because effects on $\delta\tau_{mean}(\mathbf{r}, \Delta)$ other than the sound-speed perturbation are completely ignored. For instance, Brüggen and Spruit (2000) describe the impact of changes in the upper boundary condition in sunspots due to the Wilson depression, Woodard (1997) and Gizon and Birch (2002) demonstrate that increased wave damping in sunspots can introduce shifts in travel times. Gizon and Birch (2002) also caution that local changes in the wave excitation rate (due to a lack of granulation-related wave sources in the region) can also cause changes in time-distance travel times - something that has been confirmed through the forward modelling calculations of Parchevsky and Kosovichev (2007a) and Hanasoge et al. (2008). Finally, as the interaction of acoustic waves with sunspot magnetic fields is strong in the near surface layers, the effect of the magnetic field on the travel times is not expected to be small near the surface. We shall discuss such effects in more detail in §1.3.2,

In a similar manner to $\delta\tau_{mean}(\mathbf{r}, \Delta)$, $\delta\tau_{diff}(\mathbf{r}, \Delta)$ can be related to a vertical flow $v_z(\mathbf{r}, z)$ through an integral relation:

$$\delta\tau_{diff}(\mathbf{r}, \Delta) = \int\int_S d\mathbf{r}' \int_{-d}^{0} K_{v_z}(\mathbf{r}, \mathbf{r}', z; \Delta) v_z(\mathbf{r}', z) dz \tag{1.7}$$

where K_{v_z} is the sensitivity kernel for vertical velocity. Again, equation 1.7 is approximate and ignores the sensitivity of $\delta\tau_{diff}(\mathbf{r}, \Delta)$ to, among others, the horizontal divergence of the flow.

The first efforts at computing the sensitivity of travel times to changes in the solar model were based on the ray approximation (e.g., Kosovichev, 1996; D'Silva et al., 1996; Kosovichev and Duvall, 1997; Kosovichev et al., 2000). In the ray approximation the travel time perturbation is approximated as an integral along the ray path using Fermats principle. Ray theory is based on the assumption that the perturbations to the model are smooth and that the wave packet frequency bandwidth is very large (Gizon and Birch, 2005). Bogdan (1997) showed that the energy density of a realistic wave packet was substantial away from the ray path. This result strongly suggested that perturbations located away from the ray path could have substantial effects on travel times. It is now well known that ray theory fails when applied to perturbations that are smaller that the first Fresnel zone (see, e.g., Hung et al., 2001; Birch et al., 2001).

The Born approximation method is an alternative to the ray approximation, and like many of the approaches in time-distance helioseismology, has its roots in the geophysics literature (Zhao and Jordan, 1998; Marquering et al., 1999). These sensitivity kernels, initially considered in regards to the Sun by Birch and Kosovichev (2000), allow a single scattering point between the source and receiver and it can be used to treat perturbations with length scales that are smaller than the first Fresnel zone. The Rytov approximation (e.g., Jensen and Pijpers, 2003) similarly allows for a single scattering between the source and receiver, but it differs from the Born approximation in that the effects of the perturbation on the amplitude and the phase can be easily separated. Fresnel-zone approximation kernels, which also take into account finite wavelength effects, were utilized in some later analyses, such as Jensen et al. (2000, 2001) and Couvidat et al. (2004). However, the Fresnel-zone kernels are not based on a solution to the wave equation.

1.2.2 Helioseismic Holography

The method of helioseismic (or acoustic) holography was initially proposed by Roddier (1975) and has been largely developed into a powerful local helioseismic diagnostic tool by Lindsey and Braun (1997), and in a somewhat different formulation by Chou et al. (1999). Helioseismic holography is the phase-coherent reconstruction of acoustic waves observed at the solar surface into the solar interior to render stigmatic images of sub-surface sources that have given rise to the surface disturbance.

Because nearly all of the acoustic radiation from a surface region refracts back to the surface, mostly within 50 Mm, holography can likewise use observations in one surface region, the pupil, to image another, the focus, a considerable distance from the pupil. The technique for this is called "subjacent vantage holography" (see Figure 1.5). The subjacent vantage images seismic radiation that first propagates downward from the source before refracting back to the surface. This renders the perspective of an observer beneath the source. The superjacent signature is one which travels directly to the surface.

The main computations in holography are of the "ingression" and "egression". These two quantities are estimates of the wave-field in the solar interior; the ingression is an assessment of the observed wave-field converging upon the focal point while the egression is an assessment of waves diverging from that point. The ingression, H_-, and the egression, H_+, are obtained from the wave-field at the surface, ϕ, through

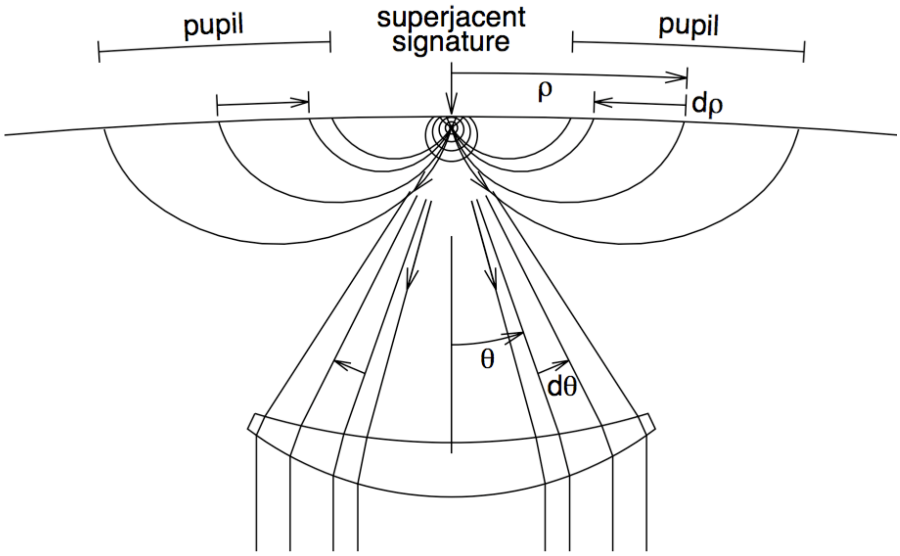

Figure 1.5: A schematic diagram from Lindsey and Braun (2000) depicting subjacent vantage imaging. The subjacent vantage images seismic radiation that initially propagates downwards from the source before refracting back to the surface. This renders the perspective of an observer directly beneath the source. As the angle, θ , of illumination at the focal point increases, the angular distance, ρ , along the pupil from its centre, above the focal point, decreases. The superjacent signature is one which travel directly to the surface.

theoretical Green's functions, $G_{\pm}$,

$$H^P_{\pm}(\mathbf{r}, z, \omega) = \int_P d\mathbf{r}' G^P_{\pm}(\mathbf{r}' - \mathbf{r}, z, \omega)\phi(\mathbf{r}', \omega), \tag{1.8}$$

where P denotes the "pupil" - the region of the surface over which the Green's function is non-zero. ω is the temporal frequency, $\mathbf{r}$ and $\mathbf{r}'$ are positions on the solar surface and z indicates the focal depth.

The ingression, egression, and surface wave-field can be combined in a number of ways to obtain estimates of solar conditions. For example, the "egression power", which is given by

$$P^P(\mathbf{r}, z, \omega) = \left\langle |H^P_+(\mathbf{r}, z, \omega)|^2 \right\rangle_{\Delta\omega}, \tag{1.9}$$

is used extensively in the detection of seismic emissions from solar flares (e.g., Donea et al., 1999; Donea and Lindsey, 2005; Donea et al., 2006b; Moradi et al., 2007;

Martínez-Oliveros et al., 2007, 2008b). It is an estimate of the frequency-averaged wave power (indicated by the brackets), over a chosen frequency range $\Delta\omega$, coming out of the horizontal position $\mathbf{r}$, at depth z seen in the pupil P. The adaptation of computational seismic holography for applications in flare seismology will be described in greater detail in §4.1.1.

Another variation, known as "local control correlations", $C^P_\pm$, is used to facilitate comparisons with surface-focused time-distance helioseismology. The correlations

$$C^P_+(\mathbf{r},\omega) = \left\langle H^P_+(\mathbf{r}, z=0,\omega)\phi^*(\mathbf{r},\omega)\right\rangle_{\Delta\omega} \tag{1.10}$$

and

$$C^P_-(\mathbf{r},\omega) = \left\langle \psi(\mathbf{r},\omega)H^{P*}_-(\mathbf{r},\omega)\right\rangle_{\Delta\omega}, \tag{1.11}$$

describe the egression and ingression control correlations respectively, which are directly comparable to centre-to-annulus time-distance correlations described in §1.2.1. The asterisk denotes the complex conjugate. Schunker et al. (2005) utilized this approach in showing the effect of the line of sight on the local control correlation in sunspot penumbra.

In a manner similar to time-distance helioseismology, surface-focused helioseismic holography can also be used to study sub-surface flows by dividing the pupil into four quadrants (e.g., Lindsey and Braun, 2000), each spanning 90 degrees and oriented in the North, South, East and West directions. We can then compute the eight corresponding control correlations, $C^{N,S,E,W}_\pm$. Various combinations of these correlations are then used to derive travel-time shifts due to the presence of flows or wave-speed perturbations.

1.3 Helioseismology of Sunspots and Active Regions

1.3.1 Sunspots

Sunspots are very large and strong magnetic flux tubes that have intersected with the solar surface. As such they represent one of the major connections of the internal magnetic field of the Sun with its wider environs, and also an ongoing challenge in the study of the Sun. They tend to occur in bands centred on the equator that extends to latitudes of $\pm30°$ and their distribution varies with the 11 year solar cycle.

Sunspots typically appear in groups of two or more, oriented roughly parallel to the solar equator, starting close together and moving apart as the group evolves, achieving separations of up to 20°. Sunspot groups lie within *solar active regions*, containing pores and smaller magnetic features that give rise to bright faculae and fine-scale filigree in the solar photosphere. A sunspot can span a lifetime of months, but more typically of weeks (Solanki, 2003). However, this life expectancy is considerably shorter than the dynamical time-scale associated with magnetic diffusion in the spot. This reduced lifetime suggests a convective instability sets in at large times and enhances the decay process, although some sunspots simply fragment before decaying. Understanding the growth and evolution of spot structures is tied to understanding the overall field configuration of the star.

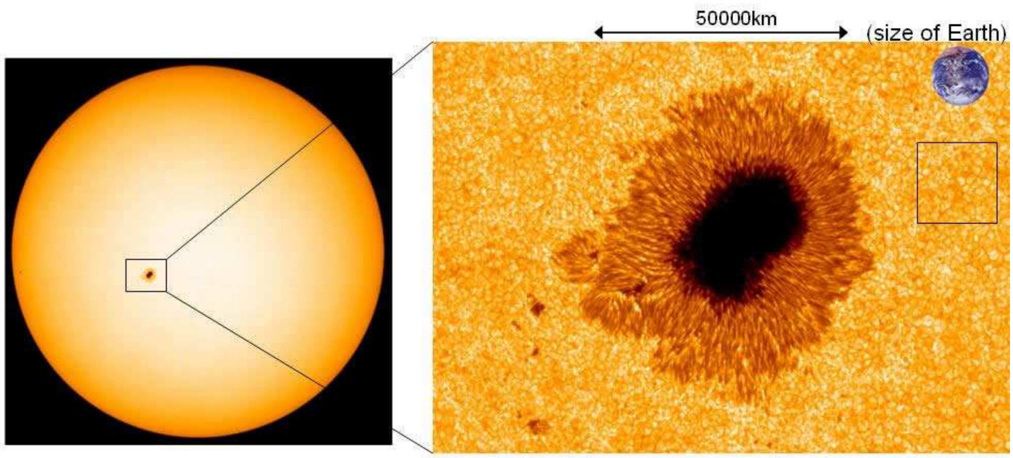

Figure 1.6: A full-disk (left) and cropped (right) high resolution image of a sunspot observed by HINODE in the 430nm wavelength band (available from http://solarb.msfc.nasa.gov). Away from the spot the granulation of the solar surface is clearly visible.

Individual flux tubes are believed to rise from deep in the convection zone to break through the surface of the Sun, since the lower gas pressure of flux tubes tends to make them buoyant. When the flux does emerge, then it is often in the form of pore structures of the order of only a Mm or so in size (Zwaan, 1978). Groups of pores are thought to have common roots in larger flux tubes that have been separated by the process of convective transport, allowing them to rise to the surface. Once at the surface, these linked tubes are then pulled together, with the relative buoyancy of the individual tubes acting to straighten their structure under the surface.

On the photosphere they are observed to develop from coalescing dark pores which almost instantaneously develop a penumbra when the magnetic field reaches a critical inclination ($\sim 35°$) from normal (Martinez Pillet, 1997). The central dark nucleus of the sunspot, the umbra, is usually associated with the strongest magnetic field, with the magnetic flux approaching a peak value of between 2700-3700 G in the core of the umbra Solanki (2003). In general, the magnetic field becomes more inclined (up to around 90°) and weaker (around 700-1000 G) with radial distance from the centre of the spot. The sunspot itself appears dark on the surface because the magnetic field inhibits fluid motion and hence the convective transport of heat (Biermann, 1941), creating the temperature deficit and the Wilson depression (a physical depression of the solar surface by around 400 km in the umbra). The Wilson depression implies that the gas pressure in the umbra is much less than that outside the spot at the same geometric level, and therefore that magnetic stresses are required in order to maintain hydrostatic equilibrium in any sunspot model.

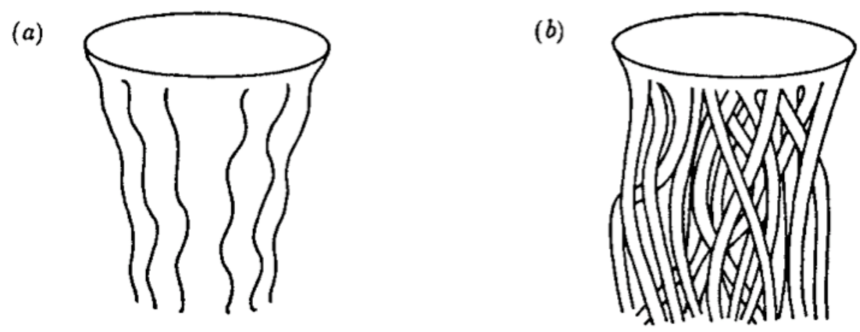

Figure 1.7: Sketch of the monolithic (left) and cluster (right) models of sunspots, from Thomas and Weiss (1992).

Sunspots are easily observed at the surface (e.g., Figure 1.6), but determining general sub-surface structure is no trivial matter. There are two main hypotheses for the structure of the flux tube that forms the spot : the monolithic model (Cowling, 1976) and the cluster (spaghetti) model (Parker, 1975) (see Figure 1.7). Determining the parameters of these tubes, i.e., typical size, field strength etc,. will help reveal details of the operation of the solar dynamo and how magnetic field is transported up through the convection zone. The monolithic model assumes that the sunspot can be represented as a single flux tube, whereas the fibril model fragments the flux tube into many small strands below the surface due to the fluting or interchange instability. This latter model is able to explain observational phenomena such as the high thermal flux in the penumbra and umbral dots. However, one argument against the cluster model is that the potential field in the observable layers produced by a collection of buried magnetic monopoles held together at a great depth has a maximum field that increases much more rapidly with the size of the sunspot than shown by the observations (Solanki, 2003).

Unfortunately, as we shall see in the next section, current linear inversion techniques do not yet allow helioseismology to probe the internal structure of the flux tube with sufficient precision to distinguish between monolith and cluster models. However, the agreement between high resolution observations of bright umbral dots (e.g., Riethmüller et al., 2008) and recently developed radiative MHD numerical simulations of sunspot structure by Heinemann et al. (2007) and Rempel et al. (2009) provide compelling support for the monolithic picture: convection within the flux tube produces rising and expanding plumes with fields that are locally reduced, and these plumes correspond to umbral dots. However, this is certainly not the end of the story. The large dynamic range of sunspot behaviour in both the temporal and spatial domains, has meant that fully-fledged computational modelling of the whole spot has only recently become possible. We may still be in for a surprise in the future, as both our observations and modelling of sunspot structure are bound to improve significantly. The reviews by Solanki (2003), Thomas and Weiss (2004) and Tobias and Weiss (2004) (and references therein) have excellent discussions regarding other sunspot models and related observations.

1.3.2 Sunspot Seismology

Sunspot seismology, particularly measurements from time-distance helioseismology that attempt to recover the three-dimensional local wave propagation and flow speed structure, has the potential to answer some of the challenges of understanding sunspots. As outlined in the previous section, realistic models of sunspots are now being developed and refined and have had much success in explaining the finer points of the observed surface phenomena and the general large dynamic range of spot behaviour. Therefore, detection of the properties below the surface (albeit with a resolution that is still crude in comparison, for instance, with the size of a flux tube) is critical for understanding and comparing with these and other theoretical models beneath the photosphere.

The propagation of waves through the Sun's convection zone is affected by perturbations generated from advection of material or from changes in the sound-speed of the medium relative to equilibrium. These two effects can be separated, at least to first order. Since propagation speed is linked to both the local temperature and magnetic field, one can then attempt to determine the shape of the field region and estimate the strength of these parameters. For example, in the geometrical acoustics (ray) approximation, the ray time is presumed to be sensitive only to the perturbations along the ray path (Γ). This can be expressed in terms of the sound speed (c) and the flow velocity ($\mathbf{v}$):

$$\tau = \int_\Gamma \frac{ds}{c + \mathbf{v} \cdot \hat{\mathbf{n}}}, \tag{1.12}$$

where ds is the increment of path length, and $\hat{\mathbf{n}}$ is a unit vector tangent to the ray. The sign of $\mathbf{v} \cdot \hat{\mathbf{n}}$ depends on the direction of propagation, as a result, the travel times in opposite directions differ due to the effects flows.

If the variations of these travel times ($\delta\tau$) obey Fermat's principle, then we can simply take the integral over the unperturbed ray path:

$$\delta\tau = \frac{1}{\omega} \int_\Gamma \delta\mathbf{k} \cdot d\mathbf{r}, \tag{1.13}$$

where $\delta\mathbf{k}$ is the perturbation of the wave vector ($\mathbf{k}$) due to structural inhomogeneities and flows along Γ. Following Kosovichev and Duvall (1997), the variation of the travel time (to first order approximation) can then be written as:

$$\delta\tau = -\int_\Gamma \left[\frac{(\hat{\mathbf{n}} \cdot \mathbf{v})}{c^2} + \frac{1}{v_p}\frac{\delta c}{c} + \left(\frac{\delta\omega_c}{\omega_c}\right)\frac{\omega_c^2 v_p}{\omega^2 c^2} + \frac{1}{2v_p}\left(\frac{a^2}{c^2} - \frac{(\mathbf{k} \cdot \mathbf{a})^2}{k^2 c^2}\right)\right] ds \tag{1.14}$$

where δc is the change in sound speed, $v_p = \omega/k$ is the phase speed and $\mathbf{a} = \mathbf{B}/\sqrt{4\pi\rho}$ is the vector Alfvén velocity (with $\mathbf{B}$ being the magnetic field strength and ρ the plasma density). The difference between the reciprocal travel times is related to flows:

$$\delta\tau_{diff} = -2 \int_\Gamma \frac{(\hat{\mathbf{n}} \cdot \mathbf{v})}{c^2} ds, \tag{1.15}$$

while the mean of the travel time differences is sensitive to the structural differences (i.e., in sound speed or in magnetic field) between the Sun and the model:

$$\delta\tau_{mean} = -\int_\Gamma \left[\frac{1}{v_p}\frac{\delta c}{c} + \left(\frac{\delta\omega_c}{\omega_c}\right)\frac{\omega_c^2 v_p}{\omega^2 c^2} + \frac{1}{2v_p}\left(\frac{c_A^2}{c^2} - \frac{(\mathbf{k} \cdot \mathbf{c_A})^2}{k^2 c^2}\right)\right] ds \tag{1.16}$$

Equations (1.15) and (1.16) both specify inverse problems since a line integral is involved. By solving the inverse problem, we are able to produce tomographic reconstructions of the flows and structural differences in 3D and in the process (theoretically) separate the magnetic field effects from the variations of the sound speed and acoustic cut-off frequency. This is because the magnetic field also introduces a directional dependence in the structural differences, thus producing an anisotropy in reconstructed structural differences. In practice however, this separation has not been achieved, in part due to limitations imposed by the noise. But as we shall see below (and in Chapters 2 and 3), there are numerous other complications (e.g., associated with the actual helioseismic observations themselves, the data reduction and analysis process, and the previously mentioned assumption of linear sensitivity of travel times to changes in the near-surface sound/wave speed, etc.) which have severely impeded our ability to correctly infer sub-surface structure.

Inferring Sub-Surface Structure

Over the years, time-distance observations of sunspots and active regions using data from MDI and GONG have been used to analyse the near-surface behaviour of material flows and wave-speed variations beneath sunspots. One of the most well known inversion results, produced by Kosovichev et al. (2000), is reproduced in Figure 1.8. Using ray-path approximation sensitivity kernels, Kosovichev et al. (2000) found that the absolute difference in wave-speed between a sunspot (AR 8131) and the quiet Sun is up to 1 km s^{-1}.[2] In their analysis, they detected a two-region structure below the sunspot. The shallow sub-surface layers exhibited a decrease in the sound speed ($\delta c^2/c^2 \sim -0.1$ at a depth of 4 Mm, which they say would correspond to a 10% temperature decrease) relative to the quiet Sun, while the deeper layers (7-15 Mm) exhibited an increase in the sound speed ($\delta c/c > 0$). The authors noted that the two-structure wave-speed profile they detect could be caused by a variety of physical effects, for example thermal and magnetic perturbations, but they did not favor the sole contribution of the magnetic field. The perturbations vanish at depths greater than 15 Mm, which may be an indication of the vertical extent of active regions or perhaps of the poor resolution of the inversions there. Similar two-region structure for the sunspot was confirmed by: Jensen et al. (2001) and Couvidat et al. (2004) using Fresnel-zone approximation kernels; Hughes et al. (2005) using ray-approximation kernels and GONG data; Couvidat et al. (2006) using Born-approximation sensitiv-

[2] According to Gizon and Birch (2005), the quiet Sun sound speed is about 20 km s^{-1} at a depth of 4 Mm and 35 km s^{-1} at 10 Mm.

ity kernels; Zharkov et al. (2007) and Zharkov and Thompson (2008) using Rytov-approximation sensitivity kernels. Overall, inversions based on the four different inversion kernels, have all provided similar results on sunspot interior sound-speed variations.

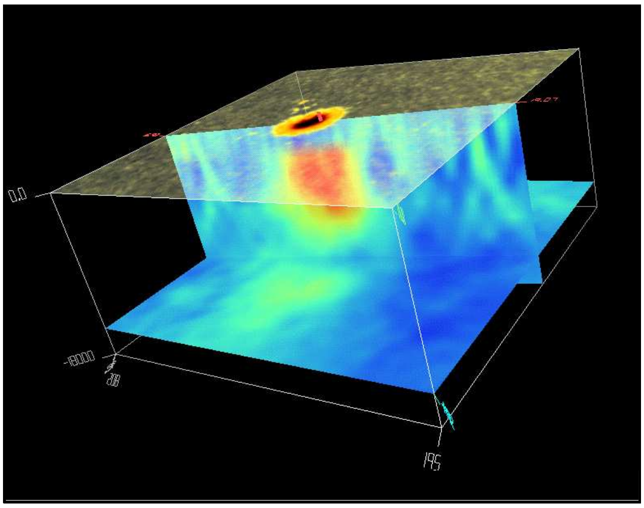

Figure 1.8: Sound-speed perturbation below a sunspot derived from SOI/MDI data. Three planes are shown: on top the continuum intensity at the surface, showing the sunspot with the dark central umbra surrounded by the somewhat brighter, filamentary penumbra. The second plane is a vertical cut from the surface to a depth of 24 Mm showing areas of faster sound speed as reddish colours and slower sound speed as bluish colours. The third plane (bottom) is a horizontal cut at a depth of 22 Mm showing the horizontal variation of sound speed over a region of 150 × 150 Mm. This figure was obtained from soi.stanford.edu website.

These inversion results led many to strongly believe that the two-region structure detected below a sunspot did indeed have a physical origin, and could not easily be dismissed as an artefact of the data reduction process or the numerical algorithm used. However, in the sub-photospheric magnetic regions, the ratio of magnetic to gas pressure is close to unity, leading to the contention that the magnetic field effects are systematic and significant. On the other hand, the higher wave speeds measured at a depth of 10 Mm below sunspots are unlikely to be due only to the direct effect of the magnetic field, as this (erroneously) implies very large field strengths of a several tens of kG (Gizon and Birch, 2005). The likely cause is possibly a combination of magnetic and structural/thermal effects (Brüggen and Spruit, 2000; Basu et al., 2004). However, through numerical simulations of wave propagation through a model sunspot, Cally et al. (2003) and Crouch et al. (2005) (see next section) were able to reproduce the phase shifts measured by Hankel analysis without the need for a thermal perturbation, thus questioning the interpretation of travel-time anomalies in terms of linear perturbations to the wave speed. This stresses the need for a proper solution of the forward problem of time-distance helioseismology in sunspots.

Theoretical Modelling

Early theoretical work on the interaction of solar oscillations with magnetic fields was motivated by observations of wave absorption by sunspots (Braun et al., 1987). Spruit (1991) was the first to suggest that the magnetic field of the sunspot is responsible for the absorption, this in turn initiated a number of studies analysing the interaction of acoustic waves with magnetic fields (e.g., Spruit and Bogdan, 1992; Cally and Bogdan, 1993; Cally et al., 1994; Cally, 1995; Bogdan and Cally, 1997; Cally and Bogdan, 1997). These studies have now provided us with a somewhat clearer picture, with the absorption of p-modes by sunspots now believed to be the result of partial mode conversion of the incoming p-mode into slow magneto-acoustic waves. These slow magneto-acoustic waves tend to behave like an Alfvén wave far below the conversion zone – a thin layer where the acoustic sound speed is close to the Alfvén speed.

Later, Cally (2000) demonstrated that an inclined magnetic field is required to explain the observed p-mode absorption by sunspots. The first agreements between p-mode absorption and the magnetic field strength of sunspots were reported by Cally et al. (2003) and Crouch et al. (2005) soon after, showing that mode conversion by non-vertical magnetic fields can provide a reasonable agreement with the Hankel analysis observations of wave absorption and phase shifts (e.g., Braun et al., 1988, 1992; Braun, 1995). They also demonstrated that the phase shift and power absorption of wave packets inside a sunspot depends on the central frequency of this wave packet. Figure 1.9 clearly illustrates this acoustic mode conversion mechanism for inclined magnetic fields. The observational signatures of the mode conversion process (i.e. upward propagating magneto-acoustic waves) has also recently been the focus of numerous works (e.g., Schunker and Cally, 2006; Khomenko and Collados, 2006; Cally, 2007; Cally and Goossens, 2008).

1.3.3 Forward Modelling

There has long been a need for MHD simulations to be developed for testing observational inferences and analysing the interaction of solar oscillations and wave

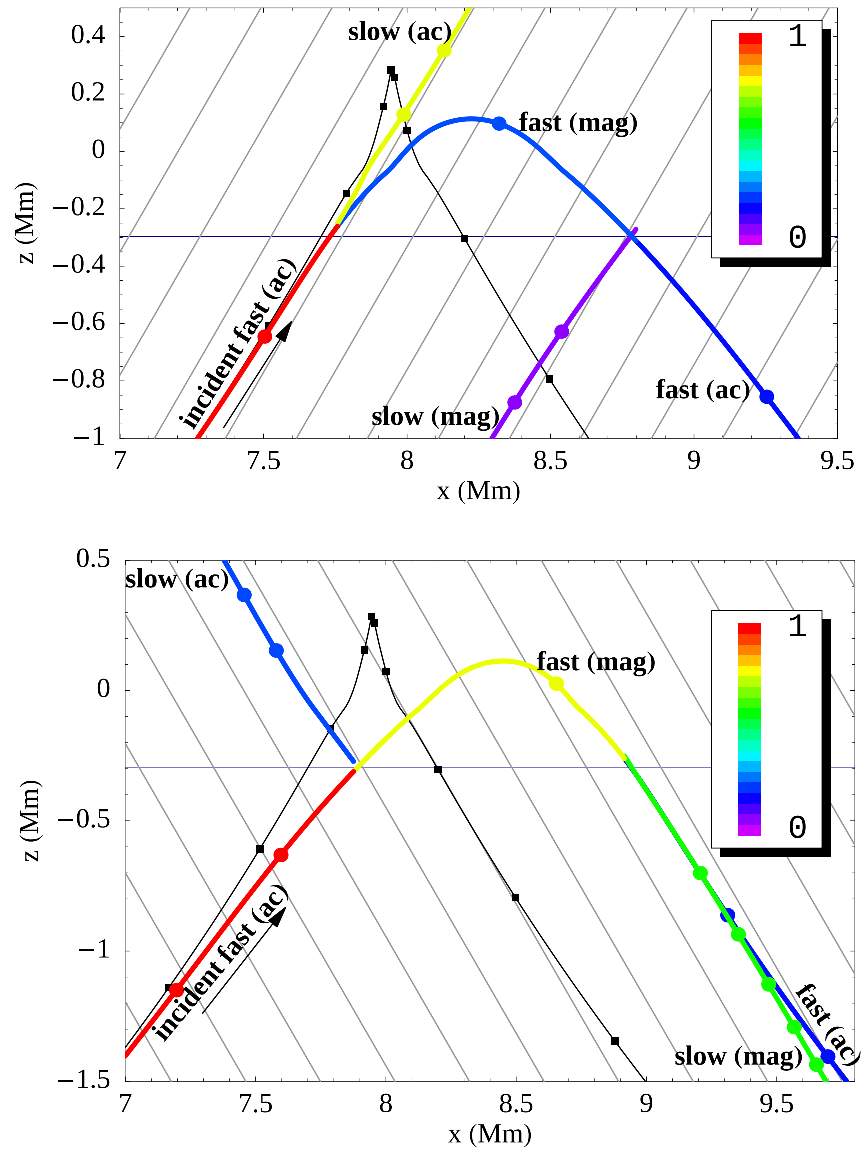

Figure 1.9: Physical space ray diagram from Cally (2007). Ray paths in the $x-z$ vertical plane in model surface layers with 2 kG uniform magnetic field inclined at $\pm 30°$ respectively to the vertical, as shown by the background grey lines. The incoming 5 mHz rays (shown in red) have lower turning points at $z = -5$ Mm. The horizontal grey line indicates where the sound and Alfvén speeds coincide, which is approximately where mode conversion happens. The fractional energy remaining in each resulting ray is indicated by the colour legend. The dots on the ray paths indicate 1 min group travel time intervals. The thin black curve represents the acoustic ray that would be there in the absence of magnetic field.

propagation in regions of strong magnetic fields. The above-mentioned results have emphasized the fact that our current forward modelling and data analysis techniques are not yet developed well enough to allow robust conclusions about the sub-surface structure (or flows, for that matter) in and around solar active regions. As Birch (2004) points out, there are two main approaches that are used to study the forward problem: the linear forward problem and direct numerical forward modelling through simulations.

Linear forward modelling is an approach which we have already discussed. Used in the context of linear inversions, it comprises of the computation of the linear sensitivity of travel times to small changes in the model (i.e. sensitivity kernels). The great advantage of the linear forward problem is that it is relatively computationally inexpensive and can provide an intuitive understanding of the forward problem. The accuracy of the Born approximation for magnetic perturbations has been tested by Gizon et al. (2006) using the exact solution for waves impacting a toy model consisting of a magnetic cylinder in an otherwise uniform medium. If the Born approximation were to be valid for sunspot-like magnetic fields, then linear inversion methods could be employed. For a 1 kG magnetic field, they find that the Born approximation would appear to be valid except close to the solar surface (the first few 100 km). Thus, the assumption of small perturbations clearly breaks down in active region sub-photospheres. These results imply that near-surface magnetic fields cannot be treated in the Born approximation and that some other form of forward modelling will be required.

The other approach to the forward problem is direct numerical simulation. Through the construction of computational models that mimic the interaction of the solar wave spectrum with various perturbations (e.g., magnetic field, sound speed, flow etc.) as closely as possible, we are able to obtain the complete non-linear response of travel times to changes in the model. These simulations will lend a clearer interpretation to the observations through the validation of the results obtained from the linear forward problem, as well as allowing the exploration of parameter regimes where the linear approach is not valid – e.g. in sunspots and active regions where MHD effects are most dominant. When these interactions are well understood, the next steps will be to use this knowledge to infer interior magnetic structures.

MHD Ray Theory

MHD ray theory has traditionally provided a very useful conceptual framework in which to understand wave propagation, even though this is questionable at the surface where the pressure and density scales vary rapidly, since the assumption of slowly varying coefficients may not be justified. Traditionally, the modelling of the motion of wave packets through the Sun has been achieved via the high-frequency ray approximation. One can understand a ray as a geometric construction linking points on the surface, often termed the source and the receiver, through the intermediate solar material. The wave-energy can be considered as travelling along ray paths from a source to a receiver in this high-frequency approximation. A more general ray theory, including mode conversion was developed by Cally (2006) and later extended in Schunker and Cally (2006).

Although ray theory is an approximation, it has often performed surprisingly well in local helioseismic analyses when compared with a full wave-mechanical description. Bogdan (1997) emphasized this fact by showing that a wave packet formed through the superposition of p-modes, trapped in the same acoustic cavity, can travel along a bundle of rays (the sum of ray paths). This bundle follows the WKB ray-path predicted by the eikonal approximation, but it has a finite extent in both space and time that varies inversely with the range of wave-numbers and frequencies spanned by the p-modes which comprise the packet.

However, Bogdan (1997) also points out that the "broadening" of a such a bundle (which results in the travel time being sensitive not only to the local velocity field along the ray path, but also to conditions in the surrounding medium as well), which is a clear consequence of wave effects, questions whether the use of the ray approximation is fully justified. However, in practice, this effect is probably not as important as it might seem. As described in §1.2.1, in almost all time-distance measurements, travel times are averaged over a small range of travel distances and locations. Cross-correlations are computed for a large number of pairs and points, and then pairs with similar distances and locations have their cross-correlations averaged together to get a single measurement for the travel time. So in effect, the ray path used is then actually a "ray bundle", consisting of a number of rays covering the region of propagation. The broadening of such a bundle by wave effects might very well be small compared to the extent of the bundle itself (Giles, 1999). Another limitation of ray theory (and the WKB approximation in general) is that it tends to break-down in mode conversion regions. This issue has been addressed at some length by Cally

(2005, 2006); Schunker and Cally (2006), in the latter case using the general theory set out in Tracy et al. (2003).

Regardless of these shortcomings, ray theory has been used in helioseismology for some time, being one of the several methods that have been applied to asymptotic inversions of helioseismic frequency measurements in the past (e.g., Gough, 1984), and in general, it has performed well beyond its formal domain of applicability. A prime example is the agreement between the wave mechanical analysis of Cally (2005), the ray theory modelling of Cally (2006) and the recent results of Hansen and Cally (2009), who find very good agreement between generalized ray theory and previously published exact solutions (Cally, 2001, 2009b). In another recently completed work, Moradi and Cally (2008) successfully applied ray theory to numerical forward modelling through the application of a three-dimensional ray tracer (based entirely on MHD ray theory) to simulate magneto-acoustic ray propagation and model travel-time inhomogeneities in a toy sunspot model (see Chapter 2). With the ability to quickly and accurately generate artificial travel-time perturbation profiles, this numerical forward model is a potent tool as ray tracing is traditionally much less cumbersome and computationally expensive when compared to other forms of numerical simulations, such as realistic simulations of fully-compressible non-linear magneto-convection which are rapidly becoming feasible (e.g., Stein and Nordlund, 2000, 2006; Stein et al., 2007; Steiner, 2007), offering a more robust way of validating the various methods of local helioseismology (e.g., Braun et al., 2007; Georgobiani et al., 2007; Zhao et al., 2007). However, simulating wave propagation in a fully consistent manner as well as treating small-scale and non-linear convection, which are not easily resolved, requires significant computational power and expense.

MHD Simulations of Wave Propagation

Another approach to generating artificial data is through wave propagation simulations using waves excited by sources that are specified, but intended to mimic the generation of waves by convection (e.g., Hanasoge et al., 2006; Cameron et al., 2007; Shelyag et al., 2007; Parchevsky and Kosovichev, 2007b; Khomenko et al., 2008a). This approach substantially reduces the computational expense as well as having the advantage of being able to rapidly simulate multiple data sets, which will allow for statistical studies. Another advantage of this approach is that the wave sources can be tuned, e.g., to simulate reduced wave excitation in sunspots (Parchevsky and Kosovichev, 2007a; Hanasoge et al., 2008).

In this regard, a first step is to devise a sufficiently general manner of computing wave propagation in a magnetized plasma. The linearized ideal MHD equations provide a reasonable starting point, since MHD oscillations in the photosphere and below are governed by predominantly linear physics (e.g., Bogdan, 2000). Cally and Bogdan (1997), Rosenthal and Julien (2000), and Cally (2000) performed MHD simulations in two dimensions in order to study rates of mode absorption in magnetic flux tubes. Subsequently, Cameron et al. (2007, 2008) developed and validated numerical techniques with which to perform three-dimensional linear MHD computations, with a focus on recovering the magnetic field distribution on the basis of wave-scattering measurements. In Chapter 3 we utilize the 3D ideal MHD solver, developed in the works of Hanasoge et al. (2006, 2007) and Hanasoge (2008), to simulate MHD wave propagation in regions of strong, sunspot-like magnetic fields. This numerical forward model, which also assumes linear wave propagation and time stationary background states, provides us with a sound way of validating results obtained from MHD ray theory, as well as the results obtained from the linear forward problem.

1.4 Solar Flare Seismology

The detection of significant seismic emission from solar flares or "sunquakes" – circular waves propagating outward along the solar surface from an impulsive flare ∼30–60 minutes after the impulsive phase – is a major discovery with a broad range of diagnostic and control applications for helioseismologists and flare analysts alike as flare acoustic transients represent the most localized coherent sources (temporally as well as spatially) that we are currently aware of. They are also the hardest acoustic radiation (i.e., the most intense at high frequencies) known to date, and the only acoustic waves that are known to be generated in plain view above the solar surface (Lindsey and Donea, 2008).

Sunquakes emanate from compact sources that encompass only a small fraction of the energy emitted from flares, thus helioseismology of sunquakes offers us the opportunity to explore not only the acoustics of flares themselves, but also the subphotospheres of the active regions that produce them. But, before we delve into the details of sunquake generation, in the proceeding section I shall provide a brief overview of both the observational signatures and basic physical mechanisms of the solar flares that are their catalysts.

1.4.1 Solar Flare Observations

Solar flares result from rapid release of magnetic energy in the solar corona and are typically observed as enhancements in the emission of a wide range of wavelengths – including radio, Hα (Balmer-α emission of neutral hydrogen), ultra violet (UV), extreme ultra violet (EUV), soft X-rays (SXR) and hard X-rays (HXR). Because of their conspicuous appearance, they have been extensively studied since they were observed for the first time in white light by Carrington (1859).

The intensity and energy output of solar flares varies greatly. The strength of a solar flare is commonly given by its SXR flux in 1-8 Å at 1 AU, where a C-class flare has a flux of the order of 10^{-3} cm^{-2}s^{-1}. Some flares are so weak that they are on the edge of detection by current SXR telescopes. Others are so powerful that their SXR flux is one (M-class flares), two (X-class flares), or even more orders of magnitude larger than C-class flares. The total amount of energy released during a solar flare in the form of thermal and non-thermal charged particles, kinetic energy and shock waves can exceed 10^{32} ergs.

Photospheric and Chromospheric Observations

Most of the optical light which travels from the Sun to the Earth is emitted from the photosphere. In white light, we generally observe a relatively quiet Sun, except for the presence of some dark sunspots on it. Huge flares are sometimes observed in the white light, which are called "white light flares". They appear as a short-lived increase of the solar continuum emission, with a duration of 1-10 minutes, but they are rare. Carrington (1859) first observed a white-light flare as a local and short-duration brightening on a white light picture of the Sun. However, with progress in spectroscopic and monochromatic image observations we have been able to examine the appearance of solar flares in the chromosphere by using chromospheric lines, such as Hα (6563 Å).

In Hα observations we can observe brilliant flashes associated with flares. In many large-scale and long duration flares, we observe a two-ribbon structure – i.e., two narrow and bright long regions (called "flare ribbons") which lie on either side of the magnetic neutral line (e.g., see Figure 1.11). The sub-structure of these flare ribbons consists of small bright points, called "Hα kernels". They brighten rapidly, although the light curve of the Hα flux integrated over the flaring region only shows a gradual change as shown in Figure 1.10. This brightening is thought to be caused by

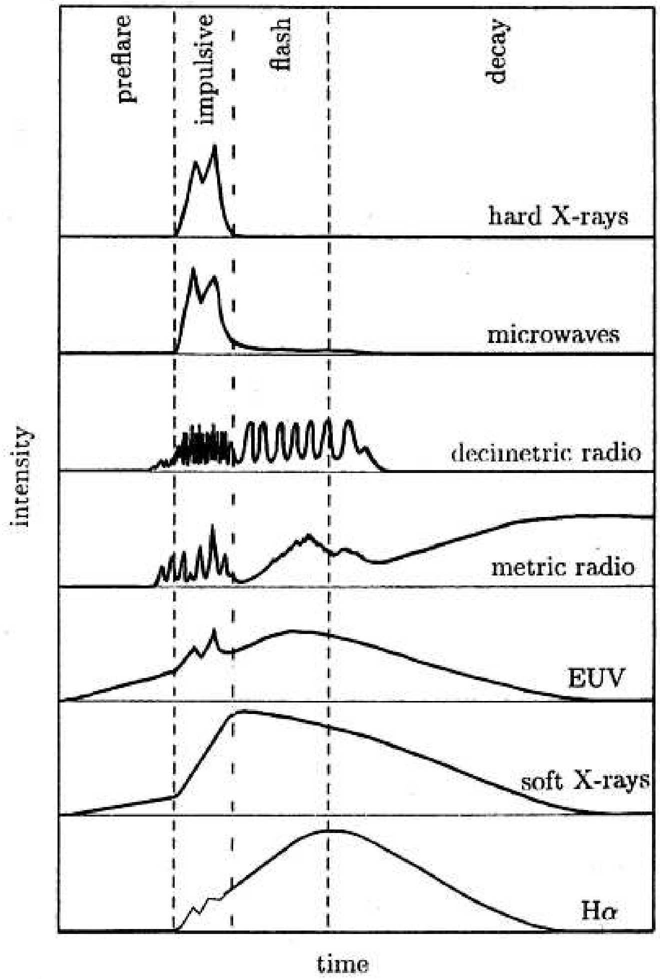

Figure 1.10: A schematic profile of the flare intensity at several wavelengths. The various phases indicated at the top vary greatly in duration. In a large event, the pre-flare phase typically lasts a few minutes, the impulsive phase 3 to 10 minutes, the flash phase 5 to 20 minutes, and the decay one to several hours (from Benz, 2008).

precipitation of non-thermal electrons from the corona into the chromosphere, which stimulates the excitation and ionization of hydrogen atoms (Ricchiazzi and Canfield, 1983; Canfield et al., 1984).

Solar flares usually occur following the emergence of new flux. This flux emergence carries magnetic energy into the corona, leading to the creation of magnetic-inversion regions. Shear motion on the photosphere also makes the magnetic field more complex and stores the magnetic energy in the corona. Large flares, such as X-class flares, often occur at flare-generative δ-type sunspots – sunspots that have two or more umbrae of opposite polarities within a common penumbra. Such volatile active regions are thought to be generated by the emergence of strongly twisted magnetic bundles (Kurokawa, 1987; Kurokawa et al., 2002). When the fields are extremely sheared, an instability occurs. The field then tends to be restored to the potential configuration and magnetic free energy is released through the process of magnetic reconnection which occurs in the corona. Therefore, precise and detailed measurements of photospheric and chromospheric magnetic field evolution in flaring regions are a necessity for us to be able to examine the energy release mechanism. Magnetograms measured using photospheric lines provide us with a wealth of important information, as do chromospheric magnetic field lines which are extrapolated from the appearance in the chromosphere filtergrams in which the field lines are visible due to frozen-in plasma.

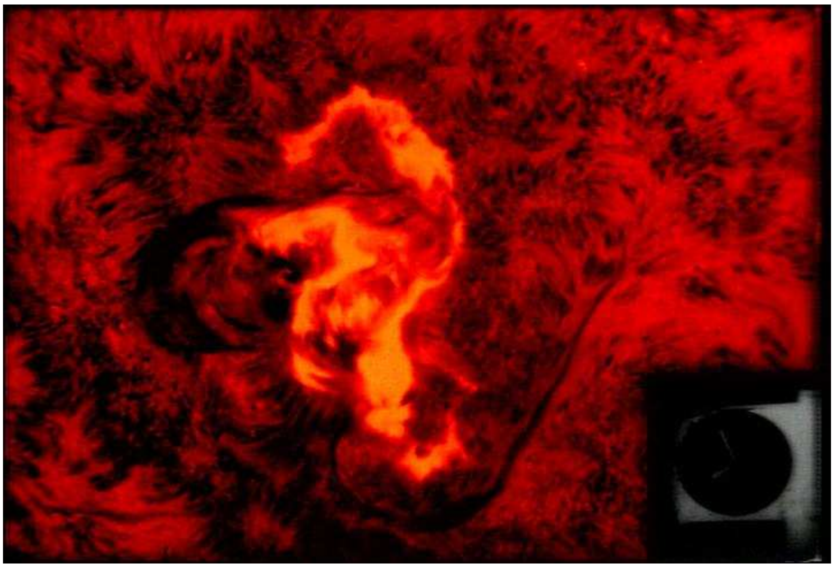

Figure 1.11: Image of a major eruptive (two-ribbon) flare in the blue wing of Hα, observed at Big Bear Solar Observatory on 7 August 1972, showing the two-ribbon structure late in the event, with bright Hα loops connecting the ribbons. The two bright flare ribbons extend along the neutral line, marked in the pre-flare state by a dark filament. Image obtained from http://www.bbso.njit.edu.

Coronal Observations

As the solar corona is dominated by magnetic forces and energy (due to the prevalence of low β plasma), magnetic reconnection has a great influence on heating and dynamics once it occurs. Generally, the phenomena which occur in the corona are much more dynamic than those in the chromosphere (average plasma $\beta \sim 1$) and the photosphere (average plasma $\beta \sim 10^4$). However, due to its high plasma temperature (more than 2 MK) and low density ($\sim 10^9$ cm^{-3}), it was very difficult to observe the structure of the corona until the advent of space-borne instruments such as *Yokkho* soft X-ray telescope (SXT) which revealed the dynamics of the magnetic corona. Subsequent observations in the SXR range have confirmed that flares are explosive events in the corona. The magnetic energy is released in the corona and then carried down to the chromosphere by energetic particles and thermal conduction. As a result, the chromospheric plasma is pumped up explosively due to the pressure enhancement. This is referred to as "chromospheric evaporation" and results in dramatic increase of the coronal density in the flare loops, resulting in the clear visibility of these loops (e.g., see Figure 1.12).

The coronal plasma is heated up to 10-40 MK just after the energy release occurs, then cools down due to thermal conduction and radiation and becoming visible in the EUV ($\sim$ 1 MK), and finally in Hα ($\sim 10^4$ K). These "post-flare loops", are generally well fitted with potential field lines. Twisted SXR loop structures in the pre-flare phase are also sometimes observed in the corona. The reconfiguration of the field structure, from the twisted configuration to potential-like loops, indicates that magnetic energy was released via the flare, resulting in the magnetic field moving to a lower state of energy. The coronal structure of solar flares are also observed in the microwave range, particularly in the impulsive phase of the flare, where gyro-synchrotron emission produced by energetic non-thermal electrons (accelerated during the flare), is radiated in microwaves. Consequently, flare loops, which contain these energetic electrons, are lit up.

Magnetic Reconnection

Magnetic reconnection theory has been applied to solar flares by many authors, such as Parker (1957), Sweet (1958), and Petschek (1964). However, the reconnection model proposed by Carmichael (1964), Sturrock (1966), Hirayama (1974), and Kopp and Pneuman (1976) (together known as the "CSHKP" model, depicted in Figure

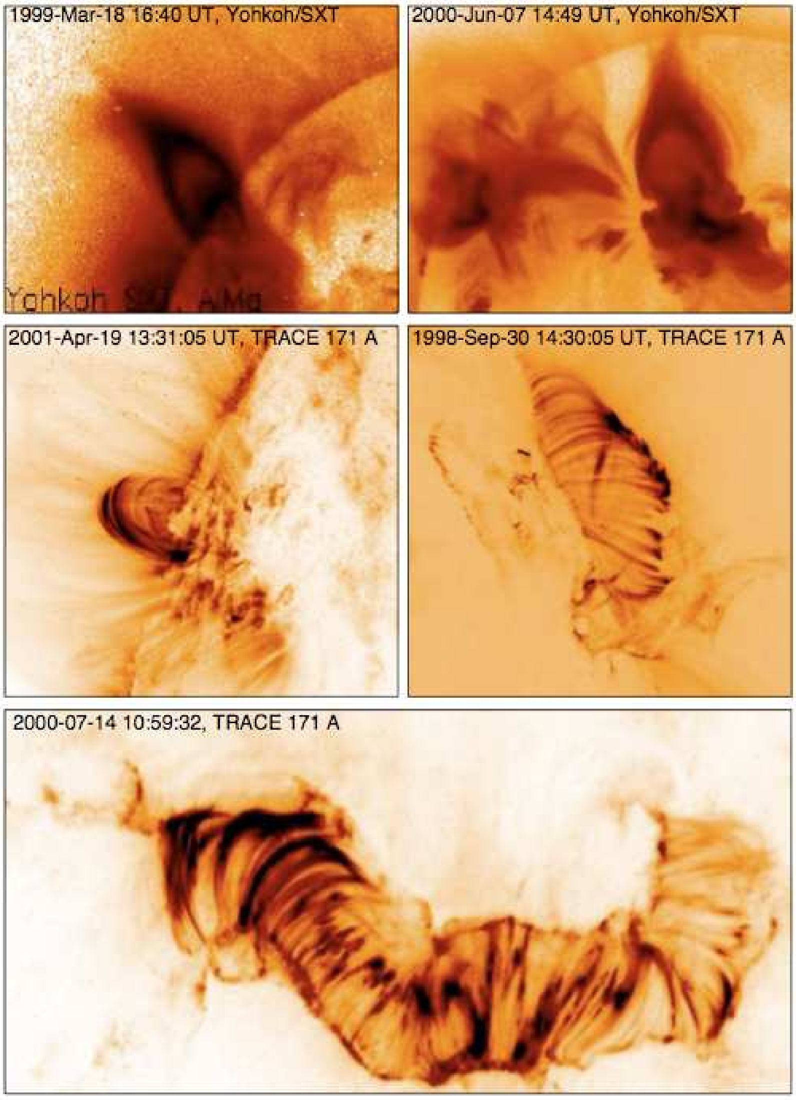

Figure 1.12: Soft X-ray and EUV images of flare loops and flare arcades with bipolar structure. Yohkoh/SXT observed flares (18 March 1999, 16:40 UT, and 7 June 2000, 14:49 UT) with "candle-flame"-like cusp geometry during ongoing reconnection, while TRACE sees post flare loops once they have cooled down to ∼1-2 MK, when they are already relaxed into a near-dipolar state. Examples are shown for a small flare (19 April 2001, 13:31 UT, GOES class M2), and for two large flares with long arcades, seen at the limb (30 September 1998, 14:30 UT) and on the disk (14 July 2000, 10:59 UT, X5.7-class flare). Images obtained from Beatty and Beatty (2007).

1.13), has now generally been accepted as the standard model of solar flares. This reconnection model attempts to explain the observed phenomena, such as Hα two-ribbon structure, post-flare loops, SXR flare loops, filament eruptions, coronal mass ejections and their influence on geomagnetic storms, and so on, in terms of the physical mechanism that releases the energy stored in flaring active region magnetic fields.

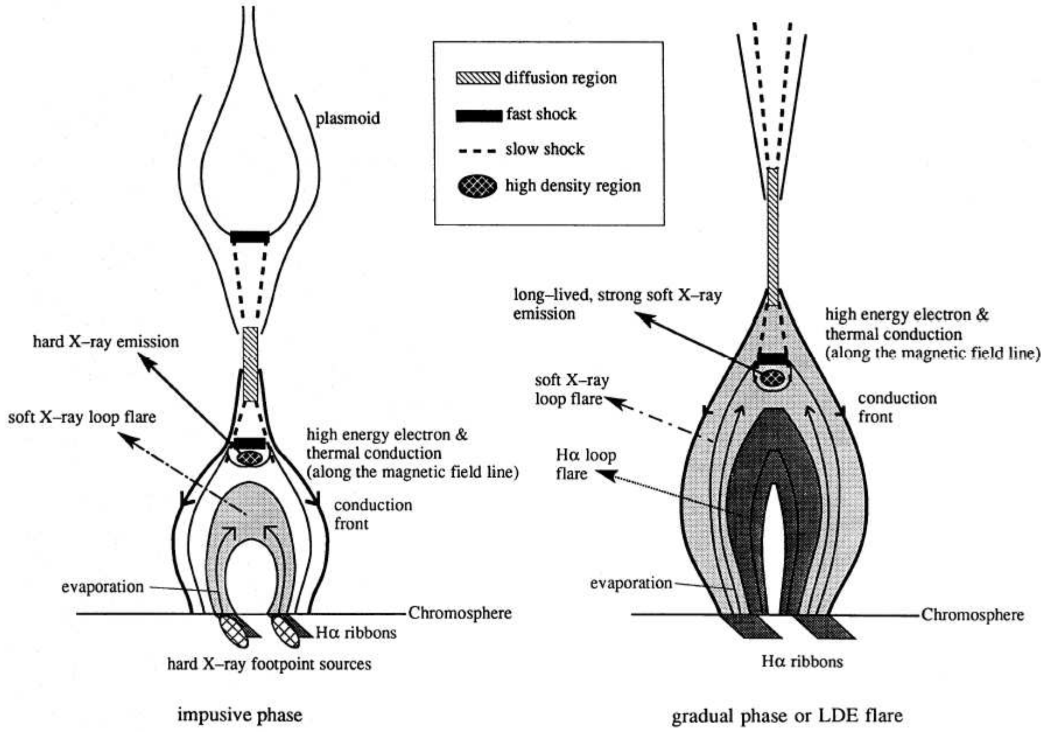

Figure 1.13: A comprehensive illustration of the CSHKP standard model, reproduced from Magara et al. (1996), showing a cusp-type flare in the impulsive (left) and in the gradual phase or a long duration event (LDE) flare (right).

The CSHKP model suggests that the magnetic field lines, at greater and greater heights, successively reconnect in the corona. This model can successfully explain well-known features of flares, such as the growth of flare loops, and the formation of the Hα two-ribbon structures at their footpoints. As Asai et al. (2004) point out, Hα flare ribbons are caused by the precipitation of non-thermal particles, and/or the effect of thermal conduction. As the magnetic field lines reconnect, the reconnection points (X-points) move to higher altitudes. As a result, the newly reconnected field lines have their footpoints further out than those of the field lines that have reconnected earlier.

Hence, the chromospheric material composing the ribbons does not actually move, but rather the ribbons shift due to the changing locations of heating and excitation in the chromosphere. A good review of the relationship between magnetic reconnection and the Hα two-ribbon structures is presented in Pneuman (1981). The same can be said for the "motion" of HXR footpoint sources, which are considered to be more directly associated with the production of high-energy electrons in the reconnection region, rather than Hα or UV sources.

1.4.2 Seismic Emission From Solar Flares

While the magnetic reconnection mechanism and the general observational phenomena of solar flares are now relatively well established (at least phenomenologically), there still remain a number of unresolved problems or puzzles associated with certain flare observations, with one of the most intriguing perhaps being the basic mechanism by which a flare excites helioseismic waves. As we have already seen, solar flares release large amounts of energy at different layers of the solar atmosphere, including at the photosphere in the case of exceptionally major events. Therefore, it is expected that large flares would be able to excite acoustic waves on the solar surface, thereby affecting the p-mode oscillation characteristics. Instances of seismic transients emitted into the solar interior in the impulsive phases of some solar flares offer a promising diagnostic tool, both for understanding the physics of solar flares and for the general development of local helioseismology.

Acoustic modes that are always present on the Sun are today generally accepted to be excited by turbulence in the convection zone (e.g., Goldreich and Kumar, 1988). Long before however, Wolff (1972) speculated that solar oscillations could be excited by solar flares as a result of the mechanical impulse produced by the thermal expansion exerted by a large flare towards the solar interior. He estimated the damping times to be longer than a day for the free modes. He went on further to suggest that these, and perhaps comets, were the primary source of solar oscillations reported by Leighton et al. (1962). However, Kosovichev and Zharkova (1998) were the first to actually identify and analyse a flare-induced seismic event on the solar surface, emanating from the X2.6-class flare of 9 July 1996. The surface manifestation of this phenomenon was the appearance of "ripples" (surface acoustic waves, see Figure 1.14) on the solar surface, which we identify today as sunquakes. Earlier attempts to detect flare associated effects were mostly contradictory and inconclusive. For example, Haber et al. (1988) found a 14% greater power in the flaring region, while

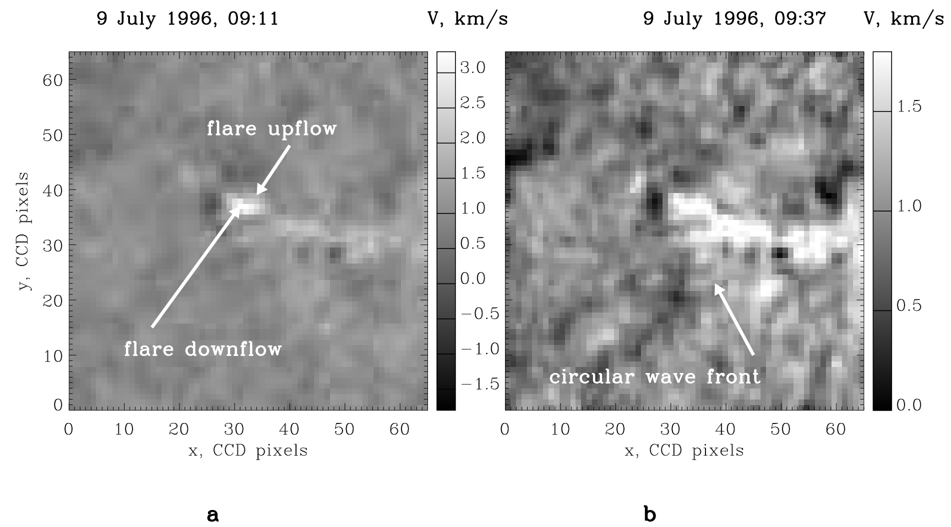

Figure 1.14: MDI Dopplergrams of the 9 July 1996 flare region at 9:11 UT (a) and 09:37 UT (b). Bright areas correspond to down flows and dark areas to up flows. Images reproduced from Kosovichev and Zharkova (1998).

Braun and Duvall (1990) found no such effect for the energetic flares in AR 5395 of 10 March 1989. The difficulty in detecting any flare-related photospheric response is primarily due to absorption of mode power by large sunspots which can absorb as much as 50–70% of the power of the $p-$modes (Braun et al., 1987). Therefore, any excitation induced by a short duration, impulsive flare has to compete with the effects of absorption associated with the intense magnetic fields of the host active region.

Using an analogy to water waves, Podesta (2003) used an inviscid, incompressible fluid, to model the seismic waves generated by the 9 July 1996 sunquake. He found that distances between successive wave crests were larger than observed, and concluded that the sunquake is primarily composed of acoustic (p-mode) rather than surface (f-modes) waves. Hence, we can expect the acoustic waves which penetrate through the sub-surface layers to reappear at the surface without much distortion or signicant decay. This is clearly observed as well, for example, in the case of the 9 July sunquake, for which the seismic waves reportedly propagated a distance of $\sim$120 Mm (Kosovichev and Zharkova, 1998). However, as the penetration depth of these waves is dependent on the travel distance, photospheric and shallow, sub-photospheric inhomogeneities (in particular, strong magnetic fields found in sunspots and active regions) most likely affect the propagation of waves with shorter travel distances (i.e., smaller depths, where the ratio of magnetic to gas pressure is much greater). This opens up the possibility of utilising the seismic signatures as a kind control facility for the discrimination of slow magneto-acoustic wave excitation, and considerations relative to issues respecting mode conversion in sunspot penumbrae.

Overall, the detection of seismic emission from solar flares is heavily dependent on their amplitude relative to the background solar noise. As Ambastha (2008) points out, in theory, all flares could be expected to have seismic consequences at some level[3], but because of the high solar noise, the seismic waves may not easily be seen on individual Dopplergram images. As a consequence, for a long time after the initial discovery by Kosovichev and Zharkova (1998), these events were thought to be an extremely rare phenomenon. However, with the advancement of powerful local helioseismic techniques such as computational seismic holography (Lindsey and Braun, 2000) (see also §1.2.2 and §4.1.1) which allows us to accurately image the seismic sources of the waves, we have now detected numerous seismic sources of varying intensity produced by a variety of X- and high M-class flares (Donea and Lindsey, 2005; Donea et al., 2006b; Besliu-Ionescu et al., 2006; Moradi et al., 2007; Martínez-Oliveros et al., 2007, 2008b). Almost all of these have occurred in complex active regions. Indeed, as we shall see in Chapter 4, recent developments in the study of flare acoustic emissions have bolstered the view that seismic emission from flares offers major new insights both into flare physics and helioseismology, ranging from a greatly improved understanding of flare dynamics and kinematics, to an understanding of the role played by coronal, photospheric and sub-photospheric magnetic fields.

1.5 Basis for this Research

As Werne et al. (2004) point out, the key to local helioseismology is the effective application of local seismic diagnostic techniques to determine the structure of the solar interior with the finest possible resolution. Indeed, as we have already touched on in the preceding sections, there are a number of open questions regarding certain important phenomena in the field (in particular, the extent and magnitude of magnetic-field configurations in and near active regions, the nature of thermal anomalies, sub-surface flows and flare-driven seismic events) which we hope local helioseismic analysis will

[3]Recently, Karoff and Kjeldsen (2008) and Karoff (2008) have presented evidence of a strong correlation between the energy in the high-frequency part of the acoustic spectrum of the Sun and the solar X-ray flux. The discovery could indicate that flares drive global oscillations in the Sun.

shed clear light on. However, current applications of local seismic methods in solar active regions produce ambiguous and inconsistent interpretations, to the extent that current observations of sunspots and active regions appear to be far ahead of modelling efforts.

The main motivation behind this thesis is therefore to clarify some of these issues through detailed analysis of the role of active region magnetic fields in local helioseismology. We aim to address these pertinent issues through: (i) the development of the techniques of numerical forward modelling in sunspot seismology to address certain inconsistencies with regards to observed travel-time inhomogeneities in the vicinity of sunspots, and, (ii) by undertaking a comprehensive correlative study of three seismically active flares in order to identify and analyse the distinct observational attributes associated with flare-induced energetic transients, and the subsequent seismic response of the solar interior. The key research questions that I set out to address in this thesis can thus be summarized as follows:

1. How to successfully model the effects of wave-speed inhomogeneities thought to be produced by MHD physics in solar active regions?

2. How to separate near-surface magnetic effects from sub-surface flows, sound-speed variations and other observational constraints and effects?

3. How will inferences made about sub-surface structure change as a result of incorporating these effects into the modelling process?

4. How to effectively detect and diagnose the helioseismic effects of flare-driven energetic transients?

5. What is the underlying physical mechanism that drives these powerful seismic emissions from solar flares?

6. To what extent do active region magnetic field configurations influence the seismicity of energetic transients?

To address questions (1), (2) and (3), two promising approaches for predicting the helioseismic signatures that would be expected for models of sunspots and active regions are developed and applied. The first approach, presented in Chapter 2, is centred on the development and application of a numerical forward model for time-distance helioseismology derived from MHD ray theory. The main aim of the numerical simulations is to shed light on a major uncertainty associated with surface-focus travel time measurements obtained from time-distance helioseismology, which is isolating the effects of the magnetic field from those thought to be associated with thermal or sound-speed perturbations. As briefly touched on in §1.3.2, this has proven to be quite a complex task, and has yet to yield reliable results when extracting travel times from the cross-correlation function. In order to analytically decouple these effects, we first formulate a realistic 3D magnetohydrostatic (MHS) sunspot model based on observed surface profiles (obtained from IVM), with a surrounding stratified Model S (Christensen-Dalsgaard et al. 1996) background atmosphere. We then model the magneto-acoustic ray propagation and analyse the resulting travel-time perturbations that will then directly account for both the sub-photospheric wave-speed, and thermal variations, produced by the magnetic field. This work shows that it is now feasible to use ray theory in model sunspots to produce travel-time shifts than can meaningfully be compared with observations.

The second approach is presented in Chapter 3. Continuing on from the theme of the previous chapter, we investigate the direct contribution of strong, sunspot-like magnetic fields to helioseismic wave travel-time shifts. This time we employ two numerical forward models: the MHD ray tracer developed in Chapter 2, and a 3D ideal MHD solver developed by Hanasoge (2007) which is used to simulate MDI-like vertical velocity data cubes which can then be analysed using local helioseismic methods. Our main aim here is to formulate a comparative study between the two forward models and also to test MHD ray theory for possible application to future inverse methods. To accomplish this goal, we once again formulate an artificial sunspot model, this time comprising of a MHS sunspot model embedded in a background atmosphere consisting of a truncated polytrope with solar-like pressure and density profiles. The artificial wave travel-time shifts are derived using a variety of timedistance measurement techniques. We also investigate the dependence of these time shifts on frequency and phase-speed filtering. To compare theory with observations, we calculate the travel-time shifts using MHD ray theory and also isolate and analyse the direct contribution from purely thermal perturbations to the observed time shifts.

The results presented in Chapter 4 are centred on flare seismology and aimed at addressing the final three questions: (4), (5) and (6). Utilising data from numerous ground- and space-based solar observatories, we present detailed findings of three recently discovered sunquakes which have provided us with a remarkably consistent and compelling perspective on some of the basic physical processes which underlie seismic emission from flares. The first flare analysed, an X1.2-class solar flare occurring in AR 10720 on 15 January 2005, produced the most powerful sunquake that has been detected to date. The discovery was made using helioseismic holography to image the source of seismic waves emitted into the solar interior from the site of the flare. Further analysis showed that the flare of 15 January 2005 exhibited the same close spatial alignment between the sources of the seismic emission and impulsive visible continuum emission as previous flares, reinforcing the hypothesis that heating of the low photosphere may drive the acoustic emission. However, it was a major exception in that there was no signature to indicate the inclusion of protons in the particle beams thought to supply the energy radiated by the flare. The continued strong coincidence between the sources of seismic emission and impulsive visible continuum emission in the case of a proton-deficient white-light flare lends substantial support to the "back – warming" hypothesis, that the low photosphere is significantly heated by intense Balmer and Paschen continuum-edge radiation from the overlying chromosphere in white-light flares.

The M7.4-class flare of 14 August 2004 is the next flare to be analysed. Observed in AR 10656, this flare produced a detectable sunquake, confirming earlier inferences that relatively low-energy flares may be able to generate sunquakes. We carry out an electromagnetic acoustic analysis of the flare from radio to hard X-rays and introduce the hypothesis that the seismicity of the active region is closely related to the heights of coronal magnetic loops that conduct high-energy particles from the flare. In the case of relatively short magnetic loops, it appears that chromospheric evaporation populates the loop interior with ionized gas relatively rapidly, expediting the scattering of remaining trapped high-energy electrons into the magnetic loss cone and their rapid precipitation into the chromosphere. This is seen to increase both the intensity and suddenness of the chromospheric heating, satisfying the basic conditions for an acoustic emission that penetrates into the solar interior. This mechanism appears to be a prospective source of the energy required to drive a powerful acoustic transient into the solar interior.

The analysis of the seismic emissions detected from the M6.7-class solar flare of 10 March 2001 rounds out the results presented in Chapter 4. Emanating from AR 9368, and in close proximity to the solar limb, this unusually impulsive solar flare embodied certain emission characteristics which appeared to closely correspond with previous instances of seismic emission from acoustically active flares. Using standard local helioseismic methods, we identified the seismic signatures produced by the flare that, to date, is the least energetic (in SXR) of the flares known to have generated a detectable acoustic transient. Holographic analysis of the flare shows a compact acoustic source strongly correlated with the impulsive HXR, visible continuum, and radio emission. Time-distance diagrams of the seismic waves emanating from the flare region also show faint signatures, mainly in the eastern sector of the active region. The strong spatial coincidence between the seismic source and the impulsive visible continuum emission reinforces the theory that a substantial component of the seismic emission seen is a result of sudden heating of the low photosphere associated with the observed visible continuum emission. Furthermore, potential-field extrapolations of the flare of 10 March 2001 continues to indicate the presence of a significant inverse correlation between the seismicity of a flare and the height of the magnetic loops that conduct the particle beams from the corona.

Finally, I summarize this thesis and present future prospects in Chapter 5. I also acknowledge that this thesis is based on five published journal articles and one unpublished paper, which were collaborations between myself and co-authors. In each of them, significant components of the work (initiation and key ideas, data analyses, numerical modelling, discussions and write up) were performed by myself.

Chapter 2

Modelling Magneto-Acoustic Ray Propagation In A Toy Sunspot

This chapter described the application of MHD ray theory to numerical forward modelling for time-distance helioseismology. Using the eikonal approximation in conjunction with the complete from of the magneto-acoustic dispersion relation, the magnetic rays are propagated through a semi-realistic sunspot atmosphere based on observed surface profiles derived from IVM magnetograms. Constructing a dense grid of ray paths based on travel time measurement geometries similar to those used in time-distance helioseismology, artificial ray travel-time perturbation profiles are derived and compared with actual observations. Evidence is shown that indicates positive travel-time perturbations obtained for short skip distances derived from time-distance observations of sunspots and active regions are likely to be spurious artifacts of the data reduction or analysis method used, rather than due to some physical shallow sub-surface thermal anomaly. This work shows that it is now feasible to use ray theory in model sunspots to produce travel-time shifts than can meaningfully be compared with observations.

Declaration for Thesis Chapter 2

Declaration by candidate

In the case of Chapter 2, the nature and extent of my contribution to the work was the following:

Nature of contribution	Extent of contribution (%)
Motivation for the work, development of the code, numerical modelling, discussion and analyses of results, preparation of all figures, wrote the paper (first author).	60

The following co-authors contributed to the work. Co-authors who are students at Monash University must also indicate the extent of their contribution in percentage terms:

Name	Nature of contribution	Extent of contribution (%) for student co-authors
Paul S. Cally	Motivation for the work, development of the code and theoretical framework, discussion and analyses of results.	

Candidate's Signature		**Date**	2/02/09

Declaration by co-authors

The undersigned hereby certify that:

(1) the above declaration correctly reflects the nature and extent of the candidate's contribution to this work, and the nature of the contribution of each of the co-authors.
(2) they meet the criteria for authorship in that they have participated in the conception, execution, or interpretation, of at least that part of the publication in their field of expertise;
(3) they take public responsibility for their part of the publication, except for the responsible author who accepts overall responsibility for the publication;
(4) there are no other authors of the publication according to these criteria;
(5) potential conflicts of interest have been disclosed to (a) granting bodies, (b) the editor or publisher of journals or other publications, and (c) the head of the responsible academic unit; and
(6) the original data are stored at the following location(s) and will be held for at least five years from the date indicated below:

Location(s)	**School of Mathematical Sciences, Monash University**

Signature 1		**Date**	2.2.09

2.1 Introduction

Time-distance helioseismology is a powerful diagnostic tool used in local helioseismology to probe the subsurface structure and dynamics of the solar interior, in particular in and around solar active regions. To date however, results obtained by time-distance helioseismology have not directly accounted for the effects of the magnetic field on the wave-speed in travel-time perturbation maps, forward modelling or inversions, but have indirectly included magnetic effects only through their influence on the acoustic properties of the medium (e.g., the sound speed). Standard forward-modelling is based on a number of assumptions including, but not limited to, Fermat's Principle and the ray approximation (e.g., Kosovichev et al., 2000; Zhao et al., 2001; Hughes et al., 2005), the Fresnel-Zone approximation (e.g., Jensen et al., 2001; Couvidat et al., 2004) and the Born approximation (e.g., Couvidat et al., 2006). These models do not include any provision for surface effects. In fact, no standard local-helioseismic method includes provisions for contributions from near-surface magnetic fields.

Recent work in sunspot seismology has pointed to the significant influence of near-surface magnetic fields and possible contamination due to their effects in helioseismic inversions for sound speed beneath sunspots (Couvidat and Rajaguru, 2007). Prior to this, a number of other very important results have highlighted the complications of interpreting helioseismic observations (in particular, the interaction of p modes) in the near-surface regions of sunspots (see e.g., Fan et al., 1995; Cally et al., 2003; Lindsey and Braun, 2005; Schunker et al., 2005; Schunker and Cally, 2006; Braun and Birch, 2006).

The key issues are (i) how to successfully model the effects of wave-speed inhomogeneities thought to be produced by the magnetic field in solar active regions, (ii) how to isolate such effects from those thought to be associated with temperature, flow perturbations, and other observational constraints and effects, and finally (iii) how will inferences made about subsurface structure change as a result of incorporating these effects into the modelling process? Efforts to address these issues both observationally and computationally have been largely unsuccessful, mainly because of a general lack of understanding of the process involved. But there is some light at the end of the tunnel, as there are currently under development a number of robust magnetohydrodynamical (MHD) simulations modelling helioseismic data and wave propagation that may aid our understanding considerably in the near future (e.g., see Cameron et al., 2008; Hanasoge and Duvall, 2007 and Chapter 3). In this work, we shall attempt to address some of these outstanding issues by using MHD ray theory to forward model helioseismic rays in a simulated sunspot atmosphere with the aim of modelling the magneto-acoustic ray propagation and analysing the resulting artificial ray travel-time perturbations that will directly account for wave-speed variations produced by the magnetic field. We will also address the problem of trying to isolate and analyse the thermal contributions to the observed travel-time perturbations using our simulations.

2.2 The MHS Sunspot Model

The axisymmetric sunspot model chosen for this analysis consists of a non-potential, untwisted, magnetohydrostatic sunspot model constrained to fit observed surface magnetic field profiles. The surface field is therefore quite realistic, which is important because there is evidence (Schunker and Cally, 2006) that magnetic effects on helioseismology are dominated by the top few hundred kilometres.

The sunspot also needs to be surrounded by an unperturbed, stratified atmosphere. The background model employed consists of a Global Oscillation Network Group (GONG) Model S atmosphere (Christensen-Dalsgaard, J., et al., 1996). The preferred surface field configuration of the flux tube was derived from constrained polynomial fits to the observed scatter plots of the radial (B_r) and vertical (B_z) surface magnetic field profiles (see Figure 2.1) of AR 9026 on 5 June 2000 – a fairly symmetrical sunspot near disk-centre, ideal for helioseismic analysis – obtained from IVM (Imaging Vector Magnetograph) vector magnetograms (see Mickey et al. (1996) for more details regarding the observations). In B_z we extrapolate to a peak field of 3 kG for our model at $r = 0$. The fits of B_r and B_z are then used to derive an analytical form for the potential function,

$$\Psi(r, z) = \psi_0 \left(\frac{R_0 r}{r_b(z)} \right) \tag{2.1}$$

where ψ_0 is the derived surface field at the surface ($z = Z_0$), the radius of the sunspot at the surface ($r = R_0$) is fixed at $R_0 = 16$ Mm. Instead of a current sheet along the boundary, we prescribe an analytical form for the outermost field line,

$$r_b(z) = \frac{R_0 - R_m}{(1 - c)\mathrm{e}^{-(z - Z_0)/\lambda} + c} + R_m, \tag{2.2}$$

where the field strength drops to zero and R_m and c are free parameters. We ensure

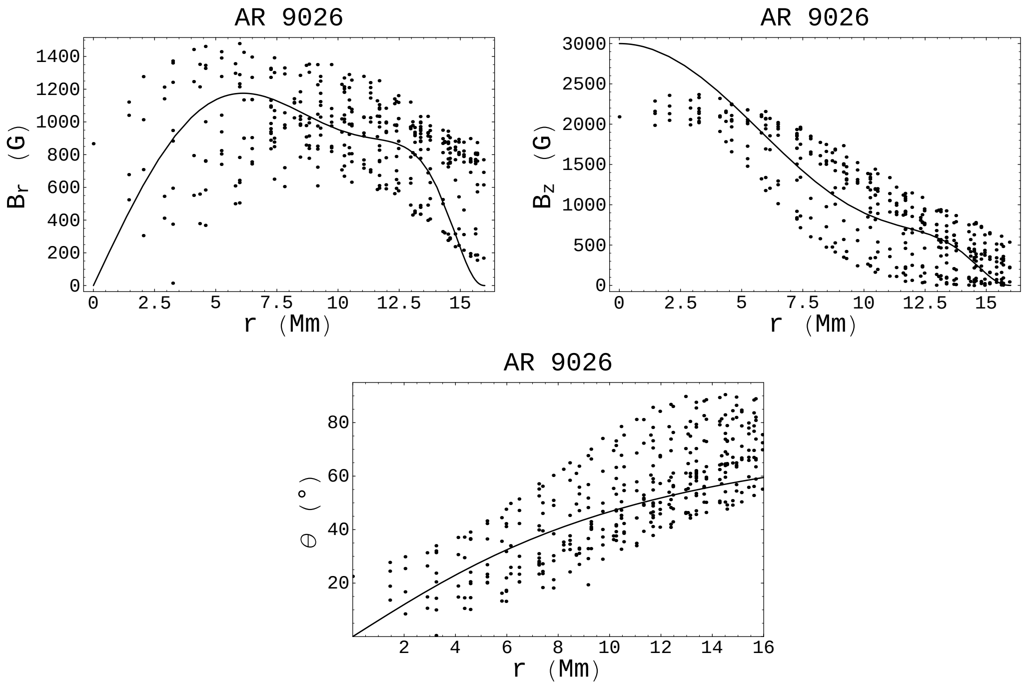

Figure 2.1: Plots of the radial (B_r, left), vertical components of the observed magnetic field (B_z, right) and magnetic field inclination from the vertical ($\theta°$) as derived from IVM surface magnetic field profiles of Active Region (AR) 9026 on 5 June 2000, shown as a function of sunspot radius (r, Mm). Solid lines indicate constrained polynomial fits. Values of B are shown in Gauss (G).

that all calculations (e.g., change in pressure, density, etc.) made across the boundary layer/transition region between the sunspot atmosphere and the external environment are both consistent and continuous along r_b.

The next step involves solving the standard equations of magnetohydrostatics (MHS), using the Model S atmosphere and its variables as the quiet-Sun environment. The magnetic pressure and tension resulting from the Lorentz force,

$$\mathbf{f}_L = \mathbf{J} \times \mathbf{B}, \tag{2.3}$$

are confined within the simulated sunspot atmosphere, where $\mathbf{J} = (\nabla \times \mathbf{B})/\mu$ represents the current density and μ the magnetic permeability. The gas pressure $p(r, z)$

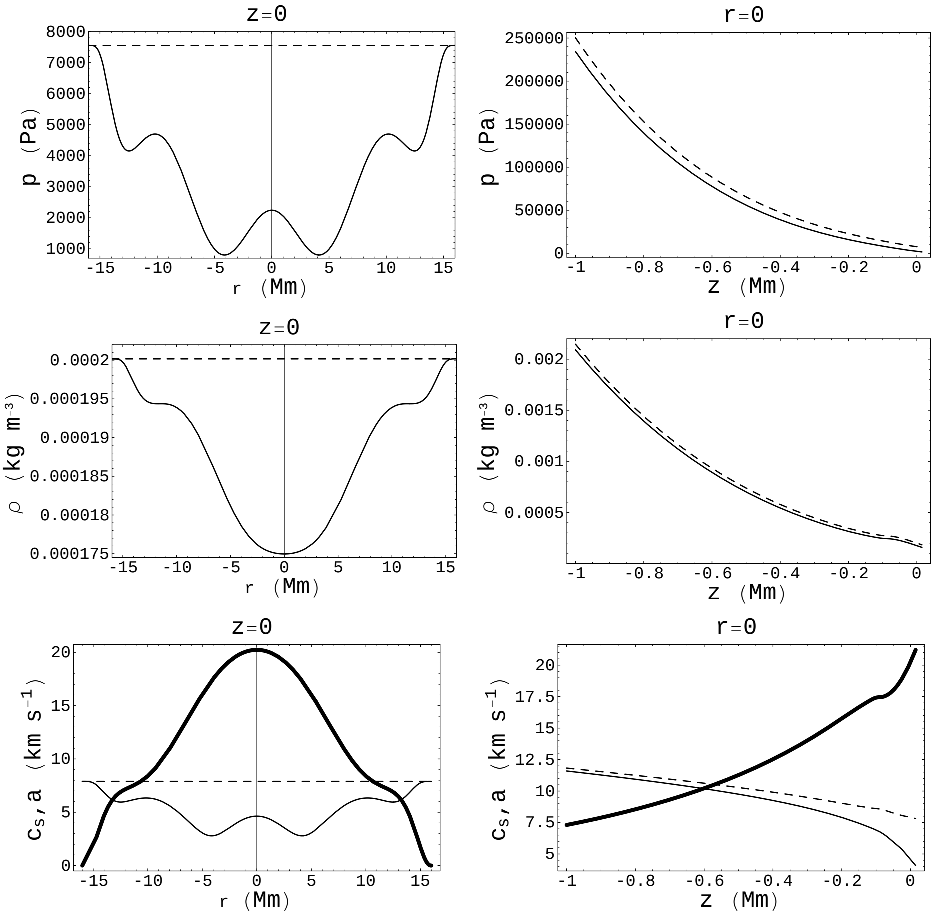

Figure 2.2: Internal pressure (p), density (ρ), sound (c_s), and Alfvén (a) speed profiles of the MHS sunspot model with an external GONG Model S atmosphere. Left-hand column profiles are calculated along the surface of the sunspot ($z = 0$), while right-hand column profiles are calculated along the axis of the sunspot ($r = 0$). Solid lines in all plots indicate internal profiles. The thick solid line in the bottom two panels indicate Alfvén speeds. The dashed lines represent GONG Model S values in all plots.

is calculated using horizontal force balance,

$$p_i(r, z) = p_e(z) + \Delta p(r, z), \tag{2.4}$$

where $p_i(r, z)$ and $p_e(z)$ denote internal and external (i.e., Model S) pressure respectively and the change in pressure is therefore

$$\Delta p(r,z) = \int_{r_b}^{r} f_{L_r} \mathrm{d}r \tag{2.5}$$

which drops to zero as we approach r_b. Once the pressure inside the sunspot and along the boundary are known, the density $\rho(r,z)$, can similarly be calculated using vertical force balance,

$$\rho_i(r,z) = \rho_e(z) + \Delta\rho(r,z) \tag{2.6}$$

where the change in density is given by

$$\Delta\rho(r,z) = \frac{1}{g}\left[\mathbf{f}_{L_z} - \frac{\partial \Delta p(r,z)}{\partial z}\right]. \tag{2.7}$$

This is essentially all that is required to then compute the modified sound speed or thermal profile of the sunspot atmosphere,

$$c_{s_i}^2(r,z) = c_{s_e}^2(z) + \Gamma_1(z)\left[\frac{p_i(r,z)}{\rho_i(r,z)} - \frac{p_e(z)}{\rho_e(z)}\right], \tag{2.8}$$

while for the sake of simplicity, assuming the ratio of specific heat (Γ_1) that appears in the sound speed is the same function of height as it is in the external atmosphere. Finally, all that is left is to calculate the Alfvén speed,

$$a^2(r,z) = \frac{1}{\mu\rho_i(r,z)}[B_r^2 + B_z^2]. \tag{2.9}$$

Some of the important internal properties of the resulting sunspot model (e.g., pressure, density, sound and Alfvén speeds) are shown in Figure 2.2. The external (Model S) profiles for each variable are also shown for reference. The near-surface thermal structure of the sunspot is also shown for reference in Figure 2.4. We can clearly see the sound-speed decrease (reaching approximately -65% at $z = 0$) as a result of the magnetic field. It is interesting to note that in our (simple) model the region of decreased sound-speed does not appear to extend as deep as 3D time-distance inversions of the real Sun have suggested. Estimates for the lateral extent of the decreased sound-speed region using tomographic imaging of the sub-surface layers of sunspots have ranged from depths of approximately $z = -2.4$ to $z = -3.5$ Mm using the Born and ray approximations respectively Couvidat et al. (2006). Nevertheless,

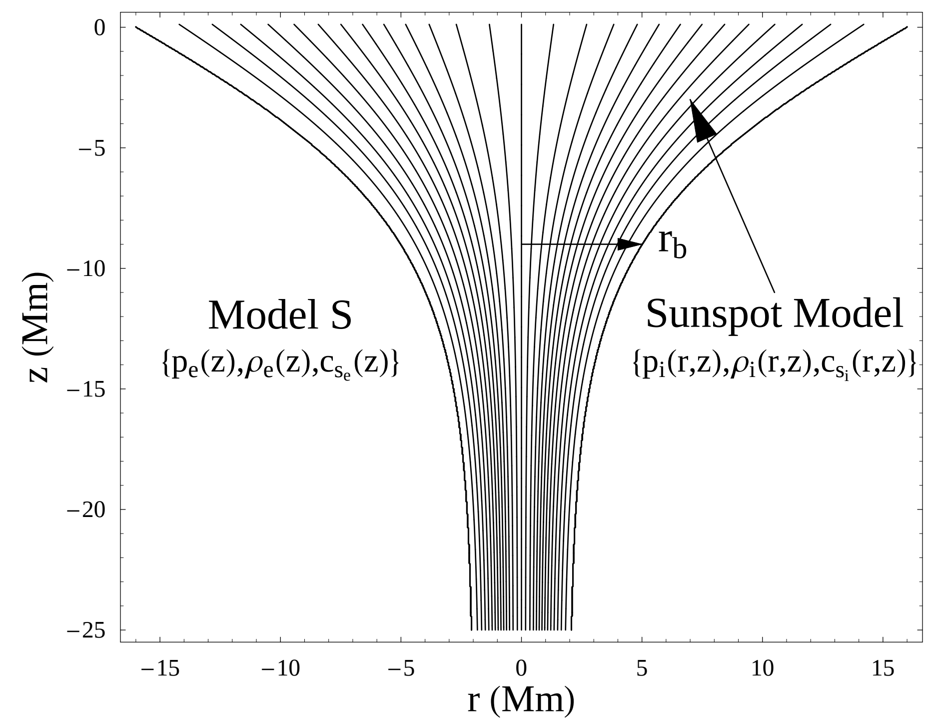

Figure 2.3: The magnetic field configuration of the MHS sunspot model. The field lines plotted indicate equidistant magnetic-flux values. Internal and external (Model S) variables are indicated for reference. r_b represents the radius of the outermost field line, which varies with depth (z) along the sunspot radius.

the sunspot model exhibits the broad features expected of a real sunspot, and presents a useful, if not totally realistic, test case.

2.3 MHD Ray-Path Calculations

The ray paths are calculated in Cartesian geometry using a fourth-order Runge-Kutta numerical scheme, in the realm of frequency dependent ray paths described by Barnes and Cally (2001). We also utilize the complete form of the three-dimensional dispersion relation (Cally and Goosens, in preparation):

$$\mathcal{D} = \omega^2\omega_c^2 a_y^2 k_h^2 + (\omega^2 - a^2 2k_\parallel^2) \times [\omega^4 - (a^2 + c_s^2)\omega^2 k^2 + a^2 c_s^2 k^2 k_\parallel^2 + c_s^2 N^2 k_h^2 - (\omega^2 - a_z^2 k^2)\omega_c^2] = 0, \tag{2.10}$$

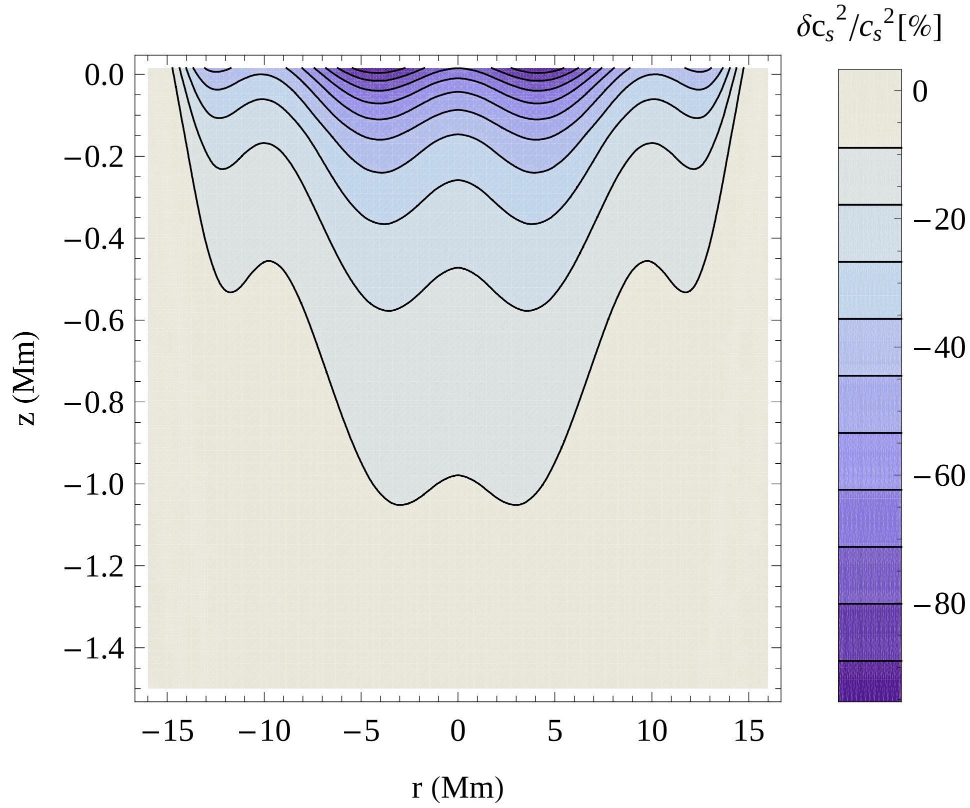

Figure 2.4: A contour plot of the thermal/sounds-speed perturbation profile of the MHS sunspot atmosphere, shown as a fraction of sound speed squared ($\delta c_s^2/c_s^2$). The sound-speed decrease observed at the surface ($z = 0$) is approximately 65%.

where k_h and $k_\parallel$ are the horizontal and parallel components of the wave-vector $\mathbf{k}$ and

$$N^2 = \frac{g}{H_\rho} - \frac{g^2}{c_s^2} \tag{2.11}$$

is the squared Brunt-Väisälä frequency, with g being the gravitational acceleration, $H_\rho(z)$ the density scale height, and $H'_\rho = \mathrm{d}H_\rho/\mathrm{d}z$ and ω_c^2 is the square of the acoustic-cutoff frequency. For completeness, we calculate the ray paths using two forms of ω_c. The most commonly used form (Deubner and Gough, 1984):

$$\omega_c^2 = \frac{c_s^2}{4H_\rho^2}(1 - 2H'_\rho), \tag{2.12}$$

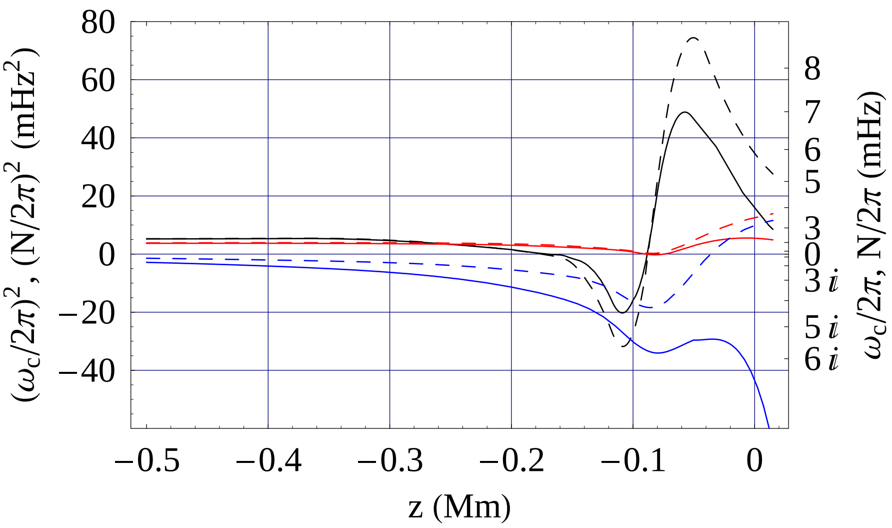

Figure 2.5: Plots of the various forms of the acoustic cutoff (ω_c) and Brunt-Väisälä (N) frequencies. A solid blue line inside the sunspot atmosphere indicates the latter, while the dashed blue line indicates Model S values. The solid black line indicates the acoustic cutoff frequency ω_c for the sunspot atmosphere, while the dashed black line indicates Model S values. The isothermal form, ω_{c_i} is indicated by the solid red line for the sunspot atmosphere, dashed red line indicates Model S values.

exhibits an extended sharp spike around $z = -100$ km (see Figure 2.5). This form of ω_c is often used by helioseismologists. However, as Cally (2007) points out, this sharp spike in the cutoff frequency is inconsistent with the WKB assumption of slowly varying coefficients on which $\mathcal{D}$ is based. A much smoother isothermal form,

$$\omega_{c_i} = c_s/2H_\rho, \tag{2.13}$$

is consistent with the derivation of $\mathcal{D}$, and does not suffer from the spike (see Figure 2.5). Unless otherwise stated, all results shown here use ω_{c_i} [1]. Naturally, the magnetic field slightly modifies both ω_c and ω_{c_i}, the results of which can be seen in Figure 2.5.

The construction of **k** is completed by specifying the governing equations of the

[1]Simulations using the form of ω_c in Equation (12) were also conducted, the results being somewhat similar to those reported in §2.4, but with slightly different timings.

ray paths as derived from the zeroth order eikonal approximation by Weinberg (1962):

$$\frac{\mathrm{d}\mathbf{x}}{\mathrm{d}\tau} = \frac{\partial \mathcal{D}}{\partial \mathbf{k}} \tag{2.14}$$

$$\frac{\mathrm{d}\mathbf{k}}{\mathrm{d}\tau} = -\frac{\partial \mathcal{D}}{\partial \mathbf{x}} \tag{2.15}$$

$$\frac{\mathrm{d}t}{\mathrm{d}\tau} = -\frac{\partial \mathcal{D}}{\partial \omega} \tag{2.16}$$

$$\frac{\mathrm{d}\omega}{\mathrm{d}\tau} = -\frac{\partial \mathcal{D}}{\partial \tau} \tag{2.17}$$

where τ parameterizes the progress of a disturbance along the ray path. For a time-independent medium, for which $\partial\mathcal{D}/\partial t = 0$ and ω is constant, the phase function $S(\mathbf{x})$ evolves according to

$$\frac{\mathrm{d}S}{\mathrm{d}t} = \mathbf{k}\cdot\frac{\mathrm{d}\mathbf{x}}{\mathrm{d}t} - \omega. \tag{2.18}$$

Hence,

$$S(\mathbf{x}) = \int \mathbf{k}\cdot\mathrm{d}\mathbf{x} - \omega t, \tag{2.19}$$

where the first term (integral) represents the contribution to the phase due to motion along the ray path, and the second term represents the Eulerian part. Since we are only going to be concerned about the change in phase due to motion along the ray path, we can ignore the Eulerian part for the rest of our analysis[2].

2.4 The 2D Ray-Path Simulations

2.4.1 The Computational Method

We iteratively find the initial wave-vector ($\mathbf{k}_{\mathrm{init}}$) by using an initial guess which comes from solving $\mathcal{D} = 0$ for the wavenumber, assuming the wavevector is in the directions α, β – where α and β are angles from the vertical and the x–z plane respectively of the initial shot. To facilitate comparisons with actual observations, our choice of $\mathbf{k}_{\mathrm{init}}$

[2]The assumption here (and in all time-distance measurements) is that the phase is always continuous along a ray path connecting two surface points. However, this assumption may not be fully justified as the recent theoretical results of Cally (2009b,a) provide strong evidence for significant phase jumps (or discontinuities) associated with fast magneto-acoustic rays that penetrate the $a = c$ level in sunspots.

ensures that the ray is initiated, and remains, on the fast-wave branch at all times. Recent numerical and analytical results have demonstrated that the observed time-distance helioseismology signals in sunspot regions correspond to fast MHD waves Khomenko et al. (2008b). Initially, we propagated the rays from an upper turning point, adjusting the initial shooting angle (α) to obtain the desired range of ray skip distances. However, given the very sensitive nature of the near-surface region of the sunspot atmosphere, we used a much finer computational grid in the top 1.5 Mm. As a result, we encountered many instances of rays initiated inside evanescent regions (which should obviously be avoided) and also obtaining very shallow rays with little or no helioseismic value (for our current analysis at least). So in order to reduce computation time and also introduce greater flexibility in choosing the desired range of ray skip distances, we initialized the rays from the minima of their trajectories (i.e., the lower turning point of the ray, $z_{\rm bot}$). Hence, the value of α was fixed at $\alpha = 90°$, allowing us to adjust the initial shooting depth $z_{\rm bot}$ to obtain the desired range of skip distances. Obviously this means that the ray timings would then be associated with the common midpoint.

A number of other important points regarding the simulations should also be noted. Firstly, in this analysis we only examine the 2D case ($\beta = 0$) where rays are confined to the x–z plane. Furthermore, by ensuring that the rays remain on the fast-wave branch at all times, we ignore the direct effects of mode-conversion effects as rays pass through the $a = c_s$ layer (where fast/slow conversion occurs, see Figure 2.4). Of course, as numerous works exploring MHD mode conversion in local helioseismology have shown (e.g., Spruit and Bogdan, 1992; Cally and Bogdan, 1993; Cally et al., 1994; Bogdan and Cally, 1997; Cally and Bogdan, 1997; Cally, 2000, 2006; Crouch and Cally, 2003, 2005; Schunker and Cally, 2006), mode transmission and conversion between fast and slow magneto-acoustic waves indeed occurs as rays of helioseismic interest pass through the $a = c_s$ equipartition level and have distinct effects on helioseismic waves that should not be ignored. But in our current analysis (and as with actual time-distance inversions) we do not directly account for these effects. As a result, the complexities of the ray-path calculations are greatly reduced. Finally, it should also be noted that we ignore any finite-wavelength effects and direct filtering of observations in our simulations.

The computational ray propagation grid extends across the 16 Mm radius of the sunspot model in regular 1 Mm spatial increments in the horizontal x-direction and down to a depth of 25 Mm in the vertical z-direction, employing a much finer grid spacing in the top 1.5 Mm, followed by 1 Mm increments down to a depth of 25 Mm. The upper boundary for the ray propagation grid was fixed at $z = 0.1$ Mm. This computational grid, though not exhaustive, allows us to obtain the desired range of skip distances required to replicate the "centre-to-annulus" skip distance geometry (i.e., averaging rays from a central point/pixel to a surrounding annulus of different sizes to probe varying depths beneath the solar surface) often employed in time-distance helioseismology for the derivation of mean travel-time perturbation maps (see Gizon and Birch (2005) for a more comprehensive description of this process). The 11 standard skip distance bin/ travel distances (Δ) usually used for these calculations are detailed in Table 2.1.

Table 2.1: The skip-distance geometries used to bin the ray travel-time measurements.

Δ	Pupil Size (Mm)
1	3.7 - 8.7
2	6.2 - 11.2
3	8.7 - 14.5
4	14.5 - 19.4
5	19.4 - 29.3
6	26.0 - 35.1
7	31.8 - 41.7
8	38.4 - 47.5
9	44.2 - 54.1
10	50.8 - 59.9
11	56.6 - 66.7

2.4.2 Travel-Time and Skip-Distance Perturbations

The ray propagation grids were computed for three frequencies, $\omega = 3.5$, 4, and 5 mHz. Both the phase (t_{p}, associated with the *phase* velocity) and group (t_{g}, associated with the envelope peak of a wave packet as it travels at the *group* velocity) ray travel times were calculated along each ray path for every radial grid position (r_{spot}, which is the radial position associated with the lower turning point of the ray) along the sunspot model. In time-distance helioseismology, centre-to-annulus travel times are extracted from Gaussian wavelet fits – usually represented by a function of the form

$$W_{\pm}(t) = A\mathrm{e}^{-\gamma^2(t\mp t_{\mathrm{g}})^2}\cos[\omega_0(t \mp t_{\mathrm{p}})], \tag{2.20}$$

(where all parameters are free) – to both the positive and negative time parts of the observed cross-correlations (Gizon and Birch, 2005). However, t_{p} is more often used in time-distance literature, primarily as a result of difficulties (mainly observational noise) associated with fitting to the envelope peak. Furthermore, because t_{p} is much more independent of the shape of the wave packet than t_{g} (as the shape of the wavepacket depends on (unmodelled) mode conversion), we shall also limit our analysis to t_{p} calculations in this analysis. We identify the phase travel time as:

$$t_{\mathrm{p}} = \frac{S(\mathbf{x})}{\omega}, \tag{2.21}$$

which is consistent with the form of t_{p} described by the Gaussian wavelet. These travel times are then subtracted from similar ray travel times calculated using the quiet-Sun atmosphere to produce *travel-time perturbation* ($\delta\tau_{\mathrm{p}}$) profiles. In general, travel-time *differences* are sensitive to sub-surface flows, while *mean* travel times are sensitive to wave-speed perturbations. However, as our model does not contain flows, we do not need to distinguish directions along ray paths.

In Figure 2.6 we see some sample $\delta\tau_{\mathrm{p}}$ profiles for $r_{\mathrm{spot}} = 4, 8, 12,$ and 16 Mm are shown as a function of ray skip distance (x) for ω = 3.5 (green), 4.0 (red), and 5.0 mHz (blue). By and large, there are significant perturbations as we approach the centre of the sunspot (i.e., regions associated with stronger surface magnetic field strength). The sign of the perturbations appears to remain exclusively negative, regardless of position on the sunspot. This means that all rays propagated within the simulated sunspot atmosphere are significantly sped up when compared to their Model S counterparts.

Furthermore, in Figure 2.7 we can see that there are also significant skip-distance perturbations (δx) associated with rays that are propagated through the sunspot atmosphere. These calculations are for similar positions and frequencies as in Figure 2.6. The exclusively positive values of δx that we can see along the sunspot radius indicates that at the same time that these rays are being sped up, they are also undertaking a longer journey than their Model S counterparts in the process, and as with $\delta\tau_{\mathrm{p}}$, the magnitude of the calculated δx appears to be closely related to surface magnetic field strength. For both $\delta\tau_{\mathrm{p}}$ and δx we also observe a particular

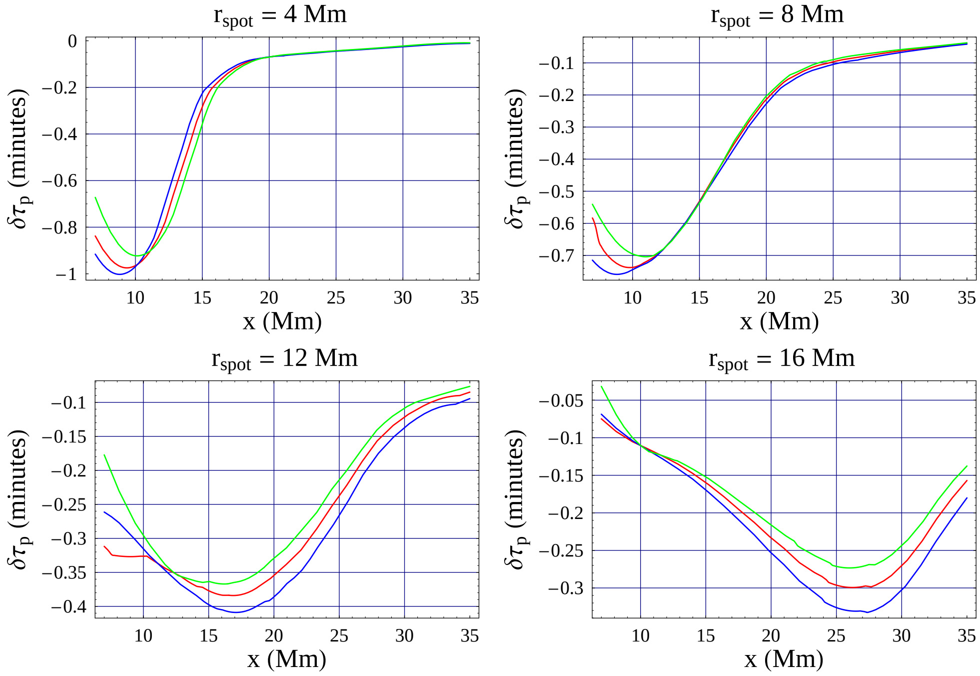

Figure 2.6: Travel-time perturbations ($\delta\tau_{\mathrm{p}}$) as a function of skip distance (x) for $r_{\mathrm{spot}} = 4, 8, 12$, and 16 Mm on the sunspot (where r_{spot} is the radial position of the lower turning point of the ray), as calculated for three frequencies: $\omega = 3.5$ (green), $\omega = 4.0$ (red) and $\omega = 5.0$ mHz (blue).

pattern of perturbation associated with each position along the sunspot. Whereas the perturbations appear to mainly decrease when we are close to spot centre (e.g., $r_{\mathrm{spot}} = 4, 8$ Mm), they appear to increase when further away (e.g., $r_{\mathrm{spot}} = 12, 16$ Mm) from spot centre. This is clearly a bi-product of both varying field strength and inclination angle of field lines (see Figure 2.1) as we move across the sunspot. Field strength tends to decrease, while field lines become more significantly inclined as we move away from centre of the sunspot.

Also clearly obvious from both Figures 2.6 and 2.7 is the presence of a significant frequency dependence of both $\delta\tau_{\mathrm{p}}$ and δx measurements in the sunspot, with the magnitudes of the perturbations increasing as the frequency is increased from 3.5 to 5.0 mHz. This is particularly evident for rays with short skip distances (i.e., surface skimmers with very shallow lower turning points). Frequency dependence of travel-time perturbations in active regions has also been observed by both helioseismic holography (Braun and Birch, 2006) and time-distance helioseismology (Couvidat and

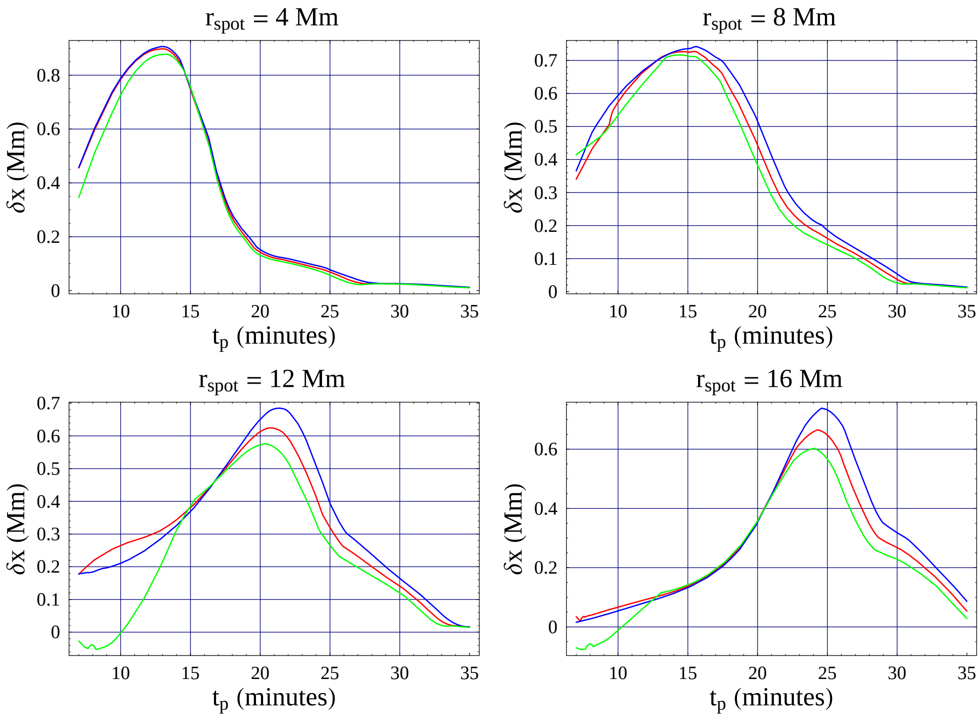

Figure 2.7: Skip distance perturbations (δ_x) as a function of phase travel time (t_p) for $r_{\text{spot}} = 4, 8, 12$, and 16 Mm on the sunspot, calculated for three frequencies$\omega = 3.5$ (green), $\omega = 4.0$ (red), and $\omega = 5.0$ mHz (blue).

Rajaguru, 2007). We shall discuss the importance of these observations in greater detail in the upcoming sections. Cally (2007) also observed a similar behaviour when modelling rays in inclined fields and described several related but distinct effects that strong magnetic fields appear to have on seismic waves, with an important "dual effect" that the magnetic field has on individual ray paths (that is, increasing their skip distances while at the same time, speeding them up considerably) being one of these effects.

A comparison between rays propagated inside the sunspot model with rays propagated in the quiet-Sun clearly reveals these effects to the naked eye. All rays shown in Figure 2.8 are initialized at a depth of $z_{\text{bot}} = -2$ Mm, with the rays inside the sunspot model (solid rays, colours identify frequencies) also being initialized at varying positions along the sunspot ($r_{\text{spot}} = 0, 4, 8, 12$, and 16 Mm). While the rays propagated inside the Model S atmosphere (dashed rays) are symmetrical about their turning points (as expected), strong asymmetries (at both turning points) are associated

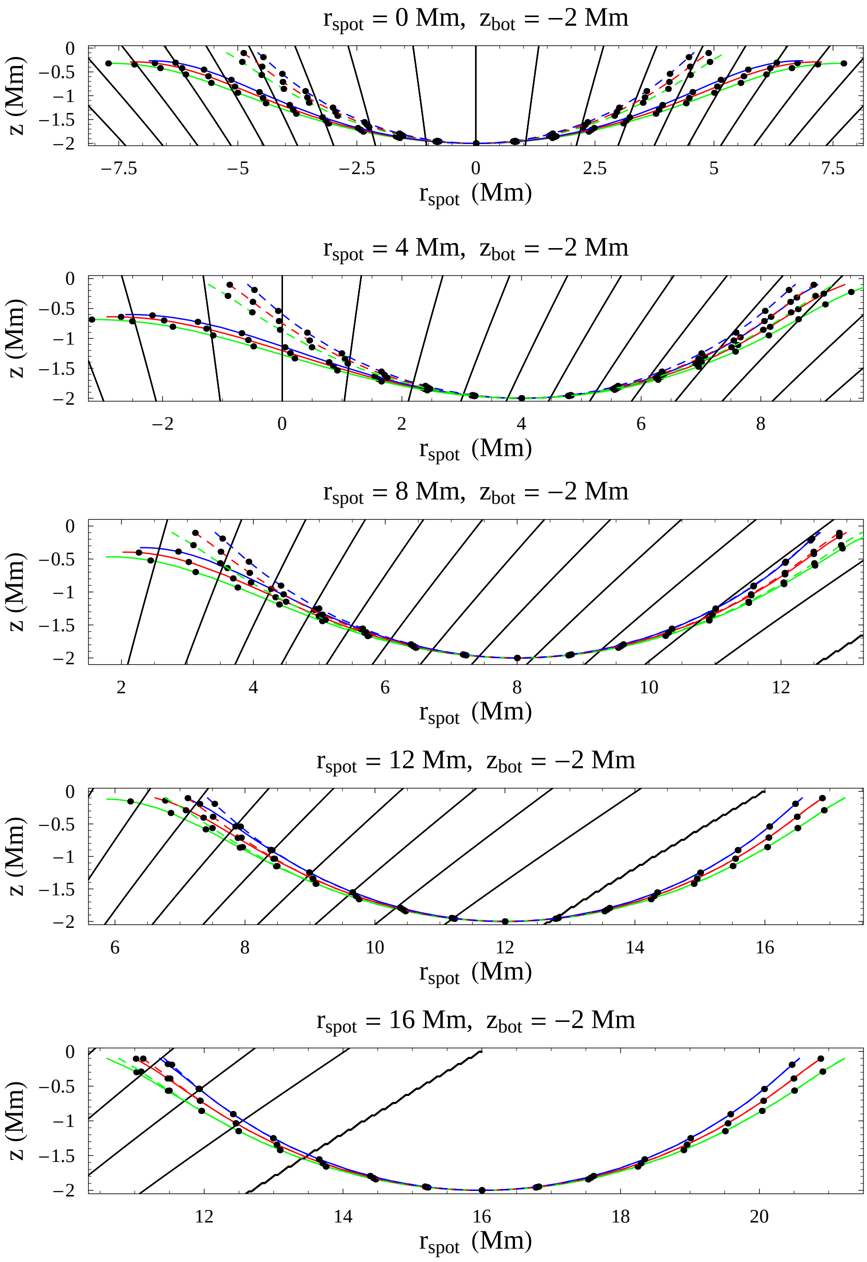

Figure 2.8: Plots of individual rays propagated through the simulated sunspot (solid rays) and Model S (dashed rays) atmospheres, calculated for three frequencies: $\omega = 3.5$ (green), $\omega = 4.0$ (red), and $\omega = 5.0$ mHz (blue). The top of each frame indicates the initial depth ($z_{\rm bot}$, Mm) and radial grid position of the lower turning point of the ray ($r_{\rm spot}$, Mm).

with the same rays when initiated inside the sunspot. We can clearly see that the rays inside the sunspot (at all three frequencies) appear to have undergone a longer skip distance, in a slightly shorter amount of time (dots along ray paths indicate one-minute t_g intervals), confirming the perturbation profiles of Figures 2.6 and 2.7. Of course Figure 2.8 shows a very small sample of rays initialized at a given depth, but even so, they are quite clearly indicative of the large-scale effects of the magnetic field on ray propagation – effects which are more pronounced as we approach the spot centre and in regions of significantly inclined magnetic fields.

2.4.3 Binned Travel-Time Perturbation Profiles

The mean ray travel-time perturbations ($\delta\tau_\mathrm{p}^\mathrm{m}$) for each frequency and grid position were calculated and binned into 11 skip distances ($\Delta_1 - \Delta_{11}$) of various sizes (outlined in Table 2.1). The $\delta\tau_\mathrm{p}^\mathrm{m}$ profiles of the bins are shown in Figure 2.9. Once again, we can see the clear frequency dependence of travel-time perturbations evident in all bins, with perturbations increasing with increasing frequency as before. Also, all $\delta\tau_\mathrm{p}^\mathrm{m}$ bins contain negative perturbations as we saw before in Figure 2.6. We also observe that the magnitude of $\delta\tau_\mathrm{p}^\mathrm{m}$ decreases as we move away from the centre of the sunspot (i.e., decreasing field strength) for the smaller bins (e.g., $\Delta_1 - \Delta_3$).

These smaller bins are representative of shallow rays that spend a considerable proportion of their journey inside the magnetic field, consistent with the larger magnitude of the perturbations seen in these bins. Larger bins (e.g., $\Delta_4 - \Delta_{11}$) sample rays with much deeper lower turning points, hence a considerable amount of the journey undertaken by these rays would be spent in the quiet-Sun Model S atmosphere. Therefore the magnitude of the perturbations tends to be smaller than that for the smaller bins. However, they are found to increase in magnitude as we move away from the centre of the sunspot as rays sample larger areas of the magnetic field throughout their journey across the sunspot radius.

It should be noted that for the smaller bins (particularly for $\Delta_1 - \Delta_3$), it becomes quite difficult to obtain a sufficient sampling of rays to average near the centre of the flux tube, even with a very fine grid spacing of $\Delta z = -0.025$ Mm in the very sensitive top 1.5 Mm of the computational grid. Consequently, we end up with somewhat coarse $\delta\tau_\mathrm{p}^\mathrm{m}$ bins. No such restriction is encountered when using the Model S/quiet Sun atmosphere, which tends to suggest that strong near-surface magnetic fields are severely restricting the propagation of helioseismic rays with very shallow lower turning points.

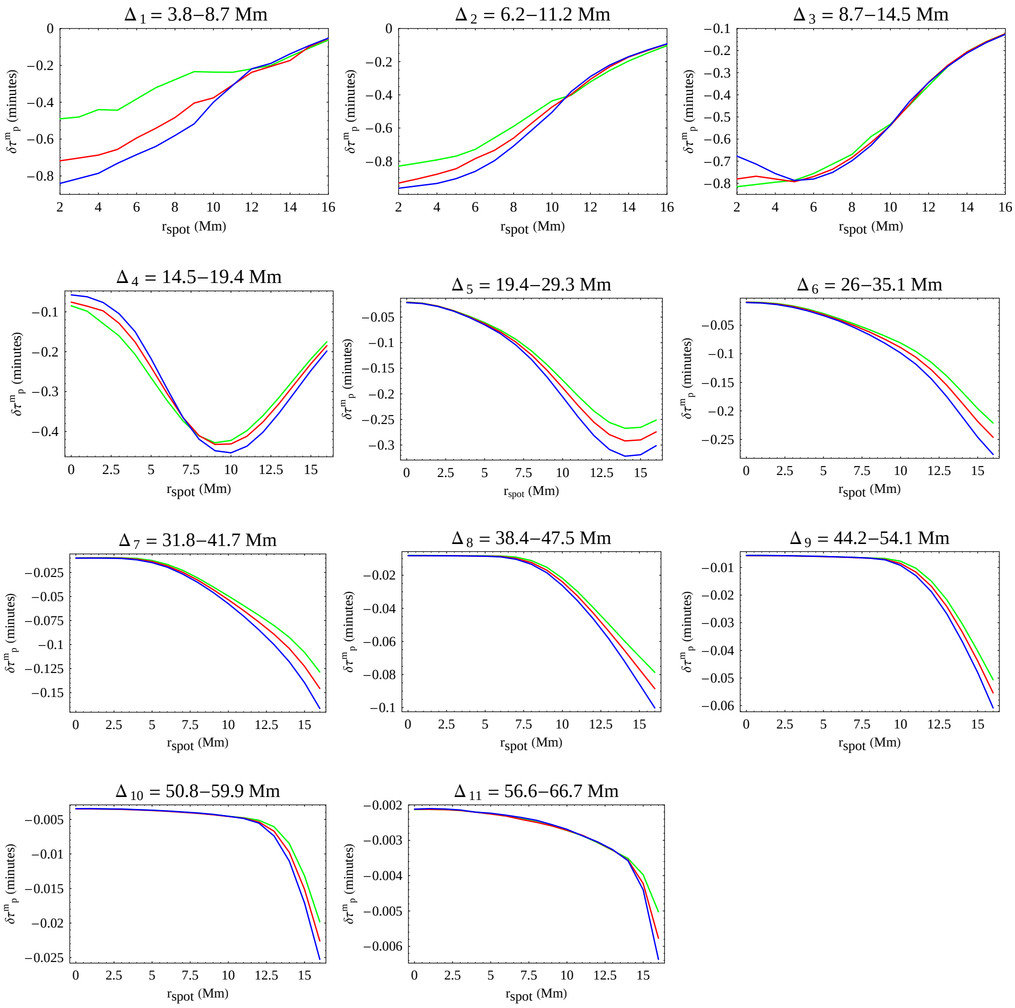

Figure 2.9: Binned (mean) travel-time perturbation ($\delta\tau_{\rm p}^{\rm m}$, minutes) profiles as a function of position ($r_{\rm spot}$, Mm) on the sunspot, calculated for three frequencies: $\omega = 3.5$ (green), $\omega = 4.0$ (red), and $\omega = 5.0$ mHz (blue). Annuli number and sizes are indicated on the top of the frame of each bin.

2.4.4 Comparison With Observations

Although our sunspot model has many of the qualitative features we might expect in a real spot, it is nonetheless rather *ad hoc*, and consequently our time-distance results do not warrant detailed comparison with solar observations. Nevertheless, it is of interest to qualitatively compare the $\delta\tau_{\rm p}^{\rm m}$ results obtained from our simulations to those reported for AR 8243 (18 June 1998) by Couvidat et al. (2006). S. Couvidat kindly provided us with the actual set of travel time maps used in their analysis.

To compare the $\delta\tau_{\mathrm{p}}^{\mathrm{m}}$ profiles as closely as possible, we first compute the azimuthal average of the four $\delta\tau_{\mathrm{p}}^{\mathrm{m}}$ maps presented in Figure 3 of Couvidat et al. (2006) (corresponding to Δ_1, Δ_3, Δ_6 and Δ_9, noting that the travel-times were obtained without a frequency bandpass filter), to obtain $\delta\tau_{\mathrm{p}}^{\mathrm{m}}$ profiles of AR 8243, akin to our artificial, common midpoint $\delta\tau_{\mathrm{p}}^{\mathrm{m}}$ profiles contained in Figure 2.9. We observe peak (positive) travel-time perturbations of ≈ 0.29 and ≈ 0.16 minutes respectively for Δ_1 and Δ_3 in the sunspot umbra, while the sign of $\delta\tau_{\mathrm{p}}^{\mathrm{m}}$ in the sunspot changes for the larger bins, Δ_6 and Δ_9, with $\delta\tau_{\mathrm{p}}^{\mathrm{m}}$ ranging from ≈ -0.38 to ≈ -0.31 minutes respectively. The perturbations for all four bins also appear to decrease in the penumbra relative to the umbra. In comparison, if we assume a central frequency of 3.5 mHz, the artificial $\delta\tau_{\mathrm{p}}^{\mathrm{m}}$ profiles for the bins produced by our simulations (Figure 2.9, 3.5 mHz profiles indicated by solid green lines) show opposite-in-sign and larger-in-magnitude $\delta\tau_{\mathrm{p}}^{\mathrm{m}}$ for both Δ_1 (≈ -0.7 minutes) and Δ_3 (≈ -0.82 minutes), while similar-in-sign yet smaller-in-magnitude $\delta\tau_{\mathrm{p}}^{\mathrm{m}}$ profiles were observed for Δ_6 (≈ -0.22 minutes) and Δ_9 (≈ -0.05 minutes). When we consider higher frequencies, the magnitude of the artificial $\delta\tau_{\mathrm{p}}^{\mathrm{m}}$ increases with frequency for all four bins, with all perturbations being negative in sign. However, the general pattern of the artificial $\delta\tau_{\mathrm{p}}^{\mathrm{m}}$ profiles for all frequencies appears to be similar to the observations of Couvidat et al. (2006), with perturbations decreasing with increasing radius from the centre of the sunspot. The off-axis behaviour of the larger $\delta\tau_{\mathrm{p}}^{\mathrm{m}}$ bins is partly due to the common midpoint travel-time measurement geometry we have employed as well as the 2D nature of the simulations.

While the differences in the magnitudes of $\delta\tau_{\mathrm{p}}^{\mathrm{m}}$ between our simulations and those of Couvidat et al. (2006) (at a given fixed central frequency) can be explained, to some extent, by magnetic and thermal differences between our model and their sunspot, the frequency dependence of $\delta\tau_{\mathrm{p}}^{\mathrm{m}}$ and the sign change of the smaller bins in particular (i.e., positive $\delta\tau_{\mathrm{p}}^{\mathrm{m}}$ resulting from actual time-distance observations, negative $\delta\tau_{\mathrm{p}}^{\mathrm{m}}$ from the simulations) can not be dismissed as easily. Traditionally, positive $\delta\tau_{\mathrm{p}}^{\mathrm{m}}$ obtained for short skip distances in sunspots have been interpreted as representing a region of slower wave-speed propagation in the shallow sub-surface layers of the sunspot. However, as we briefly noted in the previous section, Braun and Birch (2006) (using helioseismic holography) found that, at a given fixed phase speed, travel-time perturbations within active regions exhibit a strong frequency dependence. Couvidat and Rajaguru (2007) confirmed these results using time-distance helioseismology, applying additional frequency bandpass filters (centred at 3.0, 4.0 and 4.5 mHz) to the standard phase-speed filters used in Couvidat et al. (2006) in order to determine the cause of the dark rings of negative $\delta\tau_{\mathrm{p}}^{\mathrm{m}}$ they detected in the travel-time maps (mainly associated with the Δ_2 and Δ_3 skip-distance bins) of a majority of the sunspots they studied. These rings, which are sensitive to the frequency filtering applied, are found to produce significant ring-like structures in the inversion results, mimicking regions of increased sound speed. The authors conclude that the rings are most likely to be artifacts caused by surface effects, probably of magnetic origin.

In addition to these results, the very recent work undertaken by Braun and Birch (2008) (using ridge filters, in addition to the standard phase-speed filters) provide strong evidence that the positive perturbations observed arise from the p_1 ridge or beneath it. These positive travel-time shifts were not seen in the higher order p-mode data. These results, when considered in conjunction with our artificial $\delta\tau_{\mathrm{p}}^{\mathrm{m}}$ profiles (and the results contained in in the next section), provide further evidence that positive travel-time perturbations obtained for short skip distances are likely to be artifacts or bi-products of the data reduction or analysis method used, rather than some actual physical sub-surface thermal anomaly below the sunspot.

2.4.5 Isolating the Thermal Component of Travel Time Perturbations

One of the keys to understanding the role played by near-surface magnetic fields in local helioseismology is to be able to isolate it from effects thought to be produced by thermal or flow perturbations. The simplest way to isolate such effects is to "switch off" the magnetic field when calculating the ray paths in the simulations – that is, set $a = 0$ in the simulated sunspot atmosphere, but maintain the modified sound-speed profile obtained (seen in Figure 2.4). Of course, this technically means that the model is no longer in MHS equilibrium, but this does not affect linear wave calculations.

The external atmosphere, ray-path simulations and computational grid remain identical to those described previously. The only difference is the resulting thermal travel-time perturbations ($\delta\tau_{\mathrm{p}}^{\mathrm{mt}}$) which would then be purely a result of what can be referred to as "thermal variations" along the ray path. One can then compare the resulting perturbation profiles to those obtained when the magnetic field is included in the simulations (i.e., Figure 2.9) to better understand the role of the thermal contributions to the observed $\delta\tau_{\mathrm{p}}^{\mathrm{m}}$ profiles. Figure 2.10 shows the resulting bins of the thermal component of $\delta\tau_{\mathrm{p}}^{\mathrm{mt}}$.

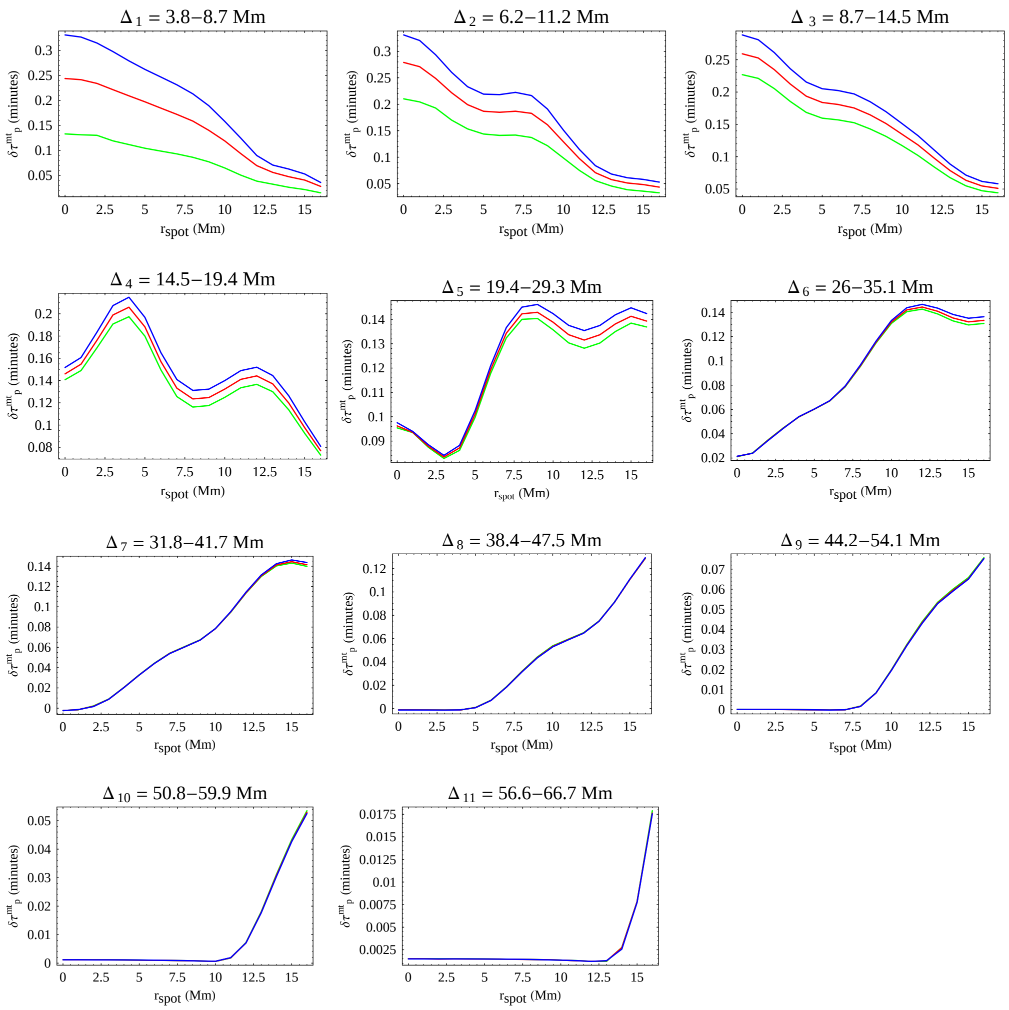

Figure 2.10: Binned thermal travel-time perturbation ($\delta\tau_{\mathrm{p}}^{\mathrm{mt}}$, minutes) profiles as a function of position (r_{spot}, Mm) on the sunspot, calculated for three frequencies: $\omega = 3.5$ (green), $\omega = 4.0$ (red), and $\omega = 5.0$ mHz (blue). Annuli number and sizes are indicated on the top of the frame of each bin.

In general, the resulting $\delta\tau_{\mathrm{p}}^{\mathrm{mt}}$ profiles are relatively smooth and all bins clearly show exclusively positive travel-time perturbations (compared to exclusively negative travel-time perturbations observed in Figure 2.9). This implies that rays are travelling considerably slower than in the Model S atmosphere – a clear contrast with simulations where the magnetic field is present. The magnitude of $\delta\tau_{\mathrm{p}}^{\mathrm{mt}}$ is also decreasing with increasing radius for the smaller bins ($\Delta_1 - \Delta_4$) and *vice versa* for the larger bins

($\Delta_5 - \Delta_{11}$), a similar behaviour to what is observed in Figure 2.9. However, when considering the magnitude of the perturbations between Figures 2.9 and 2.10, it is clear that thermal perturbations appear to be much smaller for a majority of the bins – in fact up to 400% smaller for some frequencies when comparing the perturbations in the near-surface regions $\Delta_1 - \Delta_3$. The magnitude of the perturbations become much more comparable when looking at the larger bins (Δ_7 onwards), and from Δ_8 onwards $\delta\tau_{\mathrm{p}}^{\mathrm{mt}}$ becomes ever slightly larger than the ones we see in Figure 2.9 for the same bins. Frequency dependence of $\delta\tau_{\mathrm{p}}^{\mathrm{mt}}$ is also evident, but only clearly discernible for the first six bins ($\Delta_1 - \Delta_6$) and most likely due to the effects of the change in acoustic cutoff frequency as a result of the modified thermal structure.

2.5 Summary and Discussion

Whether it be through direct observations, forward modelling, or inversions, in order to be able to confidently interpret helioseismic observations and inferences made in regions of strong magnetic field, the actual physical effects of near-surface magnetic fields on ray propagation must be better understood and taken into account when analyzing or modelling active region sub-photospheres. Our approach here is akin to forward modelling of rays, but in a simulated sunspot atmosphere based on IVM surface magnetic-field profiles with a peak field strength of 3 kG and an external field-free Model S atmosphere used as the background or unperturbed medium. The main aim of these simulations was to isolate and understand the effects of the wave-speed inhomogeneities produced by the magnetic field from those thought to be produced from thermal or sound-speed perturbations.

The magneto-acoustic rays were propagated across the sunspot radius for a range of depths to produce a skip distance geometry similar to centre-to-annulus cross-covariances used in time-distance helioseismology. The perturbations from the Model S atmosphere were calculated for each radial grid position and range of frequencies ($3.5 - 5.0$ mHz), then binned into 11 different skip-distance geometries of increasing size. A separate, yet similar, set of simulations was then produced to isolate the role played by thermal variations inside the sunspot atmosphere on the ray skip distance and travel-time perturbation profiles. This was achieved by switching off the magnetic field in the model – i.e., integrating the rays in the absence of the flux tube while maintaining the modified sub-surface sound speed structure.

These *artificial* skip-distance and travel-time perturbation profiles, which directly account for the effects near-surface magnetic fields and thermal variations separately, have provided us with a number of very distinct and interesting observations:

1. The sunspot magnetic field has a clear and distinct "dual effect" on helioseismic rays – increasing their skip distances, while at the same time, shortening their travel time (compared to similar rays in a Model S atmosphere). Higher frequency rays propagated within the magnetic field also tend to undergo a more substantial speed up than their non-magnetic counterparts.

2. There is a clear and significant frequency dependence of both ray skip-distance and travel-time perturbations across the simulated sunspot atmosphere. This frequency dependence of perturbations was prevalent for all skip-distance bins, but particularly so for shallow rays, which sample the near-surface layers of the sunspot.

3. The general pattern and magnitude of the observed time shifts (i.e., tending to increase with increasing magnetic-field strength and inclination) points to more evidence of the significant role played by the sunspot magnetic field. Rays with shorter skip distances were seen to experience greater perturbations as a result of spending a considerable proportion of their journey within the confines of the magnetic field.

4. The consistent (negative) sign of the time shifts also correctly reflects the one-layered sound- and wave-speed profile (i.e., consistent sound-speed decrease and wave-speed enhancement) of the model atmosphere.

5. With the magnetic field switched off, the simulated travel-time perturbation profiles changed sign for all bins (i.e., only positive perturbations were observed across the sunspot radius, meaning that rays in the thermal model are actually slower than their Model S counterparts), and the magnitude of these perturbations appeared to be significantly smaller in magnitude (300–400% at times) than when the magnetic field is included in the model. This was particularly evident for the bins that sample rays in the near-surface layers, whereas bins of larger skip distances produce slightly larger perturbations than the magnetic model. Frequency dependence of travel-time perturbations were also observed, but only for half of the bins. A majority of bins sampling larger skip distances did not exhibit this behaviour.

These observation as a whole tend to suggest that active-region magnetic fields play a direct and significant role in sunspot seismology, and it is the interaction of the near-surface magnetic field with solar oscillations, rather than purely thermal (or sound-speed) perturbations, that is the major cause of observed travel-time perturbations in sunspots.

The frequency dependence of these perturbations is one of the strongest indications that the magnetic field is a significant contributor to the travel-time shifts. When isolating the thermal component of $\delta\tau_{\rm p}$ we did observe some frequency dependence in a limited number of bins/skip distance geometries, certainly not to the extent that we saw when the magnetic field was included. Of course in the absence of any perturbations, rays propagated at different frequencies will naturally have slightly different upper turning points, this could certainly explain a part of a frequency dependence, but this effect combined with the (negative) sign and magnitude of the simulated $\delta\tau_{\rm p}$ profiles, along with the relatively small (positive) thermal component extracted from the perturbations, makes it very difficult for one to argue that what we are seeing in these travel-time perturbation profiles is a result of a sub-surface flow or sound-speed perturbation, as has been traditionally interpreted in time-distance literature.

Instead, these observations indicate that strong near-surface magnetic fields may be seriously altering the magnitude and lateral extent of sound-speed inversions made by time-distance helioseismology. This is because standard time-distance observations (e.g., Couvidat et al. (2006), see Section 4.2) show $\delta\tau_{\rm p}^{\rm m}$ maps derived from the averaged cross-correlations shifting from positive values for the first couple of bins (usually $\Delta_1 - \Delta_3$), to negative ones for the remainder of the bins. Traditionally, positive perturbations result in regions of decreased sound speed in inversions, while negative perturbations result in regions of enhanced sound speed. But we have clearly seen from our forward modelling that the inclusion of the magnetic field in the near surface layers consistently results in negative values for all bins of $\delta\tau_{\rm p}^{\rm m}$. This implies that any inversion of time-distance data that does not account for surface magnetic field effects will be significantly contaminated in the shallower layers of the sunspot (i.e., down to a depth of a few Mm below the surface), in strong agreement with the conclusions of Couvidat and Rajaguru (2007). Hence it is almost certain from these simulations that the two-structure sunspot sound speed profile, i.e., region of decreased sound speed immediately below the sunspot (corresponding to positive $\delta\tau_{\rm p}^{\rm m}$), is most likely an artifact due to a combination of surface effects and the use of phase-speed filtered data, instead of some kind of a "thermal anomaly". As expected, deeper sound speed profiles do not appear to be affected as much, as evidenced by the sign and magnitude of the simulated $\delta\tau_{\mathrm{p}}^{\mathrm{m}}$ for the larger bins, which appear to be consistent with actual time-distance observations. Given the flux tube becomes gas-pressure dominated at such depths, we can expect thermal effects to dominate.

Of course, we must bear in mind that some of our assumptions outlined earlier (e.g., 2D treatment of rays, the fact that we are not directly accounting for mode conversion and phase discontinuities, and even the form of the surface magnetic field and background model in general etc.) can certainly alter our results quantitatively in one manner or another. Indeed it would certainly be interesting and worthwhile to conduct a full 3D simulation (i.e., vary the shooting angle β around the sunspot) and also test the ray propagation code with other sunspot and quiet-Sun models in the future. But in any case, it would be surprising, given the self-consistency of our current results, if our qualitative conclusions were changed as a result.

Chapter 3

The Role of Strong Magnetic Fields on Helioseismic Wave Propagation

In this chapter we investigate the direct contribution of strong, sunspot-like magnetic fields to helioseismic wave travel-time shifts by conducting a comparative study between two recently developed numerical forward models: the MHD ray tracer detailed in the previous chapter, and the 3D ideal MHD solver of Hanasoge (2007) which simulates linear wave propagation in a solar-like stratified medium. Two contrasting time-distance travel time measurement schemes are used to analyse the simulated vertical velocity data cubes produced by the MHD simulations. The first scheme employs a centre-to-annulus measurement geometry to derive surface-focus travel times, while the second scheme employs a common midpoint method, in conjunction with realization noise subtraction, to extract deep-focus travel times. The latter is chosen so as to avoid oscillation signals in the sunspot region. We also isolate and analyse the direct contribution from purely thermal perturbations to the observed travel-time shifts, confirming some existing ideas and bringing forth new ones.

Declaration for Thesis Chapter 3

Declaration by candidate

In the case of Chapter 3 (Section 3.1), the nature and extent of my contribution to the work was the following:

Nature of contribution	Extent of contribution (%)
Motivation for the work, numerical modelling, discussion and analyses of results, preparation of the figures, wrote much of the text.	60

The following co-authors contributed to the work. Co-authors who are students at Monash University must also indicate the extent of their contribution in percentage terms:

Name	Nature of contribution	Extent of contribution (%) for student co-authors only
Shravan M. Hanasoge	Numerical modelling, discussion and analyses of results, wrote part of the text.	
Paul S. Cally	Discussion and analyses of results.	

Candidate's Signature	[signature]	Date 2/02/09

Declaration by co-authors

The undersigned hereby certify that:

(1) the above declaration correctly reflects the nature and extent of the candidate's contribution to this work, and the nature of the contribution of each of the co-authors.
(2) they meet the criteria for authorship in that they have participated in the conception, execution, or interpretation, of at least that part of the publication in their field of expertise;
(3) they take public responsibility for their part of the publication, except for the responsible author who accepts overall responsibility for the publication;
(4) there are no other authors of the publication according to these criteria;
(5) potential conflicts of interest have been disclosed to (a) granting bodies, (b) the editor or publisher of journals or other publications, and (c) the head of the responsible academic unit; and
(6) the original data are stored at the following location(s) and will be held for at least five years from the date indicated below:

Location(s)	School of Mathematical Sciences, Monash University

Signature 1	[signature] SHRAVAN HANASOGE	Date 4/12/08
Signature 2	[signature]	2.2.09
Signature 3		

Declaration by candidate

In the case of Chapter 3 (Section 3.2), the nature and extent of my contribution to the work was the following:

Nature of contribution	Extent of contribution (%)
Initiation, key ideas, numerical modelling, discussion and analyses of results, preparation of all figures, wrote the text (first author).	70

The following co-authors contributed to the work. Co-authors who are students at Monash University must also indicate the extent of their contribution in percentage terms:

Name	Nature of contribution	Extent of contribution (%) for student co-authors only
Shravan M. Hanasoge	Numerical modelling, contributed to discussion and analyses of results.	

Candidate's Signature		Date 4/2/09

Declaration by co-authors

The undersigned hereby certify that:

(1) the above declaration correctly reflects the nature and extent of the candidate's contribution to this work, and the nature of the contribution of each of the co-authors.
(2) they meet the criteria for authorship in that they have participated in the conception, execution, or interpretation, of at least that part of the publication in their field of expertise;
(3) they take public responsibility for their part of the publication, except for the responsible author who accepts overall responsibility for the publication;
(4) there are no other authors of the publication according to these criteria;
(5) potential conflicts of interest have been disclosed to (a) granting bodies, (b) the editor or publisher of journals or other publications, and (c) the head of the responsible academic unit; and
(6) the original data are stored at the following location(s) and will be held for at least five years from the date indicated below:

Location(s)	School of Mathematical Sciences, Monash University

[Please note that the location(s) must be institutional in nature, and should be indicated here as a department, centre or institute, with specific campus identification where relevant.]

Signature 1	SHRAVAN HANASOGE	Date 4/12/08

3.1 Surface-Focus Measurements

3.1.1 Introduction

Local helioseismic diagnostic methods such as time-distance helioseismology (Duvall et al., 1993), helioseismic holography (Lindsey and Braun, 1997) and ring-diagram analysis (Hill, 1988), have over the years provided us with unprecedented views of the structures and flows under sunspots and active regions. However, a growing body of evidence appears to suggest that interpretations of the measured statistical changes in the properties of the wave-field may be rendered inaccurate by complexities associated with the observations and wave propagation physics. As discussed in Chapters 1 and 2, incorporating the full MHD physics and understanding the contributions of phase and frequency filters, and differences in the line formation height, are thought to be central to future models of sunspots.

One of the earliest studies that highlighted the interaction of waves with sunspots was the Fourier-Hankel analysis of Braun et al. (1987), who found that sunspots can absorb up to half of the incident acoustic-wave power and shift the phases of interacting waves quite significantly (see also Braun 1995). These results were echoed over the years by a steady steam of theoretical results (e.g. Bogdan et al., 1996; Cally and Bogdan, 1997; Cally et al., 2003; Crouch et al., 2005; Cally, 2007) that have consistently emphasized the need for more sophisticated modeling and interpretation of wave propagation in strongly magnetized regions.

Important advances in our observational understanding of sunspots were also achieved by Duvall et al. (1996) and Zhao et al. (2001), who inferred the presence of flows underneath sunspots, and Kosovichev et al. (2000) who estimated the sub-surface wave-speed topology. However, while the inversion procedures applied to derive these results fail to directly account for the tensorial nature of magnetic field effects, the action of the field is mimicked via changes in the acoustic properties of the medium (the so-called wave speed). Recently however, numerical forward models of helioseismic wave (e.g. Cameron et al., 2008; Hanasoge, 2008) and ray (Moradi and Cally, 2008) propagation in magnetized atmospheres have been developed and are beginning to make inroads into this problem. In particular, the results of Moradi and Cally (2008) and Cameron (2008; private communication) strongly suggest that active-region magnetic fields play a substantial role in influencing the wave field, and that the complex interaction of magnetic fields with solar oscillations, as opposed to changes in the wave speed, are the major causes of observed travel-time inhomogeneities in sunspots.

In this section, we aim to study the impact of strong magnetic fields on helioseismic wave propagation and the consequences for time-distance helioseismology using two numerical forward models, a 3D ideal MHD solver and MHD ray theory. The simulated data cubes are analysed using the traditional surface-focused centre-to-annulus method frequently applied in the time-distance analyses of sunspots (e.g., Couvidat et al., 2006). Furthermore, we apply the same method outlined in §2.4.5 to also isolate and analyse the thermal contribution to the observed travel-time shifts.

3.1.2 The MHS Sunspot Model

The background stratification for the model atmosphere chosen for this analysis is described by a adiabatically stable, hydrostatic truncated polytrope (Bogdan et al., 1996), smoothly connected to an isothermal atmosphere. The truncated polytrope is described by: index $m = 2.15$, reference pressure $p_0 = 1.21 \times 10^5$ g cm^{-1} s^{-2} and reference density $\rho_0 = 2.78 \times 10^{-7}$ g cm^{-3}, such that the pressure and density variations are given by,

$$p(z) = p_0 \left(-\frac{z}{z_0}\right)^{m+1}, \tag{3.1}$$

and

$$\rho(z) = \rho_0 \left(-\frac{z}{z_0}\right)^{m}. \tag{3.2}$$

The photospheric level of the background model is at $z = 0$, while the upper boundary is placed at a height of $z_0 = 345$ km.

The magneto-hydrostatic (MHS) sunspot model that we embed in the background is similar in construction to that of Cameron et al. (2008) and Hanasoge (2008), where the flux tube is modelled by an axisymmetric magnetic field geometry based on the Schlüter and Temesváry (1958) self-similar solution. This approximation requires the following choices for the radial (B_r) and vertical (B_z) components of the magnetic field:

$$B_z = M\psi(z)e^{-r^2\psi(z)}, \tag{3.3}$$

$$B_r = -M\frac{r}{2}\psi' e^{-r^2\psi(z)}, \tag{3.4}$$

with $\psi' = d\psi/dz$. The above equations (3.3) and (3.4) are in cylindrical geometry; r, z refer to the horizontal radial and vertical coordinates with $r = 0$ coinciding with the centre of the flux tube, M a term that controls the magnitude of the magnetic field and hence the flux ($= \pi M$), and $\psi(z)$, the horizontal extent of the flux tube and the rate at which it spreads with altitude. Following Hanasoge (2008), the zeroth-order MHS equations (in cylindrical coordinates) can then be reduced to:

$$0 = -\partial_r p + \zeta \frac{B_z}{4\pi} \left[\partial_z B_r - \partial_r B_z\right], \tag{3.5}$$

along the horizontal (r) direction and in the vertical (z) direction,

$$0 = -\partial_z p - \zeta \frac{B_r}{4\pi} \left[\partial_z B_r - \partial_r B_z\right] - \rho g. \tag{3.6}$$

Equation (3.5) is integrated from $r = 0$ to ∞ to obtain the following equation:

$$p_c(z) = p_\infty(z) + \frac{M^2 \zeta}{4\pi} \left[\frac{1}{16} \frac{\psi'^2}{\psi} - \frac{1}{8}\psi'' + \frac{\psi^2}{2}\right], \tag{3.7}$$

where $p_c(z)$ is the pressure along the axis (centreline) of the flux tube and $p_\infty(z)$ is the hydrostatic pressure far away from the magnetic region. The horizontal pressure distribution at a given z can now be computed by integrating equation (3.5) from the centre outward:

$$p(r', z) = p_c(z) + \frac{\zeta}{4\pi} \int_0^{r'} dr B_z \left[\partial_z B_r - \partial_r B_z\right]; \tag{3.8}$$

thus the entire pressure field can be recovered through this procedure. Simplifying equation (3.6), we can obtain the density field from the pressure distribution:

$$\rho(r, z) = -\frac{1}{g} \left(\partial_z p + \zeta \frac{B_r}{4\pi} \left[\partial_z B_r - \partial_r B_z\right]\right). \tag{3.9}$$

Therefore, upon specifying parametres M and $\psi(z)$ in Equations (3.3) and (3.4), one can obtain a self-consistent MHS solution that satisfies the criteria of $\boldsymbol{\nabla} \cdot \mathbf{B} = 0$ and MHS balance. Upon solving the MHS equations of pressure and Lorentz support (described in detail in and Chapter 2 and also in Cameron et al., 2008; Hanasoge, 2008), we obtain the altered thermodynamic stratification of the underlying magnetized plasma (Figure 3.1 c).

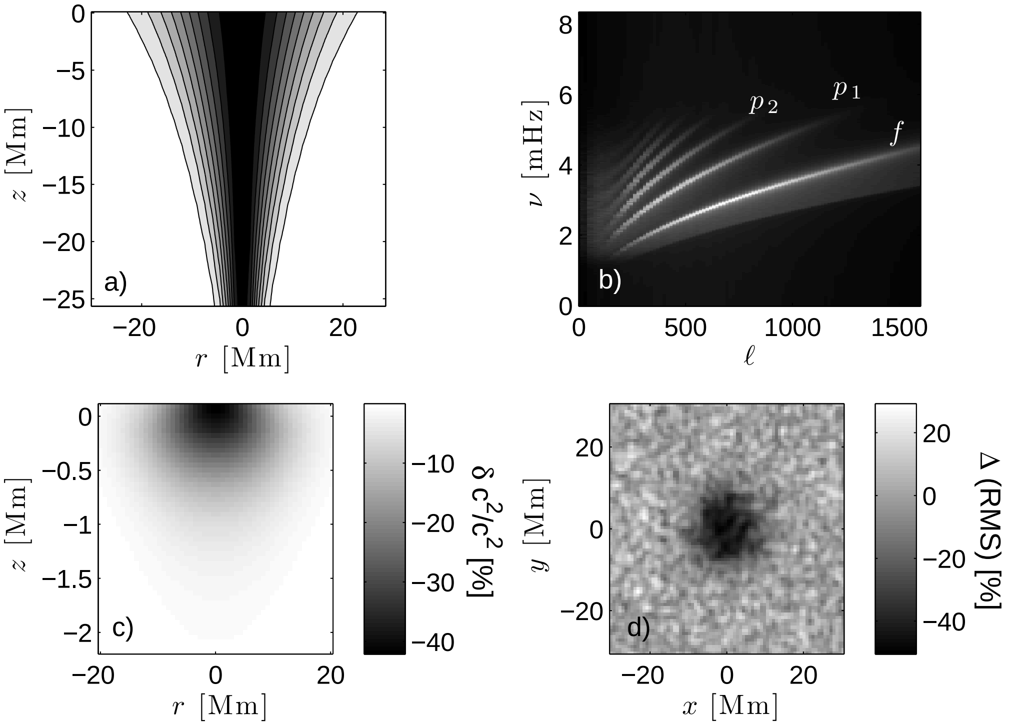

Figure 3.1: Various properties of the model sunspot atmosphere: a) shows the field configuration of the sunspot model, depicted as lines of constant magnetic flux, b) is the power spectrum of the simulated Doppler velocity data-cube with the location of the p- and f-mode ridges, c) depicts the near-surface thermal/sound speed profile and d) contains a power map normalized to the quiet Sun.

3.1.3 MHD Wave-Field Simulations

We employ the forward model of the solar wave field developed by Hanasoge (2007). We begin by linearizing and modifying the ideal MHD equations:

$$\partial_t \rho = -\boldsymbol{\nabla}\cdot(\rho_0 \mathbf{v}) - \Gamma\rho, \tag{3.10}$$

$$\partial_t \mathbf{v} = -\frac{1}{\rho_0}\boldsymbol{\nabla} p - \frac{\rho}{\rho_0} g\hat{\mathbf{e}}_z + \frac{\zeta(z)}{4\pi\rho_0}[(\boldsymbol{\nabla}\times\mathbf{B}_0)\times\mathbf{B} + (\boldsymbol{\nabla}\times\mathbf{B})\times\mathbf{B}_0] + \mathbf{S} - \Gamma\mathbf{v}, \tag{3.11}$$

$$\partial_t p = -\mathbf{v}\cdot\boldsymbol{\nabla} p_0 - \rho_0 c^2 \boldsymbol{\nabla}\cdot\mathbf{v} - \Gamma p, \tag{3.12}$$

$$\partial_t \mathbf{B} = \zeta\boldsymbol{\nabla}\times(\mathbf{v}\times\mathbf{B}_0) - \Gamma\mathbf{B} \tag{3.13}$$

$$\boldsymbol{\nabla}\cdot\mathbf{B} = 0 \tag{3.14}$$

where ρ is the plasma density, p pressure, $\mathbf{B} = (B_x, B_y, B_z)$ the magnetic field, $\mathbf{v} = (v_x, v_y, v_z)$ is the vector velocity, $g = g(z)$ is gravity with direction vector $-\hat{\mathbf{e}}_z$, $c = c(x, y, z)$ is the sound speed, $\Gamma = \Gamma(x, y, z) > 0$ is a damping sponge that enhances wave absorption at all horizontal and vertical boundaries, $\zeta(z)$ a Lorentz force "controller", and $\mathbf{S}$ is the source term. The subscript "0" indicates a time-stationary background quantity while un-subscripted terms fluctuate. The controller term ζ is such that it is constant (=1) over most of the interior but decays rapidly with height above the photosphere. It essentially attempts to achieve a two-fold purpose: (i) a reduction in the Lorentz force with increasing altitude above the photosphere and (ii) prevent the onset of negative pressure effects. A detailed discussion on the reasoning behind this term is included in Hanasoge (2008).

A Cartesian coordinate system (x, y, z) is employed, with $\hat{\mathbf{e}}_z$ denoting the unit vector along the vertical or z axis and t, time. Because we have a spatially varying magnetic structure, the background pressure, density, and sound speed adopt a full three-dimensional spatial dependence. Equations (3.10) through (3.12) enforce mass, momentum, and energy conservation respectively, while equation (3.13) is the induction equation. Equation (3.14) confirms the absence of magnetic monopoles. In interior regions of the computational box (away from the boundaries), solutions to the above equations are adiabatic since the damping terms decay to zero here.

In our computations, waves are excited by a vertically dipolar source function, $\mathbf{S} = S(x, y, z, t)\ \hat{\mathbf{e}}_z$, the structure of which has been discussed in some detail in Hanasoge (2007). Essentially, it is a phenomenological model for the multiple source wave excitation picture that is understood to occur in the Sun. The source function is highly localized along the z axis, described by a Gaussian with full width at half maximum (FWHM) of 200 km. To simulate the suppression of granulation related wave sources in a sunspot (e.g., see Hanasoge et al., 2008), the forcing term is also multiplied by a spatial function that mutes source activity in a circular region of 10 Mm radius.

We start our analysis in the frequency-horizontal wavenumber Fourier space and attempt to mimic the solar acoustic power spectral distribution as closely as possible. To ensure this, each coefficient in Fourier space is assigned a value from the output of a Gaussian distributed random number generator, which creates uniform power across wavenumbers. The computational domain is a 3D box that straddles the solar surface, extending from approximately 30 Mm below the photosphere to 2 Mm into the atmosphere. The vertical grid spacing is such that acoustic travel time between adjacent grid points is constant, while the horizontal grid points are equally spaced. Spatial derivatives are calculated using sixth-order compact finite differences (Lele, 1992) and time evolution is achieved through the repeated application of an optimized second-order five-stage Runge-Kutta scheme. We implement periodic horizontal boundaries and place damping sponges adjacent to the vertical boundaries to enhance the absorption and transmission of outgoing waves.

To avoid aliasing, we apply the two-thirds rule (Orszag, 1970), requiring that maximum captured wave-number be at most two-thirds the number of grid points. In order to avoid vertical (radial) aliasing and the subsequent spectral blocking, we apply the de-aliasing procedure described in Hanasoge and Duvall (2007), once every minute in solar time. Variables in the horizontal direction are de-aliased by applying a smooth filter that diminishes the upper third of the spectrum and leaves the important lower two-thirds untouched (also at the rate of once per minute). The numerical algorithm used was parallelized according to the Message Passing Interface (MPI) Standard. The computational box is distributed along the y-axis; all points on the x- and z-axes for a given point on the y-axis are located in-processor. The data are transposed and redistributed between processors when the solution has to be filtered and when derivatives along the y-axis need to be computed.

The final products from the simulations are vertical (Doppler) velocity data cubes, extracted at an observational height of 200 km above the photosphere. The artificial Doppler velocity data cubes have dimensions of 200×200 Mm^2 $\times$ 512 minutes, with a spatial resolution of 0.781 Mm and cadence of 1 minute.

3.1.4 MHD Ray-Path Simulations

The previous Chapter outlined the detailed steps involved in using MHD ray theory to model helioseismic ray propagation in magnetized atmospheres. Here, we provide a brief description of the magneto-acoustic ray tracing procedure for this analysis.

The ray paths are computed in Cartesian geometry in the vertical x-z plane assumed to contain both magnetic field lines and ray paths. In this case, we only require the 2D dispersion relation with the Alfvén wave factored out:

$$\mathcal{D} = \omega^4 - (a^2 + c^2)\omega^2 K^2 + a^2 c^2 K^2 k_{\parallel}^2 + c^2 N^2 k_x^2 - (\omega^2 - a_z^2 K^2)\omega_c^2 = 0 \qquad (3.15)$$

where $K = |\mathbf{k}|$, c represents the sound speed, a the Alfven speed, N^2 is the squared Brunt-Väisälä frequency and ω_c^2 is the square of the isothermal acoustic cut-off frequency. The remaining term, $k_{\|} = \hat{\mathbf{B_0}}.\mathbf{k}$ (where $\mathbf{B_0}$ is the prescribed magnetic field), represents the component of the wavevector $\mathbf{k}$ parallel to the magnetic field. The construction of $\mathbf{k}$ is completed by specifying the governing equations of the ray paths (see §2.3), derived using the zeroth order eikonal approximation (Weinberg, 1962). The equations are then integrated using a fourth-order Runge-Kutta numerical scheme. The magneto-acoustic rays stay on the fast-wave dispersion branch at all times. It should be noted that neither forward model (i.e., §3.1.3, 3.1.4) accounts for the presence of flows.

3.1.5 Modelling Surface-Focus Travel-Time Inhomogeneities

For the time-distance calculations, we compute cross covariances of oscillation signals at pairs of points on the photosphere (source at $\mathbf{r_1}$, receiver at $\mathbf{r_2}$) based on a single-skip centre-to-annulus geometry (see e.g. Couvidat et al., 2006). We cross correlate the signal at a central point with signals averaged over an annulus of radius $\Delta = |\mathbf{r_2} - \mathbf{r_1}|$ around that centre. Firstly, we filter out the f-mode ridge. Subsequently, standard Gaussian phase-speed in conjunction with Gaussian frequency filters centred at 3.5, 4.0 and 5.0 mHz with 0.5 mHz band-widths are applied in order to study frequency dependencies of travel times (e.g. Braun and Birch, 2006; Couvidat and Rajaguru, 2007). The annular sizes and phase-speed filter parametres used in estimating the times shown in Figures 3.2 and 3.4 (including the central phase speed (v) and full width at half-maximum (FWHM) used) are outlined in Table 3.1. The point-to-annulus cross-covariances, averaged over five distances, are fitted by two Gabor wavelets (Kosovichev and Duvall, 1997) to extract the required travel times. The wavelet has five parameters: the central frequency, the width and amplitude of the envelope, and the group and phase travel times. We denote by τ_+ and τ_- the measured phase travel times for the positive- and negative-time branches of the cross-covariance respectively. The reference travel times for the quiet Sun are similarly defined using a reference cross-covariance. The *phase* travel time perturbations, $\delta\tau_+$ and $\delta\tau_-$, are defined as the difference between the measured and reference travel times. As we are interested in wave-speed perturbations only, we consider mean travel-time perturbations, $\delta\tau_{mean} = (\delta\tau_+ + \delta\tau_-)/2$.

In order to compare theory with simulation, we also estimate centre-to-annulus mean time shifts, $\delta\tau_{mean}$, using the MHD ray tracing technique of §3.1.4 for the same sunspot model (§3.1.2). The single-skip magneto-acoustic rays do not require filtering. Instead, they are propagated from the upper turning point of their trajectories, in both the positive and negative x directions, at a prescribed frequency with horizontal increments of 1 Mm across the sunspot. The required range of horizontal skip distances is obtained by altering the shooting angle at which the rays are initiated. The skip distances are then binned according to their travel path lengths, Δ, while the travel times are averaged across both the positive and negative horizontal directions. Again, we only concern ourselves with the mean phase time shifts.

Table 3.1: Annulus radii and phase-speed parameters used for the surface-focus measurements

Δ (Mm)	v (km s^{-1})	FWHM (km s^{-1})
3.7–8.7	17.71	11.94
6.2–11.2	21.11	11.94
8.7–14.5	24.36	11.94

3.1.6 The Travel Time Profiles

MHD Wave-Field Simulations

Figure 3.2 shows maps of $\delta\tau_{mean}$ as well as the frequency filtered azimuthal averages of $\delta\tau_{mean}$ obtained using time-distance centre-to-annulus measurements for the measurement geometries indicated in Table 3.1. The $\delta\tau_{mean}$ map for $\Delta = 6.2 - 11.2$ Mm clearly displays positive travel-time shifts, reaching a maximum of around 25 seconds at spot centre. A similar travel-time shift is observed from the azimuthal average of $\delta\tau_{mean}$ when a frequency filter centred at 3.5 mHz is applied to the data. We also observe the magnitude of the positive $\delta\tau_{mean}$ steadily decrease as we increase the frequency filter to 4.0 mHz, with negative $\delta\tau_{mean}$ starting to appear in the profile, and by 5.0 mHz the travel times observed inside the sunspot are completely negative. For the larger annuli, negative time shifts of increasing magnitude are consistently observed as we increase the central frequency of the filter. In fact, all $\delta\tau_{mean}$ maps for Δ larger than $8.7-14.5$ Mm that we measured displayed similar $\delta\tau_{mean}$ behaviour to the $6.2 - 11.2$ and $8.7 - 14.5$ Mm bins (albeit with smaller time shifts).

It is important to take note of both the signs of the travel-time perturbations and their apparent frequency dependence. Positive $\delta\tau_{mean}$ have traditionally been interpreted as indicative of a region of slower wave propagation in the shallow subsurface

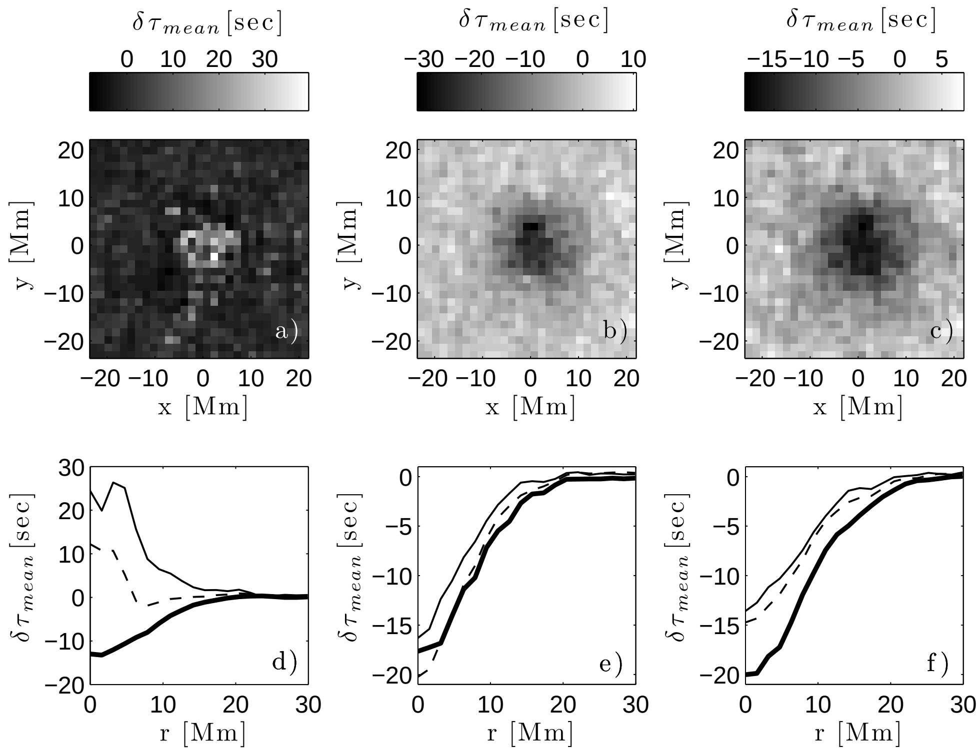

Figure 3.2: Center-to-annulus time-distance $\delta\tau_{mean}$ maps (no frequency filtering) and azimuthal averages for Δ= 3.7-8.7 (a,d), 6.2-11.2 (b,e) and 8.7-14.5 Mm (c,f) extracted from the MHD wave-field simulations of §3.1.3. Light solid lines represent Gaussian frequency filtering centred 3.5 mHz, dashed lines represent 4.0 mHz and bold solid lines represent 5.0 mHz.

layers beneath the spot, while negative times are of a wave-speed enhancement. So in essence, the $\delta\tau_{mean}$ profiles that we have derived from the simulation would appear to indicate a traditional "two-layered" wave-speed structure (e.g., Kosovichev et al., 2000; Couvidat et al., 2006) beneath the sunspot. However as can be seen in Figure 3.1, the thermal profile of our model atmosphere is a "one-layer" sunspot model ($\delta c^2/c^2 < 0$) and of the order of $\sim -40\%$. Similarly, changes in the sub-surface wave speed, $(c^2 + a^2)/c_0^2 - 1$ (where c_0 is the unperturbed sound speed), lie only in the positives $\sim$ 0–200% (Figure 3.3), with the greatest enhancements seen near the surface. The large decrease in the sound speed we observe in our model also raises the possibility that current methods of linear inversion may lie beyond their domains of applicability.

We also observed that travel times associated with the smallest measurement geometry are most sensitive to the phase-speed filter used, i.e., when the phase-speed parameters were adjusted to filter all background power below the p_1 ridge, negative $\delta\tau_{mean}$ were obtained. This behaviour was noted by Braun and Birch (2008), who determined the causative factor to be the background power between the p_1 and f ridges. It is unsettling that the sign of the time shift may be reversed at will, through small changes in the filter width and centre.

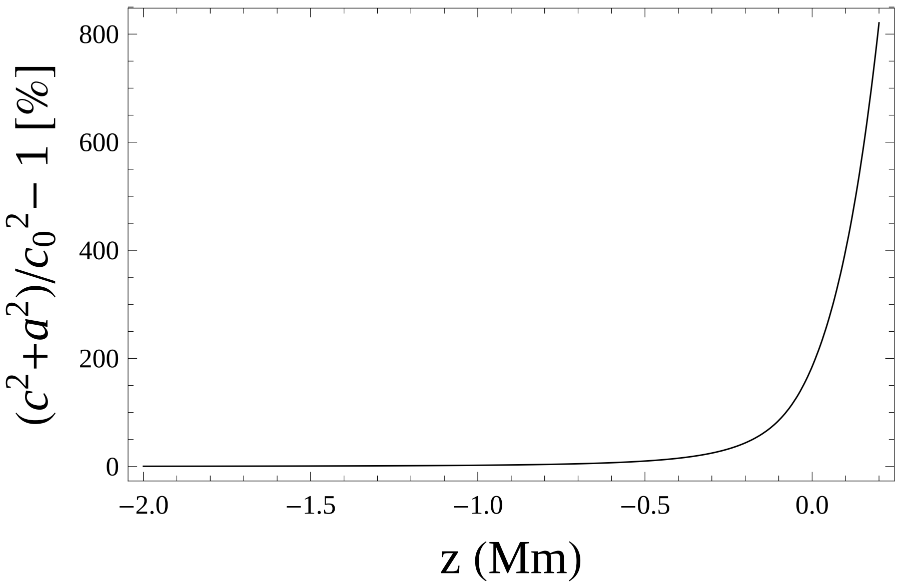

Figure 3.3: Wave-speed enhancement profile of the model atmosphere (3.1.2) at spot centre, shown here as a function of depth (z). A fast wave increase of approximately 200% is observed at the surface ($z = 0$).

MHD Ray-Path Simulations

Figure 3.4 (frames a-c) show the resultant $\delta\tau_{mean}$ profiles derived from the MHD ray tracer for identical measurement geometries as used for the time-distance calculations. The similarities between the ray $\delta\tau_{mean}$ profiles and their time-distance counterparts in Figure 3.2 are striking. Firstly, the ray travel-time perturbation profiles contain predominantly negative travel-time shifts for all frequencies, albeit with slightly smaller magnitudes. Secondly, a similar frequency dependence of $\delta\tau_{mean}$ is also observed. Generally, high frequency rays propagated within the confines of a magnetic field are expected to i) travel faster and ii) propagate longer distances than low frequency rays (Cally, 2007; Moradi and Cally, 2008). However, one significant difference we can observe in these profiles is the absence of any positive travel-time shifts for the $\Delta = 3.7 - 8.7$ Mm bin. This is significant because the exclusively negative $\delta\tau_{mean}$ we observe across all geometries not only reflects the one-layered wave- and sound-speed profiles below the surface, but also highlights the effects that phase-speed filtering can have on time-distance measurements (recall that ray calculations require no such filtering). Nonetheless, the overall self-consistency between these results and those in §3.1.6 are very encouraging, despite the 2D nature of the ray calculations.

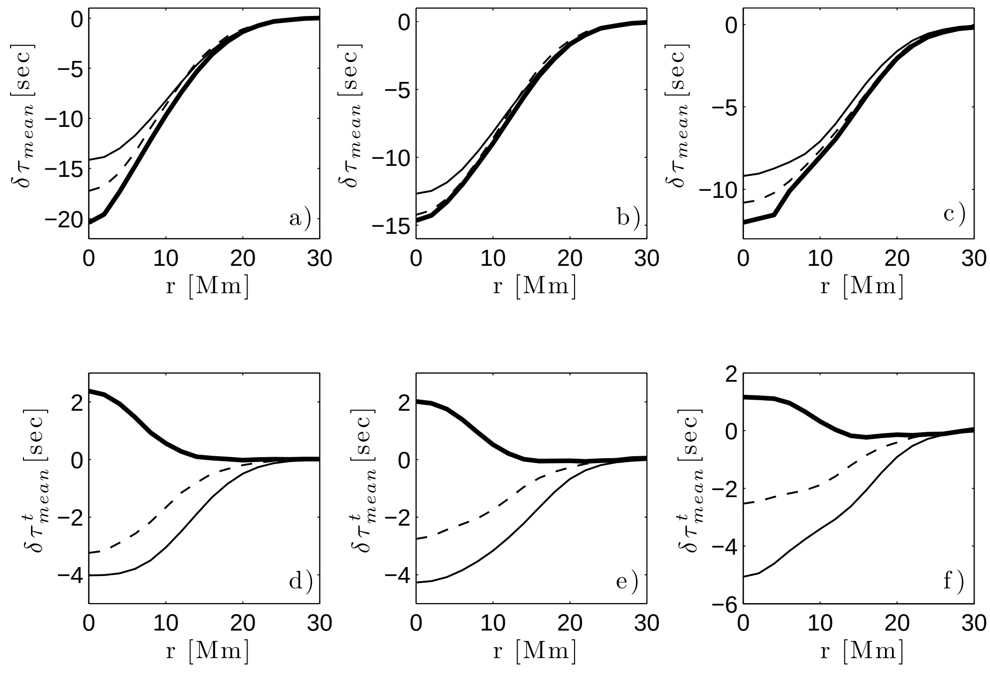

Figure 3.4: Center-to-annulus ray $\delta\tau_{mean}$ and $\delta\tau^t_{mean}$ profiles for Δ= 3.7-8.7 (a,d), 6.2-11.2 (b,e), and 8.7-14.5 Mm (c,f) computed using the MHD ray calculation recipe of §3.1.4. Light solid lines represent 3.5 mHz, dashed lines represent 4.0 mHz and bold solid lines represent 5.0 mHz.

The Thermal Contribution of Travel-Time Shifts

Given the fact that ray theory appears to succeed in capturing the essence of the travel-time variations as derived from the MHD simulations, we can isolate the thermal component of the measured $\delta\tau_{mean}$ using the same approach as Moradi and Cally (2008) to ascertain the contribution to the travel-time shifts from the underlying thermal structure. To do this, we re-calculate the ray paths in the absence of the flux tube while maintaining the modified sound-speed profile obtained in §3.1.2. The resulting *thermal* travel-time perturbations, $\delta\tau^t_{mean}$, would then be purely a result of thermal (sound-speed) variations along the ray path. Of course, the model is no longer in MHS equilibrium, but this does not affect linear wave calculations.

The resulting $\delta\tau^t_{mean}$ profiles, presented in Figure 3.4 (frames d-f), surprisingly show that, even without the magnetic field, ray theory produces negative travel times – the exception being for rays propagated at 5.0 mHz. This indicates that the contribution from the underlying thermal structure is significant enough to modify the upper turning point of the ray paths, thus shortening the ray travel times. The appearance of negative travel times for a model with a decrease in sound speed would appear to be somewhat counterintuitive, since from standard ray theory, one would expect negative time shifts with increases in sound speed. The most likely explanation for this phenomenon, is that since both the sound speed and plasma density differ from the quiet Sun, consequent changes in the acoustic cut-off frequency ($c/2H$, where H is the density scale height) in the near-surface regions of our model modifies the ray path for waves with frequencies less than 5.0 mHz quite significantly, thereby causing negative travel-time shifts. However, we cannot rule out that a more realistic background atmosphere and/or a full account of the Wilson depression in the model may also nullify this effect entirely.

Larger thermal contributions to the travel-time shifts at lower frequencies is also reflective of the fact that the upper turning point of the fast mode rays (waves) at higher frequencies is much higher in the atmosphere (in the region $a > c$), and as such, these rays are affected much more significantly by the rapidly increasing Alfvén speed. Hence, one would expect MHD effects to be more dominant than pure thermal variations – as evidenced by the $\delta\tau^t_{mean}$ profiles at 5.0 mHz. On the other hand, the acoustic cut-off frequency ensures that the upper turning points of lower frequency rays (waves) are slightly deeper, i.e. in the region $c > a$, resulting in a sizable thermal contribution to the travel-time perturbations.

However, when comparing with the time perturbations derived from calculations that include the magnetic field (i.e. Figure 3.4 frames a-c), MHD effects appear to be dominant contributors to the observed time shifts. This is perhaps most evident for $\Delta = 3.7 - 8.7$ Mm (Figure 3.4 d), where the thermal contribution at spot centre appears to make up approximately 11% of $\delta\tau_{mean}$ (i.e. Figure 3.4 a) at 5.0 mHz, 18% at 4.0 mHz and 28% at 3.5 mHz. For the largest bin, we see a similar contribution at 4.0 and 5.0 mHz, but a much greater contribution at 3.5 mHz (45% of $\delta\tau_{mean}$).

3.1.7 Summary and Discussion

Incorporating the full MHD physics into the various forward models used in local helioseismology is essential for testing inferences made in regions of strong magnetic fields. By comparing numerical simulations of MHD wave-field and ray propagation in a model sunspot, we find that: i) the observed travel-time shifts in the vicinity of sunspots are strongly determined by MHD physics, although sub-surface thermal variations also appear to affect ray timings by modifying the acoustic cut-off frequency, ii) the time-distance travel-time shifts are strongly dependent on frequency, phase speed filter parameters and the background power below the p_1 ridge, and finally iii) MHD ray theory succeeds in capturing the essence of centre-to-annulus travel-time variations as derived from the MHD simulations.

The most unsettling aspect about this analysis is that despite using a background stratification that differs substantially from Model S (Christensen-Dalsgaard et al. 1996) and a flux tube that clearly lacks a penumbra, the time shifts still look remarkably similar (at least qualitatively) to observational time-distance analyses of sunspots. Preliminary tests conducted with different sunspot models (e.g., different field configurations, peak field strengths etc.) have also provided similar results. Given the self-consistency of these results, as derived from both forward models, it could imply that we are pushing current techniques of local helioseismology to their very limits. It would appear that accurate inferences of the internal constitution of sunspots await a clever combination of forward modelling, observations, and a further development of techniques of statistical wave-field analysis.

3.2 Deep-Focus Measurements

3.2.1 Introduction

In the preceding section we utilized two recently developed numerical MHD forward models, in conjunction with surface-focused (i.e., centre-to-annulus) time-distance measurements, to model the observed travel-time inhomogeneities in a simulated sunspot atmosphere. However, there are numerous caveats associated with surface-focused time-distance measurements that use oscillation signals within the sunspot region, as the use of such oscillation signals is now known to be the primary source of most surface effects in sunspot seismology. These surface effects can be categorized into two groups. The first revolves around the degree to which observations made within the sunspot region are contaminated by magnetic effects (e.g., Braun, 1997; Lindsey and Braun, 2005; Schunker et al., 2005; Braun and Birch, 2006; Couvidat and Rajaguru, 2007; Moradi et al., 2009), while the second concerns the degree to which atmospheric temperature stratification in and around regions may affect the absorption line used to make measurements of the Doppler velocity (e.g., Rajaguru et al., 2006, 2007).

There have been attempts in the past to circumvent such problems by adopting a time-distance measurement geometry known as "deep-focusing which avoids the use of data from the central area of the sunspot by only cross-correlating the oscillation signal of waves that have a first-skip distance larger than the diameter of the sunspot (e.g., Duvall, 1995; Braun, 1997; Zhao and Kosovichev, 2006; Rajaguru, 2008). In this analysis, we follow up on the comparative study presented in §3.1 by using our two established forward models, in conjunction with a deep-focusing scheme known as the "common midpoint" (CMP) method to probe the sub-surface dynamics of our artificial sunspot.

3.2.2 Common Midpoint Deep-Focusing

Often utilized in geophysics applications such as multichannel seismic acquisition (Shearer, 1999), the CMP method measures the travel time at the point on the surface halfway between the source and receiver (see Figure 3.5). Cross-correlating numerous source-receiver pairs in this manner means that this method is mostly sensitive to a small region localized in the deep interior. A re-working of this method has been applied to helioseismic observations by Duvall (2003), and has the obvious advantage of allowing one to study the wave-speed structure directly beneath sunspots without

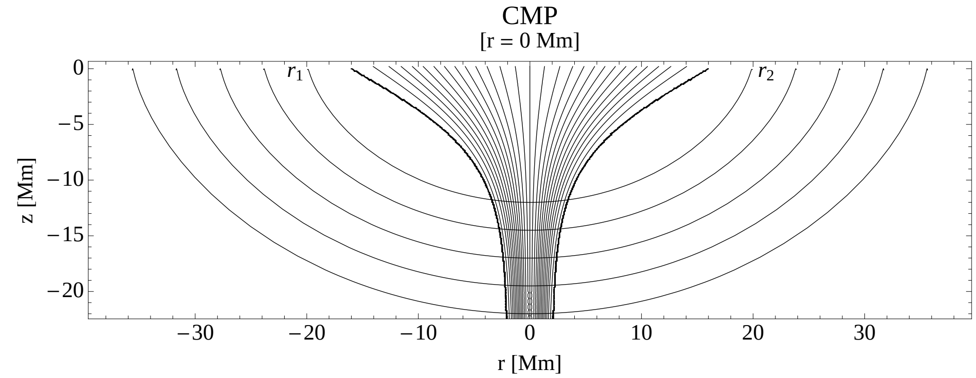

Figure 3.5: An illustration of the CMP deep-focus geometry indicating the range of rays used for this study. The CMP method measures the travel time at the point on the surface located at the half-way point between a source ($\mathbf{r_1}$) and receiver ($\mathbf{r_2}$). For the above rays, the CMP is located on the central axis of the spot ($r = 0$ Mm).

using the oscillation signals inside the perturbed region.

Our method for measuring time-distance deep-focus travel times is somewhat similar to the approach undertaken by Braun (1997) and Duvall (2003). First, the annulus-to-annulus cross-covariances (e.g., between oscillation signals located between two points on the solar surface, a source at $\mathbf{r_1}$ and a receiver at $\mathbf{r_2}$, as illustrated in Figure 3.5) are derived by dividing each annulus ($\boldsymbol{\Delta} = |\mathbf{r_2} - \mathbf{r_1}|$), into two semi-annuli (each being one pixel wide) and cross-correlating the average signals in these two semi-annuli. Then, to further increase the signal-to-noise ratio (SNR), we average the cross-covariances over three distances, respectively slightly smaller than, and larger than, Δ. In the end, the five (mean) distances chosen ($\boldsymbol{\Delta} =$ 42.95, 49.15, 55.35, 61.65 and 68 Mm respectively) are large enough to ensure that we only sample waves with a first-skip distance greater than the diameter of the sunspot at the surface (~ 40 Mm).

Due to the oscillation signal at any location being a superposition of a large number of waves of different travel distances, the cross-covariances are very noisy and need to be phase-speed filtered first in the Fourier domain, using a Gaussian filter for each travel distance. The application of appropriate phase-speed filters isolates waves that travel desired skip distances, meaning that even though we average over semi-annuli, the primary contribution to the cross-covariances is from these waves. Table 3.2 details the range of annulus radii and phase-speed filter parameters used for this study. In addition to the phase-speed filters, we also apply an f-mode filter that removes the f-mode ridge completely (as it is of no interest to us in this analysis),

Table 3.2: Annuli radii and phase-speed parameters used for the deep-focus measurements

Δ (Mm)	v (km s^{-1})	FWHM (km s^{-1})
20.20–24.75	46.74	4.94
22.10–27.05	49.95	8.38
25.40–29.95	53.03	7.24
28.30–33.35	55.97	7.63
31.30–36.70	58.77	7.66

and we also apply Gaussian frequency filters centred at $\omega = 3.5$, 4.0 and 5.0 mHz with $\delta\omega = 0.5$ mHz band-widths, to study frequency dependencies of travel times (e.g., Braun and Birch, 2008; Moradi et al., 2009). To extract the required travel times, the cross-covariances are fitted by two Gabor wavelets (Kosovichev and Duvall, 1997): one for the positive times, one for the negative times.

Even after significant filtering and averaging, the extracted CMP travel times are still inundated with noise. This is certainly an ever-present complication in local helioseismology as there is a common expectation (with all local helioseismic methods and inversions) of worsening noise and resolution with depth. Realization noise associated with stochastic excitation of acoustic waves can significantly impair our ability to analyse the true nature of travel-time shifts on the surface (and by extension, also affect our interpretation of sub-surface structure). But, as we have full control over the wave excitation mechanism and source function, we have the luxury of being able to apply realization noise subtraction to improve the SNR and obtain statistically significant travel-time shifts from the deep-focus measurements. This is accomplished in the same manner as in Hanasoge et al. (2007), i.e., by performing two separate simulations, one with the perturbation (i.e., the sunspot simulation), and another without (i.e., the quiet simulation). We then subtract the travel times of the quiet data from its perturbed counterpart (see e.g., Figure 3.6), allowing us to achieve an excellent SNR.

Finally, in order to compare theory with simulations, we once again estimate deep-focusing time shifts using the MHD ray tracer of Chapter 2. The single-skip magneto-acoustic rays are propagated from the inner (lower) turning point of their trajectories at a prescribed frequency (see e.g., Figure 3.5). These rays do not undergo any additional filtering as the required range of horizontal skip distances is simply obtained by altering the depth at which the rays are initiated. The resulting mean (phase) travel-time shifts ($\delta\tau_{mean}$) derived from both forward models are presented in Figures 3.6 and 3.7.

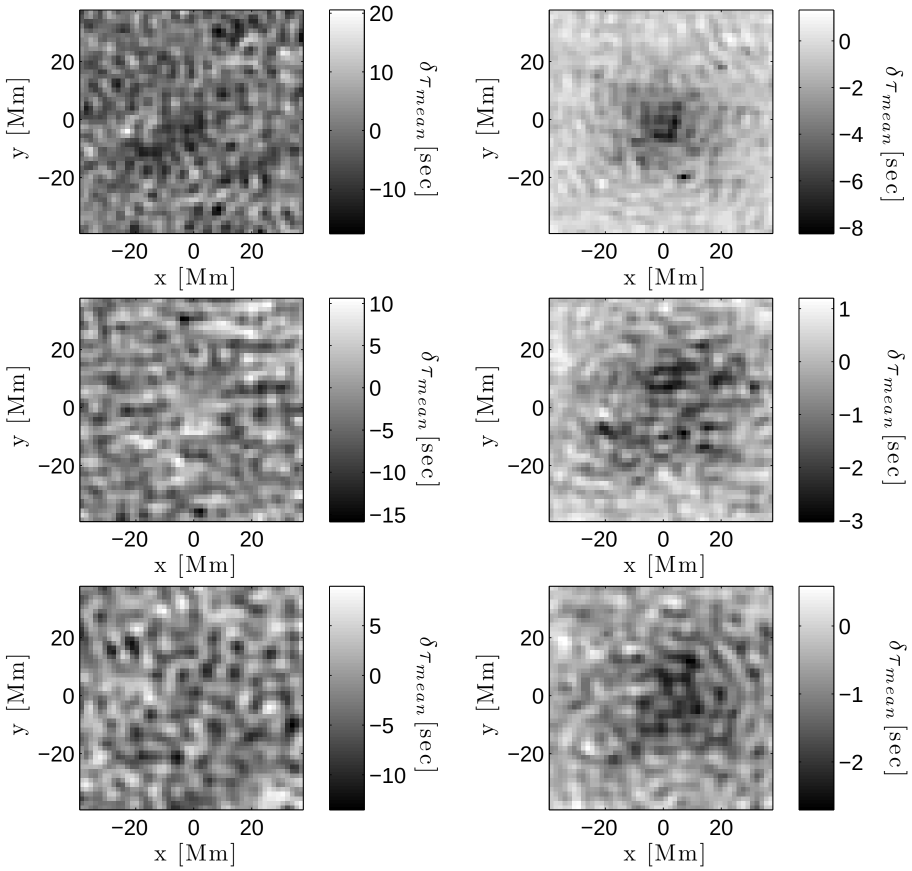

Figure 3.6: Examples of (phase-speed filtered) CMP mean travel-time perturbation ($\delta\tau_{mean}$) maps for $\mathbf{\Delta} = \mathbf{42.95}$ (top), $\mathbf{\Delta} = \mathbf{49.15}$ (middle) and $\mathbf{\Delta} = \mathbf{61.65}$ Mm (bottom). Left panels: before realization noise subtraction. Right panels: after subtraction. A frequency filter centred at 5.0 mHz has been applied to the data.

3.2.3 Results and Discussion

A number of travel time maps derived from the time-distance analysis, both before and after noise subtraction, are presented in Figure 3.6. The impact of realization noise subtraction is self-evident in these figures as it is only after removing the background noise that we are able to detect statistically significant travel-time shifts. The umbral averages of these time shifts are shown in Figure 3.7. The $\delta\tau_{mean}$ range from a couple of seconds at 3.5 and 4.0 mHz, to around five seconds at 5.0 mHz. However, even though the sizes of the measured time shifts are significant, there is no clear frequency dependence associated with the them. As we are only using waves outside of the perturbed region, and sampling depths of $\sim 13 - 23$ Mm below the surface, surface effects can be effectively ruled out as the cause of the time shifts.

It is worth noting that linear inversions of surface-focused travel time maps of actual observations have suggested a two-layered wave-speed structure below sunspots - a wave-speed decrease of $\sim 10-15\%$ down to a depth of $\sim 3-4$ Mm, followed by a wave-speed enhancement, reportedly detected down to depths of $\sim 17-25$ Mm below the surface (Kosovichev et al., 2000; Couvidat et al., 2006). However as we saw earlier, our forward model prescribes relatively shallow sub-surface perturbations, achieving a consistent sound-speed decrease (Figure 3.1), with a peak reduction of $\sim 45\%$ at the surface ($z = 0$) and less than 1% at $z = -2$ Mm, while the one-layered wave-speed enhancement (Figure 3.3) is also confined to the near-surface layers, approaching $\sim 200\%$ at the surface and around less than 0.5% at $z = -2$ Mm. Hence, it is hard to fathom that the time-distance $\delta\tau_{mean}$ we are observing can be associated with some kind of anomalous deep sub-surface perturbation. In fact, both the sound-speed decrease and wave-speed enhancement at the depths we are sampling registers at less than one-tenth of one percent, with the average plasma $\beta \sim 10^3$ – in all likelihood not significant enough to produce a 3-5 second travel-time perturbation. In order to try and identify the root cause of these apparent travel-time shifts, it is useful to compare the time-distance CMP measurements with those derived from MHD ray theory in Figure 3.7.

The ray theory CMP $\delta\tau_{mean}$ clearly appear to be significantly smaller at all frequencies, with all observed time shifts registering at less than half a second. Certainly, these time shifts are more in line with our expectations given the absence of any significant deep sound/wave-speed perturbation. But, we must bear in mind the differences between the two forward models before drawing our conclusions. With regards to helioseismic travel times, Bogdan (1997) has emphasized that they are not only sensitive to the local velocity field along the ray path, but also to conditions in the surrounding medium, hence travel times are sensitive to the wave speed in a broad region surrounding the geometrical ray path – a clear consequence of wave effects. As such, wave-like behaviour needs to be considered when interpreting travel times, something which ray theory does not clearly account for, resulting in possible underestimation of deep-focus travel times.

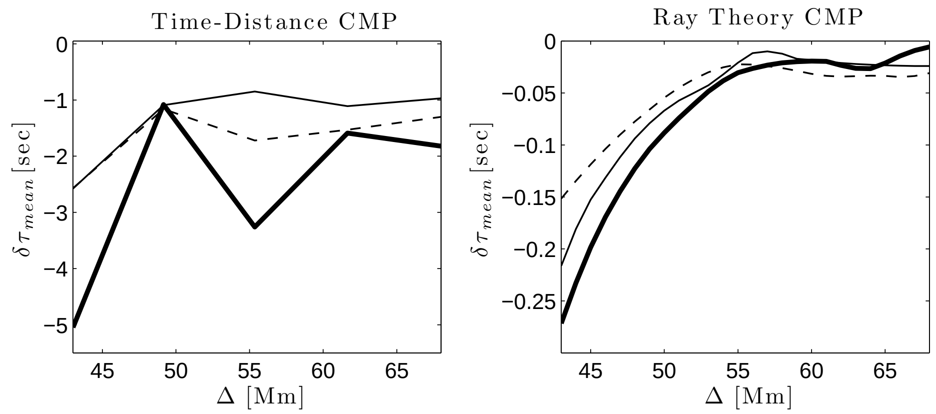

Figure 3.7: Simulated CMP travel-time shifts as a function of wave/ray travel distance (Δ). Left panel: umbral averages of the CMP time shifts derived from time-distance analysis of the simulated data. Right panel: ray theory CMP travel-time shifts derived from rays propagated at various depths and with a CMP at $r = 0$ Mm. Light sold lines are indicative of a frequency filtering centred at 3.5 mHz, dashed lines indicate 4.0 mHz and bold solid lines indicate 5.0 mHz.

On the other hand, we must also consider the effects of phase-speed filtering (which is absent in the ray theory calculations) on the time-distance measurements. If we look closely at the time-distance $\delta\tau_{mean}$ maps in Figure 3.6, we notice that they are somewhat smeared in appearance, with the central sunspot region becoming increasingly sprawled-out across the map as we increase Δ. This behaviour is most likely a consequence of both the phase-speed filtering (i.e, the size of the central frequency filter, the filter width, etc., see Couvidat and Birch, 2006), and the averaging scheme applied to the cross-correlations – both of which are a necessity in order to improve the SNR in time-distance calculations. These effects, combined with the delocalized nature of the CMP measurements, may also introduce spurious travel-time shifts. However, further testing and control simulations are required to confirm this.

3.2.4 Conclusion

At the present time, it is sufficient to say that we do not have a definitive diagnosis with regards to the above-discussed differences in the size of the deep-focus time shifts produced by the two forward models. It may well be that we are applying ray theory to regimes where it may be seriously limited. On the other hand, the very same could be said about local time-distance analysis! Whatever the case may be, these preliminary results have certainly provided us with the motivation to conduct further time-distance studies using the CMP method.

The direct (and indirect) effects of phase-speed filtering on deep-focus measurements, derived from both simulations and real data, also warrants a more detailed examination, as any artefact produced by the filtering process is likely to be even more pronounced for phase-speed filtered MDI data, where we do not yet have the luxury of realization noise subtraction. These issues are something that we hope to address in the very near future with some ongoing comparative studies.

Chapter 4

Flare Seismology

This chapter presents an in-depth correlative study of three recently discovered seismically active flares. A general introduction is provided first, followed by an overview of computational seismic holography, which is used extensively in this chapter to image the source of seismic emission from the surface ripples that emanate from a seismically active flare. We then present our findings for the X1.2-class flare of 15 January 2005, with a detailed account of the acoustic emissions produced by the flare and supporting observations which confirm previous instances of strong spatial and temporal correlation between acoustic signatures in seismically active flares, and impulsive HXR and continuum emission. These observations support the notion that acoustic emission is likely produced by back-warming of the low photosphere due to radiation from a heated overlying chromosphere. We then continue our analysis by closely examining the seismic emissions produced by the less-energetic M-class flares of 14 August 2004 and 10 March 2001. Both flares embodied certain emission characteristics which appeared to closely correspond with previous instances of seismic emission from acoustically active flares. Further analysis, from the acoustic to electromagnetic spectrum, is conducted with results confirming that sudden heating of the low photosphere during a white-light flare is a major contributor to the pressure transient required to drive a sunquake. Extending our analysis to the magnetic field topology of the host active regions, we also find evidence that suggests that the coronal magnetic field configuration plays an intricate role in determining the seismic properties of an acoustically active flare.

Declaration for Thesis Chapter 4

Declaration by candidate

In the case of Chapter 4 (Section 4.2), the nature and extent of my contribution to the work was the following:

Nature of contribution	**Extent of contribution (%)**
Motivation for the work, collected most of the observations, data reduction and analysis, discussion and analyses of results, preparation of figures 4.1-4.4 and 4.7, wrote much of the text (first author).	50

The following co-authors contributed to the work. Co-authors who are students at Monash University must also indicate the extent of their contribution in percentage terms:

Name	**Nature of contribution**	**Extent of contribution (%) for student co-authors only**
Alina Donea	Data reduction, prepared figures 4.5-4.6, discussion and analyses of results, wrote part of the text.	
Charlie Lindsey	Provided GONG data for and assisted in the generation of figures 4.1-4.2, discussion and analyses of results, wrote part of the text.	
Diana Besliu-Ionescu	Provided initial observations, discussion of results.	10
Paul S. Cally	Discussion and analyses of results.	

Candidate's Signature		**Date** 2/2/09

Declaration by co-authors

The undersigned hereby certify that:

(1) the above declaration correctly reflects the nature and extent of the candidate's contribution to this work, and the nature of the contribution of each of the co-authors.
(2) they meet the criteria for authorship in that they have participated in the conception, execution, or interpretation, of at least that part of the publication in their field of expertise;
(3) they take public responsibility for their part of the publication, except for the responsible author who accepts overall responsibility for the publication;
(4) there are no other authors of the publication according to these criteria;
(5) potential conflicts of interest have been disclosed to (a) granting bodies, (b) the editor or publisher of journals or other publications, and (c) the head of the responsible academic unit; and
(6) the original data are stored at the following location(s) and will be held for at least five years from the date indicated below:

Location(s) **School of Mathematical Sciences, Monash University**

Signature 1	Charles A. Lindsey	**Date** 01-06-09
Signature 2		19.01.2009
Signature 3		19/01/09
Signature 4		2.2.09

Declaration by candidate

In the case of Chapter 4 (Section 4.3), the nature and extent of my contribution to the work was the following:

Nature of contribution	Extent of contribution (%)
Motivation for the work, data reduction and analysis, preparation of figures 4.8-4.11, contributed to discussion and analyses of results, wrote part of the text (second author).	35

The following co-authors contributed to the work. Co-authors who are students at Monash University must also indicate the extent of their contribution in percentage terms:

Name	Nature of contribution	Extent of contribution (%) for student co-authors only
Juan Carlos Martinez Oliveros	Motivation for the work, data reduction and analysis, prepared figures 4.14, 4.16-4.21, discussion and analyses of results, wrote part of the text (primary author).	35
Diana Besliu-Ionescu	Preparation of figures 4.12-4.13, wrote part of the text.	15
Alina Donea	Preparation of figure 4.15, wrote part of the text.	
Paul S. Cally	Discussion and analyses of results.	
Charlie Lindsey	Discussion and analyses of results.	

Candidate's Signature	[signature]	Date 2/02/09

Declaration by co-authors

The undersigned hereby certify that:

(1) the above declaration correctly reflects the nature and extent of the candidate's contribution to this work, and the nature of the contribution of each of the co-authors.
(2) they meet the criteria for authorship in that they have participated in the conception, execution, or interpretation, of at least that part of the publication in their field of expertise;
(3) they take public responsibility for their part of the publication, except for the responsible author who accepts overall responsibility for the publication;
(4) there are no other authors of the publication according to these criteria;
(5) potential conflicts of interest have been disclosed to (a) granting bodies, (b) the editor or publisher of journals or other publications, and (c) the head of the responsible academic unit; and
(6) the original data are stored at the following location(s) and will be held for at least five years from the date indicated below:

Location(s)	School of Mathematical Sciences, Monash University

Signature 1	[signature]	Date 06-01-2009
Signature 2	Charles A. Lindsey	06-01-2009
Signature 3	[signature]	19.01.2009
Signature 4	[signature]	19/01/09
Signature 5	P. Cally	2.2.09

Declaration by candidate

In the case of Chapter 4 (Section 4.4), the nature and extent of my contribution to the work was the following:

Nature of contribution	Extent of contribution (%)
Motivation for the work, data reduction and analysis, preparation of figures 4.22-4.24, discussion and analyses of results, wrote part of the text (second author).	40

The following co-authors contributed to the work. Co-authors who are students at Monash University must also indicate the extent of their contribution in percentage terms:

Name	Nature of contribution	Extent of contribution (%) for student co-authors only
Juan Carlos Martinez Oliveros	Motivation for the work, data reduction and analyses, preparation of figures 4.25-4.28, discussion and analyses of results, wrote part of the text (first author).	40
Alina Donea	Discussion and analyses of results, wrote part of the paper.	

Candidate's Signature		Date 19/01/09.

Declaration by co-authors

The undersigned hereby certify that:

(1) the above declaration correctly reflects the nature and extent of the candidate's contribution to this work, and the nature of the contribution of each of the co-authors.
(2) they meet the criteria for authorship in that they have participated in the conception, execution, or interpretation, of at least that part of the publication in their field of expertise;
(3) they take public responsibility for their part of the publication, except for the responsible author who accepts overall responsibility for the publication;
(4) there are no other authors of the publication according to these criteria;
(5) potential conflicts of interest have been disclosed to (a) granting bodies, (b) the editor or publisher of journals or other publications, and (c) the head of the responsible academic unit; and
(6) the original data are stored at the following location(s) and will be held for at least five years from the date indicated below:

Location(s)	School of Mathematical Sciences, Monash University

Signature 1		Date 06-01-2009
Signature 2		19/01/09
Signature 3		

4.1 Introduction

Although most large solar flares appear to be acoustically inactive, certain energetic flares radiate intense seismic transients into the solar interior during the impulsive phase. These wave packets radiate thousands of kilometres from the flaring region into the solar interior, but most of this energy is refracted back to the solar surface within approximately 50 Mm of the source and within an hour of the beginning of the flare. The surface manifestation is a wave-packet of ripples accelerating outward from the general source region that is sometimes obvious in raw helioseismic observations. Kosovichev and Zharkova (1998) discovered the first known instance of seismic emission, from the X2-class flare of 1996 July 9 in AR7978, identifying the phenomenon by the name "sunquake."

Donea et al. (1999) later applied computational seismic holography to helioseismic observations of the flare to image the seismic source of the sunquake. The source was clearly visible in the 2.5-4.5 mHz spectrum and even more pronounced in the 5.0-7.0 mHz spectrum. However, follow-up efforts to detect seismic emission from several other flares, some even considerably larger than the X2.6-class flare of 9 July 1996, showed no indications of significant acoustic emission (Donea and Lindsey, 2004). These were the first indications that led the sunquake hunters to believe that some flares were far more efficient emitters of seismic energy into the solar interior than others.

Soon after the spectacular "Halloween Flares" of October 2003, Donea and Lindsey (2005) used helioseismic holography to analyse both the X17-class flare of 28 October and the X10-class flare of 29 October and observed considerable acoustic emissions. Even though the acoustic signatures from the October 2003 flares were somewhat less energetic than that of the X2.6 flare of 9 July 1996, they were, nonetheless, quite conspicuous. Donea and Lindsey (2005) also considered the possibility that relatively weak flares might be able to produce detectable sun quakes and that acoustically active flares might indeed be much more common than previously thought. This turned out to be the case, as a comprehensive survey of helioseismic observations of flares using data from SoHO-MDI covering a significant fraction of Solar Cycle 23 by Donea et al. (2006a) and Besliu-Ionescu et al. (2006) has shown. This survey led to the discovery of numerous acoustically active flares, including considerable seismic transients emitted from the relatively small M9.5-class flare of 9 September 2001.

Donea et al. (2006b) extensively analysed the seismic transient of the M9.5 flare which occurred in AR 9608. The helioseismic signatures of this flare drew our attention to several important points: the acoustic signature of the flare was quite compact and was spatially and temporally consistent with the white-light signature, reinforcing the suggestion that sudden heating of the photosphere may contribute significantly to the seismic emission detected. They also found that the acoustic signature was spatially and temporally coincident with suddenly changing magnetic signatures, suggesting that suddenly changing magnetic forces might have contributed to the seismic emission. The fraction of energy emitted into the sub-photosphere as seismic waves remained a small fraction of the total energy released in the flare. The persistence of a sudden, co-spatial white-light signature in flares where no energetic protons were evident was consistent with acoustic emission driven by back-warming of the low photosphere by radiation from a heated overlying chromosphere.

In this chapter, we report on three follow-up discoveries to the M9.5 flare, beginning with the most conspicuous seismic transient discovered to date which emanated from the relatively moderate X1.2-class flare of 15 January 2005 (§4.2). This result was followed closely by the discovery of a number of strong acoustic emissions from less energetic M-class flares, namely the M7.4-class flare of 14 August 2004 (§4.3) and the M6.7-class flare of 10 March 2001 (§4.4) which to date is the smallest flare known to have produced a detectable acoustic transient. With excellent supporting observations from ground-based facilities (e.g., GONG, Big Bear Solar Observatory (BBSO), Imaging Vector Magnetograph (IVM) and Nobeyama Radio Heliograph (NoRH)) and other modern space-borne observatories (e.g., SoHO, Reuven Ramaty High-Energy Solar Spectroscopic Imager (RHESSI), Geostationary Operational Environmental Satellite (GOES) and Transition Region and Coronal Explorer (TRACE)), these discoveries have lead to a remarkably consistent and compelling perspective on some of the basic physical processes which underlie seismic emission from flares.

4.1.1 Computational Seismic Holography

Before we proceed with our analyses, I shall briefly review the adaptation of computational seismic holography for applications in flare seismology.

In subjacent vantage holography (see §1.2.2 and Figure 1.5), when the surface ($z = 0$) acoustic field at any point $\mathbf{r}'$ in the pupil is expressed as a complex amplitude $\hat{\psi}$ for any given frequency ω, the acoustic egression can be expressed as

$$\hat{H}_{+}(\mathbf{r},\ \omega)\ =\ \int_{pupil} \hat{G}_{+}(\mathbf{r},\ \mathbf{r}',\ \omega)\ \hat{\psi}(\mathbf{r}',\ \omega) d^2\mathbf{r}'. \tag{4.1}$$

In this formalism, $\hat{G}_+(\mathbf{r},\ \mathbf{r}',\ \omega)$ is a Green's function that expresses the disturbance at the focus, $\mathbf{r}$, due to a measured point source at surface point $\mathbf{r}'$ from which the acoustic wave is supposed to propagate backwards in time to the focus.

The relation between the complex amplitude, $\hat{\psi}(\mathbf{r},\ \omega)$, of frequency appearing in equation (4.1) and the real acoustic field, $\psi(\mathbf{r},\ t)$, representing the surface acoustic field in the MDI observations as a function of time is expressed by the Fourier transform:

$$\psi(\mathbf{r},\ t) \ = \ \frac{1}{\sqrt{2\pi}} \int_{-\infty}^{\infty} e^{i\omega t}\ \hat{\psi}(\mathbf{r},\ \omega)\ d\omega. \tag{4.2}$$

The same applies to the acoustic egression:

$$H_+(\mathbf{r},\ t) \ = \ \frac{1}{\sqrt{2\pi}} \int_{-\infty}^{\infty} e^{iwt}\ \hat{H}_+(\mathbf{r},\ \omega)\ d\omega. \tag{4.3}$$

In this formalism, the egression power – which is used extensively in holography of acoustic sources and absorbers – can then be simply written as,

$$P(\mathbf{r},\ t) \ = \ |H_+(\mathbf{r},\ t)|^2. \tag{4.4}$$

Equation (4.4) is used to produce "egression power maps", which show compact positive signatures in the spatial and temporal neighbourhoods of localized seismic transient emitters. The signature of a localized absorber illuminated by ambient acoustic noise is a similarly sharp deficit in egression power, appearing as a silhouette against a generally positive background when rendered graphically.

In computational seismic holography, $P(\mathbf{r}, t)$ is separately derived from computations of $\hat{H}_+(\mathbf{r}, \omega)$ over $2-4$ mHz and $5-7$ mHz ranges of the spectrum. In practice, there are major diagnostic advantages to the $5-7$ mHz spectrum, as it avoids the much greater quiet Sun ambient noise at lower frequencies, which competes unfavourably with acoustic emission into the pupil from the flare. Due to a shorter wavelength, the high frequency band also provides us with waves that have a finer diffraction limit. These advantages come at some expense in temporal discrimination, as the egression power signatures that result are temporally smeared to a minimum effective duration of order

$$\Delta t \ = \ \frac{1}{\Delta\nu} \ = \ \frac{1}{2\ \text{mHz}} \ = \ 500\ \text{s}. \tag{4.5}$$

This smearing operates in both directions in time, meaning that the acoustic signature of the flare $P(\mathbf{r}, t)$, once the computation is complete, will invariably commence several minutes before the actual onset of the flare and last for several minutes afterward even if the actual acoustic disturbance was instantaneous.

4.2 The Solar Flare of 15 January 2005

4.2.1 Active Region Morphology

AR 10720 was a complex active region that appeared on the solar disk on 11 January 2005 and soon became one of the largest and most active sunspot regions of Cycle 23. In the period January 15 – 20, AR 10720 produced 5 X-class solar flares, including an X7.1 on January 20, which produced an intense solar proton storm. However, helioseismic observations sufficient to show seismic emission were acquired only for the X1.2 flare of January 15. This flare was observed by numerous space and ground-based solar observatories, including SoHO-MDI, RHESSI, GOES, TRACE, and GONG. AR 10720 itself was observed by the Imaging Vector Magnetograph (IVM) at the Mees Solar Observatory in the general time frame of the 15 January flare.

AR 10720 was dominated by a single δ-configuration sunspot. The top row of Figure 4.1 shows continuum intensity (left) and line-of-sight magnetic field (right) of the active region shortly before the flare. The 15 January 2005 solar flare in AR 10720 was classified as X1.2, localized at N14E08 on the solar surface. The GOES satellite measured a $1.2 \times 10^{-1}\mathrm{Jm}^{-2}$ X-ray flux in the 1-8 Å range integrated over the duration of the flare. Excess X-ray emission began at 00:22 UT, reaching a maximum at 00:43 UT, and ending at 01:02 UT. There was significant white-light emission with a sudden onset, as indicated by the intensity difference signatures shown in the second row of Figure 4.1, and this coincided closely with HXR signatures indicating high-energy particles accelerated into the chromosphere. However, unlike the flares of 2003 October 28 – 29 (Donea and Lindsey, 2005), there were no signatures to indicate the inclusion of high-energy protons in these particle influxes.

4.2.2 The Helioseismic Data

The MDI data consist of full-disk Doppler images in the photospheric line Ni I 6768 Å, obtained at a cadence of 1 minute, in addition to approximately hourly continuum intensity images and line-of-sight magnetograms. The MDI data sets are described in more detail by Scherrer et al. (1995). For the flare of 15 January 2005, we analysed a dataset with a period of 4 hours around the time of the flare. For the purpose of our analysis, the MDI images obtained (Dopplergrams, magnetograms and intensity

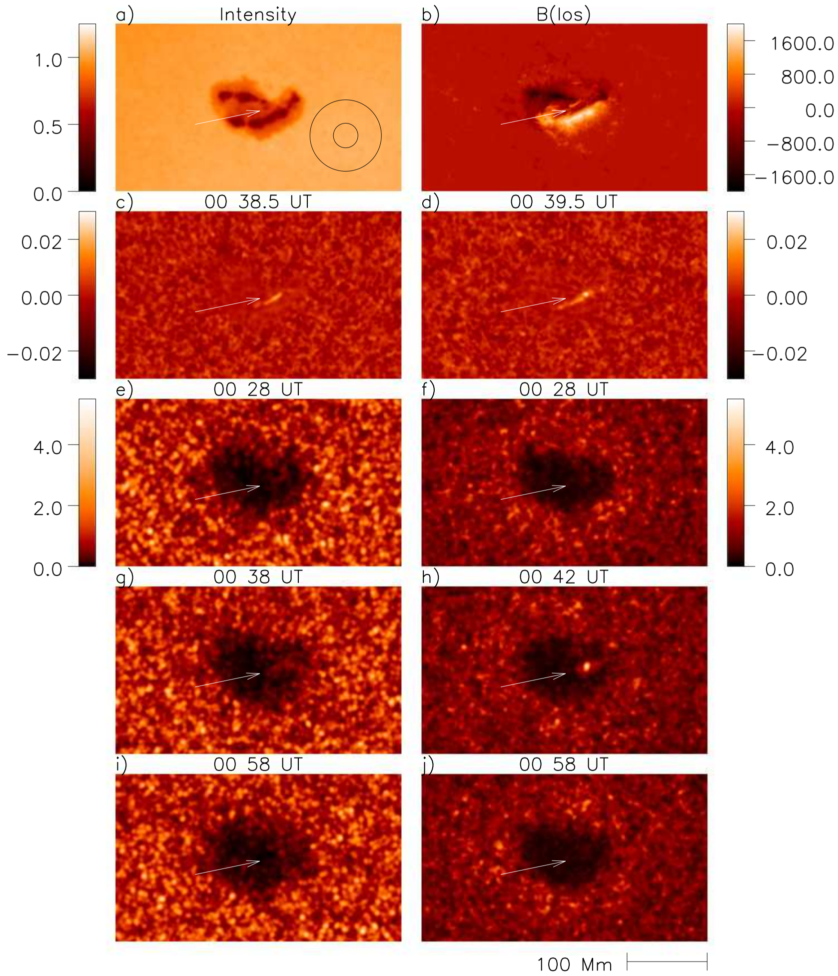

Figure 4.1: Egression power snapshots of AR 10720 on 15 January 2005. The top frames show an MDI visible continuum image of AR 10720 (left) at 00:00 UT and a magnetogram (right) at 00:28 UT. The second row shows GONG continuum intensity differences 30 seconds before and after the time that appears above the respective frames. The bottom three rows show egression power maps before (row 3), during (row 4), and after (bottom row) the flare at 3.0 mHz (left column) and 6.0 mHz (right column). The annular pupil for the egression computations is drawn in the top left panel. To improve statistics, the original egression power snapshots are smeared by convolution with a Gaussian with a $1/e$-half-width of 3 Mm. Times are indicated above respective panels, with arrows inserted to indicate the location of the acoustic source. Colour scales at right and left of row 3 apply to respective columns in rows $3-5$. Egression power images and the continuum images are normalized to unity at respective mean quiet-Sun values. At 3.0 mHz this is $\sim$2 kW m^{-2}. At 6.0 mHz it is 70 W m^{-2}.

continuum) were remapped onto a Postel-projection (Deforest, 2004) that tracks solar rotation, with the region of interest fixed at the centre of the projection. The nominal pixel separation of the projection was 0.002 solar radii (1.4 Mm) with a 256×256 pixels field of view, thus encompassing a region of approximately 360×360 Mm^2 on the solar surface.

4.2.3 The Acoustic Signatures

To assess seismic emission from the flare, we computed the egression, H_+, as prescribed by equation (4.3) over the neighbourhood of the active region at one-minute intervals in t, mapping the egression power, P, as prescribed by equation (4.4), for each value of t. We call a map of P evaluated at any single t an egression power "snapshot." From this point will refer to the $5-7$ mHz bandpass simply as 6.0 mHz and to the $2-4$ mHz bandpass as 3.0 mHz. Egression power snapshots before, during and after the flare are shown in the bottom three rows of Figure 4.1 at 3.0 mHz (left column) and 6.0 mHz (right column). In these computations the pupil was an annulus of radial range $15-45$ Mm centred on the focus (Figure 4.1a).

All egression power snapshots mapped in Figure 4.1 show considerably suppressed acoustic emission from the magnetic region, attributed to strong acoustic absorption by magnetic regions, discovered by Braun et al. (1988) (see also Braun, 1995; Braun and Lindsey, 1999). Furthermore, all 6.0 mHz egression power snapshots in Figure 4.2 also show acoustic emission "halos," i.e. significantly enhanced acoustic emission from the outskirts of complex active regions (Braun and Lindsey, 1999; Donea et al., 1999). [1]

A conspicuous seismic source is seen in the 6.0 mHz egression power snapshot at 00:42 UT, whose location is indicated by an arrow in all of the frames. A close examination of the source shows that it has two components. By far the most conspicuous component is an intense, compact kernel $\sim$10 Mm in length and located on the penumbral neutral line of the δ-configuration sunspot. Somewhat more diffuse but clearly significant is a secondary, somewhat lenticular signature distributed along the neutral line out to $\sim$15 Mm east and $\sim$30 Mm west of the kernel. These signatures correspond closely with other compact manifestations of the flare. The kernel accounts for approximately 45 per cent of the egression power integrated over the

[1] Braun and Lindsey (1999) and Donea et al. (1999) found conspicuous high-frequency acoustic emission halos surrounding all large, magnetically complex active regions. In fact, the outskirts of isolated, monopolar sunspots showed measurably enhanced acoustic emission (Lindsey and Braun, 1999) but this was rather subtle.

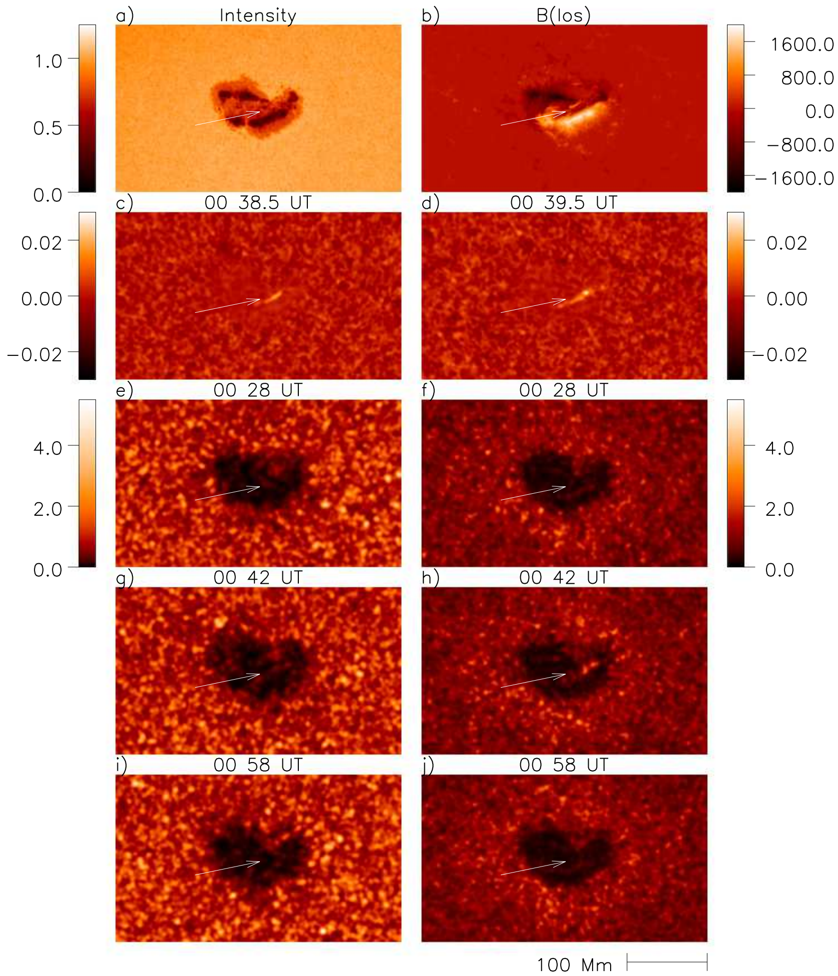

Figure 4.2: Acoustic power snapshots of AR 10720 on 15 January 2005. Details are the same as for Figure 4.1, but local acoustic power maps appear in the bottom three rows in place of egression power maps.

Table 4.1: Energy estimates of the seismic signatures of sunquakes (detected prior to the 15 January 2005 event)

Date	Class	3.0 mHz (ergs)	6.0 mHz (ergs)	1 – 8 Å X-Rays (ergs)	Visible (ergs)
1996 Jul 09	X2.6	7.5×10^{27}	2.4×10^{26}	2.8×10^{29}	———
2001 Sep 09	M9.5	1.1×10^{27}	2.0×10^{26}	6.2×10^{28}	1.2×10^{30}
2003 Oct 28	X17.2	4.7×10^{27}	9.4×10^{26}	5.0×10^{30}	———
2003 Oct 29	X10.0	9.4×10^{26}	3.5×10^{26}	1.5×10^{30}	3.8×10^{29}
2005 Jan 15	**X1.2**	2.4×10^{27}	1.0×10^{27}	3.4×10^{29}	2.0×10^{30}

region encompassing the flare signature, with the lenticular component outside of the kernel accounting for the rest.

The 3.0 mHz egression power snapshots shown in the left column of Figure 4.1 actually show a considerably stronger seismic emission signature than the 6.0 mHz signature (right column). But, because of the much greater ambient acoustic emission at this frequency, the 3.0 mHz signature is not nearly as conspicuous or significant as the 6.0 mHz signature. It appears to have only a diffuse lenticular component and no conspicuous kernel to match the 6.0 mHz kernel.

It is important to distinguish between the egression power, $|H_+(\mathbf{r},\ t)|^2$, and the local acoustic power, $P(\mathbf{r},\ t)$, which is the square modulus, $|\psi(\mathbf{r},\ t)|^2$, of the local wave amplitude ψ at the focus, $\mathbf{r}$. Each pixel in a local acoustic power map represents local surface motion as viewed directly from above the photosphere. Each pixel in the egression power map computed by subjacent vantage holography of the surface is a coherent representation of acoustic waves that have emanated downward from the focus, deep beneath the solar surface, and re-emerged into a pupil (see diagram of annulus in Figure 4.1a) 15 – 45 Mm from the focus.

Figure 4.2 shows local acoustic power snapshots of AR 10720 at 3.0 mHz (left column) and 6.0 mHz (right column) before, during, and after the flare. As in the case of egression power (Figure 4.1) all of the local acoustic power maps show a broad acoustic deficit marking the magnetic region. An enhanced local acoustic power halo surrounding the active region is clearly apparent in the 6.0 mHz snapshots. The acoustic signature of the flare is also clearly visible at 6.0 mHz. This appears to

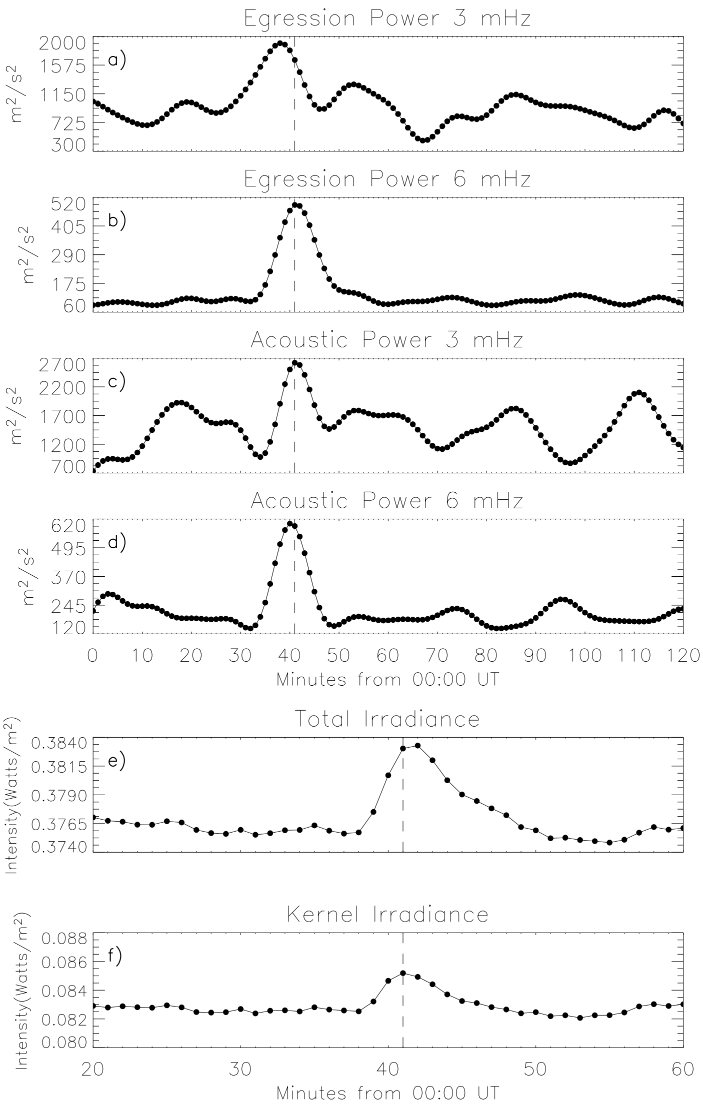

Figure 4.3: Time series of the 3.0 and 6.0 mHz egression and acoustic power (integrated over the neighbourhood of the egression power signatures) are plotted in the top four rows. The dashed vertical lines mark the time of maximum acoustic emission (00:41 UT) at 6.0 mHz. The relatively extended duration of the acoustic signatures is a result of limits to temporal resolution imposed by truncation of the spectrum (see equation 4.5). The bottom two rows show visible continuum irradiance at 1 au from the flaring region along the neutral line in the neighbourhood of the flare. The emission from the neighbourhood of the kernel component of the 6.0 mHz acoustic source (plot f) is discriminated from the total (plot e).

consist of a pair of kernels, a relatively stronger one nearly coinciding in location with, but slightly east of, the 6.0 mHz egression power kernel and a weaker one $\sim$10 Mm to west and slight north, lying on the neutral line along which the lenticular component of the 6.0 mHz egression power is distributed. As in the corresponding egression power snapshot, the 3.0 mHz local acoustic power snapshots show a stronger but still less conspicuous signature than that at 6.0 mHz due to a similarly much greater background acoustic power at 3 Mm.

Figure 4.3 shows plots of the egression and acoustic power time series in the 3.0 and 6.0 mHz bands and continuum emission in the neighbourhood of the seismic signature, discriminating continuum emission in the region of the kernel component in the 6.0 mHz egression power signature from the total. The flare irradiance profiles were extrapolated by applying the assumption that the irradiance is directly proportional to the GONG continuum signature in the neighbourhood of Ni I 6768 Å(Donea and Lindsey, 2005).

The flare of 15 January 2005 produced the most conspicuous acoustic signature of any flare with a detectable seismic emission. This appears to be because such a large fraction of the energy was released into the high-frequency ($5-7$ mHz) spectrum, where the competing ambient acoustic power is so far suppressed. Table 4.1 shows the energy estimates of the seismic transients radiated into the active region sub-photosphere by five flares that have produced conspicuous seismic signatures[2] compared with energy emitted in X-rays in the first 20 minutes of the flare. It should be noted that the 3.0 mHz energy for the flares preceding the 15 January 2005 flare are actually calculated at 3.5 mHz. Extrapolating through the missing $4-5$ mHz acoustic spectrum for the flare of January 15, we project a total acoustic emission of $\sim 4 \times 10^{20}$ J ($\sim 4 \times 10^{27}$ erg).

4.2.4 Visible Continuum Emission

Various aspects of visible continuum emission during the 2005 January 15 flare are shown in Figures 4.1, 4.2 and 4.3. The visible-continuum images in Figures 4.1 and 4.2 were obtained by MDI at 00:00 UT, $\sim$37 min before the onset of the flare. We obtained

[2]The energy estimates in Table 4.1 were obtained by integrating the egression power over the neighbourhood of the seismic sources (e.g., those shown in Figures 1g,h for the 15 January 2005 flare). This computation is blind to waves that miss the $15-45$ Mm in the first skip. Comparative seismic holography applied to simulated acoustic transients, and to MDI observations of flares with different sized pupils, indicate that the energies quoted in Table 4.1 account for $80-95$ per cent of the total, depending on the source distribution.

visible continuum maps of AR 10720 during the flare from the GONG observatory at Mauna Loa. Technically, the GONG "continuum intensity maps" represent a measure of radiation in a $\sim$1 Å bandpass centred on the Ni I 6768 Å line, whose equivalent width is only a fraction of an Å . Frames c) and d) in Figures 4.1 and 4.2 show the difference in continuum intensity between the GONG images 30 seconds before and after at the time indicated above the frame. Continuum emission is elongated along the magnetic neutral line, corresponding closely to the lenticular component of seismic emission seen at 00:42 UT in Figure 4.1h. The brightest emission seen in the intensity difference shown in Figure 4.1d comes from a very compact kernel whose location coincides very closely with that of the conspicuous kernel of 6.0 mHz emission (Figure 4.1h).

If we assume that the continuum emission emanates isotropically from an opaque surface[3] the resulting estimate of the total energy emitted in the visible continuum is 2.0×10^{23} J (2.0×10^{30} erg). This is $\sim$500 times the total seismic energy we estimate the flare to have emitted into the holographic pupil. Continuum radiation into the neighbourhood of the 6.0 mHz kernel signature was 6.0×10^{22} J (6.0×10^{29} erg). This accounted for $\sim$30 per cent of the total, as compared to 45 per cent of the 6.0 mHz seismic signature. Continuum emission from in the neighbourhood of the 6.0 mHz kernel was significantly more sudden than that of the remainder of the acoustic signature.

The 15 January 2005 flare contributes to recent findings that relatively small flares can emit disproportionate amounts of acoustic energy (Donea and Lindsey, 2005). However, even in these cases the fraction of the energy that is released by the flare into the solar interior acoustic spectrum remains relatively small.

4.2.5 The Seismic Waves

Holography allows us to image the acoustic source of the sunquake when the surface manifestation of the seismic emission is difficult to detect. In the case of the exceptionally powerful seismic transient from the flare of 15 January 2005, the surface signature is quite evident in the raw MDI Doppler observations. To extract the seis-

[3] The assumption is that the specific intensity is independent of the vantage, which implies that the total intensity decreases in proportion to the cosine of the angle of the vantage from normal as a result of foreshortening. If the source was assumed to be optically thin, the resulting energy estimate would be greater by a factor of two. The former appears to be the more realistic estimate for the fraction of visible continuum radiation coming directly from the chromosphere, based on the thesis that ionization of chromospheric hydrogen at the temperature minimum renders the low chromosphere opaque.

mic oscillations in the observations we subtracted consecutive MDI Doppler images separated by one minute in time. We applied this Doppler-difference method to a period of observation (∼1 hour) around the time of the flare. Results are shown in Figures 4.4 and 4.5.

The Doppler signature of the flare is clearly evident at 00:40 UT (Figure 4.5, left panel). At approximately 20 minutes after the appearance of the flare signature in the sunspot photosphere (at 01:00 UT), we are able to see the seismic response of the photosphere to the energy deposited by the flare in the form of "ripples" on the solar surface. In the sequence of one-minute Doppler-difference images in Figure 4.4, we can see the asymmetrical ring-shaped wave packet propagating from the flare site with the first wave-crest appearing approximately 12 – 15 Mm from the flare in a North-Easterly direction. The lower half of the wave-packet has a much smaller amplitude and is propagating in a South-Westerly direction. The arrows in Figure 4.4 indicate the location of the observed wave fronts. The Doppler-difference images in Figure 4.5 show a close-up of the active region at the time of the flare (at 00:40:30 UT, left panel) and the resulting ring-shaped wave packet (at 01:05:00 UT, right panel).

The wave-packet was seen to propagate to a maximum distance of approximately 21 Mm from the flare signal, hence travelling a total distance of 6 – 9 Mm and lasting for about 8 minutes on the surface, after which the wave amplitude dropped rapidly and the disturbance became submerged in the ambient noise. The lower half of the wave-packet (propagating towards the South – Western part of the active region, indicated by the lower of the two arrows superimposed on the Doppler-difference images in Figures 4.4 and 4.5) was much smaller in amplitude and obscured for much of the 8 minutes.

4.2.6 Hard X-Ray Emission

The *TRACE* data for the 15 January 2005 flare in the white-light channel have a variable cadence for the period 00:00:00 – 01:00:00 UT. Figure 4.6 shows the *TRACE* white-light image taken at 00:17:54 UT, approximately 10 minutes before the onset of the X1.2 flare with the *RHESSI* 12-25 keV contours overlaid. The *RHESSI* HXR image is averaged over the period 00:41:33 – 00:42:34 UT. The time of peak intensity in this energy band occurs at 00:42:04 UT, a close temporal correlation with the maximum of the seismic emission detected at 6.0 mHz. The HXR emission is thought to represent bremsstrahlung emission from high-energy coronal electrons impinging into the chromosphere (Brown, 1971).

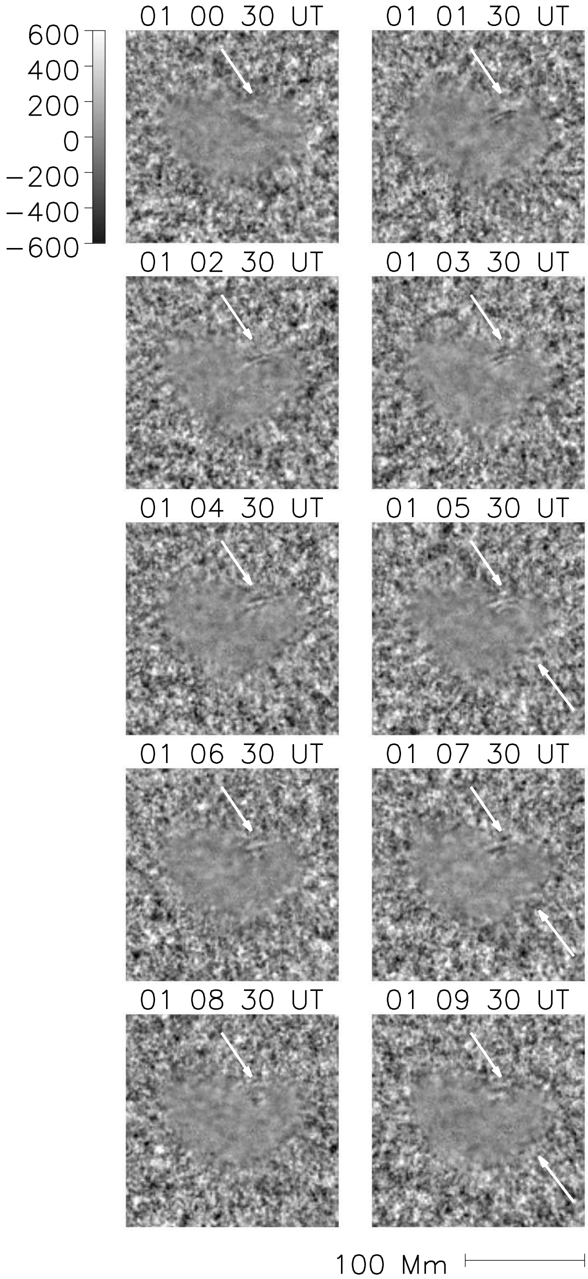

Figure 4.4: One-minute MDI Doppler-difference images showing the expanding ring-shaped wave packet produced by the 15 January 2005 flare. The arrows pointing in the South–East direction (i.e. upper arrows) show the location of the upper-half of the wave front while arrows pointing in the North–West direction (i.e. lower arrows) indicate the lower half of the wave front. Grey-scale at top left expresses Doppler velocity differences in units of ms^{-1} and applies to all frames in the figure.

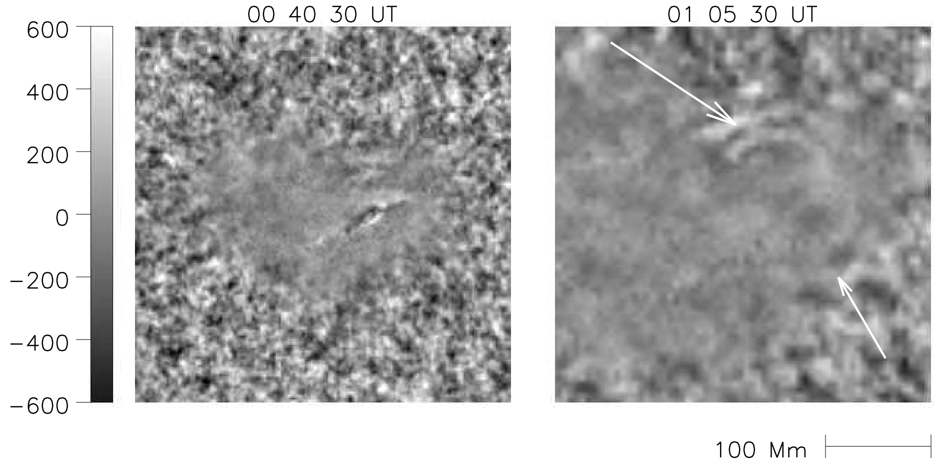

Figure 4.5: Magnified MDI Doppler-difference images showing ring-shaped seismic waves accelerating outward from the site of the 15 January 2005 flare. The left panel shows the local Doppler signature along the magnetic neutral line during the impulsive phase of the flare at 00:40:30 UT. Arrows in the right panel indicate locations of the ripples propagating outwards from the site of local disturbance 25 minutes later.

The 12 − 25 keV emission at 00:42:00 UT extends along the neutral magnetic line. We identify three compact HXR sources (see the numbers in Figure 4.6). Source 2 is the strongest, while source 3 is the weakest. These could represent the foot-points of a complex magnetic loop. However, source 1 (which emits 50 per cent of the total flux) spatially coincides with the lenticular component of the 6.0 mHz seismic source (see Figure 4.1). This reinforces the role of non-thermal particles in supplying the energy that drives the seismic emission. Similar comparisons have been observed in other flares (Donea and Lindsey, 2005).

Furthermore, Figure 4.7 reveals that the velocity impulse of the flare in the sunspot photosphere was almost as sharp as the HXR flux detected in the 4 − 25 keV (0.5 − 4 Å) energy range by the *GOES* satellite, but the maximum HXR emission (observed at ∼00:43:00 UT) appears to have occurred ∼2 minutes after the maximum velocity depression at the photosphere (00:41:00 UT). In fact, a sudden drop of approximately 100 ms^{-1} in the mean velocity of the Doppler signal (an upflow) is observed in the 3 minute period from 00:38:00-00:41:00 UT. The *RHESSI* HXR peak in the higher energy band of 25 − 50 keV plotted in Figure 4.7 occurs at ∼00:41:00 UT, which temporally coincides with both the maximum of the seismic source at 6.0 mHz and

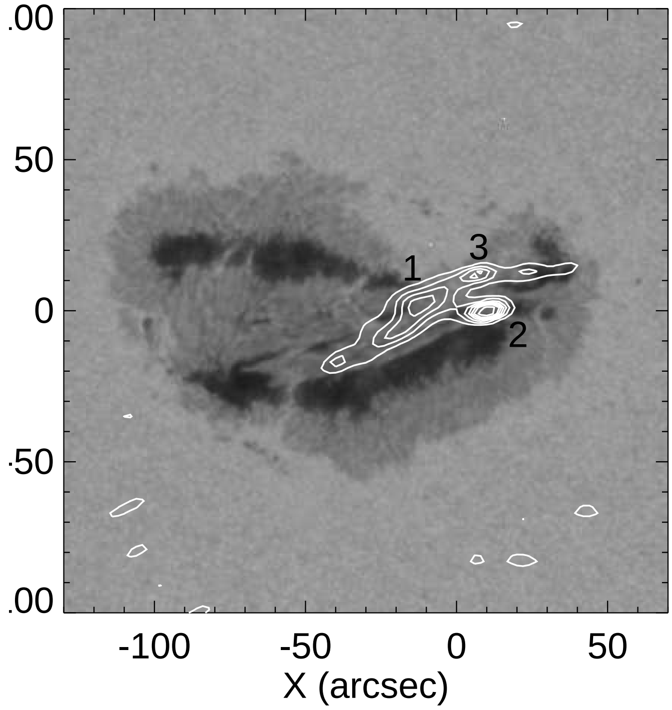

Figure 4.6: TRACE white-light image of AR 10720 on 15 January 2005 (00:17:54 UT) with the 12-25 keV *RHESSI* contours (10, 20, 30, 40, 50, 60 and 80 per cent of the maximum flux). The (0,0) coordinates correspond to the location of the seismic source.

the velocity depression at the photosphere. We also note that the peak emission in the $3-12$ keV energy band detected by both *GOES* ($1-8$ Å) and *RHESSI* (occurring at $\sim$00:44:00 and $\sim$00:47:00 UT respectively, but not plotted), also have a close temporal correlation with the maximum of the seismic emission.

4.2.7 Summary and Discussion

The X1.2-class flare of 15 January 2005 produced one of the most powerful sunquakes detected to date and by far the most conspicuous, on account of exceptionally powerful emission above 5 mHz from a compact source. Certain qualities exhibited by the flare of January 15 are shared by all other known acoustically active flares. The first is the coincidence between strong compact acoustic sources and nearby signatures of HXR emission. This suggests that high-energy particles supply the energy that drives the acoustic emission, and it is evident from the electromagnetic emission attributed to

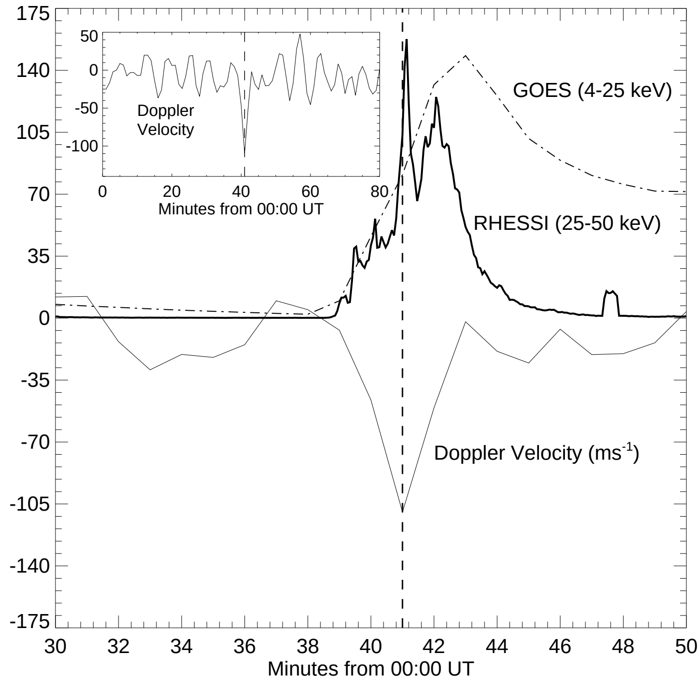

Figure 4.7: The HXR flux in the 4 − 25 (0.5 − 4 Å) and 25 − 50 keV energy ranges as observed by GOES (dot-dashed curve, multiplied by a factor of $10^{6.5}$ Wm^{-2}) and RHESSI (bold curve, multiplied by a factor of $10^{-2.8}$ counts) respectively. The solid curve represents the 1-minute mean averages of the Doppler velocity (ms^{-1}) in the quake region for the period 00:00:00 − 01:20:00 UT. The dashed vertical line represents the observed maximum emission at 6.0 mHz.

these particles that they contain more than sufficient energy for this purpose. The appearance of sudden, conspicuous white-light emission from the flare of 15 January 2005 closely co-spatial with the location and morphology of the holographic signatures is similarly characteristic of all other known acoustically active flares so far.

Kosovichev and Zharkova (1998) proposed that seismic emission into the solar interior in sunquakes is the continuation of a chromospheric shock and condensation resulting from explosive ablation of the chromosphere and propagating downward through the photosphere into the underlying solar interior. Chromospheric shocks are well known under such circumstances, based on red-shifted Hα emission at the flare site at the onset of the flare. The theory of their dynamics was worked out at length by Fisher et al. (1985a,b,c) and others since. The hypothesis that solar interior emission is a direct continuation of such shocks was considered by Donea and Lindsey (2005), who found the signature of a strong downward-propagating chromospheric transient in Na D_1-line observations of the flare of 2003 October 29. However, we are now aware of similar chromospheric transient signatures with no significant attendant holographic signature to indicate seismic emission into the active region sub-photosphere[4].

In these instances, the signature of sudden white-light emission is relatively weak. Following Machado et al. (1989), Donea et al. (2006b) proposed to attribute the lack of seismic emission where there is a strong chromospheric transient but only a weak or absent white-light signature to strong radiative damping that depletes the chromospheric transient before its arrival into the low photosphere.

In all acoustically active flares encountered to date, there is a strong spatial correlation between the sources of seismic emission and sudden white-light emission. This remains conspicuously the case for the flare of 15 January 2005, as a comparison between Figures 1d and 1h shows. In some instances, e.g., the large flares of 2003 October 29, the source of the white-light emission has been much more extensive than the source of the acoustic emission, the former many times the area of the latter and encompassing it. However, in these instances the temporal profile of visible continuum emission significantly away from any of the sites of seismic emission has been comparatively sluggish and diffuse. What has particularly and consistently distinguished the white-light signature in the neighbourhood of the acoustic emission has been the suddenness of its appearance, on a time scale of a minute or two, and possibly considerably less than a minute given that the observations of continuum emission associated with flares to date have been limited to a cadence of one minute.

It should be kept in mind that the energies released in known seismic transients have invariably been a small fraction of the energy released into the visible continuum spectrum. The actual fraction has varied considerably, from a few millionths, in the case of the flare of 2003 October 29 (Donea and Lindsey, 2005), to a few thousandths, for the flare of 15 January 2005. However, if only the sudden-onset continuum emission in the neighbourhood of the seismic sources is included, then the ratio for the flare of 2003 October 29 is similar to that of the flare of 15 January 2005. This is what is listed in Table 4.1 of this study.

The close coincidence between the locations of sudden white-light emission and

[4]An example is seen in the western foot-point of the magnetic loop that hosted 2003 October 29 flare (see right frame in second row of Figure 8 labelled "Red [0 min]" in Donea and Lindsey (2005)). The corresponding signature of sudden white-light emission, seen in Figure 9 of the same, shows only a weak signature at the same location. The seismic signature, seen in the lower left corner of the upper right frame of Figure 11 of the same, shows correspondingly weak seismic emission.

seismic transient emission in all acoustically active flares to date suggests that a substantial component of the seismic emission seen is a result of sudden heating of the low photosphere associated with the visible continuum emission seen. A complete analysis of wave emission as a result of transient heating involves detailed considerations of energy and momentum balance. An approximate account of these was undertaken by Donea et al. (2006b). Basic considerations of momentum balance are described in Section 4.3 of Donea et al. (2006b), adapting the discussion by Metcalf et al. (1990) of momentum balance in chromospheric transients to transients similarly excited by sudden heating in the low photosphere.

Donea et al. (2006b) devised a rough, preliminary physical model to estimate the energy of the seismic transient to be emitted as a result of sudden, momentary heating of the low photosphere to a degree consistent with the transient white-light signature closely coincident with the seismic source in the M9.5-class flare of 2001 September 9. Their estimate expressed the energy, E, of the seismic transient in terms of the thermal energy, U, radiated or dissipated into the low photosphere, and the fractional increment, $\delta p/p$, in pressure that would result from the heating:

$$E \; = \; \frac{1}{2} H \frac{(\delta p)^2}{p} \; = \; \frac{1}{3} \, \frac{\delta p}{p} \, \delta U, \tag{4.6}$$

where H is the e-folding height of the photospheric density. This relation appears to be roughly consistent with the few-percent continuum intensity variations observed for the flare of 2001 September 9, if the relation between δp and δI, the variation in continuum intensity, can be approximated by the Stefan-Boltzmann law,

$$\frac{\delta p}{p} \; = \; \frac{\delta T}{T} \; = \; \frac{1}{4} \frac{\delta I}{I}, \tag{4.7}$$

and the heating is accomplished within a duration not excessively longer than $\tau_{ac} = 1/\omega_{ac} \sim 40$ s, where ω_{ac} is the acoustic cut-off frequency in the low photosphere (see Section 4 of Donea and Lindsey (2005)). A similar exercise applied to the flare of 15 January 2005 leads to similar results. In fact, the ratio of the seismic energy to the electromagnetic energy is roughly the same for both of these flares, as are the mean intensity increments if credible boundaries are chosen over which to take the mean. To the extent that we can resolve the fine details, acoustic emission from the flare of 15 January 2005 could reasonably be the result of photospheric heating similar to that of the 2001 September 9 flare but over approximately twice the area.

Differences between the two flares could be attributed to differing photospheric or sub-photospheric thermal conditions and differing magnetic fields, for which the foregoing approximation contains no account.

A detailed examination of the physics of heated magnetic photospheres is needed to lend credibility to the hypothesis that seismic emission from acoustically active flares is driven by sudden heating of the low photosphere by any mechanism whatever. At this point we will only say that this hypothesis appears to be consistent with our present limited understanding of the observations. However, there is some controversy as to the implications of visible continuum emission during flares with respect to heating of the low photosphere. In the case of the flares of 2003 October 28 − 29, the signature of high-energy protons along with the particles that gave rise to X-ray emission lent considerable weight to the interpretation of visible continuum emission in terms of a heated low photosphere, as protons are sufficiently massive to penetrate to the bottom of the photosphere and heat it directly by collisions. The flare of 15 January 2005, on the other hand, confronts us with an instance of intense seismic emission with no indication of high-energy protons among the energetic particles that supply the energy on which the acoustic emission depends. Energetic electrons consistent with HXR signatures cannot penetrate into the low photosphere in anywhere near sufficient numbers to account for the heating required by the seismic signatures (Metcalf et al., 1990). Chen and Ding (2006) also affirm that the white-light flare signatures highlight the importance of radiative back-warming in transporting the energy to the low photosphere when direct heating by beam electrons is impossible.

In such cases, it appears to be well established that the origin of white-light emission would have to be entirely in the chromosphere, where energetic electrons dissipate their energy (Metcalf et al., 1990; Zharkova and Kobylinskii, 1991, 1993), mainly by ionizing previously neutral chromospheric hydrogen approximately to the depth of the temperature minimum. Nevertheless, even in these instances, it appears that the low photosphere itself would be significantly heated as a secondary, but more or less immediate, effect of chromospheric ionization. This is primarily the result of Balmer and Paschen continuum edge recombination radiation from the overlying ionized chromospheric medium, approximately half of which we assume radiates downward and into the underlying photosphere. When the intensity, δI, of this downward flux is commensurate with a temperature perturbation, δT, consistent with the Stefan-Boltzmann law (equation [4.7]), the result of such a flux is understood to be heating of the low photosphere such as to bring about a temperature increment of roughly this order within a few seconds (Donea et al., 2006b; Machado et al., 1989; Metcalf et al., 2003). Heating of the photosphere by the mechanism described above is known as “back-warming” (Metcalf et al., 2003) and a substantial fraction of the continuum emission seen in white-light flares is thought to represent the downward flux from an ionized chromosphere thermally re-emitted by the now heated photosphere. In this light, the strong correlation between sources of white-light and seismic emission into the solar interior might be regarded as strong support for the back-warming hypothesis when this relation persists in flares devoid of protons among the high-energy particles that drive the flare. This is certainly the case for the flare of 15 January 2005.

Donea and Lindsey (2005) and Donea et al. (2006b) summarize our understanding of the relationship between the efficiency of seismic emission and the suddenness of the heating that drives the seismic transient. Based on these considerations, one has to suspect that the perceptibly more sudden profile of continuum emission in the neighbourhood of the kernel component of the 6.0 mHz emission accounts to a significant degree for the disproportionate power in the 6.0 mHz egression-power signature. This is one of the many aspects of flare acoustics that would benefit from detailed modelling, including a careful account of magnetic forces.

A clear understanding of the physics of seismic emission could also help us to penetrate another major technical issues in active region seismology – the effects of molecular contamination of seismic signatures in sunspots. In the non-flaring sunspot photosphere, contamination by molecular lines may be negligible, simply because apparent shifts in the wavelength of the line used for Doppler measurements are constant and therefore do not find their way into the acoustic spectrum. However, visible and UV radiation produced by white-light flares is probably capable of disassembling such molecules, opening the likelihood of false Doppler transients under conditions that would give rise to significant seismic emission.

4.3 The Solar Flare of 14 August 2004

4.3.1 Active Region Morphology

AR 10656 first appeared on the solar surface on 7 August 2004 at coordinates S12E55 ($-758''$,$-253''$) as an α sunspot. Over the next seven days, the active region continued to increase in magnetic complexity and evolved to a $\beta\gamma\delta$ type. During the period 8 – 16 August it produced 2 X-class, 36 M-class and more than 150 C-class solar flares.

On 14 August, the active region was situated at S13W36 (542″,−298″) and was characterised by a strong δ configuration in the centre of the sunspot, and an overall configuration of $\beta\gamma\delta$. At 05:36 UT an M7.4-class solar flare occurred, peaking at 05:44 UT and concluding at 05:52 UT (as given by GOES12) with an X-ray flux of 3.8×10^{-2}J m^2. This flare produced significant seismic emissions, but it should be emphasised that the same active region produced two other significant seismic transients within a period of 48 hours: the first was generated by an X1.0 flare on 13 August 2004; the second was generated by the M9.4 solar flare on 15 August 2004 (Besliu-Ionescu et al., 2006; Donea et al., 2006b).

4.3.2 The Helioseismic Data

The MDI data we utilized consist of full-disk Doppler images in the photospheric line Ni I 6768 Å, obtained at a cadence of 1 minute, in addition to approximately hourly continuum intensity images and line-of-sight magnetograms. The MDI data sets are described in more detail by Scherrer et al. (1995). For the flare of 14 August 2004, we analysed a dataset with a period of 4 hours around the time of the flare. We also obtained visible continuum maps of AR 10656 during the flare from the GONG observatory at Mauna Loa. Technically, the GONG “continuum intensity maps” represent a measure of radiation in a ≈0.7 Å bandpass centred on the Ni I 6768 Å line, whose equivalent width is 0.07 Å.

For the purpose of our analysis, all MDI and GONG images were remapped as a Postel-projection (Deforest, 2004) that tracks solar rotation, with the region of interest fixed at the centre of the projection. The nominal pixel separation of the projection was 0.002 solar radii (1.4 Mm) with a 256×256 pixel field of view. Other (non-helioseismic) supporting data utilized in this study include: HXR observations from RHESSI, SXR emission data from GOES, Hα emission from the BBSO, and radio emission from NoRH. We will compare these observations with the holographic reconstructions.

4.3.3 The Acoustic Signatures

To assess seismic emission from the flare, we computed the egression over the neighbourhood of the active region at 1-minute intervals, mapping the egression power for each minute of observation. The resulting egression power movies and snapshots (acoustic/egression power sampled over the solar surface at any definite time) are computed over 2.0 mHz bands, centred at 3.0 mHz and 6.0 mHz.

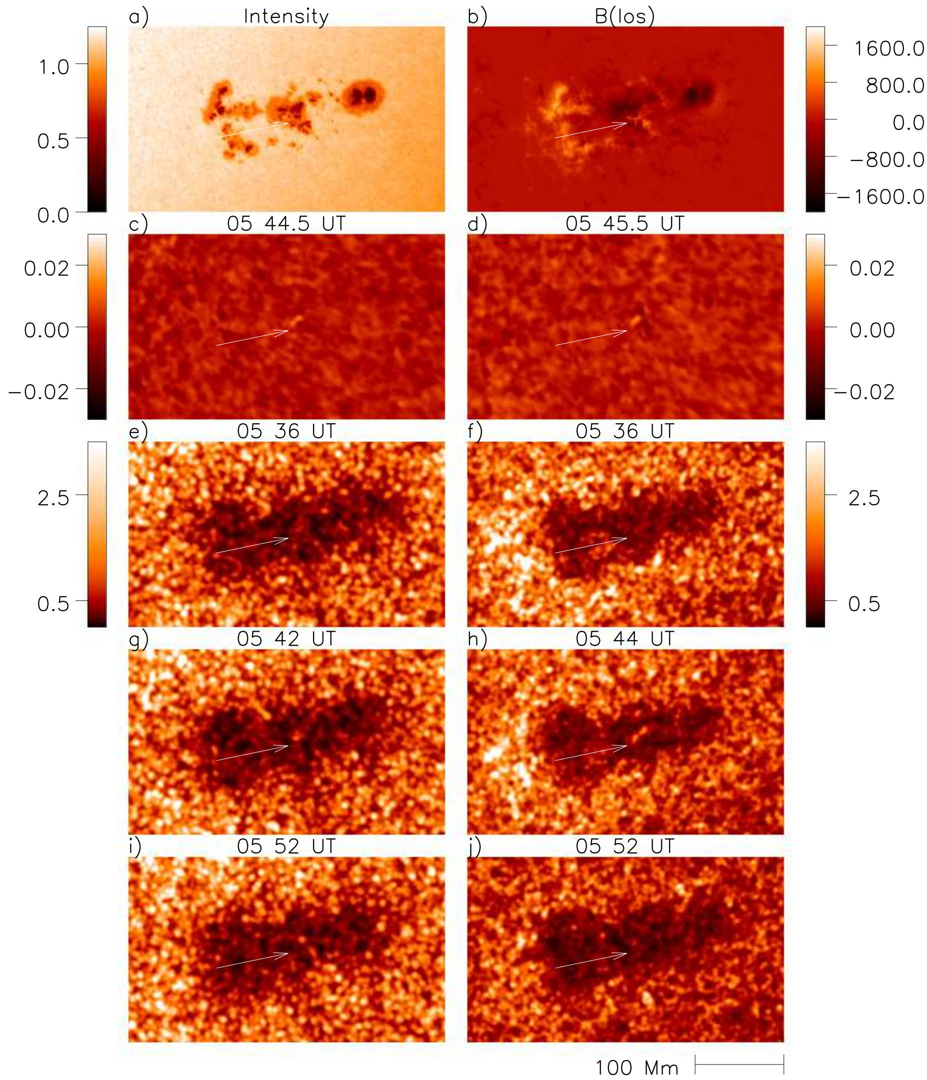

Figure 4.8: Egression power snapshots of AR 10656 on 14 August 2004 integrated over a 2.0 − 4.0 mHz and 5.0 − 7.0 mHz frequency band. Top frames show a MDI visible continuum image of AR 10656 (left) at 06:24 UT and a magnetogram (right) at 05:44 UT. Second row shows GONG continuum intensity differences 30 seconds before and after the time that appears above the respective frames. Bottom three rows show egression power maps before (row 3), during (row 4), and after (bottom row) the flare at 3.0 mHz (left column) and 6.0 mHz (right column). Times are indicated above respective panels, with arrows inserted to indicate the location of the acoustic source. Color scales at right and left of row 3 apply to respective columns in rows 3 − 5

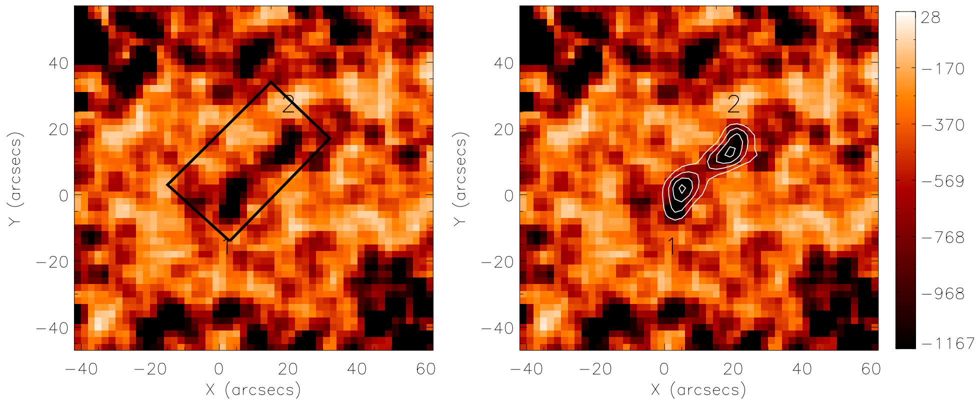

Figure 4.9: A magnified image of the 6.0 mHz egression power snapshot seen in Figure 4.8(h) taken at 05:44 UT. The color map of the image was inverted for a better visualisation of the acoustic source morphology. The left panel shows the acoustic kernels (labelled 1 and 2) and the right panel shows the same image but with egression power contours overlaid. The acoustic source 1 appears to be the stronger of the two. The rectangle represents the mask used to study the time series in the region of the seismic emission.

Egression power snapshots before, during and after the flare are shown in the last three rows of Figure 4.8 at 3.0 mHz (left column) and 6.0 mHz (right column). In these computations the pupil was an annulus of radial range $15-45$ Mm centred on the focus. To improve the statistics, the original egression power snapshots are smeared by convolution with a Gaussian with a $1/e$-half-width of 3 Mm. The egression power images and the continuum images are also normalised to unity at respective mean quiet-Sun values. At 3.0 mHz this is $\sim$2.0 kW m^{-2}. At 6.0 mHz it is 70 W m^{-2}.

All egression power snapshots mapped in Figure 4.8 show considerably suppressed acoustic emission from the magnetic region, attributed to strong acoustic absorption by magnetic photospheres, discovered by Braun et al. (1988). Furthermore, all 6.0 mHz egression power snapshots in Figure 4.8 show acoustic emission "halos," *i.e.* significantly *enhanced* acoustic emission from the outskirts of complex active regions (Braun and Lindsey, 1999; Donea et al., 1999). Looking at Figure 4.8, a significant excess of acoustic emission is evident at 05:44 UT in the 6.0 mHz egression power snapshot, indicated by an arrow in all of the frames, appearing to lie across the penumbral magnetic neutral line and spanning $\approx$25 Mm in length.

Upon closer inspection, we can see from the magnified egression power snapshot in Figure 4.9 that there are in fact two separate components to the seismic source

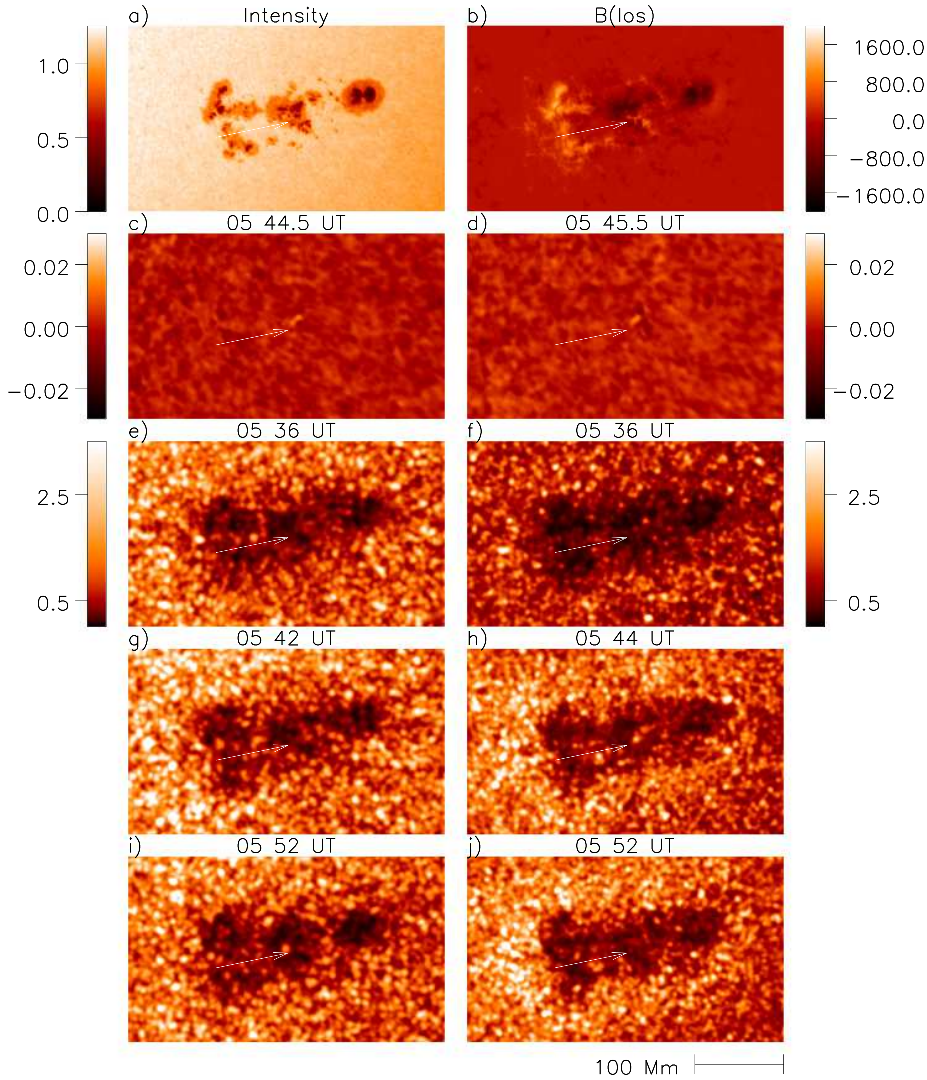

Figure 4.10: Acoustic power snapshots of AR 10656 on 14 August 2004. Details are the same as for Figure 4.8, but local acoustic power maps appear in the bottom three rows in place of egression power maps.

(acoustic kernels) that appear to be separated by $\sim$7 Mm when they initially appear (05:39 UT), and because of their close proximity and evolution with time, they seem to appear as one extended source in Figure 4.8. These acoustic kernels coincide closely with HXR signatures (see Section 4.3.7 and Figure 4.21), indicating that high-energy particles accelerated above the chromosphere contribute to the excitation of the seismic source. The egression power map in Figure 4.9 is smeared by a factor of 0.004, in order to emphasise the source geometry and the acoustic kernels. The map also shows kernels that we associate with the fluctuating acoustic noise of the active region.

The source geometry also closely corresponds with other compact manifestations of the flare including significant white-light emission with a sudden onset, as indicated by the intensity difference signatures shown in the second row of Figure 4.8, and microwave emission at 17 and 34 GHz. The 3.0 mHz egression power snapshots (Figure 4.8) also shows emission during the flare. In fact, from the egression and acoustic power time series of Figure 4.11, it appears that we have a distinct and considerably stronger seismic emission at 3.0 mHz than at 6.0 mHz. This is because of a much greater ambient acoustic noise at 3.0 mHz which renders the considerably greater 3.0 mHz seismic emission signature no more conspicuous than 6.0 mHz.

Figure 4.10 shows the local acoustic power snapshots of AR 10656 at 3.0 mHz (left column) and 6.0 mHz (right column) before, during and after the flare. Each pixel in a local acoustic power map represents the local surface motion as viewed directly from above the photosphere, which should not be confused with the egression power computed by subjacent vantage holography of the surface, where each pixel is a coherent representation of acoustic waves that have emanated downward from the focus, deep beneath the solar surface, and re-emerge into a pupil $15-45$ Mm from the focus.

As in the case of the 6.0 mHz egression power, the local acoustic power maps show a broad acoustic deficit marking the magnetic region and an enhanced local acoustic power halo surrounding the active region which is also clearly apparent. The acoustic source is difficult to distinguish in either the 3.0 or 6.0 mHz acoustic power signatures.

4.3.4 Visible Continuum Emission

Figure 4.12 shows the time dependence of the visible continuum irradiance normalised to the quiet-Sun and integrated over the area of the seismic source. At 05:39 UT the

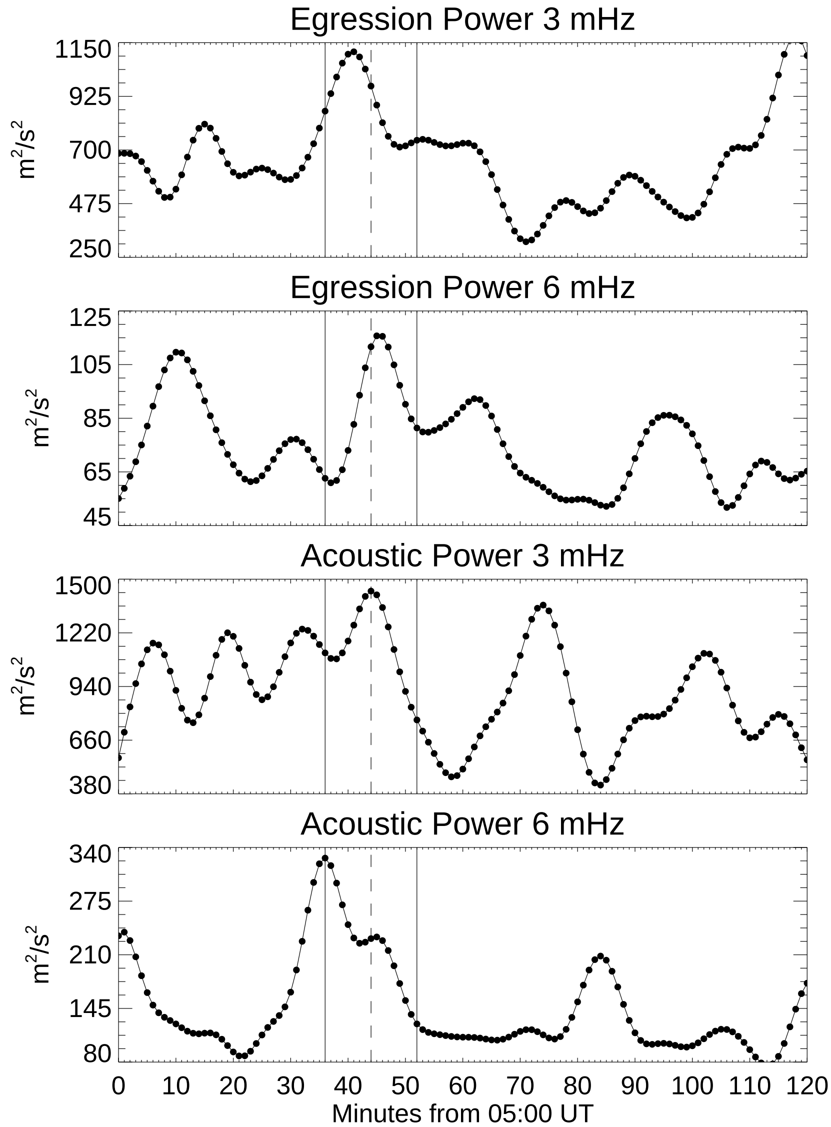

Figure 4.11: The 3.0 and 6.0 mHz egression power and acoustic power time series, integrated over the neighbourhood of the egression power signatures, are plotted in the top four rows. The vertical lines represent the beginning (05:36 UT), maximum (05:44 UT) and ending (05:52 UT) times of the GOES X-ray flare. The relatively extended duration of the acoustic signatures is a result of limits to temporal resolution imposed by truncation of the spectrum (see equation 4.5).

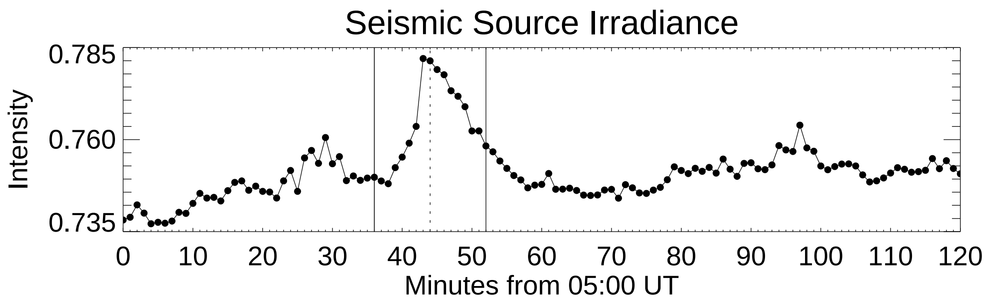

Figure 4.12: Time dependence of the visible continuum irradiance normalised to the quiet Sun and integrated over the area of the seismic source. The vertical lines show the flare times as in Figure 4.11. The maximum emission in white light continuum temporally coincides with the 6.0 mHz seismic emission at its maximum.

irradiance began to increase for ∼4 minutes, then underwent a sudden jump at 05:42 UT for approximately 2 minutes and then slowly decreased to the background level. The maximum irradiance was approximately 4% above the quiet-Sun mean. The white light flare signature is spatially co-aligned with the emission of the seismic sources as imaged in Figure 4.8.

4.3.5 The Magnetic Field Topology

Schunker et al. (2005) have shown that magnetic forces are of particular significance for acoustic signatures in penumbral regions, where the magnetic field is significantly inclined from vertical. Therefore, understanding the 3-D magnetic configuration of the coronal loops hosting flares would give us a powerful control utility for seismic diagnostics of active region sub-photospheres. This will be useful for addressing questions concerning the MHD of inclined magnetic fields, the role of fast and slow magneto-acoustic mode coupling in magnetic photospheres, sub-photospheric thermal structure, and how wave generation by turbulence in active region sub-photospheres differs from that in the quiet sub-photosphere.

In Figure 4.13 we have shown the time series of the mean and the root mean square (RMS) values of the line-of-sight (LOS) magnetic field, integrated over area of the seismic source (the integration area is plotted in Figure 4.9 - black rectangle - and its area has a value of ≈247 Mm^2). The vertical lines mark the time frame of the flare. The mean LOS magnetic field shows a steady increase from 05:10 to 06:00 UT with a strong variation as a sudden decrease, at the maximum of the flare (05:44

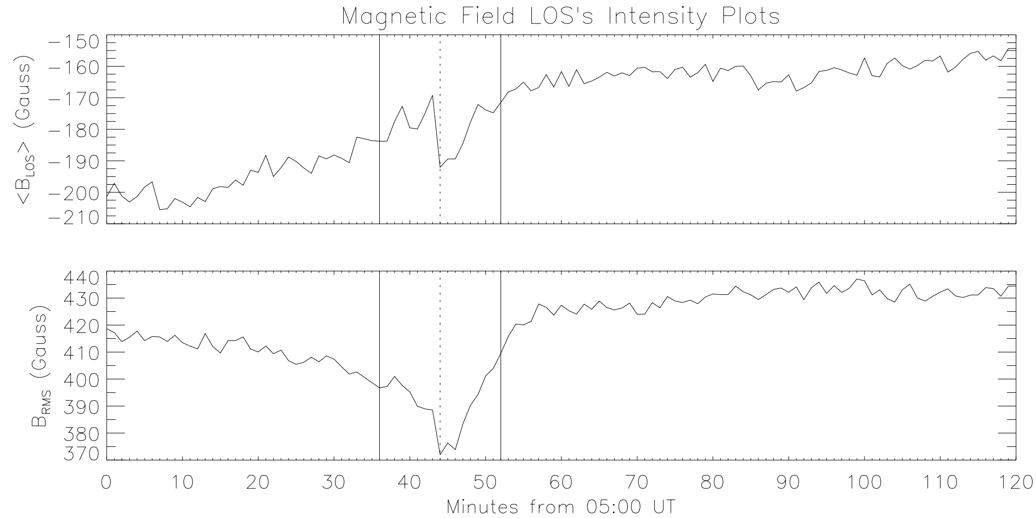

Figure 4.13: Time series of the mean and the root-mean-square of the LOS magnetic field integrated over the area of the seismic source.

UT). The RMS of the magnetic field intensity shows a sudden decrease of about 9.6% of the background level, and a sudden recovery to a 3.6% increased background, as compared to the background level before the flare (similar changes have been observed by Kosovichev and Zharkova, 2001; Sudol and Harvey, 2005; Ambastha et al., 1993; Wang et al., 2005).

To obtain a general idea of the configuration of the coronal magnetic field lines in AR 10656 we computed the potential field extrapolation by applying the code described in Sakurai (1982) to the MDI line-of-sight magnetogram. According to this extrapolation (Figure 4.14, left frame), the field lines whose footpoints were planted in the general region of the acoustic emission were relatively low and compact, suggesting that the magnetic loops, into which particle acceleration occured during the reconnection, were relatively short. The right frame in Figure 4.14 shows the appearance after the flare maximum of more magnetic field lines connecting the positive and negative polarities. A small difference in the line-of-sight magnetic field configuration in the region of the acoustic emission described by the inclined rectangle is also noticeable.

4.3.6 The Seismic Waves

We computed differences between consecutive Doppler frames, separated by one minute in time, around the time of the flare to reconstruct time-distance profiles

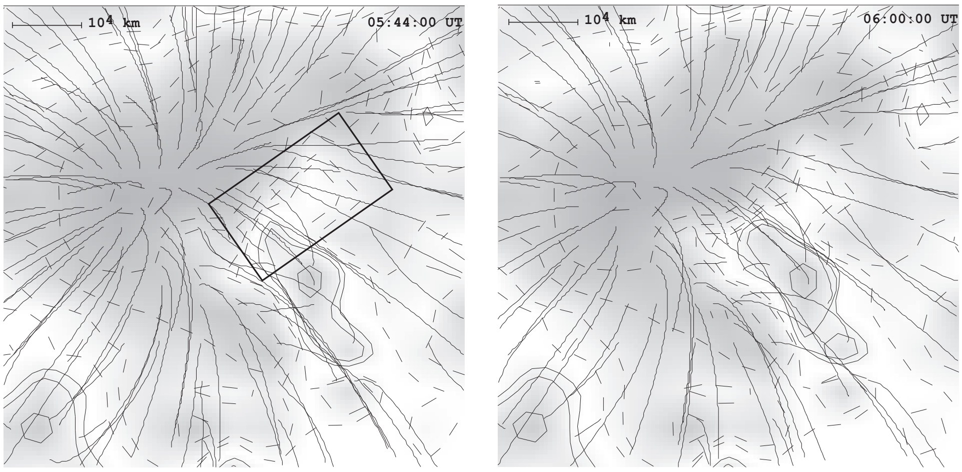

Figure 4.14: Potential magnetic field extrapolation of SoHO-MDI magnetograms of AR 10656. Left: Magnetic field extrapolation at 05:44:00 UT. Right: Magnetic field extrapolation at 06:00:00 UT. The greyscale background image shows the absolute value of the line-of-sight magnetic field. The dashed lines represent the negative magnetic polarity, while the solid lines represent the positive magnetic polarity. The contour lines levels are 50, 100, 300, 500, 1000 G. In the image North is up, the dimension are 104 by 104 arcsec centred at (462,−303) arcsec.

of this seismic emission. In this sequence we see a surface ripple propagating in the North direction, over the range -50° to $+20^{\circ}$ from due north in a reference frame centred on the seismic source. The surface ripple represents acoustic waves that propagated tens of Mm into the solar interior from the acoustic source and were refracted back to the surface 30 minutes after the impulsive phase of the flare. Because of the strong fluctuating motions of the background, the ripple is difficult to see in individual Dopplergrams. They are easily recognised in a movie of differences of consecutive Doppler frames. Even so, we are able to see the ripple at approximately 06:10 − 06:15 UT. The arrows in Figure 4.15 indicate their location. The ripples expand into the north quiet Sun before becoming submerged into the ambient noise.

We do not see an expanding wave moving southward, either because the signal is too weak to be detected by eye or the emission to the north is simply stronger. The seismic wave is highly anisotropic, its amplitude varies with angle. The strongest amplitude is observed in the north direction. In section 4.3.7 we will see that this direction is also approximately the direction of the motion of HXR footpoints. A similar behaviour was reported by Donea and Lindsey (2005) in the seismically active flares of the October 2003. The fronts of the eastern, southern and western acoustic

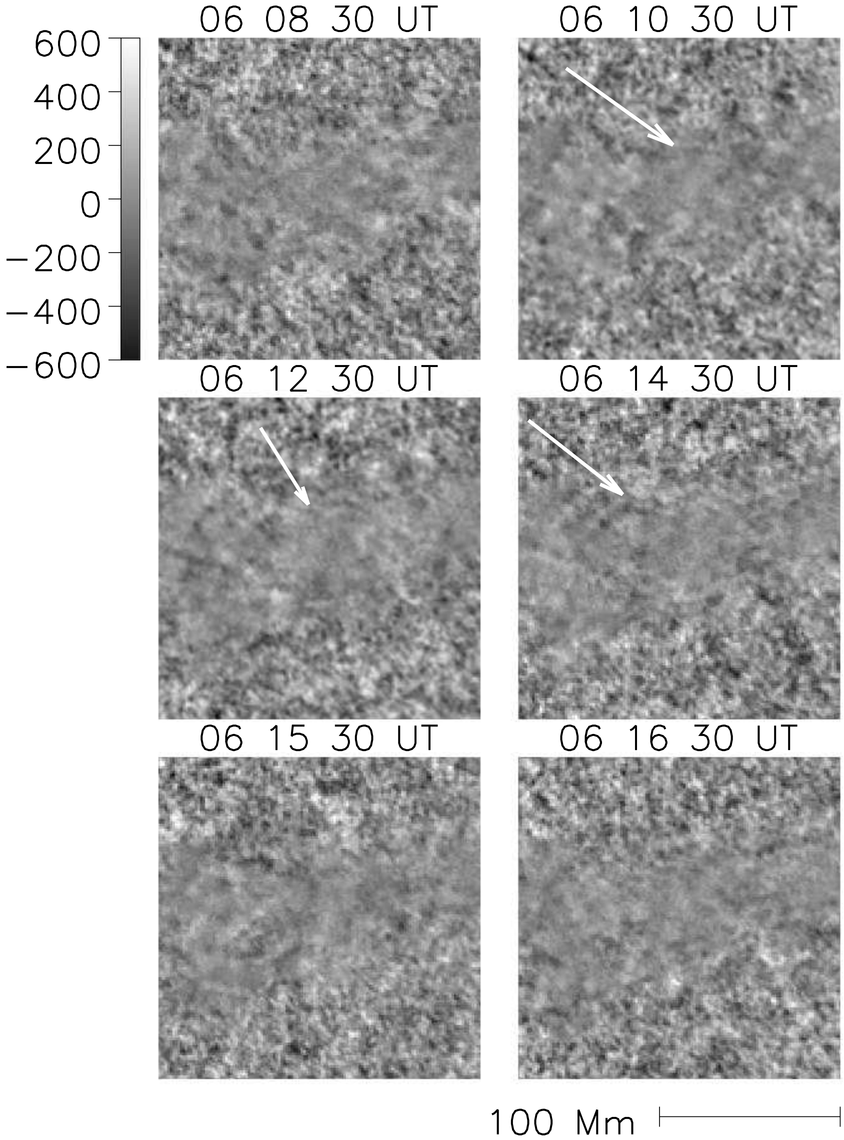

Figure 4.15: Observations of surface ripples at the specified times emanating from AR 10656 following the impulsive phase of the flare. Arrows show the location of the surface ripples. Only the north angular sector of the ripple can be seen by eye.

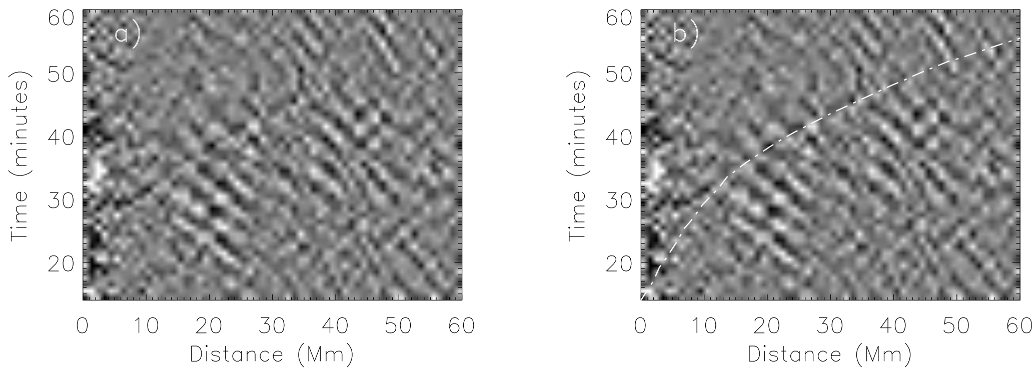

Figure 4.16: Time-distance propagation amplitude of the surface ripple averaged over curves of constant radius, over azimuths from -50 to $+20°$ is rendered in gray tone in both frames. The curve superimposed in the right frame represents the wave travel time, t, for a standard model of the solar interior. The time 05:30 UT is represented by $t = 0$.

seismic wave propagate through the sunspot, and are exposed to a locally strong magnetized environment, thus causing significant damping of the oscillations in that region. As a result, the amplitude of the observable surface waves in these fronts are somewhat distorted and decay much faster.

Figure 4.16a shows a time-distance amplitude profile for the ripple described above. The Doppler difference amplitude was averaged along curves of constant radius in the reference frame described above over the -50 to $+20°$ range of azimuths over which the surface ripple was visible. This resulting gray-tone plot is shown in Figure 4.16(b) with the theoretical group travel time plotted for reference.[5]

4.3.7 Radio and HXR Emission

The flare of 14 August 2004 was observed with NoRH, at 17 GHz and 34 GHz, and RHESSI. Unfortunately, the totality of the impulsive and main phases of the flare was not observed by RHESSI, and as a result, images and time profile of the HXR emission just prior to, and after the maximum of the flare, are not available.

[5]This travel time, $t(\rho)$, is defined by the path integral

$$t(\rho) \; = \; \int_{\Gamma(\rho)} \frac{ds}{c}, \tag{4.8}$$

where Γ represents the path of least time through the quiet sub-photosphere connecting surface points separated by an angular distance ρ along the surface, and c represents the sound speed.

Figure 4.17 shows the total flux time profiles of the event in microwaves, soft and hard X-rays. The GOES total fluxes in the two channels 1 − 8 Å and 0.5 − 4 Å are shown in the top graph of Figure 4.17. Figure 4.17b shows the HXR-RHESSI time profile in the two channels 15 − 25 keV (black line) and 25 − 50 keV (red line). Figure 4.17c shows the microwave time profiles obtained using the Nobeyama Radio Polarimeter (NoRP) data at 17 GHz (red line) and 35 GHz (black line). In Figure 4.17d, we plotted the normalised total GOES flux at 1 − 8 Å and the NoRP flux at 35 GHz. The empirical relation observed between the SXR and HXR flux or microwaves is the Neupert effect (Neupert, 1968). It is clear from Figure 4.17d, that this effect is present and that the NoRP 35 GHz emission lags behind the GOES SXR by 43 seconds. The microwave emission did not present a significant thermal component, suggesting relatively inefficient trapping of the accelerated electrons in the coronal magnetic field. This result is of significant importance to the process of transportation of energy from the reconnection site into the lower layers of the chromosphere and further into the photosphere where the sun quake was produced.

It has already been established that a close relationship exists between HXR and radio fluxes in the impulsive phase of a flare (e.g. see Kundu et al., 2001; Bastian et al., 1998). Based on this relationship, it is generally believed that essentially the same population of energetic electrons is responsible for both HXR and radio emission. The radio emission is thought to be produced by accelerated nonthermal electrons orbiting magnetic field lines and trapped in the coronal magnetic field. The HXR emission is produced by Coulomb collisions of these energetic electrons with the dense chromospheric plasma.

The maximum brightness temperature of the radio source at 17 GHz (Figure 4.18, left panel) was measured to be 4.67×10^7 K, with a spectral index, δ, of -3.67. These results indicate that a non-thermal emission process for the microwave radiation is at work; the non-thermal emission region was also confirmed using the variance technique [6] for solar radio image analysis (Grechnev, 2003). This technique allows us to plot a radio map of the non-thermal emission from the active region by also subtracting any contribution from thermal sources in the corona. From the variance map

[6] We calculate a variance map of a set of radio images using the following equation:

$$\sigma_{ij}^2 = \frac{1}{N}\sum_{k=1}^{N} x_{ijk}^2 - \frac{1}{N^2}\left(\sum_{k=1}^{N} x_{ijk}\right)^2 \tag{4.9}$$

where $i = 1, 2, \ldots, L$ is the image row number, $j = 1, 2, \ldots, M$ the column number and $k = 1, 2, \ldots, N$ is the image number in the data set.

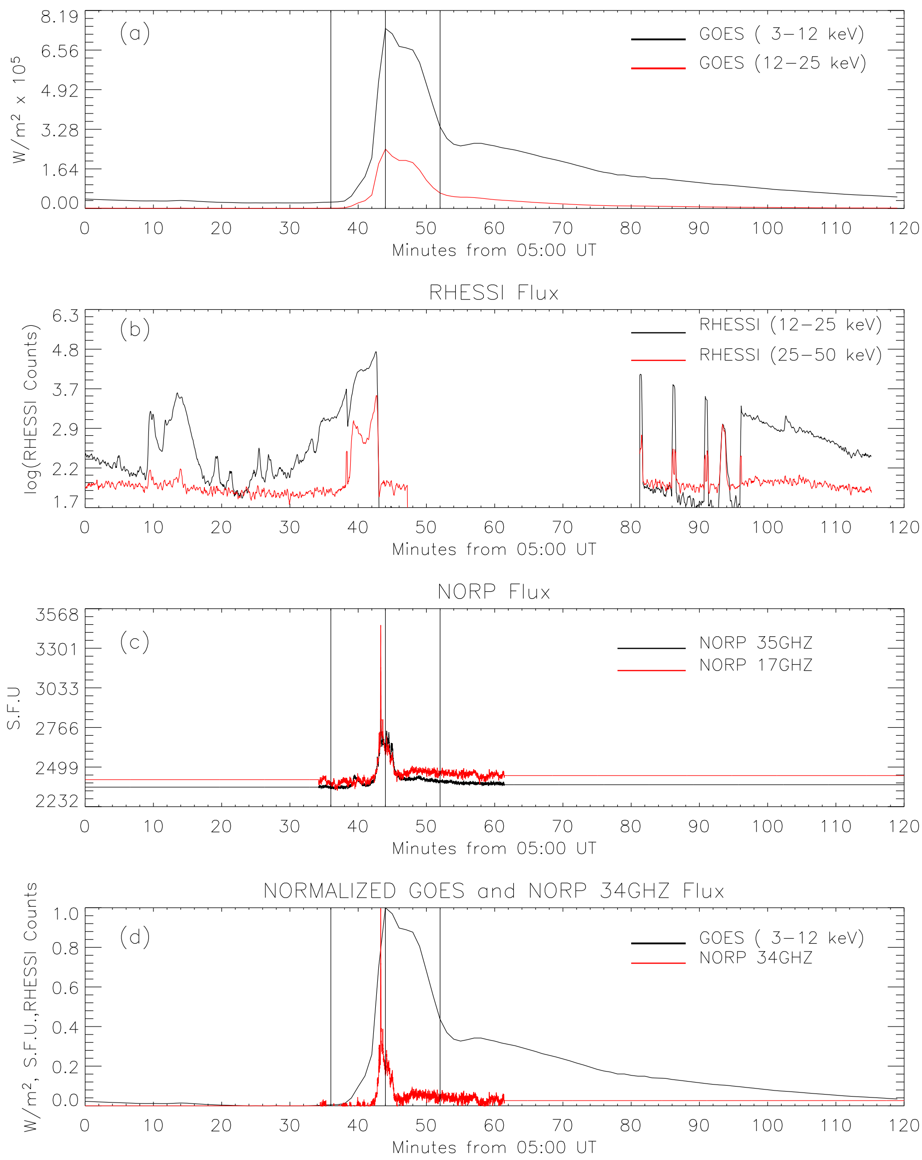

Figure 4.17: Integrated flux time profiles from GOES, RHESSI and NoRP. Frame a) shows GOES soft X-ray 1 − 8 Å and 0.5 − 4 Å channels; b) RHESSI time profiles in two channels 12 − 25 keV (black line) and 25 − 50 keV (red line); c) NoRP microwave time profiles at 17 (red line) and 35 GHz (black line); d) Normalised total GOES total flux (black line) and NoRP microwave flux at 35 GHz (red line). The vertical lines show the beginning, maximum and end of the event.

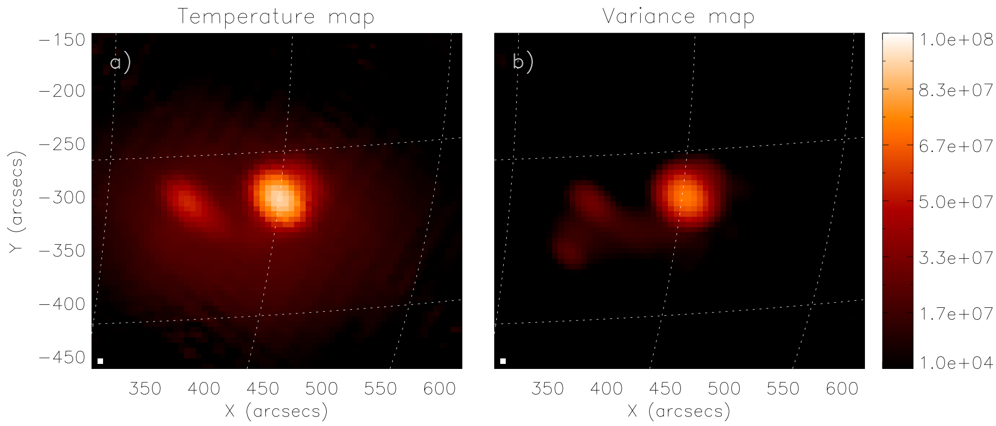

Figure 4.18: Temperature and variance maps of AR 10656 obtained from NoRP. Panel (a) shows the brightness temperature radio map at 17GHz and panel (b) shows the variance map, which identifies a non-thermal radio source at the location of the main spot of the AR 10656.

(Figure 4.18, right panel) we infer that the non-thermal emission is compact and well correlated with the HXR emission region. The flux of electrons with energies $\gtrsim$25 keV is very small, $\approx$6% of the flux registered in the 12 − 25 keV energy band, and possibly did not make a significant contribution to the seismic emission. A delay of 43 seconds is observed between the microwave emission (05:43:17 UT) and the maximum in the seismic signature (05:44:00 UT). A similar delay is observed between the NoRP 35 GHz emission and the GOES SXR.

Figure 4.19 shows a sequence of images of the 14 August 2004 flare taken by the Transition Region and Coronal Explorer (TRACE) overplotted with the contours of the NoRH microwave emission at 17 GHz (large red contours) and RHESSI 12 − 25 keV HXR (small black contours). We applied the MEM-SATO algorithm (Sato et al., 1999) available in the standard RHESSI software to reconstruct RHESSI images from grids 3, 4, 5, 6, and 8 using an integration time of 1 to 4 seconds. As seen in Figure 4.19, the impulsive phase of the flare has a simple compact morphology in both HXR and microwaves until the minute prior to the flare maximum, when the HXR source evolves into an extended source composed of three smaller kernels (as seen in Figure 4.20). The radio source maintained its morphology after the flare maximum. The close temporal and spatial correlation between the microwave and X-ray emissions in this flare indicates a sudden energy deposition into the chromosphere by non-thermal electrons. This is in agreement with the prediction made by Kosovichev

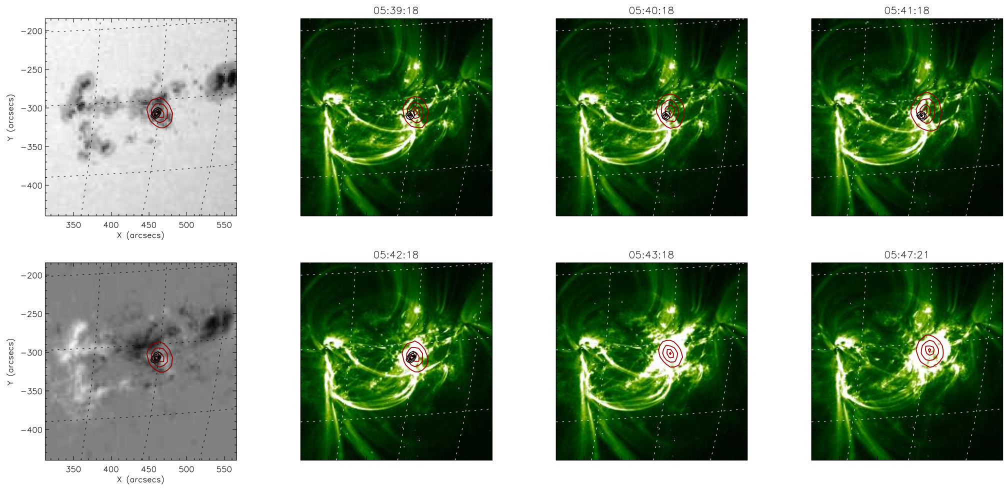

Figure 4.19: First column shows the MDI intensity continuum and magnetogram images of AR 10656 with the microwave emission at 17 GHz (red large contours) and RHESSI $12-25$ keV (black small contours) overplotted. Evolution of the flare at 171Å as observed by TRACE is shown in the last three columns for the specified times. RHESSI $12-25$ keV HXR emission (black contours) with contour levels of 50%, 80% and 95% of the maximum source intensity, and NoRH microwave emission at 17 GHz (red contours) at 20%, 50%, 80% and 95% of the maximum intensity of the radio source are also shown. The field of view is $256'' \times 256''$ with north is upward.

and Zharkova (1998). Figure 4.19 also shows a spatial correlation between the flare region observed by TRACE at 171 Å and the microwave and HXR sources.

The temporal evolution of the HXR feature, with respect to the photospheric magnetic neutral line, can be seen over a sequence of MDI magnetograms taken around the time of flare-maximum (Figure 4.20). The HXR footpoint appears to be moving in the north$-$ north$-$east direction, a motion which is not parallel to the photospheric neutral line. Furthermore, we can clearly see that the source maintains its compact HXR structure until the last minute of observation (05:42 UT), reinforcing the observations shown in Figure 4.19. In this last minute, the source appears to evolve into an elongated shape that covers both magnetic polarities lying around the neutral line. This new elongated source is composed of three kernels, two of which are located in the positive magnetic region and the third one is located near the final position of the compact source observed at 05:42 UT. We remark that the motion and evolution of the RHESSI source is seen as projected over the egression power maps. The frames in Figure 4.20 show first a loop-top emission (compact kernel) which gradually moves towards the footpoints along a single magnetic loop, the one

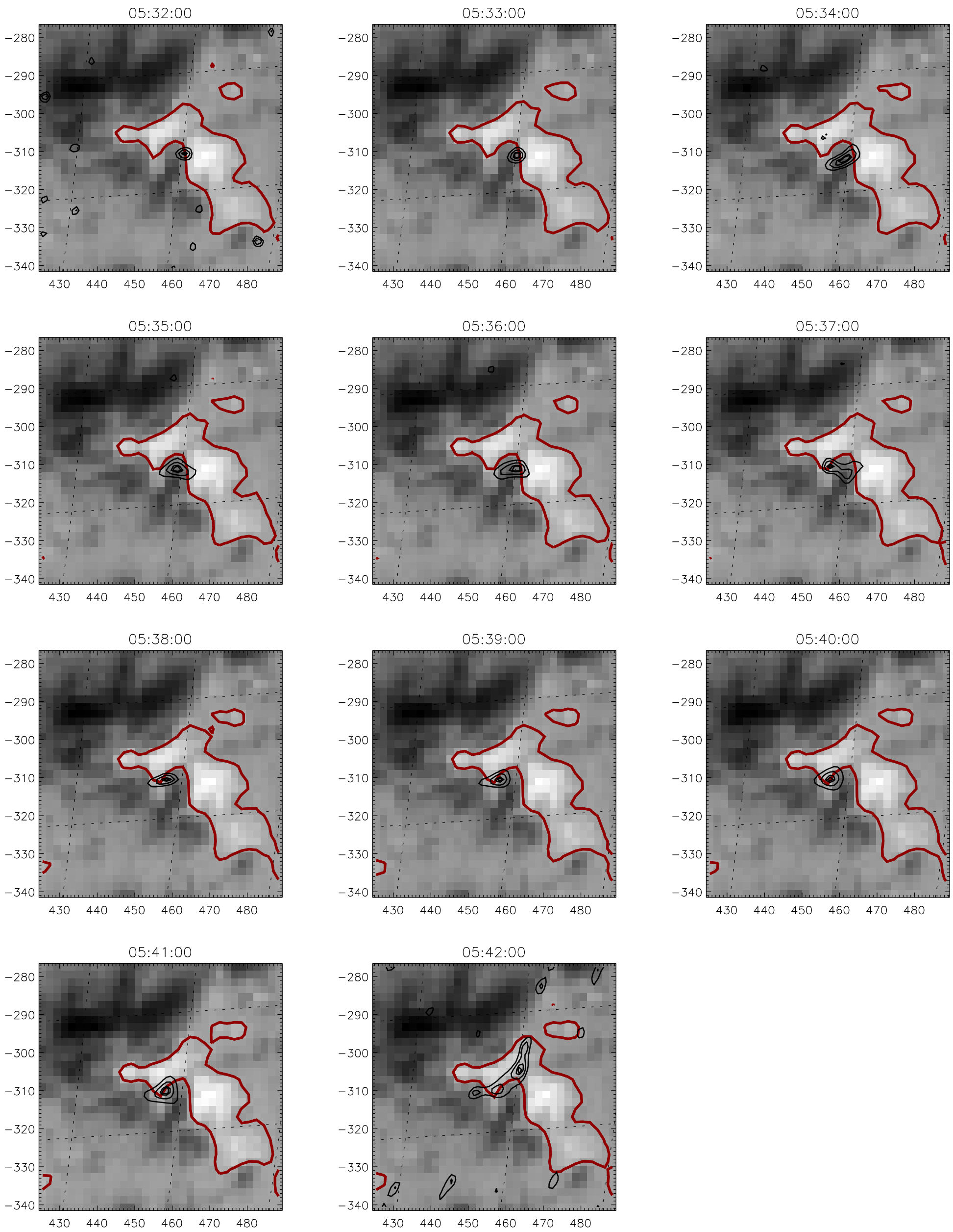

Figure 4.20: Evolution of the MDI magnetogram (background) and RHESSI-HXR source 12 − 25 keV (black contours, with levels 50%, 80% and 95% of the maximum source intensity) from 05:32:00 UT to 05:42:00. The red line is the magnetic neutral line of the MDI magnetogram. North is up and East to the left.

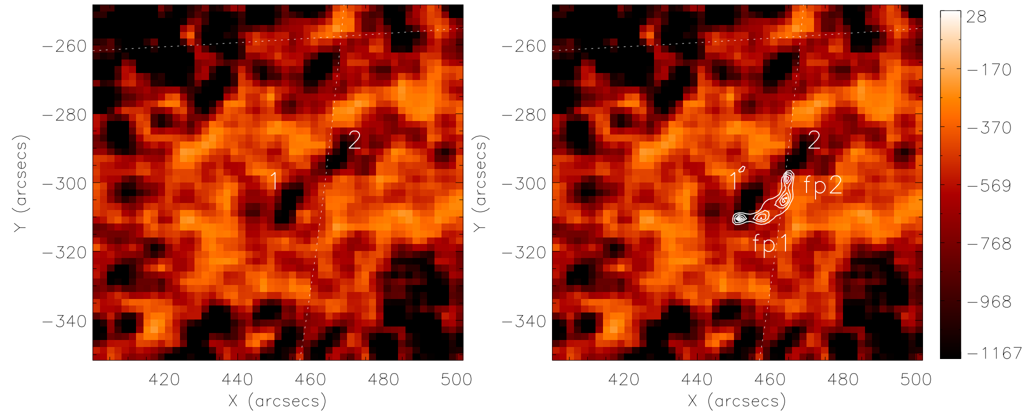

Figure 4.21: Egression power snapshots of AR 10656 with RHESSI HXR contours overlaid. Left: Egression power map at 6.0 mHz, with contour levels of 50%, 65%, 80% and 95% of the maximum source intensity. Right: Egression power map and RHESSI contour plots, with levels of 30%, 50%, 70% and 90% of the maximum source intensity. The colour map of the egression power map was inverted for a better visualisation of the acoustic source.

that hosted the seismically active flare. The break-up of the HXR emission kernels began at 05:42 UT. After this time, no RHESSI data where available, but following a similar study done by Donea and Lindsey (2005), we can predict that the RHESSI footpoints and the seismic source will match in the following two minutes. Figure 4.21 shows that the egression power snapshot at 6.0 mHz and the HXR sources have a similar morphology, with two of the four HXR sources (fp1 and fp2 in Figure 4.21) having a strong spatial correlation with the acoustic kernel sources in the egression power snapshot.

4.3.8 Summary and Discussion

The detection of seismic transients from the M-class flares opens a new era of studying seismically active solar regions. Acoustically active flares are the most compact, most impulsive, and highest-frequency solar acoustic sources discovered to date. Moreover, they are the only known sources of acoustic waves that operate in the outer, visible, solar atmosphere. This makes the transients they release into active region sub-photospheres understandable in a way that wave generation by sub-photospheric convection is not.

We carried out a study of the M-class flare of 14 August 2004 from AR 10656, including HXR emission, seismic emission into the solar interior in the $2.5-7.0$ mHz spectrum and radio emission up to 34 GHz. We applied holographic and other standard time-distance diagnostics to helioseismic observations of the seismic transient emitted by the flare. These clearly show the signature of an expanding wave packet centred on a source of HXR emission. The holographic images show a seismic source morphology composed of two kernels approximately perpendicular to the magnetic neutral line of the active region in the penumbra of one of the sunspots. The kernels are spatially aligned close to similar HXR kernels in the $12-25$ keV energy range. Visible continuum emission, similarly aligned with the holographic kernels, reinforces the hypothesis, based on similar instances in other seismically active flares, that heating of the photosphere contributes to the observed seismic emission, possibly as a result of back-warming by the chromospheric source of the continuum emission.

The loss of HXR observations before HXR maximum encumbers our ability to conduct a realistic comparative analysis based on timing. Nevertheless, a simultaneous rise in the HXR flux with the 17 GHz and 34 GHz radio flux suggests that the same particles, relativistic electrons, produce both the radio and HXR emission. The radio signature, attributed to gyro-synchrotron emission from relativistic electrons, is highly impulsive, both at the onset and the ensuing decline phases.

Gyro-synchrotron emission from flares is often characterized by an impulsive rise followed by a rapid but sometimes only partial decline in brightness temperature. Then follows a slow decline of the remaining signature over many minutes. The latter behaviour is broadly attributed to electrons that are trapped in a magnetic flux tube because they were injected into the tube in a direction that lies outside of the magnetic loss cone (Kundu et al., 2001). These electrons may be scattered into the loss cone by ambient thermal electrons in the flux tube and leak into the chromosphere over a duration that depends on the scattering rate, which in turn depends on the density of ambient thermal electrons in the flux tube. Whether these temporarily trapped electrons can contribute to seismic emission depends on the foregoing duration, since a significant contribution to the seismic transient is thought to depend critically on thick target heating that is relatively sudden, within about a minute or so. A rapid increase in the thermal free electron and ion density due to ablation of the upper chromosphere might facilitate the rapid injection of initially trapped relativistic electrons into the loss cone significantly increasing both the magnitude and suddenness of chromospheric and photospheric heating thought to contribute to seismic emission. Chromospheric ablation into the magnetic flux tube by relativistic electrons initially injected into the loss cone can greatly enhance scattering by ambient electrons and ions in the magnetic flux tube, if the flux tube is filled with this material sufficiently rapidly. How rapidly this occurs must depend critically on the length of the flux tube, for example. Coronal flux tubes no more than a few Mm in length can be highly populated with dense thermal plasma within 30 seconds or so, whereas longer flux tubes would require several minutes to do so.

In the case of the flare of 14 August 2004 the decay of the 17 GHz and 34 GHz emission following the initial rise is quite rapid. This suggests that relativistic electrons are either injected predominantly into the loss cone of the magnetic flux tube at the outset or that trapped electrons not initially injected into the loss cone are scattered into it rapidly, which could enhance the seismic emission. The magnetic extrapolation of the region suggests that the field lines connecting the photospheres in the neighbourhood of the seismic source to their conjugate footpoints are indeed short, only a few Mm in length. This may explain both the rapid and complete decrease in synchrotron emission following the impulsive onset and the occurrence of a relatively strong sudden white-light signature, and may help to explain a commensurate, relatively strong seismic transient emitted from a flare that otherwise is relatively weak.

4.4 The Solar Flare of 10 March 2001

4.4.1 Active Region Morphology

During the peak of Solar Cycle 23, a highly compact and impulsive flare was observed in AR 9368 on 10 March 2001 by a number of solar observatories, including SoHO, Yohkoh, RHESSI, GOES and the Nobeyama and Mitaka Solar Observatories in Japan. Located at N27 W42 in heliocentric coordinates, the flare began at 04:00 UT and ended at 04:07 UT, peaking at 04:05 UT. GOES SXR observations marked it as a M6.7 class, while enhanced emission at continuum near the Ca II 8542 Å line, which lasted about 30 seconds, showed a good time correlation with the peak of microwave radio flux at 7.58 GHz, leading to it being classified as type I white-light flare (Liu et al., 2001; Ding et al., 2003). SoHO also observed a coronal mass ejection and a coronal dimming associated with the flare.

The active region itself emerged on 2 March 2001 at N27 E48 location as a small spot of α type magnetic class. It then slowly developed into $\alpha\beta$ type configuration, with an emerging magnetic flux of opposite polarity also developing near main leading and following spots on 6 March. Uddin et al. (2004) reported significant changes in active region which occurred between 8 and 10 March 2001. On 8th March the following spot began to fragment and continued on 9th and 10th March. This activity was further accompanied by flux emergence of positive polarity. On the other hand, the leading spots did not show any considerable changes. However, on 9 March 2001 a M1.5-class impulsive flare occurred near the leading spots, by which time the active region had developed into a $\beta\gamma$ configuration, which continued through to 10 March 2001.

4.4.2 The Helioseismic Data

The SoHO-MDI data consists of full-disk Dopplergrams, magnetograms, and continuum images in the photospheric line Ni I 6768 Å, obtained at a cadence of 1 minute. A data set with a period of ∼4 hours encompassing the flare was chosen for the analysis. The MDI images were remapped onto a perspective that tracks solar rotation, with the region of interest fixed at the centre of the frame. The Dopplergrams were also corrected for small effects due to reduced oscillatory amplitudes in magnetic regions, following the method outlined in Rajaguru et al. (2006). The MDI images were then Postel-projected on to the frame with a nominal separation of 0.002 solar radii (∼1.4 Mm). The field-of-view of the MDI images analysed was 256×256 pixels, thus incorporating a region of $\sim 360 \times 360$ Mm on the solar surface.

4.4.3 The Helioseismic Signatures

We utilize two different, but complementary, helioseismic techniques to analyse the seismicity of the acoustic emission produced by the flare. The first method employed was the time–distance technique described by Kosovichev and Zharkova (1998). We generate the time–distance plot over a selected range of azimuths from the primary HXR and magnetic–transient sources, in this case $+135^o$ to $+225^o$, in order to gauge the expanding signal from this region and compare this signal with a curve that represents the theoretical group travel time. The resulting signature, manifested as a "ridge" in the time-distance diagram, was significant, but as was expected, appeared to be quite weak (see Figure 4.22). This is more than likely a consequence of the relatively small energy released by the flare (class M6.7 in X-rays) that produced the sunquake. The theoretical curve appears to match the observed ridge with a delay of approximately 5 minutes from the time of the flare maximum. A temporal delay of such nature was contemplated by Zharkova and Zharkov (2007) (with our case being

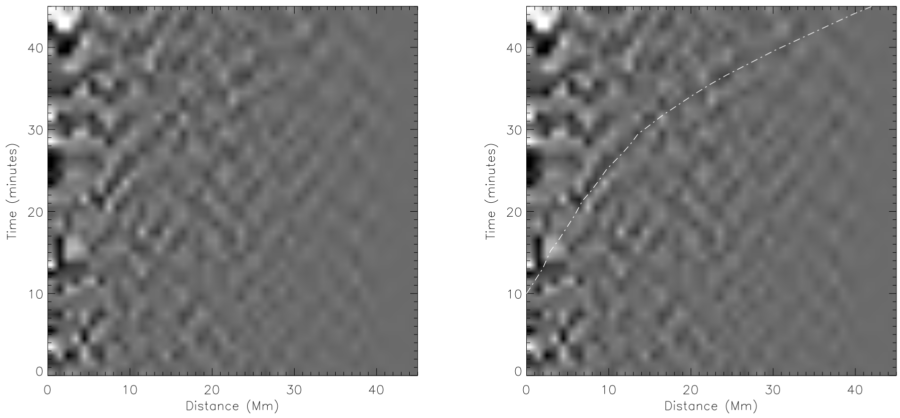

Figure 4.22: Time-distance diagram indicating the amplitude of the ridge associated with the seismic disturbance observed in AR 9368 averaged over curves of constant radius in the azimuth range $+135^o$ to $+225^o$ are rendered in gray in both frames. The white curve superimposed in the right frame represents the wave time travel for a standard model of the solar interior. The time represented as 0 along the vertical axis of the plot is 04:07 UT.

of slightly longer duration). According to Zharkova and Zharkov (2007), this delay is due to the time required for the electrons to move along the magnetic field lines and hit the upper photosphere or chromosphere. The velocity and acceleration of the expanding wave packet was also computed. The velocity of the wave-front was calculated to be close to 13 $\mathrm{km\,s^{-1}}$ between 5 and 9 Mm, and then about 66.67 $\mathrm{km\,s^{-1}}$ between 29 and 33 Mm. The mean acceleration of the wave-front was also estimated to be approximately 3.35 $\mathrm{km\,s^{-2}}$.

The second method employed in our analysis was computational seismic holography, to image the acoustic source of the sunquake. This method has been used extensively in the analysis of acoustically active flares, with great success in identifying numerous seismic sources from solar flares (Donea et al., 1999; Donea and Lindsey, 2005; Donea et al., 2006b; Moradi et al., 2007; Martínez-Oliveros et al., 2007).

To assess the seismic emission from the flare, we computed both the acoustic and egression power over the neighbourhood of the active region at one-minute intervals, mapping them for each minute of observation. In a similar manner to the two previous flares analysed, the acoustic and egression power movies and snapshots are computed over 2.0 mHz bands, centred at 3.0 and 6.0 mHz. The higher frequency band has a number of advantages because it avoids the much greater ambient noise of the

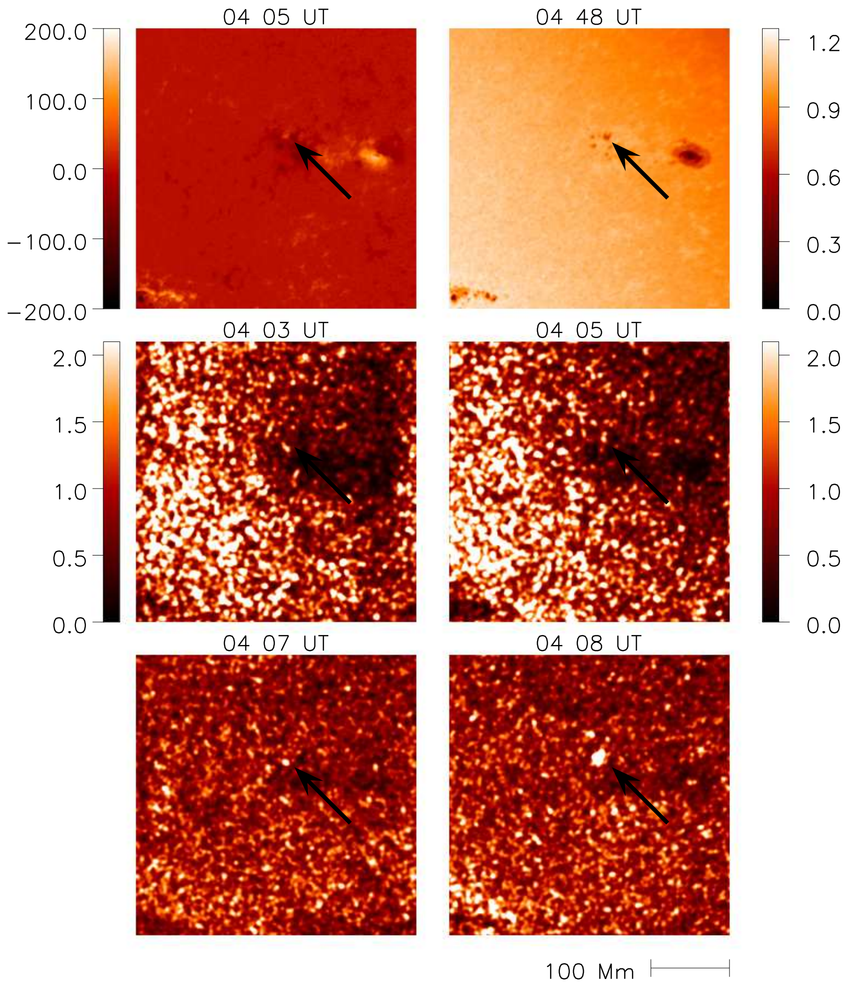

Figure 4.23: Egression and acoustic power snapshots of AR 9368 on 10 March 2001 integrated over 2.0 − 4.0 mHz and 5.0 − 7.0 mHz frequency bands and taken at the maximum of the correspondence frequency. Top frames show MDI magnetogram of the active region (right) at 04:05 UT and a visible continuum image at 04:08 UT(left). Second row shows egression power at 3.0 mHz (left) and 6.0 mHz at the respective maxima. The bottom row show acoustic power. Times are indicated above respective panels, with arrows inserted to indicate the location of the seismic source.

quiet Sun that dominates the 2.0–4.0 mHz frequency band, and due to a shorter wavelength it also provides us with the images that have a finer diffraction limit. This is particularly important when considering that this flare is the weakest flare (in SXR) that we have analysed to date.

Acoustic and egression power snapshots at the maximum of the flare are shown in Figure 4.23. In these computations, the pupil was an annulus of radial range 15 – 45 Mm centred on the focus. To improve the statistics, the original egression power snapshots are smeared by convolution with a Gaussian with a 1/e-half-width of 3 Mm. The egression power images and the continuum image are also normalized to unity at respective mean quiet-Sun values. The acoustic signature of the flare – consisting of a bright compact source – is clearly visible at 6.0 mHz in the both acoustic and egression power snapshots at 04:05 UT (indicated by the arrows in Figure 4.23). At 3.0 mHz the egression and local acoustic power snapshots show a less conspicuous signature than at 6.0 mHz due to a much greater background acoustic power at 3.0 mHz.

The temporal profiles of the seismic source, seen in the acoustic/egression time-series in Figure 4.24 correspond closely with other compact manifestations of the flare including significant white-light emission with a sudden, impulsive onset as discussed by Li et al. (2005) and Uddin et al. (2004). The spatial and temporal features of the seismic source observed also coincides closely with the HXR signature reported by Li et al. (2005), indicating that high-energy particles accelerated above the chromosphere contribute to the generation of the seismic source. We will discuss their observations in more detail in the next section.

The Multi-Wavelength Signatures

The multi-wavelength properties of the extremely impulsive white-light flare of 10 March 2001, have previously been studied in detail by a number of authors (Liu et al., 2001; Ding et al., 2003; Uddin et al., 2004; Li et al., 2005); all emphasizing the impulsiveness of the flare and the strong spatial and temporal coincidence of the hard HXR emission with the enhanced continuum emission.

The observations of Uddin et al. (2004) showed that the flare embodied a very hard spectrum in HXR, a type II radio burst, and a coronal mass ejection. GOES SXR observations classified it as a M6.7 class, beginning at 04:00 UT, reaching its maximum at 04:05 UT, and ending at 04:07 UT. A very important characteristic of the flare of 10 March 2001 is its duration, which was approximately seven minutes, indicating

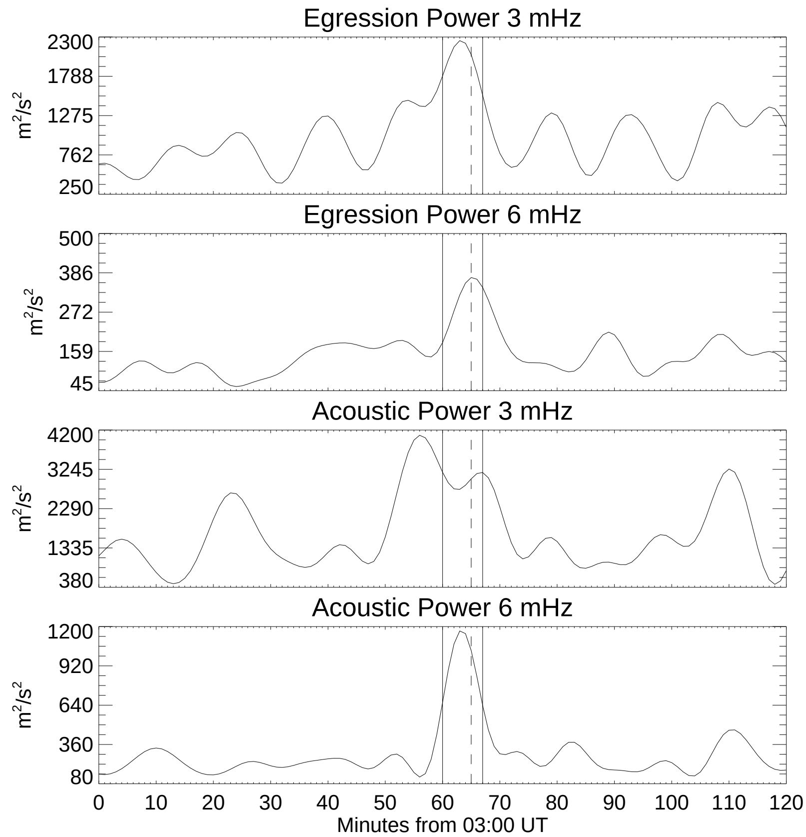

Figure 4.24: The 3.0 and 6.0 mHz egression and acoustic power time series, integrated over the neighbourhood of the egression power signatures. The vertical lines represent the beginning (04:00 UT), maximum (04:05 UT), and end (04:07 UT) times of the GOES X-ray flare.

that the physical processes associated with the flare also had a very short duration. Uddin et al. (2004) made a detailed study of this flare at different wavelengths and determined that all three main phases of the flare could be observed clearly in different temporal profiles in HXR at different energy bands (Figure 4.25). The precursor phase was observed to occur at 04:03 UT with a duration of 15 seconds, the impulsive phase between 05:03:15 and 04:03:40 UT, and the gradual phase after 04:03:40 UT. Also, they calculated the column emission measure, the spectral index of the flare signal and the temporal variation of the temperature. They found that the emission has a non-thermal component before 04:04 UT and thermal component after 04:05 UT. From the observed profiles, they concluded that a very fast acceleration of the electrons occurs during the impulsive phase.

Uddin et al. (2004) also emphasized the spatial and temporal correlation of the HXR source and the continuum emission. They also commented on the uncommon change of magnetic flux they detected, concluding that it indicates that the white-light flare was triggered by a new emerging flux that induces a flux cancellation. As a result, they conclude that magnetic reconnection occurred in the upper atmosphere of the sunspot region; thereby high-energy electrons precipitate along magnetic field lines and deposit energy at the sunspot region, which produce the HXR and continuum enhancement.

The importance of this particular type of spatial and temporal correlation between the different types of multi-wavelength signatures described above, in the presence of a seismic source, was first identified and discussed in depth by Martínez-Oliveros et al. (2007). They identified a significant temporal correlation between the fluxes at different frequencies and energy bands (for the M7.4 class flare of 14 August 2004) which were seen to be directly related to two electron populations - one trapped in the magnetic field, and another precipitating into the chromosphere. The highly impulsive character of this flare indicates that the trapped population of electrons in the magnetic field was injected into the chromosphere very fast. The electrons had no time to thermalise in the coronal loop, but were evacuated by rapid precipitation, therefore they did not produce a significant emission in microwave. Indeed, this type of emission is absent in the microwave profile reported by (Uddin et al., 2004). The radio emission does not show a long exponential decay, implying that high-energy electrons that are generally trapped for a significant amount of time in long coronal loops that extend to great heights, are evacuated by rapid precipitation in short, low-lying loops.

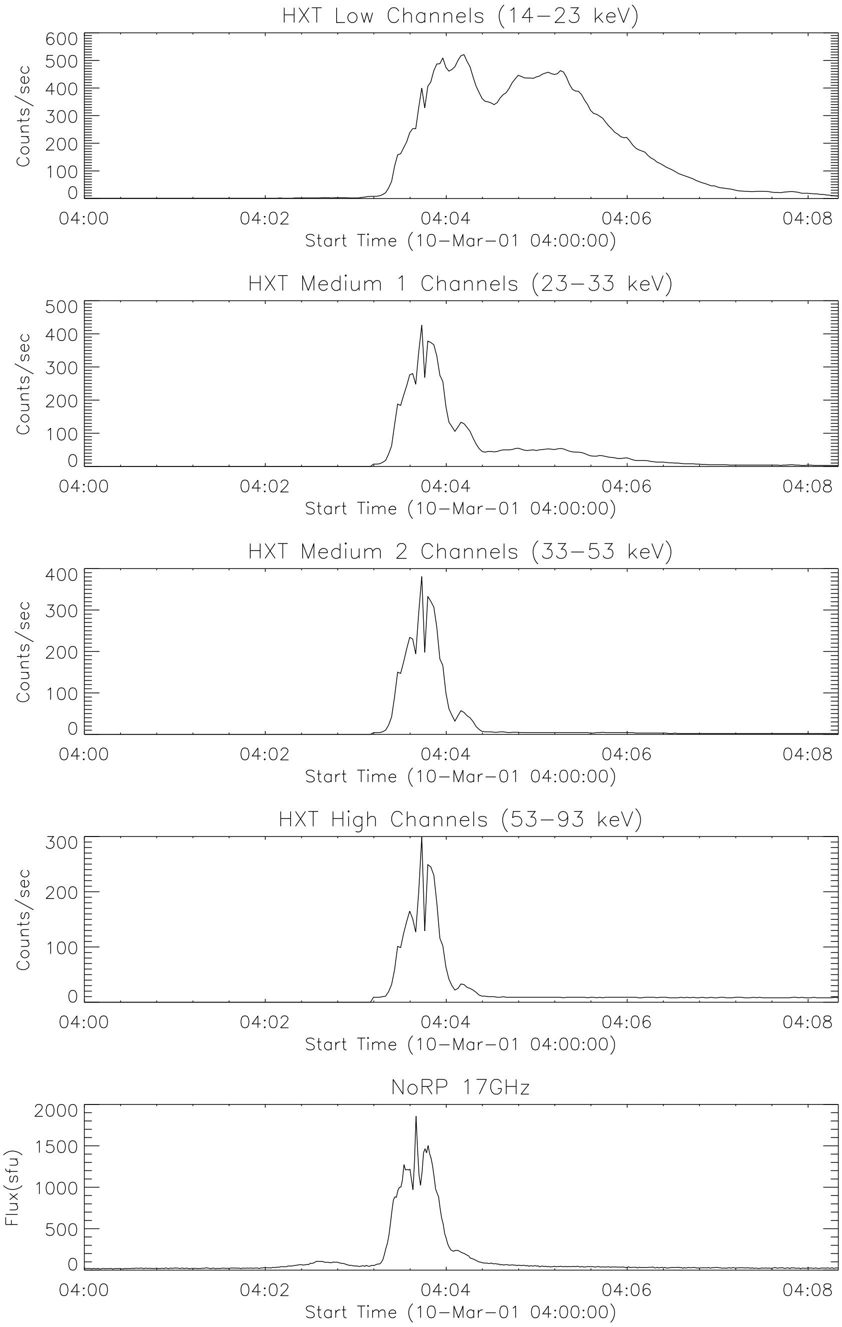

Figure 4.25: HXR and microwave time profiles of AR 9368 on 10 March 2001. The HXR fluxes were taken by Yohkoh at the L(14 − 23 keV), M1(23 − 33 keV), M2(33 − 53 keV), and H(53 − 93 keV) channels. The NoRP flux plotted correspond to the 17 GHz channel.

Li et al. (2005) also observed the white-light properties of the 10 March 2001 flare, detecting an infrared continuum enhancement of $4-6\%$ compared to pre-flare values. The study of the continuum images shows that the white-light source is located over the magnetic neutral line and that the source is most likely composed of the two footpoints of the magnetic loop, which are too close together to be resolved by the RHESSI HXR observations. They also detected a HXR source near the sunspot. The authors also concluded from their observations that the temporal and spatial coincidence of the HXR emission with the continuum emission indicates that electron precipitation may have been the main energy source of the chromospheric heating, producing the excess continuum emission. Furthermore, they suggest that the electron-beam bombardment, coupled with radiative back-warming effects, plays the main role in the heating of the sunspot atmosphere. This is significant because all instances of seismic emissions to date have exhibited very similar white-light flare characteristics - characterized in particular by the sudden appearance of the white-light signature during the impulsive phase of the acoustically active flare.

The images in Figure 4.26 show a number of the multi-wavelength signatures emitted by the 10 March 2001 solar flare. Frames 4.26a and 4.26b show the position of the magnetic transients, represented by the yellow and green circles, over the MDI-intensity continuum and magnetogram respectively. The magnetic neutral line is over-plotted (red line) in all frames for reference. Figure 4.26c shows the magnetic difference maps at the time of the maximum of the flare (04:04:01.61 UT). We can clearly see one transient coincides well with the region of HXR emission (denoted by the contours), lying across the magnetic neutral lines. In Figure 4.26d we have plotted the Doppler differences for the same time. Here we can see two photospheric signatures (spatially coinciding with the magnetic transients) that can be associated with surface perturbations of the solar photosphere. We also note that observations by Li et al. (2005) show that the white-light signature is composed of two sources, both of them being well correlated (spatially) with the magnetic transients. One strong and extended source lies in the region of the HXR and seismic source; the second one appears to correlate well with the second magnetic transient.

Uddin et al. (2004) extensively analysed the temporal and spatial behaviour of the solar flare. The maximum time in both HXR and microwave emission reported by them as well as by Li et al. (2005) (who undertook a very similar analysis), coincides very well with the maximum of the seismic emission (following the already well known delay of approximately three – four minutes (Moradi et al., 2007)). Uddin et al. (2004)

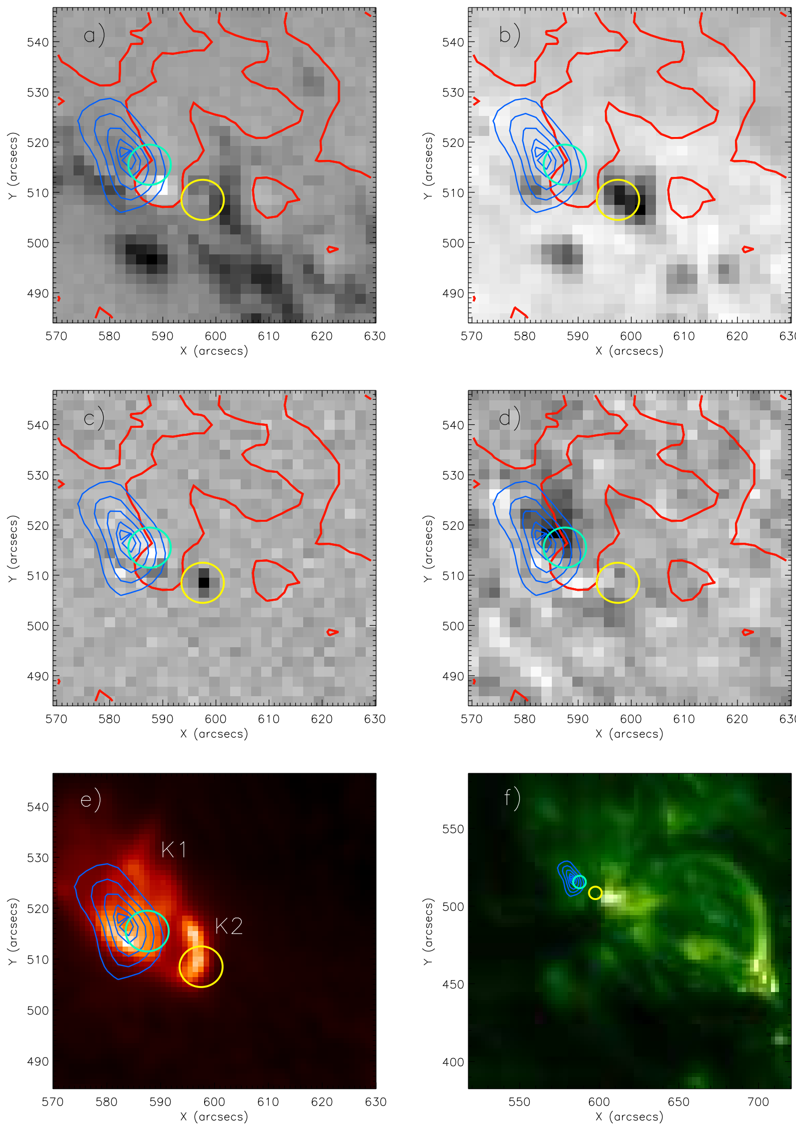

Figure 4.26: HXR contours of the 10 March 2001 flare at 04:03:38 UT overlaid over: a) MDI intensity continuum, b) MDI magnetogram, c) MDI magnetogram difference at the flare maximum, d) Doppler difference at the maximum, e) Hα and f) SoHO-EIT at 171 Å. The background images all correspond to the same time (04:04:01.61 UT). The HXR contour levels are 20, 40, 60, 80, and 90% of the maximum emission in the M2 (22-53 keV) channel. The MDI magnetogram neutral line (red line) is overlaid in the frames a), b), c) and d). The blue and yellow circles in all frames represent the relative position of the main magnetic transients. The seismic source coincides spatially with the blue circle, where there is also the HXR emission.

also discuss the spatial correlation between the different sources, showing that all three forms of emissions (white-light, HXR and microwave) are located in the region of maximum magnetic shearing. Chandra et al. (2006), in a similar work, reported the locations of two Hα kernels in the flaring region. One of these kernels is (spatially) well correlated with the HXR source (observed by Yohkoh) and the observed seismic source, suggesting the precipitation of electrons in the chromosphere. The second Hα kernel is however not correlated with any HXR source, possibly indicating proton precipitation in this region (see Zharkova and Gordovskyy (2004) for a discussion about the partial separation of electrons and protons into the loop legs).

4.4.4 Coronal Magnetic Field Reconstruction

The magnetic field topology of the active region has also been studied by other authors (Uddin et al., 2004; Li et al., 2005) and was correlated with other emissions produced by the flare. Using vector magnetograms from the Mitaka Solar Observatory (Figure 4.27), we can see that the shearing of the magnetic field lines is close to 80^o at the location of the seismic source (see the white arrow) – which would imply that a vast amount of energy was stored in the magnetic field prior to the flare. The area where the shearing is significant is very small. The seismic source itself is proved to be of a small size of 19×25 Mm. The magnetic energy released by the flare is used to accelerate particles, heat the chromosphere, and also drive the coronal mass ejection (see Uddin et al., 2004; Li et al., 2005), and produce the compact seismic source.

In order to verify the magnetic-field configuration of the active region (particularly in the corona), we computed the non-linear force free field (NLFFF) coronal magnetic field extrapolations of the active region using vector magnetograms from the Mitaka Solar Observatory. The resulting extrapolations (seen in Figure 4.28) clearly show high-altitude magnetic field lines connecting the two leading sunspots of the group, while between the leading and the following sunspots, only low-lying loops are visible (see arrow in Figure 4.28). A comparison between the extrapolations with SoHO-EIT images at 171Å (Figure 4.26f) and Figure 4.28) shows that our derived coronal magnetic-field extrapolations are in agreement with the observed magnetic field. Because of the close proximity of the sunspot to the solar limb and other observational constraints, it is not entirely possible to fully reconstruct the complete configuration of the magnetic field (in the flaring region). But nonetheless, we can qualitatively infer the overall structure of the coronal magnetic field from our estimates.

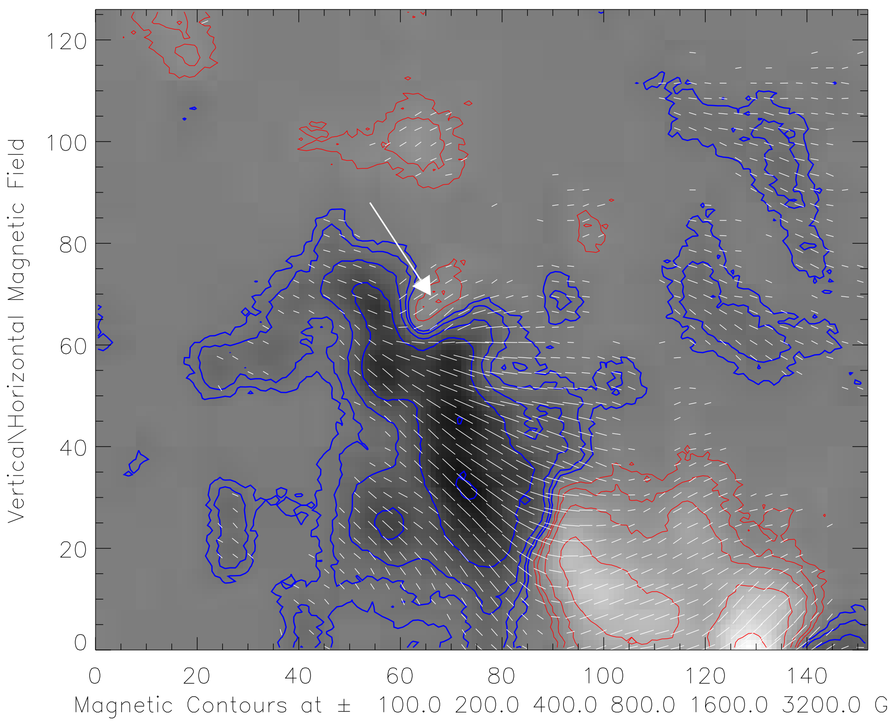

Figure 4.27: Vector magnetogram of AR 9368 taken by the Mitaka Solar Observatory (NAOJ) at 00:10:16 UT. The arrow indicates the focus of the seismically active region.

In a closely related work, Chandra et al. (2006) conducted a detailed study of the dynamics of 10 March 2001 flare. As mentioned previously, they identified two Hα kernels, with only one kernel (K1) found to be spatially correlated with the HXR emission (see Figure 4.26e) and therefore with the seismic source. The second Hα kernel, labelled K2, has an elongated structure. No HXR emission has been correlated with this source, we have also not detected any seismic source from this region despite the white-light signature present at $\approx$ 04:04 UT. These findings, along with observations of the flaring region made by the SXR telescope onboard Yohkoh, led the authors to propose a possible configuration of the magnetic field composed of two magnetic loops sharing one footpoint ("three-legged" configuration), and associated with the single HXR source observed by Yohkoh. One of the loops appears to be connecting the shared footpoint with an opposite-polarity region associated by Chandra et al. (2006) with a secondary, stronger, yet distant microwave source. The second loop is a low-lying loop connecting the shared footpoint with another located inside the region with a high degree of magnetic shearing. Furthermore, it is important to state that the two kernels observed by Chandra et al. (2006) spatially coincide remarkably well with the magnetic transients observed in Figure 4.26e), with only one of them also being well correlated with the HXR emission and the Doppler signature.

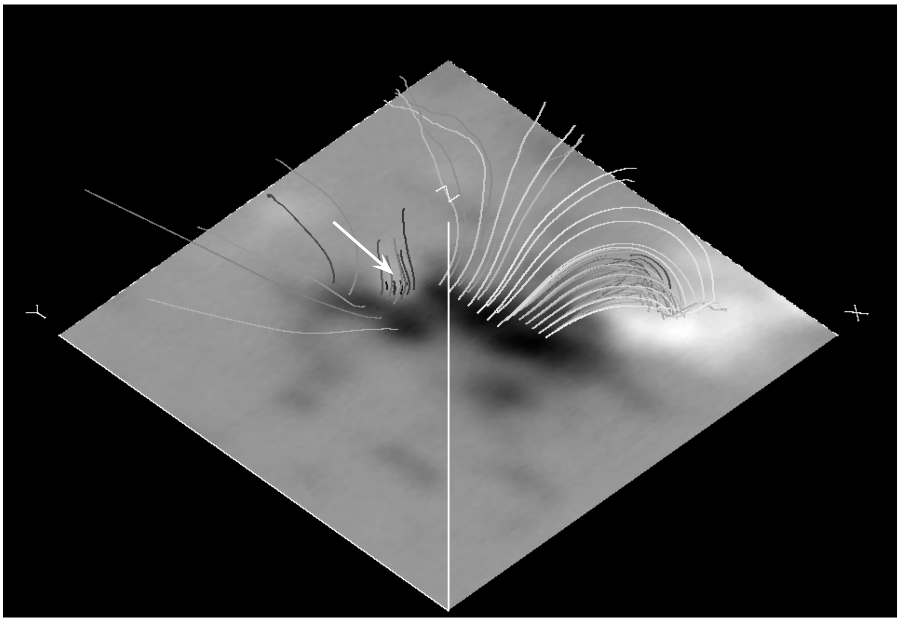

Figure 4.28: NLFFF magnetic field extrapolations of AR 9368. The arrow shows the low-lying magnetic field region associated with the seismic emission.

The existence of a relationship between the height of the coronal magnetic loops and the seismicity of active regions, has previously been proposed in Martínez-Oliveros et al. (2007). The idea behind this assertion was that electrons in short, low-altitude magnetic loops precipitate more effectively than long, high-altitude loops because of enhanced scattering by thermal electrons ablated from the chromosphere. Electrons whose pitch angles are greater than the loss-cone threshold, are trapped in the corona until they are scattered into the loss cone. Eventually, these electrons precipitate into the chromosphere and, depending on their energy, into the photosphere, transferring efficiently energy and momentum to the system. This scattering rate is greatly increased when the population of thermal electrons in the loop is large. This generally depends on the ablation of chromospheric gas into the corona by the fraction of electrons that were initially injected into the loss cone. The volume of a short, low-lying loop is much smaller than that of a long high-altitude loop. The electron density that results from a given mass of the chromosphere having been ablated is thus inversely proportional to this volume. Hence, given these understandings, we propose that short, low-lying loops become efficient scattering environments promptly greatly expediting precipitation on time scales conducive to seismic emission.

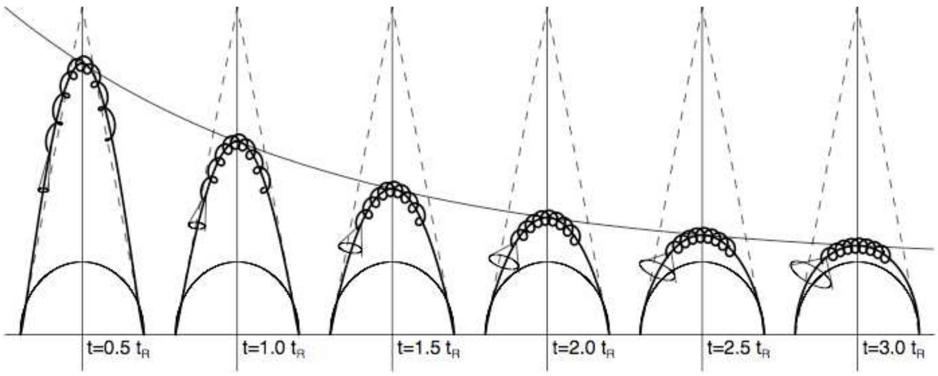

Figure 4.29: Scenario of field-line relaxation after an X-point reconnection, reproduced from Aschwanden (2004). The apex height of the field line relaxes exponentially into a force-free state from the initial cusp shape. In the process, the loss cone angle of the trapped particles gradually opens up and releases more particles from the trap.

As illustrated in Figure 4.29, the collapse or relaxation of a high-altitude loop into a low-altitude one due to reconnection can greatly expand the loss cone, which would then enhance the precipitation distribution if pitch angles were left unchanged (Aschwanden, 2004). As we understand it, such a collapse facilitates electrons, initially trapped in the coronal magnetic field, to precipitate into the chromosphere and photosphere. Observation in Hα (Uddin et al., 2004) of this flare, show the evolution of the filaments in the flaring region, changing from a potential configuration to a sigmoidal structure due of the high shearing of the magnetic field, with a post-flare relaxation of the magnetic field lines also observed in Hα. This suggests that the above scenario of electron injection could very well take place, making the electron precipitation process much more efficient.

4.4.5 Summary and Discussion

The standard flare scenario divides the flare process into a number of phases. In this scenario, the flare particles are accelerated to relativistic or super-relativistic velocities in the corona and injected into magnetic field loops whose footpoints are in active-region chromospheres. Inevitably, some particles are going to be trapped in the coronal magnetic field, while others, those in the magnetic loss cone, will precipitate directly into the chromosphere. Eventually the majority of the trapped particles are either scattered into the loss cone and precipitated, or thermalized (or both) by thermal plasma in the magnetic loop. In the case of the very sudden and impulsive flare of 10 March 2001, the hypothesis is that acceleration and injection of particles into the magnetic loop occurred in a short period of time (Uddin et al., 2004).

This kind of phenomenon can be described using the trapping and injection model proposed by Aschwanden (2004). In this model (Figure 4.29) the rate of precipitation of charged particles into the chromosphere is controlled by the relaxation time of the system. The aperture angle of the loss cone changes with time, significantly opening as the magnetic field collapses to a more potential configuration. It is important to note that in this model, the time of acceleration and injection of the particles into the magnetic field are almost the same and relatively short compared with the precipitation and trapping time. It is fair to assume that if the relaxation time is short, the aperture of the loss cone also will change rapidly, allowing more particles to reach the chromosphere in a short period of time. This depends on efficient scattering of high-energy electrons into the expanded loss cone, which is greatly enhanced by chromospheric ablation of thermal plasma into short, low-lying loops. Rapid evacuation of trapped electrons is suggested by observations of a rapid decay in non-thermal microwave emission. As a general rule, thermalization of particles in a magnetic trap is small compared to losses due to precipitation. Hence, high-energy electrons evacuated from the coronal loop in this way contribute to HXR bremsstrahlung emission substantially as well as their counterparts that were initially injected into the loss cone.

A much more complex model of particle precipitation, in which processes such as non-thermal excitation and ionization of hydrogen atoms, and non-thermal plasma heating (coulomb and ohmic) is explored by Aboudarham and Henoux (1986), Zharkova and Kobylinskii (1993), and Zharkova and Zharkov (2007). Interestingly, the latter show the ohmic heating of the corona by the electron beams is so effective that the corresponding particle-induced downward propagating shocks are almost depleted of energy, leaving very little energy to reach the photosphere and induce any kind of seismic activity. Perhaps this is the explanation for why we did not see any seismic sources at the location of the Hα K2 kernel in Figure 4.24. However, we also want emphasize here the possibility that photospheric heating also contributes to flare acoustic emission.

As the whole flaring process occurred relatively rapidly (and given the highly-impulsive properties of the 10 March 2001 flare, it is not unreasonable to assume so), the solar chromosphere was heated quite suddenly. The multi-wavelength emissions of the flare also clearly indicate this. Furthermore the strong spatial and temporal correspondence between the different types of emissions point to radiative back-warming playing a significant role in the heating mechanism. This conclusion was in fact drawn by both Li et al. (2005) and Ding et al. (2003) to explain the origin of the continuum feature of the 10 March 2001 flare in terms of an "electron-beam-heated flare model", with chromospheric radiative back-warming Machado et al. (1989), originating in the temperature-minimum region, being the chief heating agent.

The above conclusions, when viewed in conjunction with those of Donea and Lindsey (2005), Donea et al. (2006b), Moradi et al. (2007), and Martínez-Oliveros et al. (2007), provide direct evidence of flare acoustic emission being driven, in part, by heating of the low photosphere. The basic principle here is that the chromospheric radiation further heats up the photosphere, with the result being of an optically-thick H^- bound-free absorption, which then introduces a pressure transient directly to the underlying medium. The photospheric heating hypothesis is well supported by our observations and previous ones – which all indicate that instances of flare seismic emission have been characterized by a close spatial correspondence between the seismic emission and sudden white-light emission during the impulsive phase of the flare. Radiative fluxes characteristic of white-light emission seen in all acoustically active flares, if emitted downward from the chromosphere (as well as upwards) are probably sufficient to heat the photosphere a few percent within a few seconds of the onset of the incoming radiative flux.

According to rough models described by Donea et al. (2006b) and Moradi et al. (2007), such heating should cause a pressure transient in the heated layer that drives a seismic transient whose energy flux is of the order of those estimated for acoustically active flares. The energy invested into the seismic transient is in proportion to a fraction of $\delta I_c/I_c$ (the sudden component of fractional variation in the continuum intensity, I_c, over the emitting region) times the radiative energy suddenly emitted by the flare. We therefore expect acoustic emission due to photospheric heating to be inefficient in flares whose white-light signatures are weak, diffuse, or not very sudden, and this is consistent with all examples we have encountered to date.

At this point, our understanding of seismic emission from flares still remains relatively superficial. However, evidence for the general involvement of photospheric heating is now considerable. What is needed for further understanding is detailed modelling with a careful account of the physics, including radiative transfer and magnetic forces in realistic sunspot photospheres and sub-photospheres. The latter is particular important as most large solar flares are seismically inactive, which suggests that the strong magnetic fields of the hosting active regions may substantially alter the behaviour of helioseismic signals emerging from below. With such an understanding, acoustic emission from flares could contribute major benefits to seismic diagnostics of active region sub-photospheres.

Chapter 5

Summary and Perspective

In this final chapter, a summary of the research outcomes contained in Chapters 2, 3 and 4 are presented. We begin by giving a brief overview of the numerical simulations of ray and wave propagation in magnetized plasmas conducted in Chapter 2 and 3 of this thesis. This is followed by a summary of the main results and major insights into sunspot seismology that we have gained from them. We conclude by discussing some perspectives for future research in the field. In the next section, we highlight some of the main insights gained from our studies conducted in flare seismology in Chapter 4. We briefly review the observational attributes that now allow us to discriminate between acoustically active and inactive flares, and give a run down of the physical mechanisms that have now been proposed to explain the phenomena of flare-driven seismic waves.

5.1 Forward Modelling

Ever since the suggestion by Thomas et al. (1982) that waves could be used to investigate the structure and dynamics of sunspots, much effort has gone into theoretical studies and numerical simulations in order to better understand wave propagation in strongly magnetized fluids – a necessary condition for the application of local helioseismology to solar active regions. In thesis Chapters 2 and 3 we attempted to address some of the ambiguities and inconsistencies that exist in the local helioseismology of strong near-surface magnetic fields through numerical modelling of travel-time inhomogeneities in sunspots. We employed time-distance helioseismology as our preferred diagnostic tool and undertook a two-pronged approach to the numerical simulations.

Our first approach was largely motivated by the efficiency and accuracy of past applications of both MHD ray theory in probing near-surface dispersive mechanisms and mode conversion of magnetically coupled waves. If MHD ray theory could similarly be applied to numerical forward modelling, then this would provide us with a powerful, yet computationally inexpensive, diagnostic tool for sunspot seismology, including a possible application to future inverse methods. In order to facilitate this, we employed the eikonal approximation, in conjunction with the magneto-acoustic dispersion relation to model helioseismic ray propagation in a realistic and applicable sunspot model. Ray travel-time shifts were then modelled in a way to facilitate comparisons with observations made by time-distance helioseismology.

Our second approach was driven by our need for genuine artificial data sets that mimic helioseismic wave propagation in the near photospheric layers. This would allow for statistical studies of wave interactions with numerous imposed perturbations, as well as validating results obtained from the linear forward problem and MHD ray theory. To accomplish this, we used the existing 3D MHD code of Hanasoge (2007). This numerical forward model essentially follows the linear evolution of perturbations in an inhomogeneous, magnetized atmosphere – described by a flux tube embedded in a convectively and hydrostatically stable polytrope. We adopted a box geometry, with a spectral treatment in the horizontal directions, and a finite difference scheme for the vertical direction. The boundaries of the computational box consisted of periodic boundaries on the sides, while for the upper boundary we used the condition that the Lagrangian perturbation of the vertical component of the stress tensor vanishes. Time-distance helioseismology was again utilized to measure and analyse the wave travel-time inhomogeneities produced by induced perturbation in the model.

The simulations conducted in Chapters 2 and 4 together provided us with several related but distinct observations. First and foremost, we have demonstrated that MHD ray theory can now be confidently used in model sunspots to model travel-time inhomogeneities that can be effectively compared with both observations and MHD simulations. This is an important breakthrough that has many potential applications in the future, such as the development of magnetic sensitivity kernels for the inversion process. However, as the deep-focus measurements in Chapter 3 have shown, we must also bear in mind that ray theory ultimately departs significantly from wave theory as the perturbation becomes sub-wavelength in size.

With respect to the modelled travel-time shifts, we can confirm that many aspects of our results obtained through time-distance analysis – such as sensitivity of travel times to frequency and phase-speed filtering, and background power below the p_1-ridge – reflected actual observations of travel-time inhomogeneities in the vicinity of sunspots (Braun and Birch, 2006; Couvidat and Rajaguru, 2007; Braun and Birch, 2008). Overall, the (qualitative) similarity of time shifts between simulations and observations appears to suggest relative insensitivity of time-distance statistics to subtle aspects of flux tube structure. However, in order to quantify this, we would require more simulations with differing perturbations and have to delve into inversions and associated issues.

On the other hand, ray theory travel-time shifts were similarly dependent on frequency filtering, but the absence of phase-speed filtering in the process meant that ray theory time shifts were more predictable than their time-distance counterparts – particularly at small travel distances. Furthermore, ray theory simulations also allowed us to simultaneously examine the direct and indirect effects of the sunspot magnetic field, thus enabling us to partition the observed travel-time shifts in terms of their thermal and magnetic components. These simulations provided us with ample evidence that purely thermal perturbations are unlikely to be the main effect seen in surface-focused travel times through sunspots, with time shifts being overwhelmingly governed by MHD physics.

To sum it all up, we can now state with relative confidence that strong near-surface magnetic fields (in conjunction with phase-speed filtering) are directly and significantly altering the magnitude and lateral extent of inversions of sunspot structure made by time-distance helioseismology. The evidence against the "dual-layer" sub-surface structure of sunspots, derived from linear inversions of phase-speed filtered time-distance travel-time maps (i.e., Figure 1.8), is now overwhelming. Furthermore, the persistent large sound and wave speed perturbations produced by our model sunspots, coupled with the apparent non-linear nature of the observed travel-time shifts, indicates that we must now move beyond current linear inversion schemes which are derived under the assumption that sub-surface inhomogeneities are weak. Unlike in the case of convective flows, the effect of the magnetic field on helioseismic waves clearly cannot be considered to be small near the surface.

However, these results have also shown us that there is still lot of work that is needed to refine our techniques of data analysis and interpretation. Indeed, addressing some of the issues related to the use of phase-speed filtered data appears to be critical in discerning many of the inconsistencies between observations and modelling. Ridge-filtering (e.g., Braun and Birch, 2008; Jackiewicz et al., 2008; Thompson and Zharkov, 2008) provides us with a limited workaround, but does not address the issue at heart. Proper treatment of non-linear effects such as radiative transfer (Rajaguru et al., 2007) and mode conversion in magnetized plasma (Cally, 2007) are also an urgent necessity.

In fact, the latter appears to be a particularly pertinent issue given the recent results of Cally (2009b,a) which provides strong evidence for significant phase jumps (or discontinuities) associated with fast magneto-acoustic rays that penetrate the $a = c$ level in sunspots. This effect appears to be more pronounced in highly inclined field characteristic of penumbrae. Neglecting these effects could lead to significant misinterpretation of travel time-shifts observed by time-distance and helioseismic holography, as both methods work on the assumption that the phase is always continuous along a ray path joining two surface points. This could help explain puzzling surface observational phenomena, such as the "shower-glass" effect (Lindsey and Braun, 2005) and the "penumbral acoustic anomaly" (Schunker et al., 2005) – both produced by acute surface phase perturbations that obscure helioseismic observations, particularly in penumbrae.

But overall, we are making progress and must keep in mind that local helioseismology, in particular sunspot seismology, is relatively young field which is very much under development today and promises many more tantalizing discoveries. Indeed, some of the more ambitious goals for the not too distant future include, but are not limited to: the detection of longitudinal variations in the structure of the tachocline, producing reliable and self-consistent maps of 3D vector flows in the near-surface layers, and to also directly image the magnetic field in the solar interior. If measurable, this information would revolutionise our understanding of the structure and dynamics of sunspots and shed light on the true nature of sunspot structure below the solar surface: a monolithic, but inhomogeneous, magnetic flux tube? or, a tight cluster of smaller flux tubes separated by field-free plasma?

In late 2009, the Solar Dynamics Observatory (SDO) will be launched. Onboard will be the Helioseismic Magnetic Imager (HMI) – the first instrument specifically designed for local helioseismology – providing the next big technological step for helioseismology. With a high spatial resolution over the entire visible solar hemisphere, HMI will study solar oscillations and also provide high-cadence vector magnetic field measurements to aid helioseismic probing of sunspots and active region. One of the main scientific objectives of the instrument will be the study of the fine structure and the temporal evolution of magnetic regions in the upper convection zone. Within the next decade the Solar Orbiter satellite should also be launched, giving us access for the first time to the sub-surface structure and dynamics of the Sun's polar regions. Solar Orbiter's views of the far side of the Sun could also potentially be used in combination with other observations, allowing for stereoscopic local helioseismology which will enable us to probe deeper into the convection zone with improved resolution.

With these new observations, and recent advances in numerical forward modelling (Cameron et al., 2008; Moradi et al., 2009; Shelyag et al., 2009), modelling of entire sunspots by direct, realistic MHD simulations including radiative transfer (Heinemann et al., 2007; Rempel et al., 2009), coupled with ongoing progress in numerical simulations of magneto-convection (Stein et al., 2007) means that we are inching ever closer to identifying some of the underlying mechanisms that control the interplay between rotation, convection, and magnetism.

5.2 Flare Seismology

The detection of significant seismic emission from solar flares, or sunquakes, represents one of the most exciting developments in the field of local helioseismology, and solar physics as a whole. Recent developments in the study of flare acoustic emission presented in Chapter 4 encourage the view that the seismic emission from flares is a major discovery with a broad range of diagnostic and control applications for helioseismologists and flare analysts. Our understanding of the acoustics of solar flares has been greatly improved in recent years through a combination of observational and computational techniques, with the research outcomes presented in Chapter 4 now enabling us to confidently identify a number of distinct observational characteristics that distinguish acoustically active flares from others. We can briefly summarize some of these observations as follows :

- Flare seismic emissions are consistently associated with strong, downward-propagating shocks which start at the onset of the flare and are directly observed in Dopplergrams.
- Most large X-class solar flares appear to be acoustically inactive. For the few X- and M-class flares where significant acoustic emission was detected, only a very small fraction (a few hundred thousandths) of the energy released during the flare is related to the seismic emission that radiates into the sub-photosphere, or to the seismic waves propagating into the solar interior.
- The sites of seismic emission generally coincide spatially with impulsive HXR and microwave emissions, suggesting a relation to thick-target heating of the chromosphere by energetic particles.
- The sites of seismic emission similarly coincide spatially with impulsive continuum emission, suggesting acoustic emission associated with extra heating and ionization of the low photosphere.
- The location of these compact seismic sources is only occasionally associated with signatures of high-energy protons (γ-ray emission) in the footpoints of magnetic loops that mark precipitation of high-energy particles (e.g., the large X10 and X17-class flares of October 2003).
- There appears to be a significant inverse correlation between seismicity of active regions and the heights of the coronal magnetic loops that conduct high-energy particles. Shorter coronal loops are more likely to be conducive to a more rapid injection of trapped, high-energy electrons into the chromosphere at their footpoints. This enhances the magnitude and suddenness of the chromospheric heating that gives a rise to the intense visible continuum emission seen in all acoustically active flares.
- Apparent magnetic transients in GONG and MDI magnetograms suggest the possibility of seismic emission due to sudden shifts in magnetic tension forces in the photosphere as a result of reconnection.

At this point in time however, we cannot categorically claim that prospective contributions to seismic emission from flares are exhausted. For example, Ambastha et al.

(2003) and Ambastha et al. (2004) have used ring-diagram analysis to study the effect of flares on solar oscillation modes, reporting an increase in p-mode power associated with the flaring region. However, it is difficult to draw any significant connections between these results and those obtained through holography, as deeper analysis and more detailed comparisons are required. But nonetheless, the above-listed characteristics, coupled with abundant supporting observational signatures presented in this thesis, have gone a long way in corroborating certain hypotheses regarding the underlying physical mechanism behind the flare seismic emission process, while at the same time, repudiating others.

Kosovichev and Zharkova (1995, 1998) strongly favoured the notion that sunquakes were produced by chromospheric shocks driven by sudden, thick-target heating of the upper and middle chromosphere. This process states that seismic emissions into the solar interior are the continuation of a chromospheric shock and condensation resulting from explosive ablation of the chromosphere and propagating downward through the photosphere into the underlying solar interior. Chromospheric shocks are well known under such circumstances, based on red-shifted Hα emission at the flare site at the onset of the flare. The simulations were worked out at length by Fisher et al. (1985a,b,c) and others since.

The hypothesis that the observed photospheric emission is a direct continuation of such shocks was also considered by Donea and Lindsey (2005) and Kosovichev (2006). However, looking at the statistics of acoustically active events (Donea et al., 2006a; Besliu-Ionescu et al., 2006, 2008a,b), we must acknowledge that most solar flares do not produce sunquakes. This leads us to believe that, for the majority of flares, strong radiative damping depletes the chromospheric transient before its arrival at the low photosphere, thus the amount of energy that penetrates through the photosphere is insufficient to explain the helioseismic observations (Fisher et al., 1985a; Ding and Fang, 1994; Allred et al., 2005).

Having observed signatures of high-energy protons in the large X10 and X17- class flares of October 2003, Donea and Lindsey (2005), and later Zharkova and Zharkov (2007), suggested that seismic emissions could be induced via direct photospheric heating caused by protons penetrating into the low photosphere. However, the observational signatures of high-energy protons in seismically active flares are very rare. As we have seen in the analyses of the X-class flare of 15 January 2005 and the M-class flares 14 August 2004 and 10 March 2001, there are no indications of high-energy protons that could directly supply the energy required to induce a seismic transient into the solar interior. Likewise, energetic electrons, consistent with HXR signatures, appear to be physically unable to penetrate into the low photosphere in anywhere near sufficient numbers required to account for the direct heating needed by the seismic sources (Metcalf et al., 1990). However, the strong coincidence between the locations of sudden white-light emission and seismic emission in all acoustically active flares led Donea et al. (2006b) to propose that a substantial component of the seismic emission seen is a result of sudden heating of the low photosphere associated with the observed excess of visible continuum emission (radiative back-warming).

The origin of white-light emission would have to be entirely in the chromosphere, where energetic electrons dissipate their energy (Metcalf et al., 1990; Zharkova and Kobylinskii, 1991, 1993), mainly by ionizing previously neutral chromospheric hydrogen approximately to the depth of the temperature minimum. It appears that the low photosphere itself would be significantly heated as well – primarily the result of Balmer and Paschen continuum edge recombination radiation from the overlying ionized chromospheric medium. Once the transient penetrates substantially beneath the photosphere, the highly opaque ionized hydrogen blocks any significant radiative losses and allows the transient to continue undamped on its journey, until its next encounter with the solar surface. Fully consistent with the results presented in Chapter 4 of this thesis, and indeed the observational signatures of all reported flare seismic emissions to date (Lindsey and Donea, 2008), this mechanism certainly provides the most compelling scenario to explain the phenomenon of sunquakes.

Recently however, Hudson et al. (2008) have speculated that Lorentz force transients, produced by a process known as the "McClymont magnetic jerk", can account for the seismic activity of some flares. The hypothesis behind the McClymont jerk process is that the transients shifts in the magnetic signatures during the impulsive phase of seismically active flares are the result of flare-related magnetic reconnection. Indeed, transient shifts in magnetic signatures have been detected in numerous flares, some of which were acoustically active (e.g., Donea et al., 2006b; Martínez-Oliveros et al., 2007, 2008b,a) and others which were not (e.g., Zharkova and Kosovichev, 2002). Hudson et al. (2008) estimate the mechanical work that would be done on the photosphere by a sudden shift in magnetic inclination consistent with magnetic signatures. Their energy estimates appeared to be similar to those based on helioseismic observations.

However, Martínez-Oliveros et al. (2008a) recently applied the magnetic jerk hypothesis to the seismically active flare of 15 January 2005, and from their analysis, the authors concluded that this process can only partly account for the helioseismic observations of the seismic source. There are also concerns as to whether the magnetic signatures are the result of real changes in the photospheric magnetic field (Donea et al., 2006b; Moradi et al., 2007). Kosovichev and Zharkova (2001) also reported similar magnetic signatures in flares and expressed concerns about possible effects of an inversion of the Ni I 6768 Å line as a result of heating of the solar atmosphere by high-energy particles. Sudol and Harvey (2005) likewise found transient magnetic signatures in flaring photospheres. Qiu and Gary (2003) attribute the sign reversal in the MDI magnetic signature of an impulsive flare to radiative-transfer effect. Clearly, these are concerns that need to be considered.

In conclusion, it must be stated that no one, single mechanism can fully explain the mechanics of flare acoustics and their observational signatures – because to do so would be a gross over-simplification of the problem. What these results have shown us is that the study of flare mechanics, as well as helioseismology, would greatly benefit from the development of detailed models of the flare-induced seismic transients. Detailed models would need to take account for how these acoustic transients are generated, how they propagate from the corona down to the photosphere, and how they are injected into the underlying solar interior. The latter would no doubt require realistic models of active region sub-photospheres, including a full account of sub-surface thermal anomalies and magnetic fields in particular, as the existence of highly inclined magnetic fields in regions from which white-light flares generally occur are certain to be important in the flare acoustics.

The good news is that such modelling efforts are well under way. In fact, as is self-evident in Chapter 3 of this thesis, numerical simulations of helioseismic wave propagation through realistic sunspot sub-photospheres are now, not only feasible, but successfully implemented and verified. Modelling of particle acceleration and chromospheric heating in seismically active flares are also in their early stages. Besliu-Ionescu et al. (in preparation) are currently working on reproducing the observational signatures of chromospheric heating in seismically active flares using the RADYNE code of Carlsson and Stein (1994), while numerical simulations of stochastic particle acceleration and energy loss in the solar corona (using the time-dependent Fokker-Planck code of Hamilton et al., 1990) are also ongoing (Martinez-Oliveros et al., in preparation). Preliminary results from the latter appear to strongly support the notion that low-in-altitude coronal magnetic loop configurations significantly expedite the scattering of trapped high-energy electrons into magnetic loss cones, and their rapid precipitation into the upper layers of the chromosphere. Initial estimates appear to show that this will likely increase both the intensity and suddenness of the chromospheric heating, satisfying the basic conditions for an acoustic emission that penetrates into the solar interior. So it appears that we are on the threshold of being able to accurately reproduce some of the main observational characteristics associated with seismically active flares. Couple this with the improved observational capabilities expected in the very near future, courtesy of the soon-to-be-launched SDO satellite, and the future certainly looks bright for flare seismology.

Bibliography

Aboudarham, J. and Henoux, J. C. (1986). Energy deposit at temperature minimum level and white light flares. A&A, 156:73–78.

Allred, J. C., Hawley, S. L., Abbett, W. P., and Carlsson, M. (2005). Radiative Hydrodynamic Models of the Optical and Ultraviolet Emission from Solar Flares. ApJ, 630:573–586.

Ambastha, A. (2008). Helioseismic effects of energetic transients. *Journal of Astrophysics and Astronomy*, 29:93–101.

Ambastha, A., Basu, S., and Antia, H. M. (2003). Flare-Induced Excitation of Solar p modes. Sol. Phys., 218:151–172.

Ambastha, A., Basu, S., Antia, H. M., and Bogart, R. S. (2004). Solar P-Mode Characteristics Associated with Superactive-Regions Observed during OCT NOV 2003. In Danesy, D., editor, *SOHO 14 Helio- and Asteroseismology: Towards a Golden Future*, volume 559 of *ESA Special Publication*, page 293.

Ambastha, A., Hagyard, M. J., and West, E. A. (1993). Evolutionary and flare-associated magnetic shear variations observed in a complex, flare-productive active region. Sol. Phys., 148:277–299.

Asai, A., Yokoyama, T., Shimojo, M., Masuda, S., Kurokawa, H., and Shibata, K. (2004). Flare Ribbon Expansion and Energy Release Rate. ApJ, 611:557–567.

Aschwanden, M. J. (2004). Pulsed Particle Injection in a Reconnection-Driven Dynamic Trap Model in Solar Flares. ApJ, 608:554–561.

Barnes, G. and Cally, P. S. (2001). Frequency Dependent Ray Paths in Local Helioseismology. *Publications of the Astronomical Society of Australia*, 18:243–251.

Bastian, T. S., Benz, A. O., and Gary, D. E. (1998). Radio Emission from Solar Flares. ARA&A, 36:131–188.

Basu, S. and Antia, H. M. (1997). Seismic measurement of the depth of the solar convection zone. MNRAS, 287:189–198.

Basu, S., Antia, H. M., and Bogart, R. S. (2004). Ring-Diagram Analysis of the Structure of Solar Active Regions. ApJ, 610:1157–1168.

Basu, S., Antia, H. M., and Tripathy, S. C. (1999). Ring Diagram Analysis of Near-Surface Flows in the Sun. ApJ, 512:458–470.

Beatty, J. K. and Beatty, J. K. (2007). Encyclopedia of the Solar System, Second Edition, by Lucy-Ann McFadden, Paul R. Weissman, and Torrence V. Johnson. S&T, 114(1):010000.

Benz, A. O. (2008). Flare Observations. *Living Reviews in Solar Physics*, 5:1.

Besliu-Ionescu, D., Donea, A., and Cally, P. (2008a). A Comparison of the Acoustic Hardness of Acoustically Active and Non-Active Solar Flares. In *American Institute of Physics Conference Series*, volume 1043 of *American Institute of Physics Conference Series*, pages 252–255.

Besliu-Ionescu, D., Donea, A.-C., Cally, P., and Lindsey, C. (2006). Seismic emission from M-class solar flares. In *Proceedings of SOHO 18/GONG 2006/HELAS I, Beyond the spherical Sun*, volume 624 of *ESA Special Publication*.

Besliu-Ionescu, D., Donea, A.-C., Cally, P., and Lindsey, C. (2008b). Recent Developments in Solar Quakes Studies. In Howe, R., Komm, R. W., Balasubramaniam, K. S., and Petrie, G. J. D., editors, *Subsurface and Atmospheric Influences on Solar Activity*, volume 383 of *Astronomical Society of the Pacific Conference Series*, page 297.

Biermann, L. (1941). *Vierteljahresschrift der Astronomischen Gesellschaft*, 76:194.

Birch, A. C. (2004). The Current Status of Theory for Time-Distance Helioseismology. In *ESA SP-559: SOHO 14 Helio- and Asteroseismology: Towards a Golden Future*, page 138.

Birch, A. C. and Kosovichev, A. G. (2000). Travel Time Sensitivity Kernels. Sol. Phys., 192:193–201.

Bogdan, T. J. (1997). A Comment on the Relationship between the Modal and Time-Distance Formulations of Local Helioseismology. ApJ, 477:475.

Bogdan, T. J. (2000). Sunspot Oscillations: A Review - (Invited Review). Sol. Phys., 192:373–394.

Bogdan, T. J., Brown, T. M., Lites, B. W., and Thomas, J. H. (1993). The absorption of p-modes by sunspots - Variations with degree and order. ApJ, 406:723–734.

Bogdan, T. J. and Cally, P. S. (1997). Waves in magnetized polytropes. *Royal Society of London Proceedings Series A*, 453:943–961.

Bogdan, T. J., Hindman, B. W., Cally, P. S., and Charbonneau, P. (1996). Absorption of p-Modes by Slender Magnetic Flux Tubes and p-Mode Lifetimes. ApJ, 465:406.

Braun, D. C. (1995). Scattering of p-Modes by Sunspots. I. Observations. ApJ, 451:859.

Braun, D. C. (1997). Time-Distance Sunspot Seismology with GONG Data. ApJ, 487:447.

Braun, D. C. and Birch, A. C. (2006). Observed Frequency Variations of Solar p-Mode Travel Times as Evidence for Surface Effects in Sunspot Seismology. ApJ, 647:L187–L190.

Braun, D. C. and Birch, A. C. (2008). Surface-Focused Seismic Holography of Sunspots: I. Observations. Sol. Phys., 251:267–289.

Braun, D. C., Birch, A. C., Benson, D., Stein, R. F., and Nordlund, Å. (2007). Helioseismic Holography of Simulated Solar Convection and Prospects for the Detection of Small-Scale Subsurface Flows. ApJ, 669:1395–1405.

Braun, D. C. and Duvall, Jr., T. L. (1990). P-mode absorption in the giant active region of 10 March, 1989. Sol. Phys., 129:83–94.

Braun, D. C., Duvall, Jr., T. L., and Labonte, B. J. (1987). Acoustic absorption by sunspots. ApJ, 319:L27–L31.

Braun, D. C., Duvall, Jr., T. L., and Labonte, B. J. (1988). The absorption of high-degree p-mode oscillations in and around sunspots. ApJ, 335:1015–1025.

Braun, D. C., Duvall, Jr., T. L., Labonte, B. J., Jefferies, S. M., Harvey, J. W., and Pomerantz, M. A. (1992). Scattering of p-modes by a sunspot. ApJ, 391:L113–L116.

Braun, D. C. and Lindsey, C. (1999). Helioseismic Images of an Active Region Complex. ApJ, 513:L79–L82.

Brown, J. C. (1971). The Deduction of Energy Spectra of Non-Thermal Electrons in Flares from the Observed Dynamic Spectra of Hard X-Ray Bursts. Sol. Phys., 18:489–502.

Brown, T. M., Christensen-Dalsgaard, J., Dziembowski, W. A., Goode, P., Gough, D. O., and Morrow, C. A. (1989). Inferring the sun's internal angular velocity from observed p-mode frequency splittings. ApJ, 343:526–546.

Brüggen, M. and Spruit, H. C. (2000). The sign of temperature inhomogeneities deduced from time-distance helioseismology. Sol. Phys., 196:29–40.

Cally, P. S. (1995). Effects of Weak-to-Moderate Vertical Magnetic Fields on Solar f- and p-Modes. ApJ, 451:372.

Cally, P. S. (2000). Modelling p-Mode Interaction with a Spreading Sunspot Field. Sol. Phys., 192:395–401.

Cally, P. S. (2001). Note on an Exact Solution for Magnetoatmospheric Waves. ApJ, 548:473–481.

Cally, P. S. (2005). Local magnetohelioseismology of active regions. MNRAS, 358:353–362.

Cally, P. S. (2006). Dispersion relations, rays and ray splitting in magnetohelioseismology. *Royal Society of London Philosophical Transactions Series A*, 364:333–349.

Cally, P. S. (2007). What to look for in the seismology of solar active regions. *Astronomische Nachrichten*, 328:286.

Cally, P. S. (2009a). Magnetic and Thermal Phase Shifts in Local Helioseismology. MNRAS *in press*.

Cally, P. S. (2009b). Phase Jumps in Time-Distance Helioseismology. Sol. Phys. *in press*.

Cally, P. S. and Bogdan, T. J. (1993). Solar p-modes in a vertical magnetic field - Trapped and damped pi-modes. ApJ, 402:721–732.

Cally, P. S. and Bogdan, T. J. (1997). Simulation of f- and p-Mode Interactions with a Stratified Magnetic Field Concentration. ApJ, 486:L67.

Cally, P. S., Bogdan, T. J., and Zweibel, E. G. (1994). Umbral oscillations in sunspots: Absorption of p-modes and active region heating by mode conversion. ApJ, 437:505–521.

Cally, P. S., Crouch, A. D., and Braun, D. C. (2003). Probing sunspot magnetic fields with p-mode absorption and phase shift data. MNRAS, 346:381–389.

Cally, P. S. and Goossens, M. (2008). Three-Dimensional MHD Wave Propagation and Conversion to Alfvén Waves near the Solar Surface. I. Direct Numerical Solution. Sol. Phys., 251:251–265.

Cameron, R., Gizon, L., and Daiffallah, K. (2007). SLiM: a code for the simulation of wave propagation through an inhomogeneous, magnetised solar atmosphere. *Astronomische Nachrichten*, 328:313.

Cameron, R., Gizon, L., and Duvall, Jr., T. L. (2008). Helioseismology of Sunspots: Confronting Observations with Three-Dimensional MHD Simulations of Wave Propagation. Sol. Phys., 251:291–308.

Canfield, R. C., Gunkler, T. A., and Ricchiazzi, P. J. (1984). The H-alpha spectral signatures of solar flare nonthermal electrons, conductive flux, and coronal pressure. ApJ, 282:296–307.

Carlsson, M. and Stein, R. F. (1994). Radiation shock dynamics in the solar chromosphere - results of numerical simulations. In Carlsson, M., editor, *Chromospheric Dynamics*, page 47.

Carmichael, H. (1964). A Process for Flares. In Hess, W. N., editor, *The Physics of Solar Flares*, page 451.

Carrington, R. C. (1859). Description of a Singular Appearance seen in the Sun on September 1, 1859. MNRAS, 20:13–15.

Chandra, R., Jain, R., Uddin, W., Yoshimura, K., Kosugi, T., Sakao, T., Joshi, A., and Deshpande, M. R. (2006). Energetics and Dynamics of an Impulsive Flare on March 10, 2001. Sol. Phys., 239:239–256.

Charbonneau, P., Christensen-Dalsgaard, J., Henning, R., Larsen, R. M., Schou, J., Thompson, M. J., and Tomczyk, S. (1999). Helioseismic Constraints on the Structure of the Solar Tachocline. ApJ, 527:445–460.

Chen, Q. R. and Ding, M. D. (2006). Footpoint Motion of the Continuum Emission in the 2002 September 30 White-Light Flare. ApJ, 641:1217–1221.

Chou, D.-Y., Chang, H.-K., Sun, M.-T., Labonte, B., Chen, H.-R., Yeh, S.-J., and The TON Team (1999). Acoustic Imaging in Helioseismology. ApJ, 514:979–988.

Christensen-Dalsgaard, J. (2002). Helioseismology. *Reviews of Modern Physics*, 74:1073–1129.

Christensen-Dalsgaard, J., Duvall, Jr., T. L., Gough, D. O., Harvey, J. W., and Rhodes, Jr., E. J. (1985). Speed of sound in the solar interior. Nature, 315:378–382.

Christensen-Dalsgaard, J., Gough, D. O., and Thompson, M. J. (1991). The depth of the solar convection zone. ApJ, 378:413–437.

Christensen-Dalsgaard, J., et al. (1996). The Current State of Solar Modeling. *Science*, 272:1286.

Claverie, A., Isaak, G. R., McLeod, C. P., van der Raay, H. B., and Cortes, T. R. (1979). Solar structure from global studies of the 5-minute oscillation. Nature, 282:591–594.

Couvidat, S. and Birch, A. C. (2006). Optimal Gaussian Phase-Speed Filters in Time-Distance Helioseismology. Sol. Phys., 237:229–243.

Couvidat, S., Birch, A. C., and Kosovichev, A. G. (2006). Three-dimensional Inversion of Sound Speed below a Sunspot in the Born Approximation. ApJ, 640:516–524.

Couvidat, S., Birch, A. C., Kosovichev, A. G., and Zhao, J. (2004). Three-dimensional Inversion of Time-Distance Helioseismology Data: Ray-Path and Fresnel-Zone Approximations. ApJ, 607:554–563.

Couvidat, S. and Rajaguru, S. P. (2007). Contamination by Surface Effects of Time-Distance Helioseismic Inversions for Sound Speed beneath Sunspots. ApJ, 661:558–567.

Cowling, T. G. (1976). *Magnetohydrodynamics.* Monographs on Astronomical Subjects, Bristol: Adam Hilger, 1976.

Crouch, A. D. and Cally, P. S. (2003). Mode Conversion of Solar p Modes in non-Vertical Magnetic Fields - i. two-Dimensional Model. Sol. Phys., 214:201–226.

Crouch, A. D. and Cally, P. S. (2005). Mode Conversion of Solar p-Modes in Non-Vertical Magnetic Fields. Sol. Phys., 227:1–26.

Crouch, A. D., Cally, P. S., Charbonneau, P., Braun, D. C., and Desjardins, M. (2005). Genetic magnetohelioseismology with Hankel analysis data. MNRAS, 363:1188–1204.

Deforest, C. E. (2004). On Re-sampling of Solar Images. Sol. Phys., 219:3–23.

Deubner, F.-L. (1975). Observations of low wavenumber nonradial eigenmodes of the sun. A&A, 44:371–375.

Deubner, F.-L. and Gough, D. (1984). Helioseismology: Oscillations as a Daignostic of the Solar Interior. ARA&A, 22:593–619.

Ding, M. D. and Fang, C. (1994). On the propagation of chromospheric condensations in solar flares (1): Dynamic simulations. Ap&SS, 213:233–246.

Ding, M. D., Liu, Y., Yeh, C.-T., and Li, J. P. (2003). Interpretation of the infrared continuum in a solar white-light flare. A&A, 403:1151–1156.

Donea, A. C., Besliu-Ionescu, D., Cally, P., and Lindsey, C. (2006a). New Detection of Acoustic Signatures from Solar Flares. In Leibacher, J., Stein, R. F., and Uitenbroek, H., editors, *Solar MHD Theory and Observations: A High Spatial Resolution Perspective*, volume 354 of *Astronomical Society of the Pacific Conference Series*, page 204.

Donea, A.-C., Besliu-Ionescu, D., Cally, P. S., Lindsey, C., and Zharkova, V. V. (2006b). Seismic Emission from A M9.5-Class Solar Flare. Sol. Phys., 239:113–135.

Donea, A.-C., Braun, D. C., and Lindsey, C. (1999). Seismic Images of a Solar Flare. ApJ, 513:L143–L146.

Donea, A.-C. and Lindsey, C. (2004). Seismic Waves from the Solar Flares of 2003 October 28 and 29. In Danesy, D., editor, *SOHO 14 Helio- and Asteroseismology: Towards a Golden Future*, volume 559 of *ESA Special Publication*, page 152.

Donea, A.-C. and Lindsey, C. (2005). Seismic Emission from the Solar Flares of 2003 October 28 and 29. ApJ, 630:1168–1183.

D'Silva, S. (1996). Theoretical Foundations of Time-Distance Helioseismology. ApJ, 469:964.

D'Silva, S., Duvall, Jr., T. L., Jefferies, S. M., and Harvey, J. W. (1996). Helioseismic Tomography. ApJ, 471:1030.

Duvall, T. L., Jefferies, S. M., Harvey, J. W., and Pomerantz, M. A. (1993). Time-distance helioseismology. Nature, 362:430–432.

Duvall, Jr., T. L. (1995). Time-Distance Helioseismology: an Update. In Ulrich, R. K., Rhodes, Jr., E. J., and Dappen, W., editors, *GONG 1994. Helio- and Astro-Seismology from the Earth and Space*, volume 76 of *Astronomical Society of the Pacific Conference Series*, page 465.

Duvall, Jr., T. L. (2003). Nonaxisymmetric variations deep in the convection zone. In Sawaya-Lacoste, H., editor, *GONG+ 2002. Local and Global Helioseismology: the Present and Future*, volume 517 of *ESA Special Publication*, pages 259–262.

Duvall, Jr., T. L., Kosovichev, A. G., Scherrer, P. H., Bogart, R. S., Bush, R. I., de Forest, C., Hoeksema, J. T., Schou, J., Saba, J. L. R., Tarbell, T. D., Title, A. M., Wolfson, C. J., and Milford, P. N. (1997). Time-Distance Helioseismology with the MDI Instrument: Initial Results. Sol. Phys., 170:63–73.

Duvall, T. L. J., D'Silva, S., Jefferies, S. M., Harvey, J. W., and Schou, J. (1996). Downflows Under Sunspots Detected by Helioseismic Tomography. Nature, 379:235.

Evans, J. W. and Michard, R. (1962). Observational Study of Macroscopic Inhomogeneities in the Solar Atmosphere. I. Velocity Displacements of Fraunhofer Lines as a Function of Line Strength and Position on Disk. ApJ, 135:812.

Fan, Y., Braun, D. C., and Chou, D.-Y. (1995). Scattering of p-Modes by Sunspots. II. Calculations of Phase Shifts from a Phenomenological Model. ApJ, 451:877.

Fisher, G. H., Canfield, R. C., and McClymont, A. N. (1985a). Flare Loop Radiative Hydrodynamics - Part Seven - Dynamics of the Thick Target Heated Chromosphere. ApJ, 289:434.

Fisher, G. H., Canfield, R. C., and McClymont, A. N. (1985b). Flare Loop Radiative Hydrodynamics - Part Six - Chromospheric Evaporation due to Heating by Nonthermal Electrons. ApJ, 289:425.

Fisher, G. H., Canfield, R. C., and McClymont, A. N. (1985c). Flare loop radiative hydrodynamics. V - Response to thick-target heating. VI - Chromospheric evaporation due to heating by nonthermal electrons. VII - Dynamics of the thick-target heated chromosphere. ApJ, 289:414–441.

Georgobiani, D., Zhao, J., Kosovichev, A. G., Benson, D., Stein, R. F., and Nordlund, Å. (2007). Local Helioseismology and Correlation Tracking Analysis of Surface Structures in Realistic Simulations of Solar Convection. ApJ, 657:1157–1161.

Giles, P. (1999). Time-distnace measurements of large scale flows in the solar convection zone. *Ph.D. Thesis*.

Gizon, L. and Birch, A. C. (2002). Time-Distance Helioseismology: The Forward Problem for Random Distributed Sources. ApJ, 571:966–986.

Gizon, L. and Birch, A. C. (2005). Local Helioseismology. *Living Reviews in Solar Physics*, 2:6.

Gizon, L., Hanasoge, S. M., and Birch, A. C. (2006). Scattering of Acoustic Waves by a Magnetic Cylinder: Accuracy of the Born Approximation. ApJ, 643:549–555.

Goldreich, P. and Kumar, P. (1988). The interaction of acoustic radiation with turbulence. ApJ, 326:462–478.

Gough, D. O. (1984). On the rotation of the sun. *Royal Society of London Philosophical Transactions Series A*, 313:27–38.

Grechnev, V. V. (2003). A method to analyze imaging radio data on solar flares. Sol. Phys., 213:103–110.

Haber, D. A., Hindman, B. W., Toomre, J., Bogart, R. S., Larsen, R. M., and Hill, F. (2002). Evolving Submerged Meridional Circulation Cells within the Upper Convection Zone Revealed by Ring-Diagram Analysis. ApJ, 570:855–864.

Haber, D. A., Toomre, J., and Hill, F. (1988). Response of the Solar 5-MINUTE Oscillations to a Major Flare. In Christensen-Dalsgaard, J. and Frandsen, S., editors, *Advances in Helio- and Asteroseismology*, volume 123 of *IAU Symposium*, page 59.

Hamilton, R. J., Lu, E. T., and Petrosian, V. (1990). Numerical solution of the time-dependent kinetic equation for electrons in magnetized plasma. ApJ, 354:726–734.

Hanasoge, S. M. (2007). *Theoretical studies of wave interactions in the sun*. PhD thesis, Stanford University.

Hanasoge, S. M. (2008). Seismic Halos around Active Regions: A Magnetohydrodynamic Theory. ApJ, 680:1457–1466.

Hanasoge, S. M., Couvidat, S., Rajaguru, S. P., and Birch, A. C. (2008). Impact of locally suppressed wave sources on helioseismic traveltimes. MNRAS, page 1291.

Hanasoge, S. M. and Duvall, Jr., T. L. (2007). The solar acoustic simulator: applications and results. *Astronomische Nachrichten*, 328:319.

Hanasoge, S. M., Duvall, Jr., T. L., and Couvidat, S. (2007). Validation of Helioseismology through Forward Modeling: Realization Noise Subtraction and Kernels. ApJ, 664:1234–1243.

Hanasoge, S. M., Larsen, R. M., Duvall, Jr., T. L., DeRosa, M. L., Hurlburt, N. E., Schou, J., Roth, M., Christensen-Dalsgaard, J., and Lele, S. K. (2006). Computational Acoustics in Spherical Geometry: Steps toward Validating Helioseismology. ApJ, 648:1268–1275.

Hansen, S. C. and Cally, P. S. (2009). An Exact Test of Generalized Ray Theory in Local Helioseismology. Sol. Phys. *in press*.

Heinemann, T., Nordlund, Å., Scharmer, G. B., and Spruit, H. C. (2007). MHD Simulations of Penumbra Fine Structure. ApJ, 669:1390–1394.

Hill, F. (1988). Rings and trumpets - Three-dimensional power spectra of solar oscillations. ApJ, 333:996–1013.

Hirayama, T. (1974). Theoretical Model of Flares and Prominences. I: Evaporating Flare Model. Sol. Phys., 34:323–338.

Hudson, H. S., Fisher, G. H., and Welsch, B. T. (2008). Flare Energy and Magnetic Field Variations. In Howe, R., Komm, R. W., Balasubramaniam, K. S., and Petrie, G. J. D., editors, *Subsurface and Atmospheric Influences on Solar Activity*, volume 383 of *Astronomical Society of the Pacific Conference Series*, page 221.

Hughes, S. J., Rajaguru, S. P., and Thompson, M. J. (2005). Comparison of GONG and MDI: Sound-Speed Anomalies beneath Two Active Regions. ApJ, 627:1040–1048.

Jackiewicz, J., Gizon, L., and Birch, A. C. (2008). High-Resolution Mapping of Flows in the Solar Interior: Fully Consistent OLA Inversion of Helioseismic Travel Times. Sol. Phys., 251:381–415.

Jensen, J. M., Duvall, Jr., T. L., Jacobsen, B. H., and Christensen-Dalsgaard, J. (2001). Imaging an Emerging Active Region with Helioseismic Tomography. ApJ, 553:L193–L196.

Jensen, J. M., Jacobsen, B., and Christensen-Dalsgaard, J. (2000). Sensitivity Kernels for Time-Distance Inversion. Sol. Phys., 192:231–239.

Jensen, J. M. and Pijpers, F. P. (2003). Sensitivity kernels for time-distance inversion based on the Rytov approximation. A&A, 412:257–265.

Karoff, C. (2008). On Flare Driven Global Waves. *ArXiv e-prints*.

Karoff, C. and Kjeldsen, H. (2008). Evidence That Solar Flares Drive Global Oscillations in the Sun. ApJ, 678:L73–L76.

Khomenko, E. and Collados, M. (2006). Numerical Modeling of Magnetohydrodynamic Wave Propagation and Refraction in Sunspots. ApJ, 653:739–755.

Khomenko, E., Collados, M., and Felipe, T. (2008a). Nonlinear Numerical Simulations of Magneto-Acoustic Wave Propagation in Small-Scale Flux Tubes. Sol. Phys., 251:589–611.

Khomenko, E., Kosovichev, A., Collados, M., Parchevsky, K., and Olshevsky, V. (2008b). Theoretical modeling of propagation of magneto-acoustic waves in magnetic regions below sunspots. *ArXiv e-prints*.

Komm, R., Corbard, T., Durney, B. R., González Hernández, I., Hill, F., Howe, R., and Toner, C. (2004). Solar Subsurface Fluid Dynamics Descriptors Derived from Global Oscillation Network Group and Michelson Doppler Imager Data. ApJ, 605:554–567.

Kopp, R. A. and Pneuman, G. W. (1976). Magnetic reconnection in the corona and the loop prominence phenomenon. Sol. Phys., 50:85–98.

Kosovichev, A. G. (1996). Tomographic Imaging of the Sun's Interior. ApJ, 461:L55+.

Kosovichev, A. G. (2006). Properties of Flares-Generated Seismic Waves on the Sun. Sol. Phys., 238:1–11.

Kosovichev, A. G. and Duvall, T. L. (1997). Acoustic tomography of solar convective flows and structures. In *ASSL Vol. 225: SCORe'96 : Solar Convection and Oscillations and their Relationship*, pages 241–260.

Kosovichev, A. G., Duvall, T. L. . J., and Scherrer, P. H. (2000). Time-Distance Inversion Methods and Results - (Invited Review). Sol. Phys., 192:159–176.

Kosovichev, A. G. and Zharkova, V. V. (1995). Seismic response to solar flares: theoretical predictions. In *4. SOHO Workshop Helioseismology, Vol. 2, p. 341 - 344*, volume 2, pages 341–344.

Kosovichev, A. G. and Zharkova, V. V. (1998). X-ray Flare Sparks Quake Inside the Sun. Nature, 393:317.

Kosovichev, A. G. and Zharkova, V. V. (2001). Magnetic Energy Release and Transients in the Solar Flare of 2000 July 14. ApJ, 550:L105–L108.

Kundu, M. R., White, S. M., Shibasaki, K., Sakurai, T., and Grechnev, V. V. (2001). Spatial Structure of Simple Spiky Bursts at Microwave/Millimeter Wavelengths. ApJ, 547:1090–1099.

Kurokawa, H. (1987). Two distinct morphological types of magnetic shear development and their relation to flares. Sol. Phys., 113:259–263.

Kurokawa, H., Wang, T., and Ishii, T. T. (2002). Emergence and Drastic Breakdown of a Twisted Flux Rope to Trigger Strong Solar Flares in NOAA Active Region 9026. ApJ, 572:598–608.

Leighton, R. B., Noyes, R. W., and Simon, G. W. (1962). Velocity Fields in the Solar Atmosphere. I. Preliminary Report. ApJ, 135:474.

Lele, S. K. (1992). Compact Finite Difference Schemes with Spectral-like Resolution. *Journal of Computational Physics*, 103:16.

Li, J. P., Ding, M. D., and Liu, Y. (2005). Occurrence of a White-Light Flare Over a Sunspot and the Associated Change of Magnetic Flux. Sol. Phys., 229:115–125.

Lindsey, C. and Braun, D. C. (1997). Helioseismic Holography. ApJ, 485:895.

Lindsey, C. and Braun, D. C. (1999). Chromatic Holography of the Sunspot Acoustic Environment. ApJ, 510:494–504.

Lindsey, C. and Braun, D. C. (2000). Basic Principles of Solar Acoustic Holography - (Invited Review). Sol. Phys., 192:261–284.

Lindsey, C. and Braun, D. C. (2005). The Acoustic Showerglass. I. Seismic Diagnostics of Photospheric Magnetic Fields. ApJ, 620:1107–1117.

Lindsey, C. and Donea, A.-C. (2008). Mechanics of Seismic Emission from Solar Flares. Sol. Phys., 251:627–639.

Liu, Y., Ding, M. D., and Fang, C. (2001). Enhanced Emission at the Infrared Continuum in the Flare of 2001 March 10. ApJ, 563:L169–L172.

Machado, M. E., Emslie, A. G., and Avrett, E. H. (1989). Radiative backwarming in white-light flares. Sol. Phys., 124:303–317.

Magara, T., Mineshige, S., Yokoyama, T., and Shibata, K. (1996). Numerical Simulation of Magnetic Reconnection in Eruptive Flares. ApJ, 466:1054.

Marquering, H., Dahlen, F. A., and Nolet, G. (1999). Three-dimensional sensitivity kernels for finite-frequency traveltimes: the banana-doughnut paradox. *Geophysical Journal International*, 137:805–815.

Martínez-Oliveros, J. C., Donea, A.-C., Cally, P. S., and Moradi, H. (2008a). Helioseismic analysis of the solar flare-induced sunquake of 2005 January 15 - II. A magnetoseismic study. MNRAS, 389:1905–1910.

Martínez-Oliveros, J. C., Moradi, H., Besliu-Ionescu, D., Donea, A.-C., Cally, P. S., and Lindsey, C. (2007). From Gigahertz to Millihertz: A Multiwavelength Study of the Acoustically Active 14 August 2004 M7.4 Solar Flare. Sol. Phys., 245:121–139.

Martínez-Oliveros, J. C., Moradi, H., and Donea, A.-C. (2008b). Seismic Emissions from a Highly Impulsive M6.7 Solar Flare. Sol. Phys., 251:613–626.

Martinez Pillet, V. (1997). Polarimetric Measurements of Sunspots. In Schmieder, B., del Toro Iniesta, J. C., and Vazquez, M., editors, *1st Advances in Solar Physics Euroconference. Advances in Physics of Sunspots*, volume 118 of *Astronomical Society of the Pacific Conference Series*, page 212.

Metcalf, T. R., Alexander, D., Hudson, H. S., and Longcope, D. W. (2003). TRACE and Yohkoh Observations of a White-Light Flare. ApJ, 595:483–492.

Metcalf, T. R., Canfield, R. C., and Saba, J. L. R. (1990). Flare heating and ionization of the low solar chromosphere. II - Observations of five solar flares. ApJ, 365:391–406.

Mickey, D. L., Canfield, R. C., Labonte, B. J., Leka, K. D., Waterson, M. F., and Weber, H. M. (1996). The Imaging Vector Magnetograph at Haleakala. Sol. Phys., 168:229–250.

Moradi, H. and Cally, P. S. (2008). Time-Distance Modelling in a Simulated Sunspot Atmosphere. Sol. Phys., 251:309–327.

Moradi, H., Donea, A.-C., Lindsey, C., Besliu-Ionescu, D., and Cally, P. S. (2007). Helioseismic analysis of the solar flare-induced sunquake of 2005 January 15. MNRAS, 374:1155–1163.

Moradi, H., Hanasoge, S. M., and Cally, P. S. (2009). Numerical Models of Travel-Time Inhomogeneities in Sunspots. ApJ, 690:L72–L75.

Neupert, W. M. (1968). Comparison of Solar X-Ray Line Emission with Microwave Emission during Flares. ApJ, 153:L59+.

Orszag, S. A. (1970). Analytical theories of turbulence. *Journal of Fluid Mechanics*, 41:363–386.

Parchevsky, K. V. and Kosovichev, A. G. (2007a). Effect of Suppressed Excitation on the Amplitude Distribution of 5 Minute Oscillations in Sunspots. ApJ, 666:L53–L56.

Parchevsky, K. V. and Kosovichev, A. G. (2007b). Three-dimensional Numerical Simulations of the Acoustic Wave Field in the Upper Convection Zone of the Sun. ApJ, 666:547–558.

Parker, E. N. (1957). Sweet's Mechanism for Merging Magnetic Fields in Conducting Fluids. J. Geophys. Res., 62:509–520.

Parker, E. N. (1975). The Nature of the Sunspot Phenomenon. IV: The Intrinsic Instability of the Magnetic Configuration. Sol. Phys., 40:291–301.

Petschek, H. E. (1964). Magnetic Field Annihilation. In Hess, W. N., editor, *The Physics of Solar Flares*, page 425.

Pneuman, G. W. (1981). *Two-ribbon flares - Post-flare loops*, pages 379–428. Solar Flare Magnetohydrodynamics.

Podesta, J. J. (2003). The analogy between sunquakes and water waves. Sol. Phys., 218:227–246.

Qiu, J. and Gary, D. E. (2003). Flare-related Magnetic Anomaly with a Sign Reversal. ApJ, 599:615–625.

Rajaguru, S. P. (2008). Separating surface magnetic effects in sunspot seismology: new time-distance helioseismic diagnostics. *ArXiv e-prints*, 802.

Rajaguru, S. P., Birch, A. C., Duvall, Jr., T. L., Thompson, M. J., and Zhao, J. (2006). Sensitivity of Time-Distance Helioseismic Measurements to Spatial Variation of Oscillation Amplitudes. I. Observations and a Numerical Model. ApJ, 646:543–552.

Rajaguru, S. P., Sankarasubramanian, K., Wachter, R., and Scherrer, P. H. (2007). Radiative Transfer Effects on Doppler Measurements as Sources of Surface Effects in Sunspot Seismology. ApJ, 654:L175–L178.

Rempel, M., Schüssler, M., and Knölker, M. (2009). Radiative Magnetohydrodynamic Simulation of Sunspot Structure. ApJ, 691:640–649.

Ricchiazzi, P. J. and Canfield, R. C. (1983). A static model of chromospheric heating in solar flares. ApJ, 272:739–755.

Riethmüller, T. L., Solanki, S. K., Zakharov, V., and Gandorfer, A. (2008). Brightness, distribution, and evolution of sunspot umbral dots. A&A, 492:233–243.

Roddier, F. (1975). Principle of production of an acoustic hologram of the solar surface. *Academie des Science Paris Comptes Rendus Serie B Sciences Physiques*, 281:93–95.

Rosenthal, C. S. and Julien, K. A. (2000). Numerical Modeling of the Absorption and Scattering of Acoustic Radiation by Sunspots. ApJ, 532:1230–1239.

Sakurai, T. (1982). Green's Function Methods for Potential Magnetic Fields. Sol. Phys., 76:301–321.

Sato, J., Kosugi, T., and Makishima, K. (1999). Improvement of YOHKOH Hard X-Ray Imaging. PASJ, 51:127–150.

Scherrer, P. H., Bogart, R. S., Bush, R. I., Hoeksema, J. T., Kosovichev, A. G., Schou, J., Rosenberg, W., Springer, L., Tarbell, T. D., Title, A., Wolfson, C. J., Zayer, I., and MDI Engineering Team (1995). The Solar Oscillations Investigation - Michelson Doppler Imager. Sol. Phys., 162:129–188.

Schlüter, A. and Temesváry, S. (1958). The Internal Constitution of Sunspots. In Lehnert, B., editor, *Electromagnetic Phenomena in Cosmical Physics*, volume 6 of *IAU Symposium*, page 263.

Schou, J. and Bogart, R. S. (1998). Flow and Horizontal Displacements from Ring Diagrams. ApJ, 504:L131+.

Schunker, H., Braun, D. C., Cally, P. S., and Lindsey, C. (2005). The Local Helioseismology of Inclined Magnetic Fields and the Showerglass Effect. ApJ, 621:L149–L152.

Schunker, H. and Cally, P. S. (2006). Magnetic field inclination and atmospheric oscillations above solar active regions. MNRAS, 372:551–564.

Shearer, P. (1999). *Introduction to Seismology*. Introduction to Seismology, by Peter Shearer, pp. 272. ISBN 0521660238. Cambridge, UK: Cambridge University Press, September 1999.

Shelyag, S., Erdélyi, R., and Thompson, M. J. (2007). Forward modelling of sub-photospheric flows for time-distance helioseismology. A&A, 469:1101–1107.

Shelyag, S., Zharkov, S., Fedun, V., Erdelyi, R., and Thompson, M. J. (2009). Acoustic wave propagation in the solar sub-photosphere with localised magnetic field concentration: effect of magnetic tension. *ArXiv e-prints*.

Solanki, S. K. (2003). Sunspots: An overview. A&A Rev., 11:153–286.

Spruit, H. C. (1991). Absorption of p-Mode Waves by Magnetic Fields. In Gough, D. and Toomre, J., editors, *Challenges to Theories of the Structure of Moderate-Mass Stars*, volume 388 of *Lecture Notes in Physics, Berlin Springer Verlag*, pages 121–134.

Spruit, H. C. and Bogdan, T. J. (1992). The conversion of p-modes to slow modes and the absorption of acoustic waves by sunspots. ApJ, 391:L109–L112.

Stein, R. F., Benson, D., and Nordlund, A. (2007). Solar Magneto-Convection Simulations. In Shibata, K., Nagata, S., and Sakurai, T., editors, *New Solar Physics with Solar-B Mission*, volume 369 of *Astronomical Society of the Pacific Conference Series*, page 87.

Stein, R. F. and Nordlund, Å. (2000). Realistic Solar Convection Simulations. Sol. Phys., 192:91–108.

Stein, R. F. and Nordlund, Å. (2006). Solar Small-Scale Magnetoconvection. ApJ, 642:1246–1255.

Steiner, O. (2007). Recent progresses in the simulation of small-scale magnetic fields. In Kneer, F., Puschmann, K. G., and Wittmann, A. D., editors, *Modern solar facilities - advanced solar science*, page 321.

Sturrock, P. A. (1966). Model of the High-Energy Phase of Solar Flares. Nature, 211:695.

Sudol, J. J. and Harvey, J. W. (2005). Longitudinal Magnetic Field Changes Accompanying Solar Flares. ApJ, 635:647–658.

Sweet, P. A. (1958). The Neutral Point Theory of Solar Flares. In Lehnert, B., editor, *Electromagnetic Phenomena in Cosmical Physics*, volume 6 of *IAU Symposium*, page 123.

Thomas, J. H., Cram, L. E., and Nye, A. H. (1982). Five-minute oscillations as a subsurface probe of sunspot structure. Nature, 297:485–487.

Thomas, J. H. and Weiss, N. O. (1992). The theory of sunspots. In Thomas, J. H. and Weiss, N. O., editors, *NATO ASIC Proc. 375: Sunspots. Theory and Observations*, pages 3–59.

Thomas, J. H. and Weiss, N. O. (2004). Fine Structure in Sunspots. ARA&A, 42:517–548.

Thompson, M. J. and Zharkov, S. (2008). Recent Developments in Local Helioseismology. Sol. Phys., 251:225–240.

Tobias, S. and Weiss, N. (2004). Sunspots: The puzzling structure of a sunspot. *Astronomy and Geophysics*, 45(4):040000–4.

Tracy, E. R., Kaufman, A. N., and Brizard, A. J. (2003). Ray-based methods in multidimensional linear wave conversion. *Physics of Plasmas*, 10:2147–2154.

Turck-Chièze, S., Couvidat, S., Kosovichev, A. G., Gabriel, A. H., Berthomieu, G., Brun, A. S., Christensen-Dalsgaard, J., García, R. A., Gough, D. O., Provost, J., Roca-Cortes, T., Roxburgh, I. W., and Ulrich, R. K. (2001). Solar Neutrino Emission Deduced from a Seismic Model. ApJ, 555:L69–L73.

Uddin, W., Jain, R., Yoshimura, K., Chandra, R., Sakao, T., Kosugi, T., Joshi, A., and Despande, M. R. (2004). Multi-Wavelength Observations of an Unusual Impulsive Flare Associated with Cme. Sol. Phys., 225:325–336.

Ulrich, R. K. (1970). The Five-Minute Oscillations on the Solar Surface. ApJ, 162:993.

Wang, H., Liu, C., Deng, Y., and Zhang, H. (2005). Reevaluation of the Magnetic Structure and Evolution Associated with the Bastille Day Flare on 2000 July 14. ApJ, 627:1031–1039.

Weinberg, S. (1962). Eikonal Method in Magnetohydrodynamics. *Physical Review*, 126:1899–1909.

Werne, J., Birch, A., and Julien, K. (2004). The Need for Control Experiments in Local Helioseismology. In *ESA SP-559: SOHO 14 Helio- and Asteroseismology: Towards a Golden Future*, page 172.

Wolff, C. L. (1972). Free Oscillations of the Sun and Their Possible Stimulation by Solar Flares. ApJ, 176:833.

Woodard, M. F. (1997). Implications of Localized, Acoustic Absorption for Heliotomographic Analysis of Sunspots. ApJ, 485:890.

Zhao, J., Georgobiani, D., Kosovichev, A. G., Benson, D., Stein, R. F., and Nordlund, Å. (2007). Validation of Time-Distance Helioseismology by Use of Realistic Simulations of Solar Convection. ApJ, 659:848–857.

Zhao, J. and Kosovichev, A. G. (2006). Surface Magnetism Effects in Time-Distance Helioseismology. ApJ, 643:1317–1324.

Zhao, J., Kosovichev, A. G., and Duvall, T. L. (2001). Investigation of Mass Flows beneath a Sunspot by Time-Distance Helioseismology. ApJ, 557:384–388.

Zhao, L. and Jordan, T. H. (1998). Sensitivity of frequency-dependent traveltimes to laterally heterogeneous, anisotropic Earth structure. *Geophysical Journal International*, 133:683–704.

Zharkov, S., Nicholas, C. J., and Thompson, M. J. (2007). Time distance study of isolated sunspots. *Astronomische Nachrichten*, 328:240–244.

Zharkov, S. and Thompson, M. J. (2008). Time Distance Analysis of the Emerging Active Region NOAA 10790. Sol. Phys., 251:369–380.

Zharkova, V. V. and Gordovskyy, M. (2004). Particle Acceleration Asymmetry in a Reconnecting Nonneutral Current Sheet. ApJ, 604:884–891.

Zharkova, V. V. and Kobylinskii, V. A. (1991). Investigation of Nonthermal Excitation and Ionization of Hydrogen in Low-Temperature Flare Plasma - Part Two - Computational Method. *Soviet Astronomy Letters*, 17:34.

Zharkova, V. V. and Kobylinskii, V. A. (1993). The effect of non-thermal excitation and ionization on the hydrogen emission in impulsive solar flares. Sol. Phys., 143:259–274.

Zharkova, V. V. and Kosovichev, A. G. (2002). Fast magnetic field variations associated with solar flares. In Wilson, A., editor, *From Solar Min to Max: Half a Solar Cycle with SOHO*, volume 508 of *ESA Special Publication*, pages 159–162.

Zharkova, V. V. and Zharkov, S. I. (2007). On the Origin of Three Seismic Sources in the Proton-rich Flare of 2003 October 28. ApJ, 664:573–585.

Zwaan, C. (1978). On the Appearance of Magnetic Flux in the Solar Photosphere. Sol. Phys., 60:213–240.